THÈSE

En vue de l'obtention de

L'HABILITATION À DIRIGER LES RECHERCHES DE L'UNIVERSITÉ DE TOULOUSE

Délivré par : *l'Institut National Polytechnique de Toulouse (INP Toulouse)*

Présentée et soutenue le *27 novembre 2017* **par :**

Florent DUCHAINE

High Performance Code Coupling for multiphysics and multicomponent simulations in fluid dynamics

---

JURY

Eric Lamballais	Professeur - Université de Poitiers	Rapporteur
Isabelle Trebinjac	Professeure - Ecole Centrale de Lyon	Rapporteur
Denis Veynante	Directeur de recherche CNRS - EM2C	Rapporteur
Marc Errera	Maître de recherche - ONERA	Membre du Jury
Marc C. Jacob	Professeur - ISAE-SUPAERO	Membre du Jury
Thierry Poinsot	Professeur - IMFT	Correspondant

École doctorale et spécialité :
MEGEP : Dynamique des fluides
Unité de Recherche :
Centre Européen de Recherche et de Formation Avancée en Calcul Scientifique
Correspondant :
Thierry Poinsot

Contents

Remerciements

L'année 2017 aura été particulièrement riche avec dans le désordre : l'entrée en maternelle de ma première fille (Fig. 1 - gauche), la naissance de ma seconde fille (juste après avoir remis ce manuscrit dans les mains de mon correspondant Thierry Poinsot, Fig. 1 - droite), mes 10 ans de thèse, mon passage de grade d'instructeur de l'*escola de Capoeira Senzala Toulouse* (Fig. 2) et l'obtention de l'habilitation à diriger des recherches.

Figure 1: Correction de mon manuscrit d'HDR par ma première fille (gauche), promenade avec ma seconde fille (droite).

Figure 2: Passage de grade d'instructeur de l'*escola de Capoeira Senzala Toulouse*, mars 2017.

Un grand merci tout d'abord à ma femme Mélanie pour son aide et son soutien précieux dans la réalisation des divers projets dans lesquels je m'investis. Merci de m'apporter des réponses aux questions que je me pose, de me poser les questions qui m'aident à avancer. Toute ma gratitude va également à la familia Senzala Toulouse pour me donner la motivation d'aller toujours plus haut, toujours plus loin, sans oublier qu'HDR veut probablement signifier dans le contexte de la Capoeira : Habilitation à Diriger des Rodas !

Merci à Thierry Poinsot de m'avoir soutenu, poussé et challengé tout au long de mon parcours depuis ma thèse jusqu'au passage de cet ultime diplôme. J'en profite pour remercier Laurent Gicquel pour tous les échanges et les travaux que l'on a pu faire depuis ma thèse. J'apprends beaucoup avec toi, tant sur le plan scientifique qu'éducation des enfants ou des doctorants ;). Je n'aurais pu aborder tous les points décrits dans ce manuscrit sans les collaborations avec les stagiaires, doctorants et post-doctorants avec qui j'ai eu la chance de travailler. Merci à vous, à la dynamique que nous avons pu avoir et que j'espère continuer dans le future notamment grâce à l'HDR : Frédéric, Damien, Jorge, Elena, Matthieu, Nicolas, Francis, Stéphan, Charlie, Adrien, Gaofeng, Adèle, Thomas, Dimitrios, Raphael, Sandrine, Maxence, Gauthier, Sebastian, Pierre, Thomas (encore), Daniel, Nikolaos, Abdula, Luis, Jérôme, Martin, Luc, Mael, Lancelot, Nicolas (un autre), Soizic.

Je tiens également à remercier Madame I. Trébinjac ainsi que Messieurs E. Lamballais et D. Veynante pour avoir accepté le rôle de rapporteur de ce manuscrit. J'associe à ces remerciements Messieurs M. Errera et M. Jacob pour avoir examiné mes travaux durant la soutenance. Je suis très honoré que ces grands scientifiques aient participé à l'évaluation de mes travaux.

Mes pensées se dirigent également vers l'ensemble des personnes qui travaillent au Cerfacs et qui participent à en faire un super lieu pour s'épanouir : les collègues scientifiques, le formidable groupe de support informatique et également le staff administratif (merci spécialement pour l'organisation de la journée d'HDR !!). La seule personne que je citerai ici est Thierry Morel qui m'a supporté toutes ces années dans son bureau. J'ai dis la seule personne, je transgresse, merci à Jean-Claude André de m'avoir fait confiance en m'embauchant au Cerfacs en 2010 et ainsi permis de faire ce parcours. Je continue, toujours sans citer de nom afin d'être certain de n'oublier personne, par remercier tous les collaborateurs académiques et industriels avec qui j'interagi.

Enfin merci aux amis et notamment Nico et Antho (Fig. 3) qui m'ont fait le plaisir de venir à la soutenance.

Figure 3: Antho et Nico.

La soutenance et la séance de questions sont disponibles en streaming vidéo sur le site internet du Cerfacs : https://typhon.cerfacs.fr/videos/?video=MEDIA171128103544320

Introduction

This manuscript is an overview of the research activities realized mainly at Cerfacs. These works are the results of collaborations either with Cerfacs researchers (permanents, post-docs, PhD and trainees) or people from other laboratories. The main drivers of the activities are the needs for research in the aeronautical and spatial propulsion fields with strong interactions with industries of the sector.

The common points of interest between all the presented research activities are the analysis, understanding and predictions of turbulent flows with heat transfer in propulsion devices. My PhD topic (defended) in 2007 was the integration of a RANS (Reynolds Averaged Navier-Stokes) combustion solver in an optimization loop to provide a knowledge-based design system for engineers. Later, my research interests have focused on the use of Large Eddy Simulation (LES) to solve turbulent flow fields in complex geometries. The interaction with optimization science and RANS simulations was limited to specific actions and comparisons with LES.

Today, my activities are mainly oriented toward the study of turbulent reacting flows and their interaction with solid parts. Multiphysics and multi-components analysis emanating from these topics are done thanks to High Performance Computing (HPC). Indeed, addressing turbulent reactive flow phenomenon in complex geometries is CPU intensive requiring HPC systems to reduce restitution times. The principal investigations concern:

- turbulent flow fields analyzes and wall heat flux predictions with Large Eddy Simulation,
- conjugate heat transfer methodologies with unsteady flow solvers involving convection, conduction and radiation,
- coupling methodologies between unsteady flow solvers for multi-components simulations,
- code coupling on massively parallel architectures.

The first part of this manuscript presents key achievements in these fields, focusing first on heat transfer predictions with LES. The characterization of heat transfer in some specific configurations of gas turbine components is provided to support the methodologies developed and used. In the same chapter, the strategies employed to solve conjugate heat transfer problems will be introduced and illustrated on relevant problems. Then, the multi-component activities through fluid/fluid coupling will be presented on the basis of combustion chamber / turbine interactions. The tool developed in this context will be presented along with some academic and applied test cases. The first part is concluded by outcomes on code coupling on massively parallel computers.

The second part of the manuscript presents the *Curriculum Vitae* as well as administrative materials. After my PhD, I have conducted my research activities with PhD and post-doctoral students. Their contribution was an essential part of my work and they are listed in chapter 7. I have now co-directed 11 PhD students, 10 master trainees and 5 post-doctorates. This strong interaction with students is a key aspect in my research motivation and the reason why I present an *Habilitation à Diriger des Recherches*. Finally, the last part provides the list of publications (37 peer review journal papers accepted, H factor from Web Of Science: 10).

Part I

Research activities

Chapter 1

Introduction and impact of the research activities

A long term goal of my research activities is to perform an integrated numerical simulation of a full gas turbine (compressor / combustion chamber / turbine + temperature field in walls) using high-fidelity CFD methods (mainly LES: Large Eddy Simulation) for all components. This Cerfacs' challenge named Cougar started in 2011. The optimization of future aircraft engines will be based on highly detailed CFD simulations for compressor, combustion chamber and turbine. This requires coupling these simulations, something which is almost impossible on existing machines today: running simultaneous LES codes for compressor, combustor and turbine on a parallel architecture up to 500 000 cores is the ultimate challenge of 2020 for HPC but also for industry where such coupled simulations will provide keys to produce competitive engines. To optimize engines, the precise operational margin of each element must be known and this is impossible if all elements are not coupled. For example the temperature of the first stages of the turbine depends directly on the unsteady hot flow of burnt gases leaving the combustor. Predicting the lifetime of the turbine within 50 % accuracy requires to predict the temperature of the blades within a range of the order of 25 K. This is impossible if the inlet temperatures for the turbine computation are not obtained by a simultaneous coupled computation of the combustor and the turbine. Even though the ultimate objective of Cougar is to compute the full turbine, several validation steps are essential such as:

- accurate predictions of flow fields and wall heat transfer with unstructured meshes used for complex geometries,
- increase understanding of wall heat transfer mechanisms and relations with flow fields,
- development and assessment of coupling strategies for conjugate heat transfer with LES,
- development and assessment of coupling strategies for multi-components simulations with LES,
- validation of LES methodologies for turbomachinery stage simulations including near-wall turbulence models for flow and heat transfer,
- post-processing of complex turbulent flows in turbomachinery to extract relevant physical informations from the huge amount of data produced by LES.

Therefore, my long term objective (full engine simulation actually leads to a series of smaller fundamental research problems which I have tackled one by one. This has required to use a reliable high order CFD solver for compressible reacting flows: most simulations presented in this manuscript have been obtained with the LES solver AVBP co-developed by Cerfacs and IFP-En [92, 210] which is a world-standard code in the field of LES. It is an explicit solver based on hybrid grids which resolves the compressible Navier-Stokes equations in a multi-species reacting mixture. Its main features involve unstructured mesh capacities, advanced

LES modeling, non reflecting boundary conditions, multispecies gas formulations (to account for variable heat capacities and mixing in the turbine stages), turbulent combustion models, reduced and analytical chemistry ... AVBP has been tested on most biggest parallel architectures of the Top500. Its efficiency has been tested up to 200 000 processors. OpenPALM, the coupling software co-developed by Cerfacs and ONERA is used to couple code elements on parallel systems since different codes (or different instances of the same code) are used for each component of the gas turbine and must communicate on a single large machine.

The research areas investigated during my career are linked to the use of LES in a coupled context. To do so, work on technical aspects of high performance computing is also required to reduce restitution times, numerical issues of code coupling as well as physical interpretation of the simulations. The main achievements presented in this manuscript, illustrated on Fig. 1.1, concern:

- the characterization of gas turbine components thermal environment including heat transfer predictions as well as conjugate heat transfer methodologies,
- combustion chamber and turbine stage interactions focusing on LES characterization in turbomachinery,
- computer science issues linked to high performance code coupling.

The fundings of these actions came from European projects (COPA-GT, FACTOR), French projects (SIMACO3FI, ELCI, CASCADE, STRASS, TIMBER) and from direct links with industrial partners of Cerfacs. In these topics, the researches performed at Cerfacs have a strong impact on the scientific community as shown by the number of journal publications (36 accepted) and communications in conferences (44) as well as by the reviewing activities. The impact is also important in industries as Cerfacs partners such as Safran use the tools inherited from these studies and Safran's competitors are very attentive on our activities.

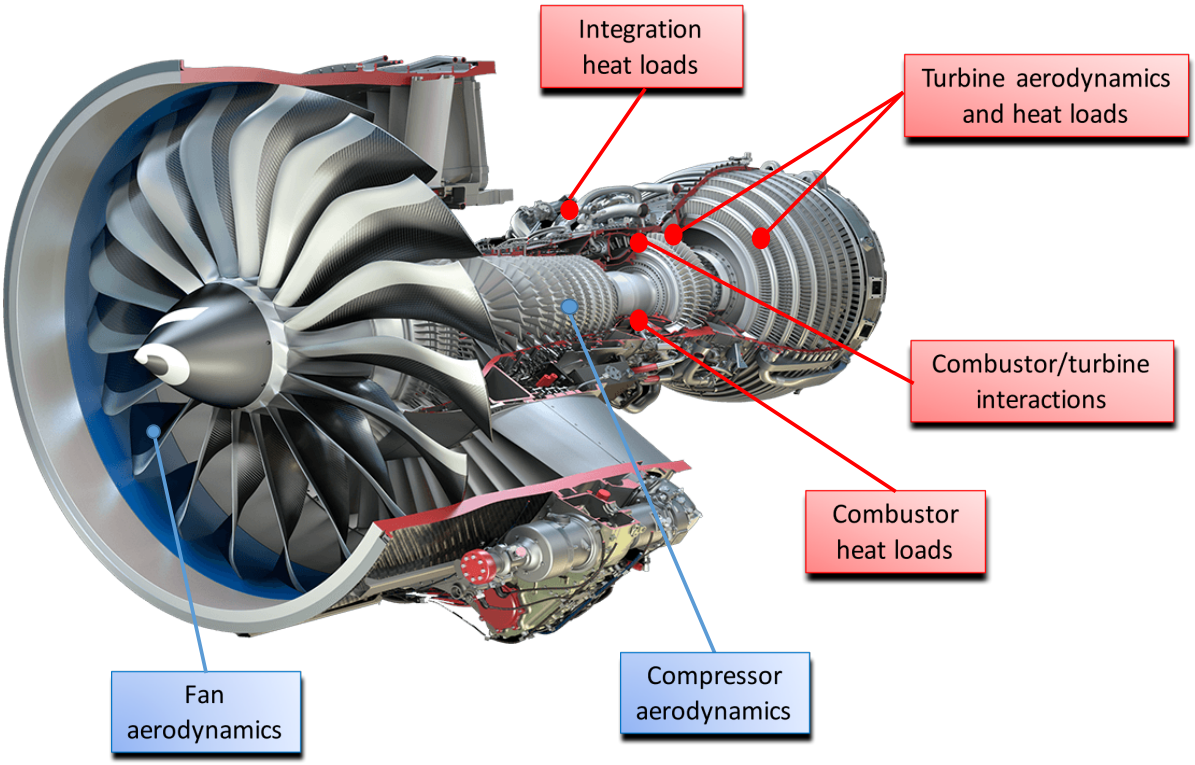

Figure 1.1: Sketch of the LEAP engine (Courtesy of Safran) describing the main zones of interest for my research activity along with the study areas.

Chapter 2

Characterization of thermal environment in gas turbine components

Determination of heat loads, as wall temperatures and heat fluxes, is a key issue in combustion applications [157, 165, 230, 74, 28]: the interaction of hot gases and reacting flows with colder walls is an important phenomenon in combustion chambers and a main design constraint in gas turbines. After combustion, the interaction of the hot burnt gases with the high pressure stator and the first turbine blades conditions the temperature and pressure levels reached in the combustor, and therefore the engine efficiency. The knowledge of the thermal environment is thus of primary importance in design phases of gas turbine component. Numerical simulations of the thermal interaction between fluid flows and solids offer new design paths to diminish development costs through important reductions of the number of experimental tests.

Moreover, wall temperatures can affect the flow fields especially when combustion is considered. For example, thermal environnement plays a key role in flame stabilization: different wall temperatures can lead to different flame patterns and localizations [235, 151, 104]. Additionally, the flame response to external forcing such as acoustics is largely influenced by its stabilization process and thus by the thermal environment [68, 151, 177, 176]. Such combustion problems are thus fully coupled since flame stabilization influences thermal environment through convection, radiation and conduction and wall temperature dictates back flow features and influences flame stabilization.

As a result modeling requires first the accurate prediction of heat fluxes (convection and radiation) as well as the joint resolution of fluid and solid parts. Turbulent heat transfer in industrial configurations usually occurs in complex geometries where flow separation and vortex shedding take place. For example, in a turbo-engine nacelle compartment, the thermal integration of some dissipative equipment (valves, pumps, generator, etc.) requires to use models to assess convective, conductive and radiative heat transfer. Those equipments represent bluff-bodies that sometimes must be air-cooled to be protected from internal heat loads and/or from the strong heat flux coming from the engine case. An accurate prediction of the local convective heat transfer is crucial to design and optimize the cooling system with the double objective of improving the equipment reliability and preserving the aircraft performance. Such prediction requires a computational method that captures accurately the aerodynamic features of the flow: back flows, vortex shedding, wakes, mixing, interactions, etc. Large eddy simulation approach is a promising method because of its ability to solve explicitly these large scale motions. The aim of this work is to develop a LES methodology that can be applied to convective heat transfer problems in industrial configurations. This methodology must guaranty a given precision at a controlled CPU cost. For the targeted problems, a special attention must be paid to the near-wall modeling. Using enough grid resolution and a proper sub-grid model, LES can behave like direct numerical simulation (DNS) when approaching the wall boundary. Thus, a wall-resolved LES should accurately predict the wall heat flux in any flow configuration without any specific

wall treatment. However, its computational cost may be very expensive for high Reynolds flows because solving the boundary layer leads to large computational grids and small time steps. The least expensive way to account for near-wall effects in LES is to model the boundary layer using a wall-function [250, 42, 209, 130]. Such an approach has been implemented and tested with AVBP in a complex geometry LES calculation by Schmitt *et al.* [235]. Nevertheless, in a typical industrial geometry where flow separation occurs, the validity of wall-function approaches is questionable[1].

For most industrial internal flows, the physical domain cannot be meshed using a structured grid and requires an unstructured grid composed of tetrahedral elements. This choice has a strong impact on the numerical approach itself. For the same spatial resolution, an unstructured grid calculation is usually more expensive and less accurate than a calculation on a structured grid. The choice of the best LES model, the grid refinement criterion, the type of wall modeling, etc., also depend on the type of grid and working with unstructured grids makes all developments complicated.

Before being applied to real cases and complex geometries, the present approach must be validated for heat transfer prediction in simple well-documented configurations. The first section of this chapter illustrates the approach used for heat transfer prediction and characterization in a wall-resolved context with the goal to assess precision on selected cases representative of the research in the field. The second section presents conjugate heat transfer methodology development for LES and examples of application.

2.1 Heat transfer predictions

Since 2007, I have been involved in the characterization of LES solvers to predict wall heat transfer. The two main solvers I worked with are AVBP (CERFACS and IPF-En) and YALES2 (CORIA). Thanks to the different researches and applied projects I was involved in, I had the opportunity to collaborate with other institutions leading to comparisons between different solvers such as: ONERA (elsA [30] and CEDRE [224]), CTR (Charles [29]), Airbus (Fluent), Cenaero (Argo [52]). Many different configurations have been studied during my research works, from low to high Reynolds and Mach numbers. The goals of these studies were to gain insights on the flow physics on the treated cases as well to provide computational guidelines for the flow solvers in terms of numerical and physical parameters. This section first illustrates the use of LES for aerothermal predictions in academic square cylinders flows with low Reynolds and Mach numbers. Then, examples when increasing the Reynolds and Mach numbers are proposed with low pressure and high pressure turbine cascades. These configurations are still far from industrial flows but provide good estimates in terms of computational methodologies and efforts to accurately predict heat transfer complex geometries. These studies lead to methodologies to predict heat transfer with a high degree of fidelity with a LES solver in a wall-resolved context. Based on this capability, an important aspect is the use of the large amount of unsteady data provided by LES to deeper analyze the flow physics. The last point presented in this section concerns the strong coupling between the thermal environment and and aerodynamics in specific conditions such as rotating as well as reactive flows which illustrates the need for conjugate heat transfer simulations to accurately predict some flow features.

2.1.1 Low Reynolds and Mach number flows

Among low Reynolds and Mach number flows occurring in gas turbines, I participated to study heat transfers in several configurations. A representative selection is proposed to illustrate the methodologies and results: nacelle mounted systems (academic configurations of square

[1]Turbulence experts will certainly want to discuss the validity of wall-law approaches versus wall-resolved models. Even if we recognize the interest of this discussion, it will not be a major axis of this manuscript. Our approach has been to use wall-resolved simulations every time is was possible and to switch to wall-laws in other cases.

cylinder [22] and tandem of square cylinders [67]), cooling technologies (ribbed channel [237, 236, 102] and impinging jets [245, 1, 2, 3]) and low pressure turbines [71].

Flow past a square cylinder

The methodology to capture heat fluxes with a high degree of fidelity was first established on the academic test of flow past a square cylinder. This work performed in collaboration with Airbus has been published in AIAA Journal [22]. Such a configuration was found to be a good candidate for the validation of forced convection turbulent heat transfer prediction by LES. First, extensive unsteady experimental results are available as reference data for the flow dynamics. Second, this configuration has been used as benchmark case for many isothermal LES studies in the past. Third, two different experimental studies provide data for the wall heat flux distribution around the cylinder. Finally, the square cylinder case is typical of the bluff-body flows encountered in practical configurations (thermal cooling for aeronautics or electronic devices, for example): flow impingement on the front face and flow separation on the side and rear faces with alternate vortex shedding and transient reattachment. On this configuration, the best results were obtained with :

- a wall-resolved approach,
- a hybrid mesh composed of prism layers at the wall and tetrahedra in the domain,
- a high-order numerical scheme (TTG family of schemes, at least third order accurate in time and space [37]),
- the Wall-Adapting Local Eddy-viscosity (WALE) sub-grid scale model that recovers the proper turbulent viscosity decrease at walls [193].

This methodology was then applied to other configurations.

The computational domain of the flow past a cylinder is described in Fig. 2.1. The vertical dimension was fixed to match a blockage ratio of $h/D = 14$, where D is the cylinder size to mimic the experiment of Lyn *et al.* [172]. Free-stream velocity and temperature are imposed at the inlet while pressure is imposed at the outlet (see Fig. 2.1) through non reflecting NSCBC [211] type boundary conditions. Slip walls are used at the top and bottom boundaries.

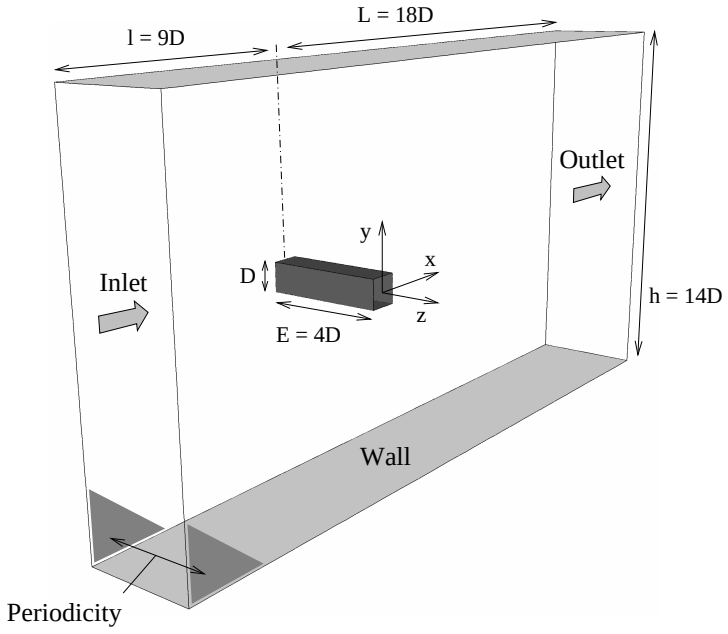

Figure 2.1: Global view of the cylinder computational domain and boundary conditions.

Heat transfer from the square cylinder to the air flow is applied through an isothermal wall condition with a uniform temperature $T_{wall} = 330$ K while the upstream flow is at $T_\infty = 300$ K. In the present case, the variation of the temperature in the boundary layer induces a variation of the fluid transport properties: the Reynolds number $Re = U_\infty D/\nu$ is calculated from the kinematic viscosity $\nu = \mu/\rho$ taken at the film temperature $T_f = 1/2\,(T_\infty + T_{wall})$. Computing ν from T_∞ or T_{wall} instead of T_f would result in 10% error on the Reynolds number. The physical parameters of the simulated cases are presented in Table 2.1. In the following, lengths are normalized by D, velocities by U_∞ and times by $t_c = D/U_\infty$.

Upstream velocity:	$U_\infty = 37.7$ m.s^{-1}
Upstream temperature :	$T_\infty = 300$ K
Upstream Mach number:	$M_\infty = 0.108$
Cylinder diameter:	$D = 1$ cm
Cylinder temperature:	$T_{wall} = 330$ K
Film temperature:	$T_f = 315$ K
Reynolds number:	$Re = 22\,050$
Outlet pressure:	$p_{out} = 101\,325$ Pa

Table 2.1: Physical parameters of the LES cases.

Two meshing approaches were tested according to the near-wall modeling strategy:

A full tetrahedral grid with a wall-function [235] (case *LES-WF*): As shown by Fig. 2.2, the grid is coarse far from the cylinder, moderately refined in the near-wake region and strongly refined close to the cylinder (Fig. 2.3, case *LES-WF*). This refinement is expected to be sufficient to capture accurately the turbulent flow generated by the Kelvin-Helmoltz instability in the detached upper and lower shear-layers and by the von Kármán-Bénart instability in the cylinder wake. On the other hand, the size of the cells adjacent to the cylinder wall is supposed to be large enough to use the wall-function approach in the logarithmic region. Figure 2.5 shows the value of the Reynolds number y^+ of the first interior grid point around the cylinder. Most of y^+ values are in the range $20-30$ which is a little below the condition $y^+ > 30$ for the logarithmic law to be fully valid.

A wall-resolved hybrid tetrahedral-prismatic grid (case *LES-WR*): When the boundary layer is explicitly solved, using prismatic layers close to wall surfaces is more efficient than tetrahedra (see for example [132, 131]). First, quadrilateral faces normal to the wall provide good orthogonality and grid-clustering capabilities which are suitable for thin boundary layers, whereas the triangulation in the tangential direction keeps the flexibility in surface modeling. Second, for the same spatial resolution in the normal direction, the prisms layers use less elements and lead to a higher minimum cell volume than the full tetrahedral grid approach because prismatic elements can have a large aspect ratio. For the wall-resolved case (*LES-WR*), the near-wall region has been meshed using five layers of prismatic elements (see Fig. 2.3) where the height of the layers, Δh, is smaller than the size of their triangle basis, Δx. To avoid numerical errors, the aspect ratio of the thinnest layer (inner layer adjacent to the wall) was limited to $\Delta x/\Delta h = 4$ far from the cylinder edges and $\Delta x/\Delta h = 3$ near the edges. Beyond these limits, the high velocity gradients (due to the shear layer) in region of strongly stretched cells may generate numerical instabilities under the form of unphysical cell-to-cell oscillations. The critical aspect ratio may depend on the flow configuration (*i.e.* the geometry of the bluff-body) as well as on the numerical method so the present values should not be considered as universal. The stretching ratio between the height of an inner layer to the adjacent outer layer was set to 1.13, leading to $1.83 < \Delta x/\Delta h < 2.45$ in the outer layer. The proper height of the inner prisms layer (Δh) was determined by a mesh convergence study based on the global Nusselt number $\overline{Nu}_g$ compared to the experimental correlation of Igarashi [116]. Figure 2.4 shows that

$\Delta h \leq 0.002$ is required to match the empirical Nusselt number. The corresponding y^+ profile is plotted on Fig. 2.5. Most of the near-wall resolution is below $y^+ < 2$ but some regions close to the edges of the cylinder reach higher values. Using this mesh constraint in the near-wall region and the same tetrahedral sizes as case *LES-WF* in other regions leads to a 3.3 million nodes grid (12.6 million cells). In comparison, a full tetrahedral grid having the same resolution would feature around 13 million nodes (60 million cells) with a smaller minimum cell volume requiring a time step four times shorter. Such a grid would cost 10 times more CPU time than the present hybrid grid.

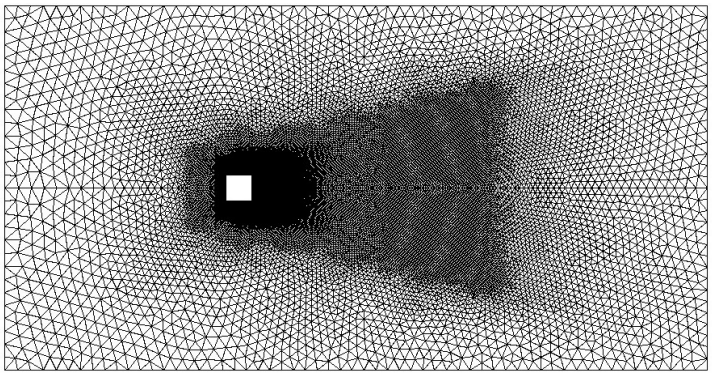

Figure 2.2: Side view of the computational grid for the cylinder simulation.

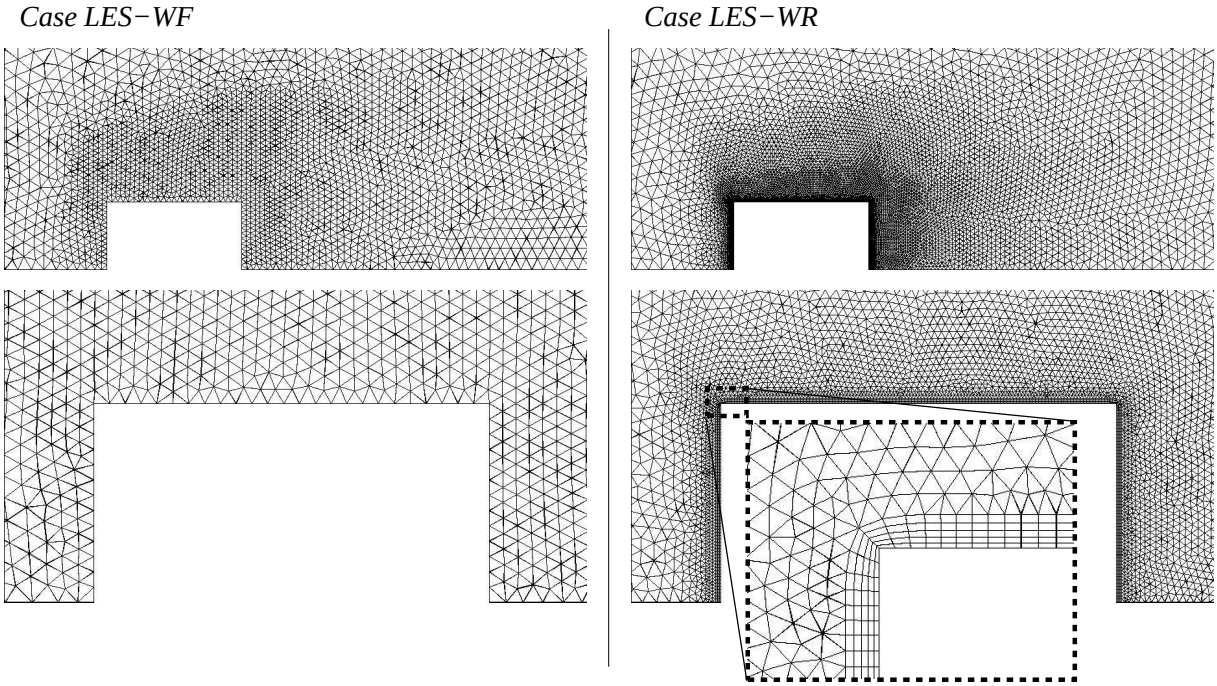

Figure 2.3: Zooms on the side view of the top half of the two unstructured grids: full tetrahedral grid (case *LES-WF*) and hybrid prismatic/tetrahedral grid (case *LES-WR*). Bottom right image is a zoom on the five layers of prismatic elements.

Validations of the aerodynamics on mean and fluctuating quantities are presented in Boileau *et al.* [22] and only heat transfer results are reported here. Both wall-treatment approaches have proved to be accurate for the flow dynamics. Their capacity to predict convective heat transfer is evaluated by comparing the computed Nusselt number with experimental data. Table 2.2 shows that the wall-function strongly under-predicts the global Nusselt number $\overline{Nu}_g$ — obtained by

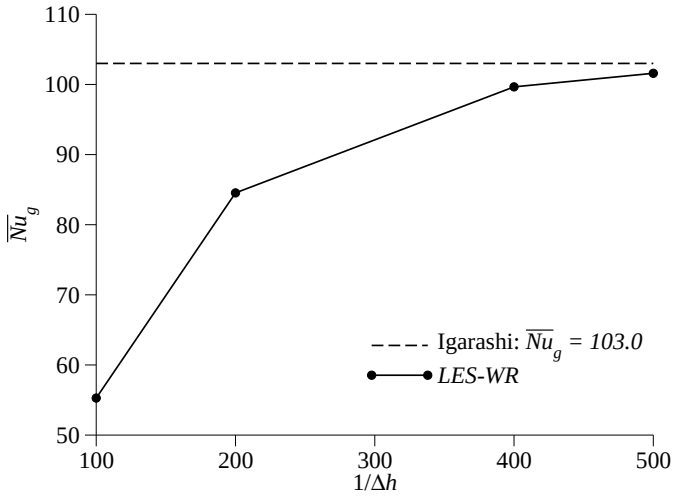

Figure 2.4: Global Nussel number of the cylinder, $\overline{Nu}_g$, for the wall-resolved case *(LES-WR)* as a function of the mesh wall resolution $1/\Delta h$ compared to the experimental correlation of Igarashi [116].

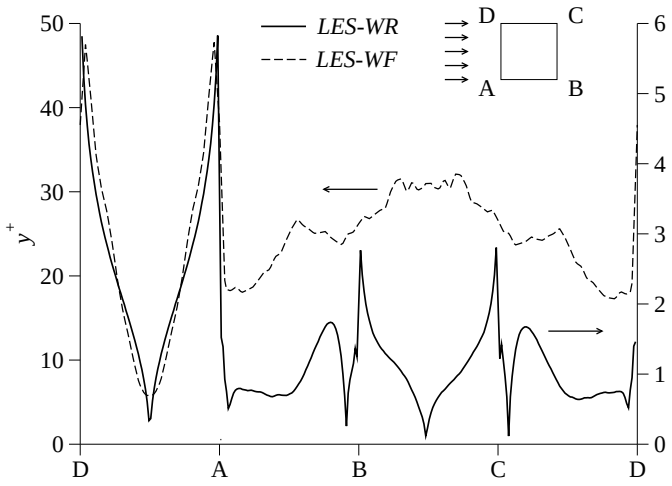

Figure 2.5: Profiles of time-averaged wall Reynolds number of the first fluid node, y^+, around the cylinder.

space-averaging the local Nusselt number profiles around the square contour — whereas the wall-resolved approach presents a very good accuracy.

A more detailed comparison is provided by the profiles of the time-averaged Nusselt number $\overline{Nu}$ around the cylinder walls. Figure 2.6 shows that all experimental profiles have similar shapes and levels although the profiles from Yoo *et al.* [276] present a slightly larger amplitude than those of Igarashi [116]. As expected from the global Nusselt results (Table 2.2), the wall-function approach does not predict the right level at any position of the cylinder face. Even the shape of the profiles is not properly retrieved. Actually, this bluff-body flow does not verify the wall-function assumption anywhere around the cylinder: the impinging flow with a stagnation point on the front face, the flow separation on the side faces and the back-flow on the back face that occur here are not compatible with the constant pressure gradient and steady attached

	$\overline{Nu_g}$	Error
Igarashi [116]	103.0	–
LES-WF	46.1	−55%
LES-WR	101.6	−1.36%

Table 2.2: Global Nusselt number $\overline{Nu_g}$ of the two present LES compared to the experimental correlation of Igarashi [116] for the given Reynolds number $Re = 22\,050$.

flow assumption of the wall-function model. Piomelli [208] showed that wall-function approaches cannot predict accurately the near-wall dynamics and wall stresses of detached flows and oscillating flows. Nevertheless, for the flow dynamics only, results have shown that good predictions are obtained in the *LES-WF* case even if the flow does not fulfill the model requirements. The velocity field around the cylinder results in flow separation and vortex shedding phenomena that depend slightly on the wall friction. As a consequence, the wall pressure and the resulting drag force are quite well predicted because they depend mainly on large eddy motions that are not very sensitive to the viscous near-wall effects. The wall heat flux, however, is directly computed by the wall-function model that fails to mimic the turbulent heat transfer in the wall boundary layer when the model assumptions are not verified.

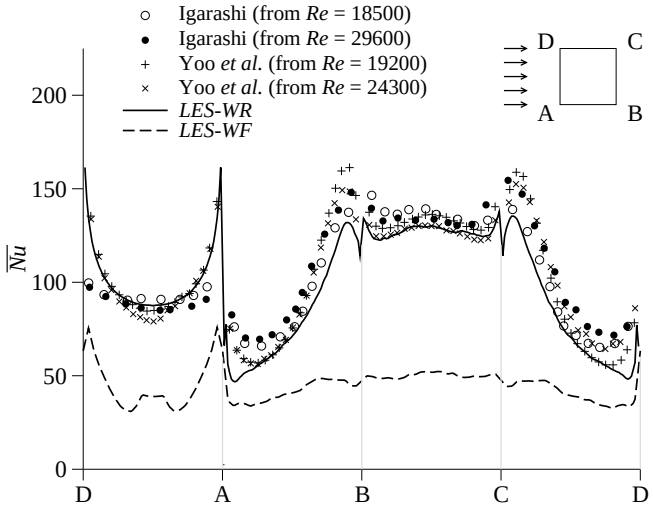

Figure 2.6: Profiles of time-averaged local Nusselt number, $\overline{Nu}$, around the cylinder walls : experimental results of Igarashi [116] (∘ and •) and of Yoo *et al.* [276] (+ and ×) compared to the present LES results (—— and - - - -).

Contrary to the wall-function approach, the wall-resolved approach is able to reproduce the experimental data, particularly on the front and rear faces (where the agreement is better with the data of Yoo *et al.*). On the side faces, the Nusselt number is slightly underestimated. This error can be related to the under-prediction of the back-flow mean velocity observed numerically, which may lead to a lower convective flux close to the cylinder walls. One can notice that the error on the Nusselt number is not correlated to the high value of y^+ mentioned before and visible on Fig. 2.5, meaning that, though y^+ is larger than 2 in some part of the cylinder wall, the space resolution of the near-wall region is adequate to predict the wall heat flux. To conclude this study, by superimposing phase-averaged Nusselt number profiles, stream lines and temperature field, Boileau *et al.* [22] highlight how the heat flux from the cylinder wall is coupled to the periodic vortex shedding.

Flow past a tandem of square cylinders

The same wall-resolved strategy was applied to two square cylinders in a tandem arrangement. Also performed in collaboration with Airbus, this work has been published in Journal of Heat Transfer [67]. The iso-surface of the Q-criterion on Fig. 2.7 shows the complex three-dimensional organization of the flow around the cylinders and in their wake. The vorticity layers (①) on Fig. 2.7) generated by the upstream cylinder destabilize in the near field of the lateral faces of this obstacle ② and form three-dimensional coherent structures ③ and ④. In conjunction with the alternate vortices ③, longitudinal structures ④ are formed in the wake of the first cylinder and are convected downstream. The downstream cylinder disturbs the development and convection of all these structures so that the wake of the upstream cylinder participates actively to heat transfer on the second one. The LES reproduces the behavior of mode 2 where vortex shedding is in phase for both cylinders as expected from the bibliography descriptions [170, 138].

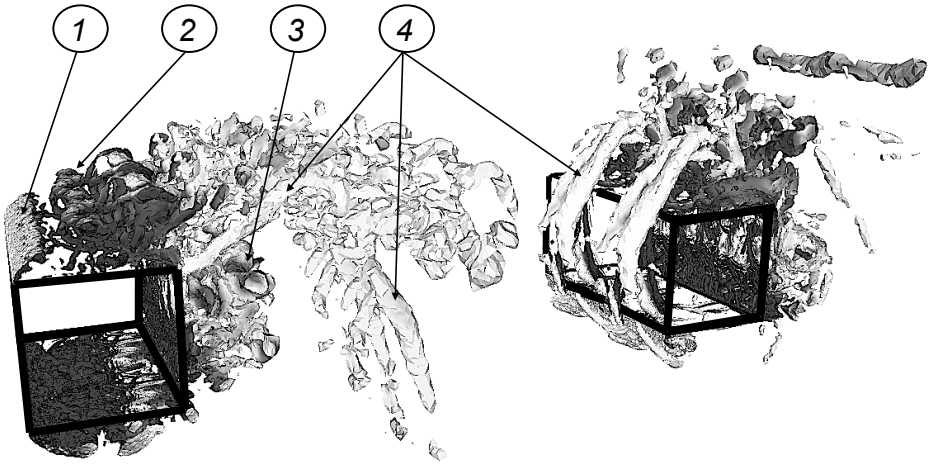

Figure 2.7: Instantaneous isosurface of Q-criterion colored by the temperature (lower temperature in white and higher temperature in dark) in the tandem cylinder simulation.

Figure 2.8 depicts mean Nusselt profiles on both cylinders compared to the experimental results of [116, 276] obtained on isolated cylinders as no experimental data are available on tandem configurations. Experimental results are scaled following the correlation of Igarashi [116]. The Nusselt number distribution of the upstream cylinder is characteristic of an isolated cylinder in terms of shape and levels. The cylinders exhibit differences in heat transfer due to the topology of the flow. First, the heat fluxes on the upstream face (A-D) of the cylinders are almost the same. Downstream faces (B-C) are subject to the highest heat fluxes over the whole geometry. On this face, the heat flux of the second cylinder is more important due to the closer proximity of the recirculation zone behind the obstacle evidenced by the aerodynamic analysis [67]. The thermal effect of the presence or not of the lateral recirculation zones (faces A-B and C-D) is clearly identified on Fig. 2.8: the Nusselt number is very low on these faces for the upstream cylinder (1) while it is rather high on the downstream cylinder (2). Finally, the shapes of the Nusselt number profiles on lateral faces present an important difference near the downstream edges (B and C): there is a peak just before the edges on the profiles corresponding to the upstream cylinder replaced by a constant value for the downstream cylinder. These peaks for the upstream cylinder are due to the interaction of the shear layers with the lateral faces evidenced by the analysis of the wall friction [67].

Table 2.3 gives global heat fluxes and Nusselt numbers integrated on the upstream and downstream cylinders as well as the root mean square values of the Nusselt numbers. The heat flux of the downstream cylinder is about 15% higher than the heat flux of the first cylinder ($\overline{\Phi}_2 \approx 1.15\overline{\Phi}_1$ and $\overline{Nu}_2 \approx 1.16\overline{Nu}_1$). Immersed in the wake of the upstream cylinder, the second

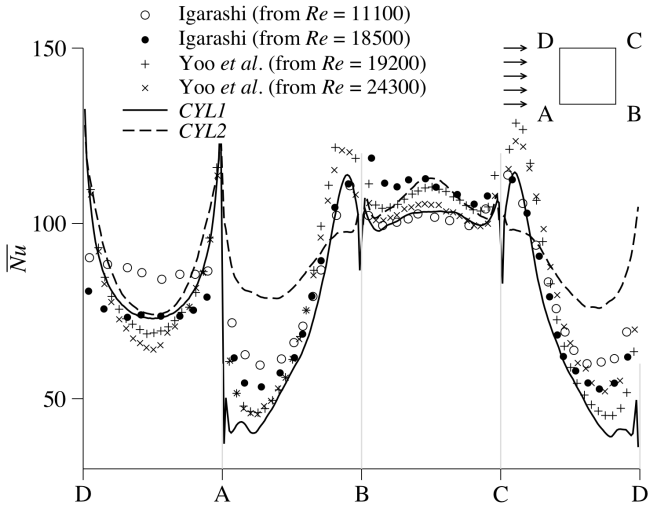

Figure 2.8: Time-averaged profiles of wall Nusselt number $\overline{Nu}$, profiles around the cylinder walls: comparison between the cylinders of the LES and experiments on isolated cylinders [116, 276].

cylinder also exhibits the highest temporal heat flux oscillations. The RMS value of the Nusselt number of the first cylinder is about 4.2% of $\overline{Nu}_1$ while the fluctuations on the second cylinder are of the order of 10.5% of $\overline{Nu}_2$. It is worth mentioning that the mean temperatures just upstream of both cylinders are approximately the same (0.5 K difference due to the mixing of the heated flow with the main flow). The corresponding mean velocity in a volume in front of them are 32.5 ms^{-1} for the upstream cylinder and 26.35 ms^{-1} for the downstream one so two opposite effects play an important role in the heat load of the downstream obstacle: (1) a reduction of the mean velocity *seen* by the cylinder can potentially reduce the Nusselt number, (2) an increase of velocity fluctuations can lead to an increase of heat transfer. In the configuration simulated during this study, the wake of the upstream cylinder increases the heat transfer of the second cylinder of more than 15% compared to an isolated cylinder. It is worth mentioning that the RANS solver used during this study performed with Airbus was not able to recover the Nusselt number profiles obtained on the downstream cylinder with the LES.

	$\overline{\Phi}$	$\overline{Nu}$	Nu'	$Nu'/\overline{Nu}$
Correlation [116]	–	82.5	–	–
LES CYL 1	3.9 W	77.2	3.2	4.2%
LES CYL 2	4.5 W	89.6	9.4	10.5%

Table 2.3: Spatially and temporally averaged wall heat flux $\overline{\Phi}$, Nusselt number $\overline{Nu}$ and corresponding fluctuating Nu' in the tandem configuration.

Heat transfer in isolated impinging jets

Cooling by impinging jets is both a fundamental research problem and an essential element in turbine technologies. Such configurations were computed during the PhD Thesis of Pierre Aillaud to check the approach described here. Results presented in this section are extracted from an article published in Physics of Fluids [2]. Due to the high heat transfer rate it can produce, impinging jet is one of the most common techniques used to cool the high pressure vanes. The literature frequently deals with multi-jet configurations that are certainly more representative of what is found in industry but add complexity compared to isolated jets when one wants to study basic phenomena [182, 181, 83, 6]. Apart from the aerodynamic conditions such as Mach and Reynolds numbers [9, 163, 226], two geometric parameters are of particular importance for heat transfer: the impinging plate curvature and the jet nozzle to plate distance [12, 196]. The second parameter is rather constant in high pressure stators whereas the first one can vary significantly from a highly curved surface close to the leading edge to a flat wall on the suction side for example (Fig. 2.9).

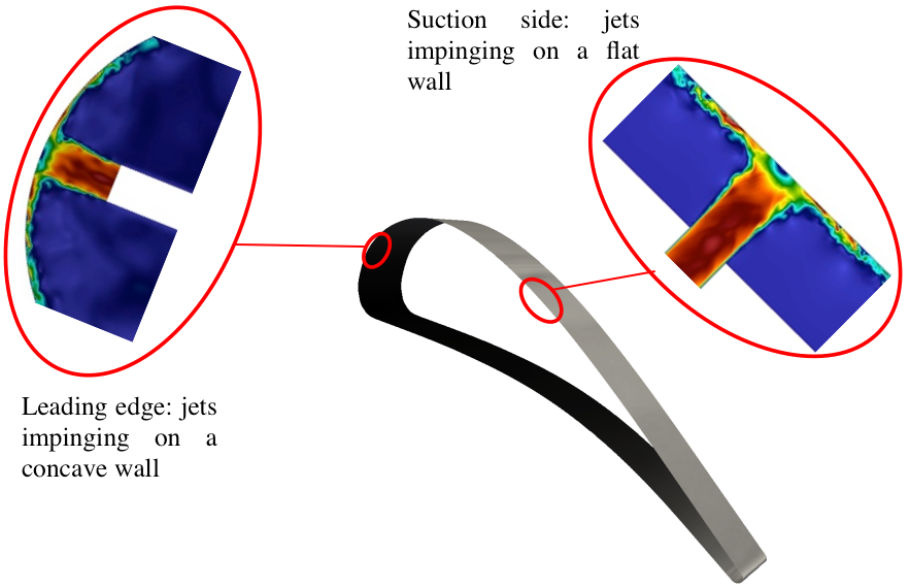

Figure 2.9: Different curvatures of impinging plates taking place in high pressure vanes: strong curvature close to the leading edge and small curvature along the suction side.

During the PhD Thesis of Pierre Aillaud, two isolated impinging jet configurations were studied: a flat impinged plate and a curved one. As LES gives access to the full 3D time-dependent flow field, this space-time information was used to provide additional details on the main mechanisms controlling radial Nusselt number distributions. Based on the one point temporal evolution of a variable $x(t)$, the common quantities that can be extracted are the first order moment (*i.e.* mean $\langle x(t)\rangle$) and the second central moment (*i.e.* variance $\langle(x(t)-\langle x(t)\rangle)^2\rangle$). Dimensionless higher order central moments, such as skewness (Sk) and kurtosis (Ku), are also useful to have a better idea of the probability density function's (PDF) shape [147]. They are also more sensitive to intermittency. Sk and Ku are, respectively, the third and fourth dimensionless central moments. The skewness evaluates the balance between the left and the right parts (with respect to the mean value) of a PDF. The skewness of a symmetric PDF, like Gaussian distributions, is 0 but the reverse is not true. For unimodal distributions (*i.e.* single peak) the skewness can also be seen as the "distance" from the mean to the peak, *i.e.* the mode (or most likely value). Positive (resp. negative) skewness implies that the mean value is greater (resp. lower) than the mode value. Only the skewness is used in this manuscript and for a more detailed description of the meaning of these two quantities in terms of PDF and sample set, the reader is referred to [253].

Heat transfer characteristics of impinging jets on a flat plate have been extensively studied

experimentally and numerically as reviewed in Dewan *et al.* [55], Viskanta *et al.* [269] and Jambunathan *et al.* [121] among others. Impinging jet flows are commonly divided in three main zones as shown in Fig. 2.10. The free jet region is defined as the zone where the jet is not

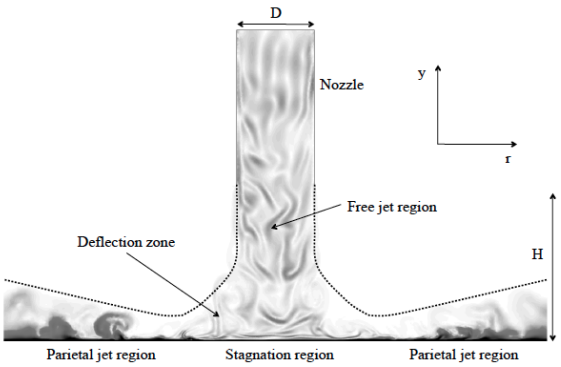

Figure 2.10: Characteristic regions of a jet impinging orthogonally on a flat plate, from [245].

affected by the presence of the plate. In this region, the jet is mainly axial and the mean axial centerline velocity is almost constant. In the stagnation region the jet starts to be influenced by the presence of the plate. There is a rapid decrease of the axial velocity and the initially purely axial jet deflects in the radial direction. The third zone is the wall-jet region which is characterized by a purely radial flow. The radial velocity initially increasing from 0 m/s at the stagnation point reaches a maximum value further downstream. Due to mass conservation, this radial acceleration of the flow induces a reduction of the wall-jet thickness. Then, the radial velocity starts to decrease and the wall-jet becomes thicker. Each zone is governed by different mechanisms making impinging jet a very challenging and suitable test case for CFD code validation.

Jet impingement a on curved surface is a specific extension and studies are not encountered as frequently as those on flat plates [269]. The flow over a concave surface is known to be unstable due to the destabilizing effect of the centrifugal force [231]. In impinging jet flows over a concave surface, one common idea is that curvature enhances heat transfer due to the presence of Görtler vortices [91, 162]: these vortices appear for laminar boundary flows on concave surfaces and have an impact on the transition process and on heat transfer in the transition and turbulent regions [255, 188, 174]. However, Görtler vortices have never been observed either in semi-circular or hemispherical cases. Studies focusing on the basic problem of a single round jet impinging on a concave plate are rather scarce [40, 162, 109]. As for the flat plate, experimental studies reporting at the same time flow and heat transfer data are scarce and to the best of the author's knowledge the only contribution for concave plate is the work of Choi *et al.*, [35] treating a 2D slot jet impinging on a semi-circular concave surface. For a single round jet impinging on a concave surface, the simplest configuration was the impinging jet on a hemispherical plate by Lee *et al.* [162] who reported heat transfer and pressure data at the wall. More recently, Hashiehbaf *et al.* [109] studied experimentally a single round impinging jet on a semi-circular concave plate. They studied the dynamics but no heat transfer data is reported.

Wall-resolved LES of a single unconfined round jet normally-impinging on a flat plate and concave plate have been performed to investigate the link between the Nusselt number distribution and the near-wall flow dynamics for a nozzle to plate distance of $H/d = 2$ [1, 2, 3]. Only the results on the flat plate case are presented. Note that prior to the results presented, a mesh independency study has been carried out [245, 1, 3]. The results for the flat plate case have been validated against experimental data available in the literature [84, 262].

The LES on the flat plate case reproduces the non-monotonic mean Nusselt number distribution with two peaks, a first one at the stagnation point and an other one in the range of $r/D = 1.5 - 2$ (Fig. 2.11). Based on the validated numerical database, the flow dynamics and the heat transfer process are investigated to establish a link between the vortical structures

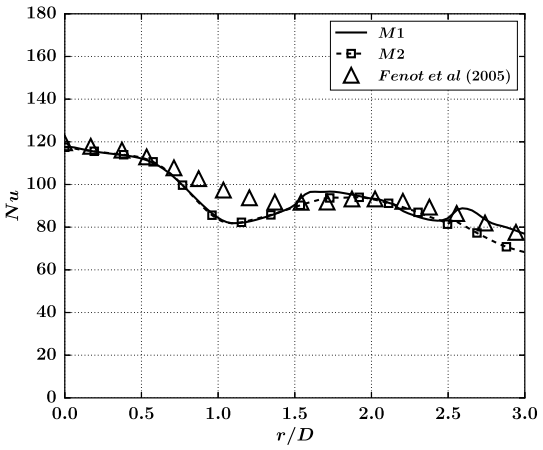

Figure 2.11: Time-averaged Nusselt number profile on the flat plate.

present in impinging jet flows and the non-monotonic mean Nusselt number distribution. For this configuration, primary and secondary vortices are evidenced using iso-surfaces of Q-criterion in agreement with the previous studies [46]. The skewness of the temporal distribution of the pressure allows to highlight the rebound of the primary vortices that is observed for a single vortex ring impinging on a flat plate but that is more difficult to characterize in a fully turbulent impinging jet flow (region A on Fig. 2.12). It appears that this rebound is the event that stops the mean heat transfer enhancement as the secondary peak in the mean Nusselt number distribution is located at the same position. In addition, the skewness of the pressure also allows to identify the location of the initiation of the unsteady separation which coincides with the location of the local minimum (region B on Fig. 2.12). This point analyzed jointly with the Nusselt number PDFs shows that this separation generates low heat transfer events, due to fluid pockets that are heated by the plate, which contribute to the local minimum of the mean Nusselt number radial distribution. This observation goes in the direction of the scenario proposed by [105] to explain the dip between the two peaks. A correlation is also observed between the location of the local minimum and the intermittent generation of a strong cold front related to a cold fluid injection induced by the secondary vortices (Fig. 2.13). These results are coherent with [46] that have highlighted a cold fluid flux towards the wall in the vicinity of a cold spot using conditional averaging.

Analyzing the skewness of the Nusselt number distribution (Fig. 2.14), two remarkable locations can be identified. The first one is related to the generation of weak thermal events and appears as localized negative skewness values at several azimuthal location at $s/D = 1.1$. These weak thermal events, not balanced by strong thermal events, are the results of the initiation of the unsteady separation of the boundary layer. Further downstream, at $1.1 < s/D < 1.9$, the flat plate exhibits relatively high skewness values $Sk > 1$. It indicates the occurrence of extreme thermal events mainly due to the formation and convection of the secondary annular structures. From the Nusselt number PDFs (Fig. 2.15), it is concluded that the heat transfer enhancement is the consequence of an imbalance between high and low Nusselt number values caused by the secondary structures, which appears to be the main mechanism inducing the positive skewness (Fig. 2.14), confirming once again the scenario proposed by Hadžiabdić and Hanjalić [105] (Fig. 2.13). Finally, the rebound of the primary vortices is found to be the event that causes the second peak representing the end of the heat transfer enhancement.

As demonstrated, high order moments and PDF analysis are powerful tools to deeper study time series and investigate relations between aerodynamics and wall heat transfer. The same analysis will be available in the PhD Thesis of Pierre Aillaud for the concave plate configuration. Such quantities along with turbulent integral timescales have been intensively used to characterize combustion chamber plane both in terms of dynamic and mixing [147, 146] as well as the convection of turbulence and hot streaks in nozzle guide vanes [254].

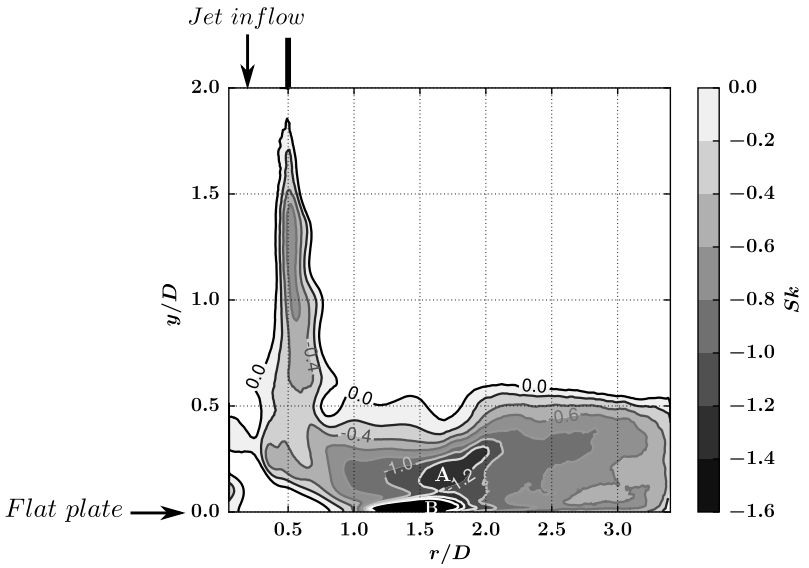

Figure 2.12: Iso-contours of azimuthal averaged skewness of the pressure temporal distribution in the $(y/D,\ r/D)$ plane. The rebound of primary vortices starts here at $r/D = 1.6$ and disappears near $r/D = 2$ (extent of region A). The intermittent formation and convection of secondary vortices generate region B where $Sk < -1.6$.

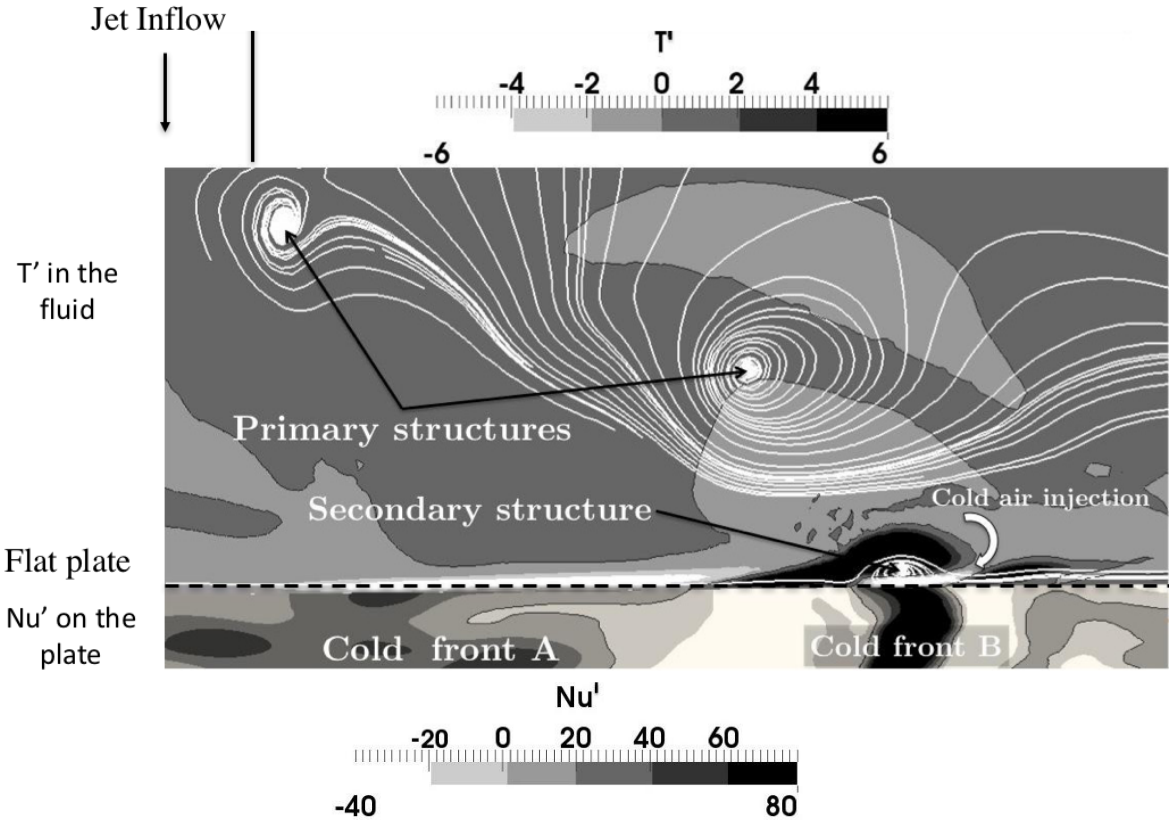

Figure 2.13: Instantaneous snapshot of the Nusselt number fluctuations, Nu', on the wall (lower part of the figure) and streamlines along with the temperature fluctuation, T', projected in the plane $\theta = 0$. $(-)$: isocontours of $Nu' = 0$ and $T' = 0$.

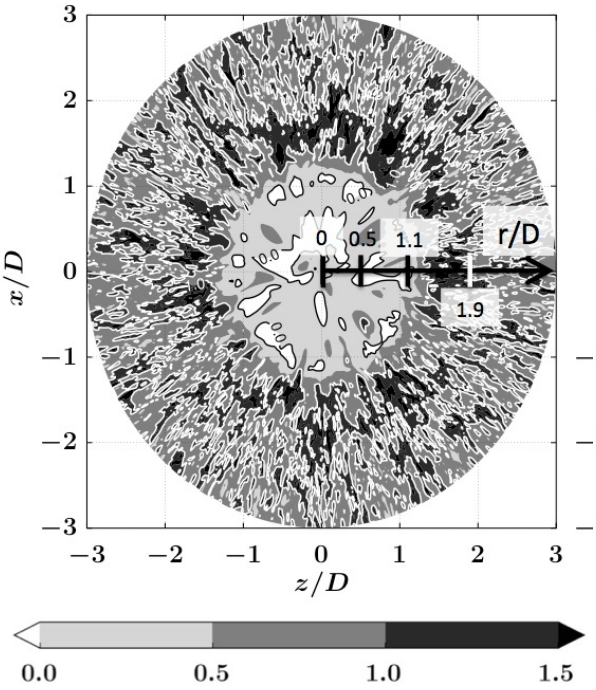

Figure 2.14: Skewness of the Nusselt number, Nu, temporal distribution on the plate in the $(x/D, z/D)$ plane. Black isocontours: $Sk = 0$. White isocontours: $Sk = 1$.

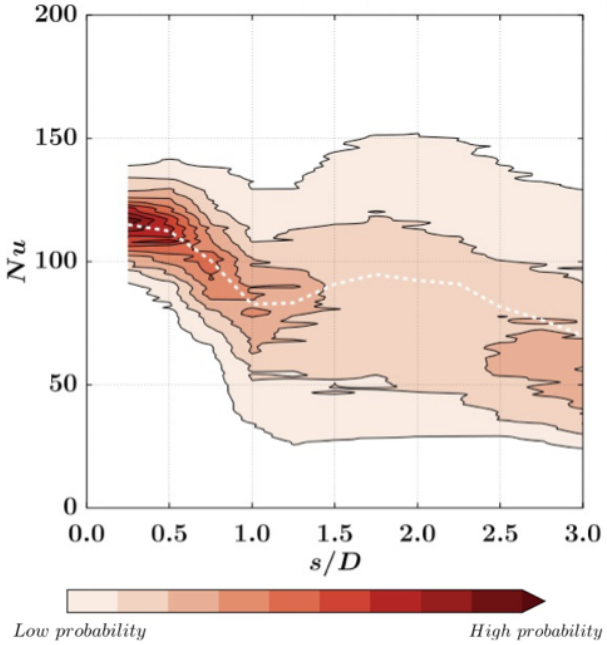

Figure 2.15: PDF of the Nusselt number Nu temporal distribution as a function of the distance to the stagnation point s/D for the flat plate. White dashed line: mean Nusselt number.

Flow and heat transfer in a low pressure turbine cascade

As a last example for low Reynolds and Mach number flows, a study on flow and heat transfer around a low pressure turbine cascade is presented. This work was done in collaboration with CORIA, LEGI and University of Sherbrooke in the context of a Summer Program of the Stanford Center for Turbulence [173] and has been published in Journal of Turbomachinery [71]. The tested configuration is a 2D highly loaded low pressure turbine blade cascade,investigated in the European research project *Aero-Thermal Investigation on Turbine End-Wall and Blades* (AITEB-2, 6FP, AST4-CT-2005-516113) [154] (Fig. 2.16). The aim of the blade design was to generate an extended recirculation bubble on the pressure side at nominal conditions. The objective of the experimental study was to document flow field and heat transfer of a highly loaded low pressure turbine airfoil with a long separation bubble on the pressure side (Fig. 2.16). For these investigations a linear cascade with a water-cooled airfoil was used.

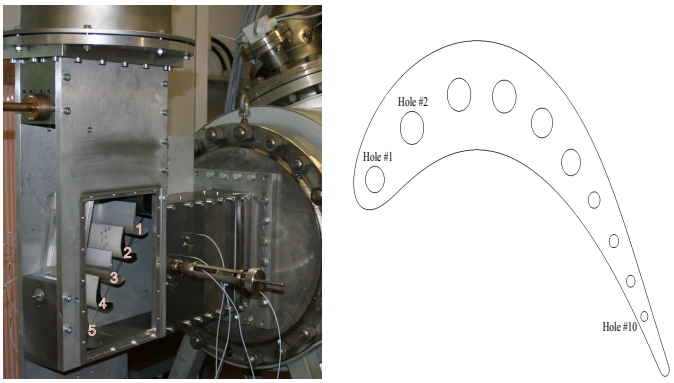

(a) (b)

Figure 2.16: (a) Test section - blades with pressure taps #2 and #4, blade with thermocouples #3, (b) geometry of the cooled blade #3.

Experimental results reveal a considerable influence of the boundary layer separation on the local heat transfer [154]. The size of the separation region on the pressure side is strongly influenced by free-stream turbulence level and Reynolds number. The influence of this separation is clearly visible in the heat transfer distributions: heat transfer on the pressure side is mainly governed by the extent of the separation bubble. In all experimental conditions the boundary layer on the pressure side separates. An increase of either the Reynolds number or the free-stream turbulence level leads to a shortening of the separation region. On the suction side the laminar boundary layer is affected by turbulent fluctuations in the free stream for high Reynolds numbers. Furthermore, a separation bubble due to a strong adverse pressure gradient occurs on the suction side for low Reynolds numbers and turbulence levels. With increasing both Reynolds number and turbulence level, this separation disappear and a bypass transition takes place: for high Reynolds numbers there is a strong effect of turbulence on heat transfer on the suction side whereas for low Reynolds number the effect on the pressure side is stronger. The experimental configuration explored in this study corresponds to the lowest turbulence level (1.6%) and to an exit Reynolds number of 150 000 (Tab. 2.4). The lowest turbulence level is chosen to avoid dealing with turbulence injection issues (injection method, length scale of the eddies, mesh resolution to transport the eddies until the blade ...) and to concentrate on the physics around the blade itself. As a result, the computations without turbulence injection are considered comparable to experimental results with a turbulent level of 1.6%. The Reynolds number of 150 000 is retained because experimental results at this point are comparable to a real low pressure turbine for the treatment of conjugate heat transfer: a large separation on the pressure side and separation bubble due to adverse pressure gradient on the suction side are observed in both flows. While this limited Reynolds number imposes less constraints on the number of grids points to resolve boundary layers than higher Reynolds number, such flow

Inlet Mach number		0.068
Outlet Mach number		0.116
Inlet Reynolds number		93 101
Outlet Reynolds number		158 088
Inlet total pressure	P_1^t	102 274.8 Pa
Inlet total temperature	T_1^t	348.06 K
Outlet static pressure		101315.9 Pa

Table 2.4: Experimental settings for the experimental blade.

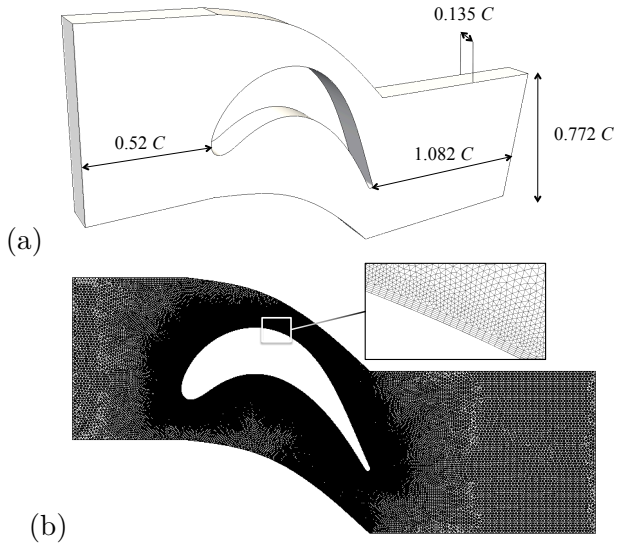

Figure 2.17: (a) Sketch of the fluid computational domain and (b) detail of the corresponding unstructured mesh grid.

features remain challenging for LES [29].

The fluid computational domain is sketched in Fig. 2.17(a) with a view of a typical mesh in Fig. 2.17(b). The spanwise size of the domain is 0.135 C with periodicity enforced on each side. This simplification neglects end-wall effects but retains the three-dimensionality of the flow and greatly reduces the number of grid cells required to model the blade. Periodicity condition is also assumed in the transverse direction to simulate only one flow passage. These two periodicity directions are justified by the experimental setup as described in [154].

A hybrid approach with prismatic layers in the near-wall region and tetrahedra in the main duct as shown in Fig. 2.17(b), is adopted to: (1) reduce the number of cells in the nearby region of the wall, (2) meet the preferential directions of the boundary layer flow and (3) limit the constraint on the acoustic time step. The mesh has five layers of prisms where the vertical length of the prism Δy is smaller than the triangle base-length Δx or Δz (here, $\Delta x \approx \Delta z$). A limit is imposed to this mesh adaptation to avoid numerical errors in these layers: the aspect ratio of the first and thinnest layer is set to $\Delta x \approx \Delta z \approx \alpha \Delta y$, with α lower than 8 (*i.e.* $x^+ \approx z^+ \approx \alpha y^+$) in agreement with known observations and boundary layer scales [227]. A convergence study of the wall friction and wall heat flux depending on wall resolution Δy have been done based on four meshes. Table 2.5 gives the main properties of the four meshes.

Figure 2.18 presents an instantaneous visualization of the flow topology around the blade obtained on mesh #4. Starting from the leading edge to the trailing edge, the pressure side exhibits 3 main phenomena (Ⓐ, Ⓑ and Ⓒ in Fig. 2.18). First, a massive flow separation Ⓐ caused by the strong concave curvature of the blade profile on the pressure side starts shortly after the leading edge. Due to shear layer instabilities, the laminar flow is then transitioning

Mesh #	M1	M2	M3	M4
mean y^+	5.7	4.6	2.5	1.3
$\Delta x/\Delta y = \Delta z/\Delta y$	4	4	4	8
# cells	9.3 M	13.2 M	37.4 M	54.8 M

Table 2.5: Properties of the four meshes used for the fluid.

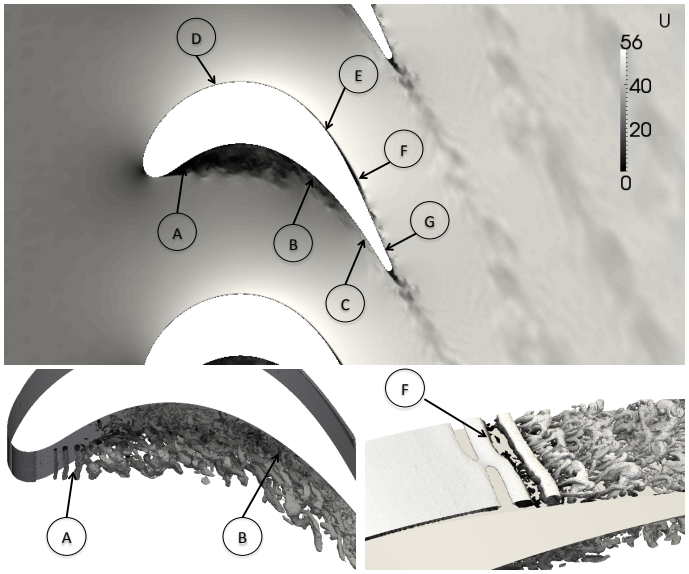

Figure 2.18: Main flow features responsible for heat transfer characteristics: velocity field (up) and iso-surface of Q-criterion (bottom). The simulation is done with mesh M4.

to turbulence. This separation creates a large recirculation bubble fed by numerous turbulent eddies of different sizes. The flow then hits the pressure side and reattaches (B). Finally, the attached turbulent flow is accelerated until the trailing edge of the blade (C).

In the same way, 4 main behaviors can be underlined on the suction side ((D), (E), (F) and (G) in Fig. 2.18). First the laminar flow accelerates up to the maximum camber point (D). Because of the consequent adverse pressure gradient, the flow strongly decelerates (E). This adverse pressure gradient yields a laminar separation bubble (F) with a free shear layer that experiences transition to turbulence. Subsequently, the separated turbulent flow reattaches and evolves downstream from a non-equilibrium turbulent boundary layer to an equilibrium one (G). These main flow features responsible for the heat transfer characteristics that are evidenced in the experiment are captured by all four simulations with an improved accuracy when mesh resolution increases (*i.e.* from M1 to M4).

The comparison between the mean temporal pressure distribution along the blade profile with experimental pressure measurements (Fig. 2.19) shows that the simulation with mesh #4 is in fair agreement with the experience. The position and intensity of the 7 main features reported previously are well predicted by the computation.

Figure 2.20-(a) presents the evolution of the normalized wall distance y^+ around the blade for the 4 meshes. Increasing the mesh resolution leads to a global decrease of y^+. The shapes of the four y^+ profiles are similar. This feature is directly linked to the resolution of the wall friction τ_w given for the 4 meshes in Fig. 2.20-(b). From the mesh convergence point of view, the wall friction levels are drastically improved from mesh #1 to mesh #3, especially in the laminar and turbulent parts of the suction side as well as in the turbulent region of the pressure side. The improvement between mesh #3 and #4 exists but is less important. Hence mesh

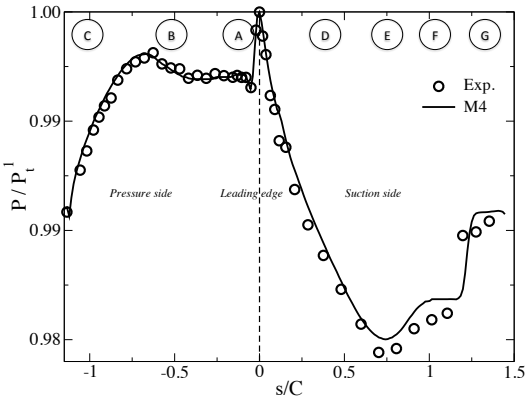

Figure 2.19: Mean temporal pressure distribution along the blade profile. The simulation is done with mesh M4. Suction side is represented on positive s/C and pressure side on negative s/C.

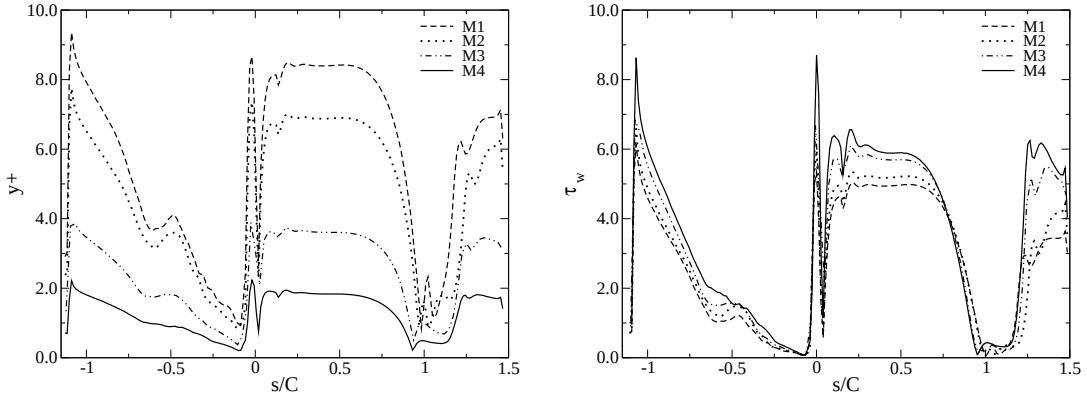

Figure 2.20: (a) Y^+ and (b) wall friction τ_w distributions along the blade profile for the 4 meshes. Suction side is represented on positive s/C and pressure side on negative s/C.

#4 is considered to be sufficient to obtain accurate heat transfer predictions on the blade. Its maximum value of y^+ is always below 2 (Fig. 2.20-(a)) and the mean value around the blade is 1.3 (Tab. 2.5). In the other directions, the aspect ratio of the prisms used to mesh the boundary layer gives normalized wall distances that are kept under acceptable values [227]: the maximum values of x^+ and z^+ are in the order of 16 (8 times the maximum of y^+, Tab. 2.5).

Mesh convergence is also evidenced by the heat transfer coefficient (HTC) h (Fig. 2.21-(a)) defined by the ratio between the wall heat flux, $q_{wall}(s)$, and the difference between the total free stream temperature, T_1^t and the local wall temperature $T_{wall}(s) = 300$ K:

$$h(s) = \frac{q_{wall}(s)}{T_1^t - T_{wall}(s)} \tag{2.1}$$

The results from meshes #3 and #4 are almost superposed except at the leading edge as well as in the turbulent regions of both the suction and pressure sides. With the finer grid, the prediction of the HTC is very close to the experimental measurements on a large part of the blade wall. From Fig. 2.21-(a), the leading edge exhibits the highest convective heat exchange caused by the thin boundary layer occurring at the stagnation point. Along the suction side, the simulation first captures the rapid decrease of heat transfer due to the strong acceleration of the flow and the thickening of the laminar boundary layer (from $s/C = 0$ to 0.25). It then shows a moderate decrease of h from $s/C = 0.25$ to 0.75 linked to a slower increase of the boundary

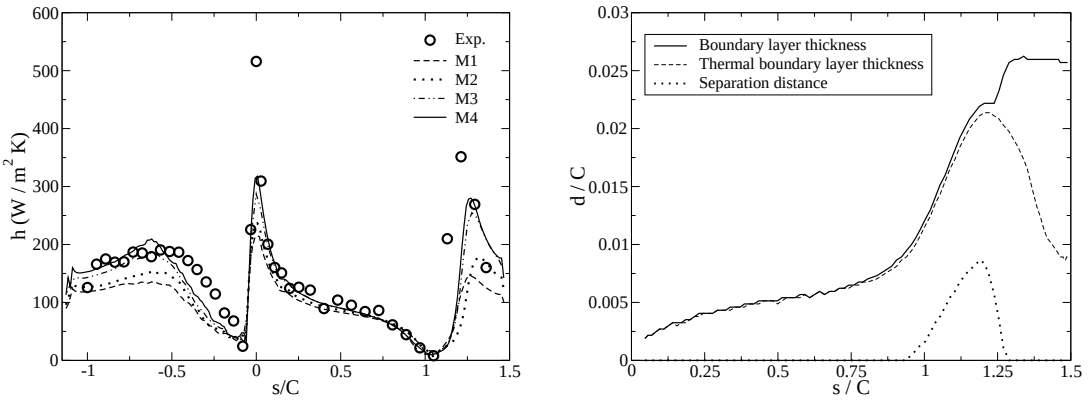

(a) (b)

Figure 2.21: (a) Convective heat transfer coefficient h distribution along the blade profile for the 4 meshes and (b) evolutions of boundary layer thicknesses along the suction side of the blade.

thickness (Fig. 2.21-(b)), followed by a strong decrease caused by the adverse pressure gradient that suddenly thickens the boundary layer thickness from $s/C = 0.75$ to 0.95. Finally a very low level of convective heat transfer is obtained when the laminar flow separates from the wall followed by a drastic increase due to the transition of the laminar boundary layer that finished with a pic when the flow reattaches ($s/C = 1.25$). The simulation predicts a reattachment of the flow slightly downstream the experimental measurements.

Along the pressure side, the simulation captures the rapid decrease of heat transfer caused by the strong acceleration of the laminar flow followed by a progressive increase in the recirculation zone. A maximum of the convective heat transfer in the reattachment region is then followed by a slight decrease of the heat transfer coefficient caused by the acceleration of the turbulent boundary layer. While the computation provides good overall levels of heat transfer coefficient, three regions of underestimation and one of overestimation can be seen. The largest underestimate is located at the leading edge where the boundary layer is known to be very thin. The heat transfer is also underestimated after the transition of the boundary layer on the suction side where the turbulent boundary layer reattaches as well as on the pressure side where the large separation takes place. This last discrepancy may be caused by under-resolved turbulent eddies that are formed in the separation bubble and participate to the heat transfer or by an interaction between the separation and the incoming turbulence which is not taken into account in the simulation [108]. Finally, the computation seems to overestimate heat transfer at the trailing edge.

In summary, with the more refined mesh (#4) the isothermal wall-resolved LES gives accurate predictions of the flow structure around the blade and gives insights to explain its complex behavior. The convective heat transfer coefficient is also accurately predicted by this high fidelity simulation. The next step is the prediction of the temperature distribution in the blade with a conjugate heat transfer simulation. This study is discussed in section 2.2.

2.1.2 Increasing Reynolds and Mach numbers

Thermal environment characterization of high pressure stages in a gas turbine is a challenging task. Due to high Reynolds and Mach numbers, the numerical requirements are far more important than in low pressure parts and the configurations are geometrically more complex than usual academic cases such as flat plates. The first step to ensure a proper determination of heat loads is of course to accurately capture the aerodynamics around the blades. The flow topology around an airfoil cascade is represented schematically in Fig. 2.22. (1) is the well-known Von Karman vortex shedding in the blade's wake. This vortex shedding creates pressure waves emitted from the unsteady boundary layer detachment at the trailing edge. These pressure

waves (2) then travel upstream and downstream, interacting with other flow regions. Part of the impacting pressure waves on the suction side wall of the underneath blade, (3), is reflected back into the main channel. Skin vortices (4) can also be created from this impact and will then interact with the flow on the suction side. Note that the downstream propagating pressure wave also interacts with the wake structures. Depending on the operating conditions, a shock wave, (5), can appear with supersonic regions. These complex flow phenomena have to be taken into account since they affect the aerodynamic field around the blade, and therefore, the heat transfer, which is one of the quantities of interest to turbine designers. An additional difficulty with these conditions is evidenced by the dependency of the flow patterns on the upstream turbulence as further discussed.

Before discussing prediction capability of heat transfer around a high pressure turbine cascade, aerodynamic predictions are first compared between (U)RANS and LES approaches illustrating the benefits of using unsteady methods, followed by a discussion on the importance of inlet conditions for LES.

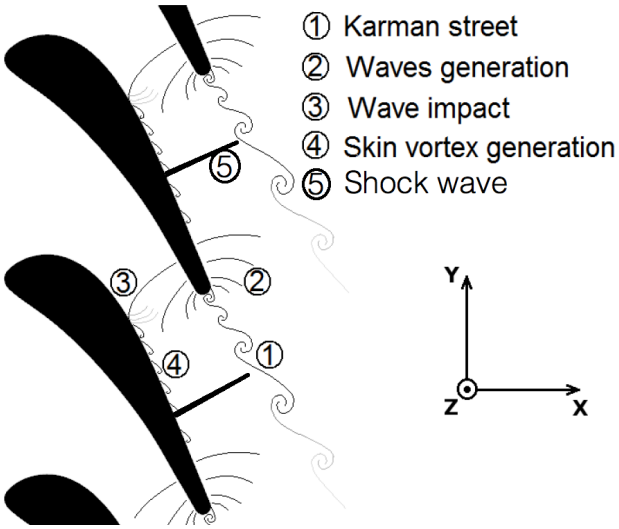

Figure 2.22: Schematic view of the flow topology around a typical cascade profile.

Turbulence modeling effect on aerodynamics

To assess predictive capacities of both turbulence closure (RANS, URANS or LES) and the mesh effect, the configuration from the work of Sieverding *et al.* [247, 246] (European Research Project BRITE/EURAM CT96-0143 on "Turbulence Modeling of Unsteady Flows in Axial Turbines") was simulated with different mesh resolutions and solvers in the context of the master training of Thomas Leonard. This work has been publish in Journal of Turbomachinery [167]. The blade is designed to study trailing edge vortex shedding on the steady and unsteady trailing blade pressure distribution of a laboratory turbine blade at high subsonic Mach number ($M_{2\,is} = 0.79$) and high Reynolds number ($Re_2 = 2,800,000$, based on the chord and outlet velocity).

Typical flow topologies obtained by RANS, URANS and LES with the elsA software are illustrated in Fig. 2.23. To complement the view, a snapshot of the experiment focusing on the trailing edge region of the flow is provided in Fig. 2.23 (d). Note that the mesh used for all the simulations contains 500,000 hexahedra with a mean Y^+ of about 5. All three numerical formulations result in distinct flow behaviors. RANS provides a mean temporal view of the flow field for the configuration under investigation. With this approach, Fig. 2.23(a), the local flow acceleration issued by the suction side flow passage restriction induces a density gradient upstream of the suction side. After the blade throat, a density gradient appears indicating the potential presence of a weak shock. The higher density gradients appear on each side of the trailing edge and are linked with the wake region induced by the blade boundary layer

separations at the end of the blade and the boundary layer itself. The time dependent description of the flow (URANS) provides new insights on the mean periodic solution, Fig. 2.23(b). With this approach, the local flow acceleration in the upstream region seems reduced if compared to RANS. The weak shock at the throat is no longer present. At the trailing edge and instead of a mixed out wake, vortex shedding appears along with pressure waves. Two distinct sets of waves are identified in agreement with Sieverding *et al.* [247, 246] and denoted on Fig. 2.23(d) by S_i and P_i respectively. Both sets of waves originate from the boundary layer separation point on the suction and pressure sides of the blade trailing edge. In URANS, the suction side generated pressure waves, S_i, propagate upstream and interact with the vortical structures present in the wake of the above blade. Their presence within the flow is clear although these S_i waves seem to be rapidly dissipated by the flow and the numerical model. The pressure side waves, P_i, also travel upstream but rapidly encounter the suction side wall of the neighboring blade located below. This interaction results in a reflected wave which eventually crosses the P_{i+1} wave.

LES provides an even finer view on the flow behavior, Fig. 2.23(c). With LES, all flow structures identified by URANS are present: the vortex shedding from the blade leading edge, both sets of pressure waves and their propagation. The P_i waves are also interacting with the main flow stream and impact the lower blade suction side wall. The differences between URANS and LES appear on these instantaneous views. The trailing edge sheds vortical structures that are more persistent in LES than in URANS producing more interactions between the wake and S_i waves.

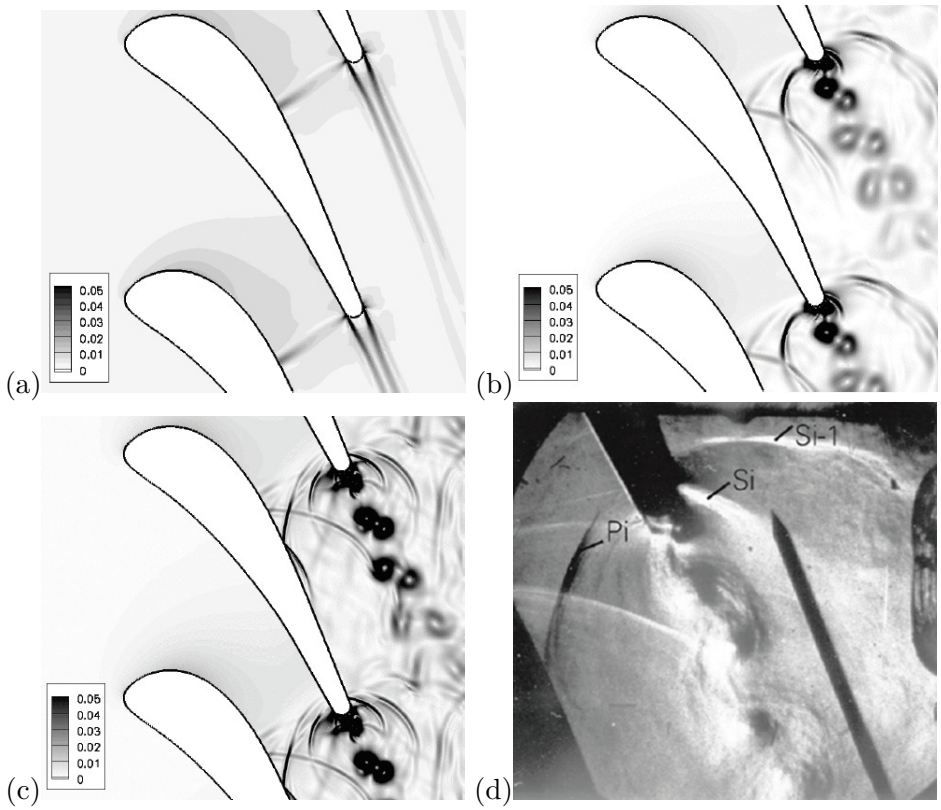

Figure 2.23: Norm of the density gradient as obtained by use of (a) RANS, (b) URANS, (c) LES at given instants and (d) a direct view at the trailing edge flow dynamics as seen in the experiment [247, 246].

A validation of the mean flow predictions is obtained by comparing the isentropic Mach distributions along the blade surface predicted by the three numerical approaches and measured experimentally, Fig. 2.24. Again, going from a purely stationary numerical model to an unsteady model clearly improves the flow predictions. Hence and in agreement with the discussion started above, the RANS prediction leads to a local miss-representation of the flow field. In particular, a

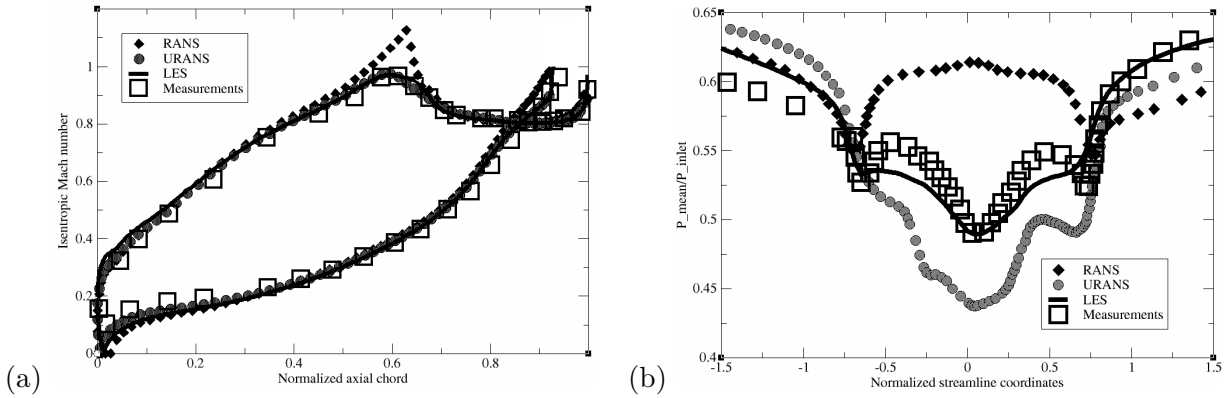

Figure 2.24: Mean isentropic mach distribution along the blade wall predicted numerically and measured in the experiment (a) and mean pressure distribution along the blade trailing edge (b).

Experiment	URANS (error)	LES (error)
0.219	0.276 (+26%)	0.228 (+4%)

Table 2.6: Wake shedding frequency expressed in terms of Strouhal number.

passage shock ($M_{is} > 1$) appears with RANS when it is not present in the experiment. URANS and LES allow net improvements when compared to RANS, with relatively small and only localized distinctions between the two unsteady flow approaches and for this blade quantity. URANS and LES both provide unsteady results but they are different: LES captures the wake shedding frequency than URANS 2.6. The Strouhal number is obtained from the signal pressure of a probe located at the trailing edge. It is worthwhile to point out that the frequency contents of the URANS and LES signals are very different, showing an almost unique frequency in URANS which capture only the deterministic vortex shedding and a broader range for LES illustrating the resolution of a turbulent activity. Differences are also identified when looking at the trailing edge mean pressure field (Fig. 2.24). For this specific region, only LES recovers the pressure level measured experimentally.

To complete the analysis, the boundary layer profiles obtained numerically are compared to experimental measurements on the pressure and suction sides, close to the trailing edge, Fig. 2.25. While the velocity profiles are correctly estimated by the RANS simulation, LES fails to accurately estimate the gradients in the near-wall region. This issue is more critical on the suction side of the vane than on the pressure side. This analysis highlights the difficulty in performing LES of near-wall flows and it indicates that a particular attention should be paid to the near-wall mesh.

From these results, it seems to be important to take into account unsteady flow feature to well reproduced the mean quantities disqualifying the RANS approach. Use of URANS offers a net improvement over RANS and higher order closures seem recommended to better capture turbulence interactions [160]. Finally, LES captures most of the physics reported by the experimentalists. Further investigations need however to be conducted as LES predictions are by construction mesh dependent as well as very sensitive to numerics and wall modeling.

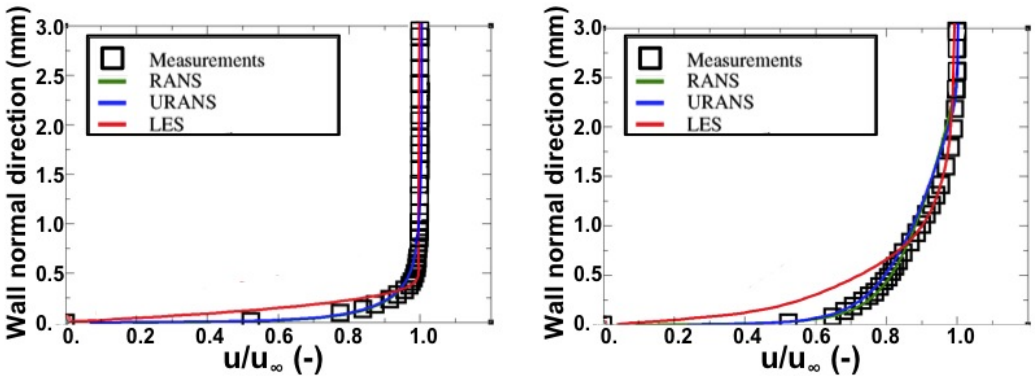

Figure 2.25: Evaluation of the boundary layer velocity profiles close to the vane trailing edge: (left) pressure side and (right) suction side, From [95].

Sensitivity of aerodynamics to inflow condition

To evaluate the sensitivity of the flow topology to inlet conditions, different LES were carried out on the T120 transonic blade experimentally tested at UniBw (Munich) during the European project AITEB II [251, 94]. To do so, the nominal operating point is targeted ($Ma_2 = 0.87$ and $Re_2 = 390,000$, Fig. 2.26) and different simulations are obtained by changing inflow specifications with and without turbulence injection during the PhD Thesis of Mael Harnieh. The results presented are extracted from a conference paper published in ASME TurboExpo 2017 [108].

The mesh is hybrid, composed of 24 millions tetrahedrons and 10 millions prisms. The mean y^+ is around 1-2. At nominal conditions without turbulence injection, a recirculation zone is found on the pressure side of the blade (Fig. 2.26). This is created by the detachment of the boundary layer on the pressure side where the geometry presents a strong curvature and by the reattachment of the boundary layer downstream. On the suction side, a supersonic zone is evidenced confirming that the flow is transonic. Thus, lot of activity of waves and shocks are expected. As exhibited on Fig. 2.26, acoustic waves are generated at the trailing edge due to temporal fluctuation of vortex shedding and are reflected on the suction side of the adjacent blade[39]. Due to transonic zone and temporal evolution of wake produced by the blade, the weak shock wave is oscillating around an average position. The shock induces a transition of the blade boundary layer for laminar to turbulent. This transition is likely to affect the losses and thus load of the blade.

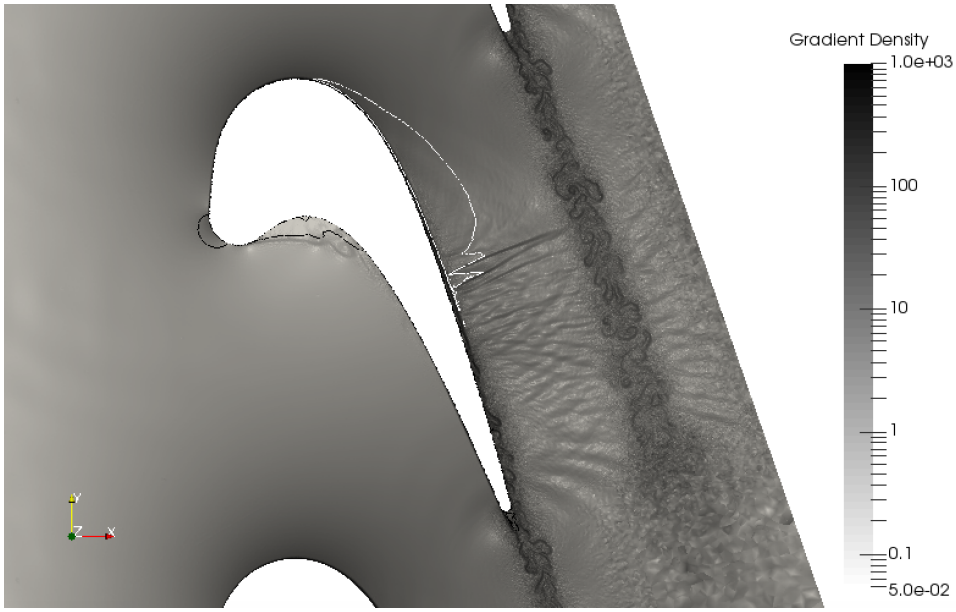

Figure 2.26: Instantaneous field of ρ gradient density at mid-span. Isocontour of $Ma = 1$ is plotted in white. Isocontour of null axial velocity is plotted in black.

A first set of simulations were obtained by changing the inlet total pressure by 4% to coincide with the experimental uncertainty compared to the nominal operating point. Investigation of dissipation field has proved that the majority of irreversibilities occurs in the turbulent boundary layer on the suction side and in the wake. Comparison of test cases shows a non linear interaction between the losses and the inlet total pressure. The pressure distribution around the blade is very sensitive to inflow specification (Fig. 2.27). The pressure distribution on the suction side is different because the inflow specification affects the flow rate and hence the shock position. Indeed, the larger the flow rate is, the larger the maximum Mach number is, which impacts the shock position. In contrast, the pressure side is not affected compared to the reference case. As a result, the response of LES depends on the capacity of the CFD tool to capture the correct losses within the flow as well as the expansion ratio.

The second set of LES concernes the effect of the turbulence injection on flow topology

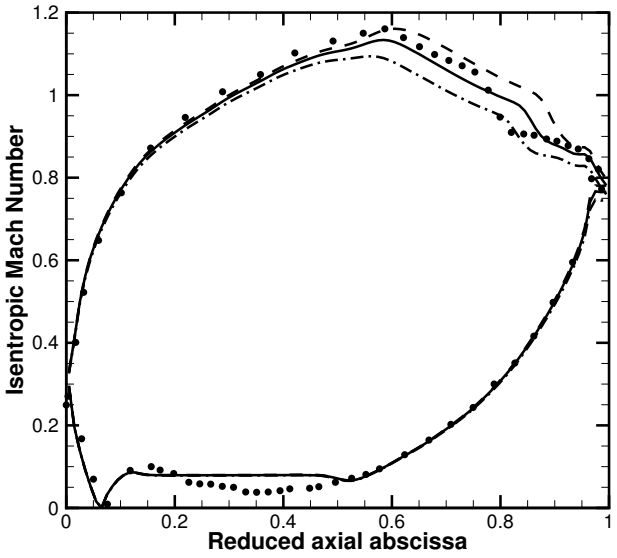

Figure 2.27: Isentropic Mach number along the blade: •, experiment; — LES reference case; — —, LES +4% on inlet total Pressure; — · —, LES -4% on inlet total Pressure.

and dissipation field. A synthetic turbulence injection is used [32, 103]. Results show that prediction is improved in the recirculation zone, the boundary layer staying attached on the blade wall (Fig. 2.28). On suction side, both laminar and turbulent boundary layer produce more irreversibilities. As a result, mean flow topology in this region is very different and prediction is improved as well as shock position. Isentropic Mach number reaches higher levels and the shock position is moved upstream compared to the reference case.

A deep analysis of losses induced by laminar and turbulent boundary layers, flow separations, wakes and main stream is under study in the PhD Thesis of M. Harnieh [108].

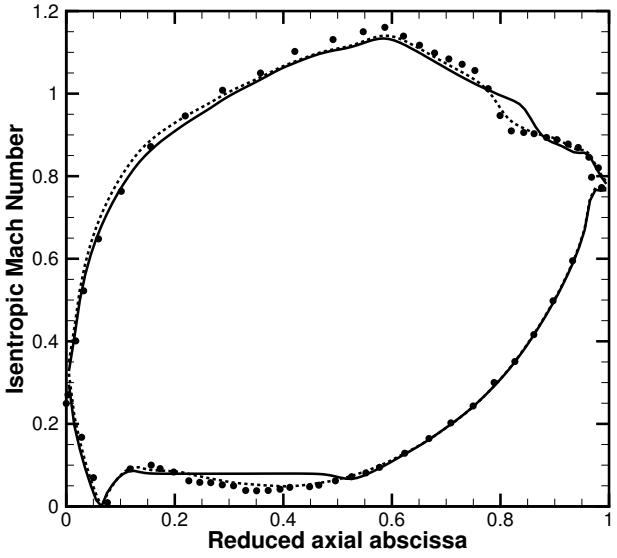

Figure 2.28: Isentropic Mach number along the blade: •, experiment; - LES reference case; - - , LES turbulence injection.

Prediction of wall heat transfer.

As presented, flow prediction is a key element in turbine flow aerodynamics and heat transfer understanding and today LES seems the most promising CFD approach for this. To gauge such tools, the LS89 turbine blade cascade has recently focused attention from the LES community, as it is a realistic turbine blade linear cascade configuration studied at VKI by [8]. It represents an excellent test case with a comprehensive database for comparison and has proven to be very sensitive to the turbulence injected; *i.e.* both the integral length scale and the turbulent intensity are of importance as shown in [98, 39]. Certain operating points from the database have been more thoroughly studied due to the difficulty to correctly predict certain fields such as the heat transfer when high Reynolds numbers are encountered. On the suction side for example, it is necessary to correctly predict the boundary layer transition to capture the interactions between the streaky structures generated in the boundary layer and the thermal boundary layer, critical for the correct estimation of the heat transfer in that specific region of the blade. However, the lack of information concerning the integral length scale in [8] has been tackled in many ways. Some authors have used a range of values as [98], others have estimated it from available data and presumed features as in [125]. Pichler *et al.* [207] have even simulated the grid located ahead of the cascade in the experiments to obtain the length scale value and characterize the turbulence to use. While the latter was ruled out due to cost, the values used in this paper have been taken from the literature. Overall, an extensive range of simulations has been performed to test various effects such as the influence of a higher intensity level and the different physics that might be encountered in this test case. Here, specific issues related to the turbulence injection process are addressed by using a reference refined mesh LES to analyze the possible loss of information on this specific difficulty whenever using alternative approaches and coarsened meshes. This work is extracted from the PhD Thesis of Luis Segui, part of which has been published in the 2017 European Turbomachinery Conference [239].

Although the integral length scale imposed at the inlet remains an open question, the quality of the injected turbulence is to be accounted for [64]. Indeed, classical synthetic type injection methods, [149], require some adaptation to develop a physical energy spectrum. Such modeling strategies add onto the difficulty of having an adequate boundary condition implementation and adequate grid resolution as well as numerical schemes. As such, different methods and LES codes will in fact inevitably produce different inflows or turbulent fields prior to the blade. To discriminate the importance of the initial spectrum and move away from synthetic turbulent spectrum that does not give physical solutions, a pre-computed turbulence approach is used to provide information to the boundary conditions. A precursor simulation [56] represented in Fig. 2.29, performed using the same code, is coupled in this study to the inlet domain to overcome any issue related to the adaptation length underlined previously. For this specific case, only modeling and grid resolution are expected to play a role and can be compared to the synthetic turbulence injection methodology previously mentioned.

The turbulent field to be injected into the main domain must be a homogeneous isotropic turbulent (HIT) field as the turbulence injected experimentally is of grid-turbulence type. Computationally, it means that it is necessary to keep the turbulent production in the precursor at the desired level [81, 201]. In terms of boundary conditions specification, the coupling software OpenPALM [70] is used to send the local velocity perturbation field from the precursor simulation to the inflow domain. The precursor field is taken into account in the main domain simulation through characteristic conditions as in [212]. To account for the mean velocity, the Taylor hypothesis is used in this specific application [252] in conjunction with the bulk velocity field of the main simulation. Computationally, this implies that the plane from which the information is extracted in the precursor is not fixed, but moves in the axial direction at the mean bulk velocity of the flow as prescribed by the main domain. Note that such a hypothesis is relevant since the inlet Mach number is low and fluctuations are of the order of 15% of the mean velocity [164].

To check the quality of the injected turbulence, a quasi-DNS simulation test case has been performed for a spatially decaying turbulent flow [239]. Spectra and correlations are compared

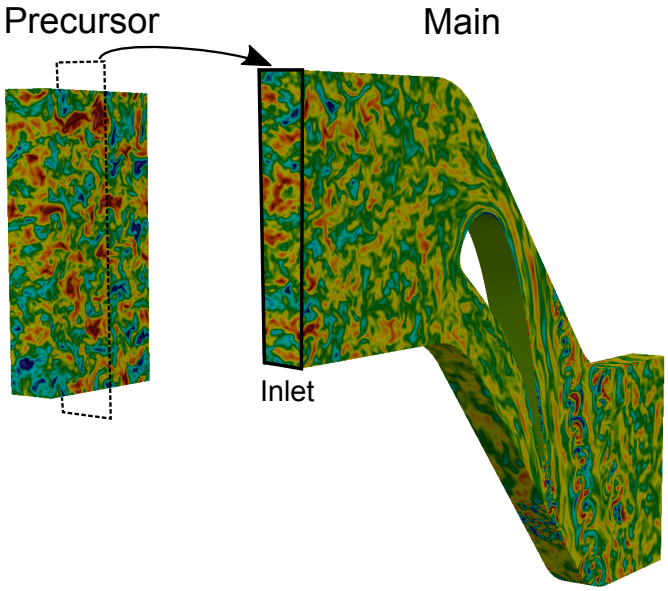

Figure 2.29: Global process of the precursor technique; fluctuations extracted from the precursor domain are transferred to the inlet of the main domain.

while the applicability of the Taylor hypothesis will be assumed a priori considering a low Mach number at the inlet. Figure 2.30 shows the Q-criterion of the main channel colored by the norm of the vorticity field for (a) synthetic and (b) precursor injection methods. Two distinct turbulent fields are clearly observed. This is confirmed by the fact that the spectrum quality at the inlet differs and is clearly improved when using the precursor simulation, Fig. 2.31. The precursor simulation follows the Kolmogorov tendency up to high wave-numbers, the high limit being associated to twice the characteristic cell size. The synthetic injection spectrum on the other hand peaks at a lower wavenumber because of the construction method and decays very rapidly indicating that the energy is not properly distributed. Figure 2.31 shows the turbulent kinetic energy decay curve as a function of the axial distance to the channel inlet: the precursor follows quite accurately the analytical evolution of a temporally decaying HIT which it is not the case for the synthetic injection. Note nonetheless that this spatial evolution of the kinetic energy as well as turbulent features will be impacted and only the precursor method provides the proper turbulent flow and a more physical turbulent injection in this case.

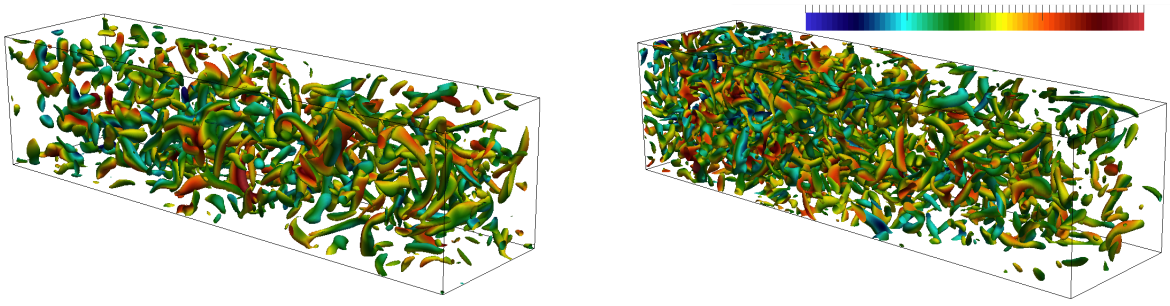

(a) (b)

Figure 2.30: Q-criterion of channel for a) synthetic b) precursor method colored by vorticity.

In Figure 2.32, both the effects of turbulence injection method and inlet turbulence intensity are investigated on the MUR235 operating condition of the LS89 using a 60 M cells mesh

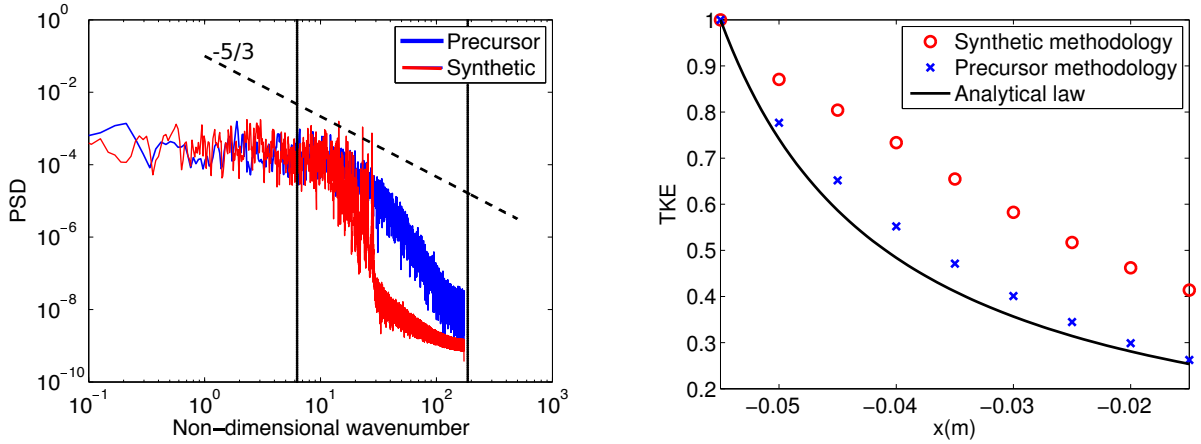

(a) (b)

Figure 2.31: Turbulence injection methods comparison. (a) Spectrum comparison at inlet plane. Limits given by size of domain and smallest cell. (b) TKE decay evolution between inlet and leading edge

with a mean y^+ of about 5. It is difficult to exactly impose the same integral length scales in both methodologies and this leads potentially to uncontrolled discrepancies. Both turbulence injection numerical predictions produce a similar heat transfer coefficient distribution over the whole blade, whatever the value of the injected turbulence intensity. Increasing the turbulent intensity shows an improved agreement around the leading edge region, complemented with a great improvement on the pressure side region. The suction side however remains the most challenging. An earlier transition seen when injecting a level of 18% turbulence intensity seems to improve the heat flux prediction, notably near the region of $s = 25$ mm. The existence of streaks in the buffer layer are observed in all cases when free-stream turbulence is present [239]. This is not the case for the MUR129 operating case without inlet turbulence where no structure is observed on neither pressure nor suction side. This leads to the conclusion that stretching at the leading edge of the blade and realignment of vortices due to the pressure gradient are responsible for the known spanwise structures characteristic of this region, [274]. These specific structures can henceforth be linked to the leading edge heat transfer enhancement. It is furthermore noted that this process is quite insensitive to the inlet turbulent intensity.

By refining the mesh up to 213 M cells (mean y^+ of about 3), the increase in resolution allows smaller structures to reach the leading edge as confirmed by Fig. 2.33 where smaller turbulent structures can be observed when the finer mesh is used. Aside from the previous effect on turbulence, the most noticeable effect of the grid resolution is the acoustic waves emanating from the vortex shedding from the trailing edge seen in Fig. 2.33. The strong acoustic waves that are then reflected from the blade are much less intense in the refined mesh. Differences may be partly explained by the different refinement in the trailing edge region as well as the potential impact of the different turbulent fields in this specific region of the flow. In the coarse case, the flapping characteristic of the vortex shedding is much more intense than for the finer mesh which sheds further downstream as seen in Fig. 2.34. A similar effect has been shown by [263], due to a variation of the Mach number.

The presence or absence of the waves has a direct impact on the boundary layer, and thus, on the heat transfer coefficient shown in Fig. 2.35. Indeed, the boundary layer of the coarse mesh transitions upstream when compared to the fine mesh. The acoustic waves seem to be driving the transition location, where even low-amplitude waves are seen to lead to a pre-transition for the 213M mesh. Figure 2.35 also shows that the fine mesh predicts more accurately the shock position and the level of h downstream of the shock if compared to the coarse mesh. This work is still an active one and new results on finer grids with associated discussions on transition processes will presented in the PhD Thesis of Luis Segui (end of 2017).

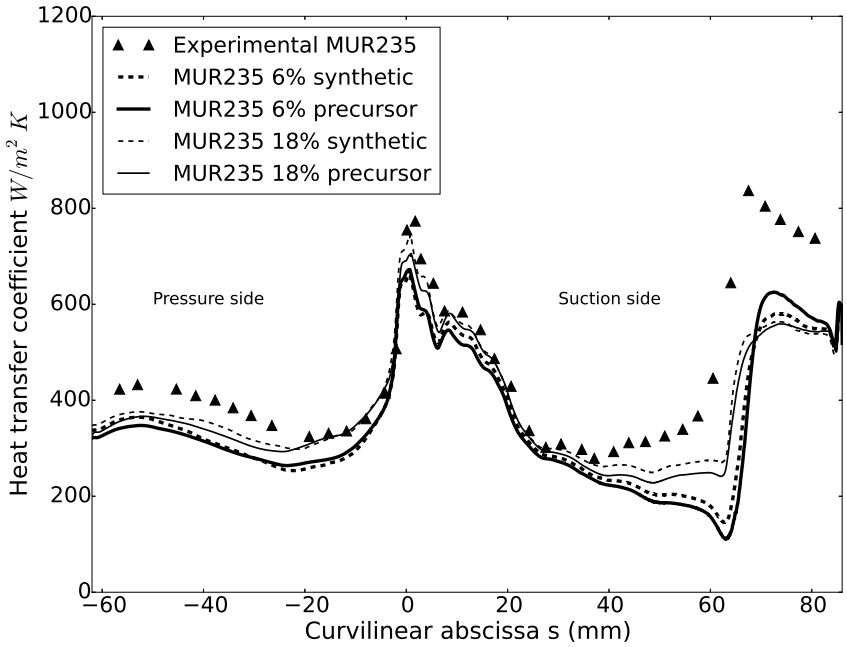

Figure 2.32: Heat flux comparison of turbulence injection methods for the LS89 - MUR235 operating point with a 60M grid cells. Suction side is represented on positive s and pressure side on negative s.

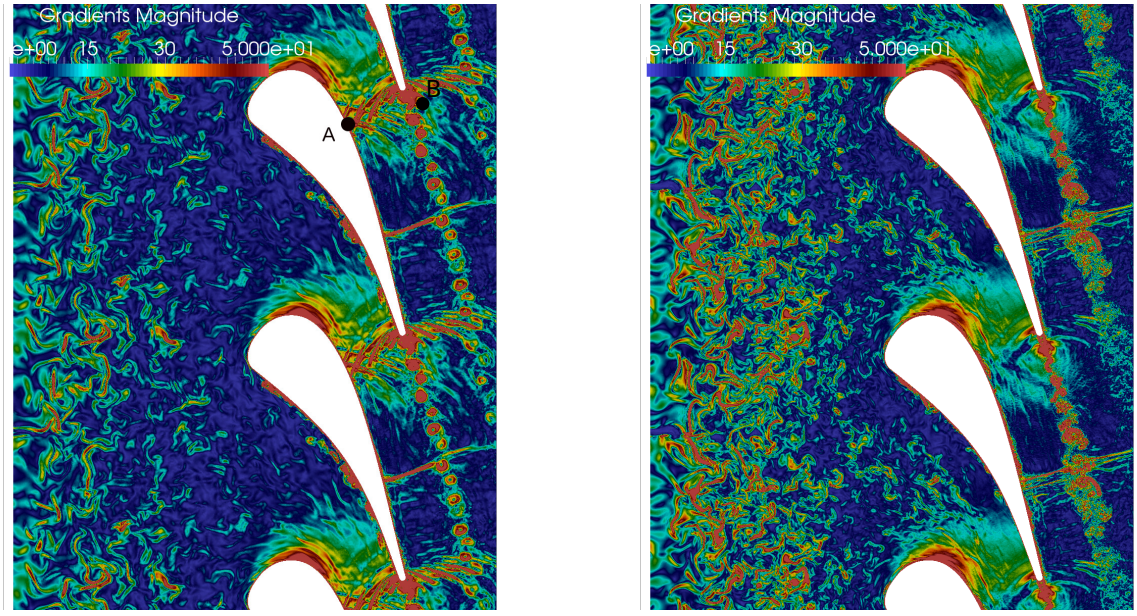

(a) (b)

Figure 2.33: Density gradient fields for a) 60M and b) 213M cells mesh.

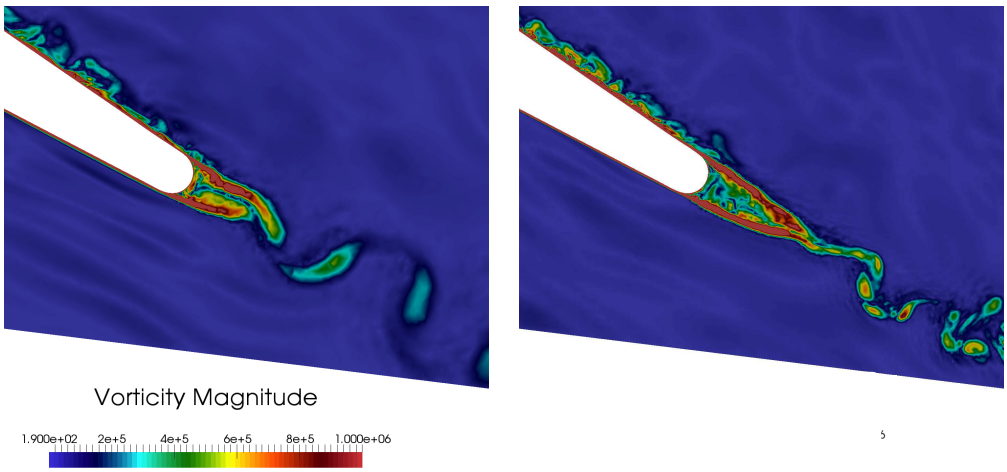

(a) (b)

Figure 2.34: Blade wakes: instantaneous views of the vorticity magnitude fields for a) the 60M and b) 213M cell meshes.

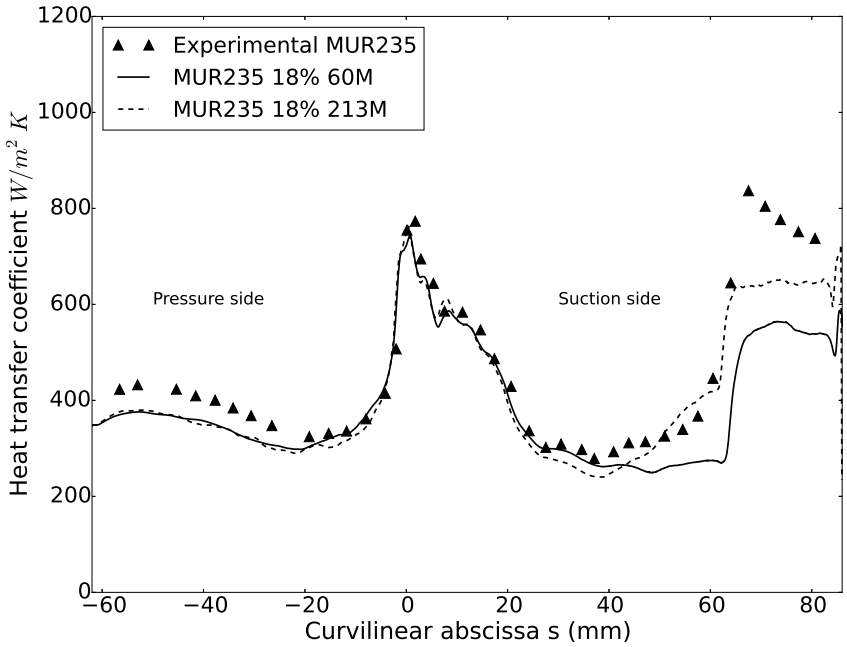

Figure 2.35: Heat flux comparison of MUR235 with fine mesh. Suction side is represented on positive s and pressure side on negative s.

2.1.3 When temperature has a strong impact on the flow physics.

In the results presented until this point, the focus was on thermal aspects induced by aerodynamics. To do so, different temperatures or heat fluxes are imposed to both free stream and walls and the goal is to quantify heat transfer on solid frontiers. Most of the time, a linear relation is expected between heat flux and a temperature difference at each discrete location x of the wall surface:

$$\phi(x) = h(x)\left(T_{ref}(x) - T_w(x)\right) \tag{2.2}$$

with h the so-called convective coefficient, T_{ref} a reference temperature and T_w the local wall temperature. This Newton law of cooling states that the rate of heat loss ϕ of a body is proportional to the difference in temperatures between the body T_w and its surroundings T_{ref}. As such, it is equivalent to a statement that the heat transfer coefficient h is independent of the temperature difference for a given flow regime. Such conditions are often met in forced convection on given ranges of operating condition expressed both in terms of flow regime and temperature difference and imply a moderate dependency of the aerodynamics to the thermal conditions. When temperature variations become larger and the flow field is driven by the thermal field, such a relation has a smaller range of validity and the knowledge of heat transfer in given conditions requires the study of the system either experimentally or numerically. Two main situations representative of this flow regimes where encountered during my research activities:

- buoyancy driven flow topology in ribbed rotating channels
- laminar premixed flame stabilisation on bluff bodies.

Buoyancy driven flow topology in a ribbed rotating channel

Turbine blades often use internal channels where air from the compressor flows to cool it down. These systems must maximize heat transfer while minimizing airflow rate to avoid engine power penalties. This leads to a new class of fundamental questions linked to wall heat transfer in rotating systems. Ribs are used to promote turbulence in the channels as well as to increase the surface between air and solid and thus increasing the total amount of heat extracted from the blade. To evaluate LES in this rotating context, the experimental test case of the VKI rotating facility by Di Sante *et al.* [57] is investigated (Fig. 2.36) during the PhD Thesis of Thomas Grosnickel. The results presented are extracted from a conference paper presented at the ASME TurboExpo 2017 [102]. The experimental test rig consists of a straight channel mounted on a wooden disk. Eight ribs are placed on one side of the channel to introduce turbulence in the channel and is representative of an existing gas turbine cooling technology. The rotation speed for this study is around 130 rotations per minute (RPM) yielding a rotation number of

$$Ro = \frac{\Omega D_h}{U_0} = 0.38 \tag{2.3}$$

where Ω, D_h and U_0 are respectively the rotation speed, channel hydraulic diameter and bulk velocity of the flow.

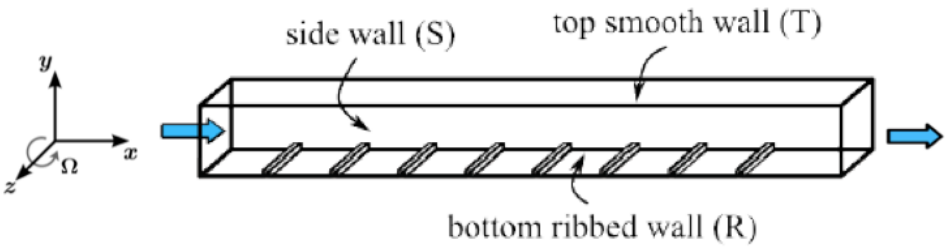

Figure 2.36: Scheme of the numerical domain used for the rotating ribbed channel.

Considering the simple case of a 2D channel flow in the (x,y) plane rotating around the z axis, as shown on Fig. 2.37, the Coriolis force will balance the wall-normal pressure gradient. Based on the stability analyses developed by Bradshow *et al.* [25], boundary layers on the pressure side will destabilize, while the ones on the suction side will stabilize. The main impact on the flow quantities is a change in the near-wall turbulence level. More precisely, the stabilized (destabilized) side sees a decrease (increase) in turbulence intensity, implying an increase of the symmetry loss of the main flow velocity profile compared to a laminar rotating channel. Previous observations have been experimentally reported by Johnston *et al.* [126] and later confirmed by the DNS of Kristoffersen *et al.* [150] and Lamballais et al. [159].

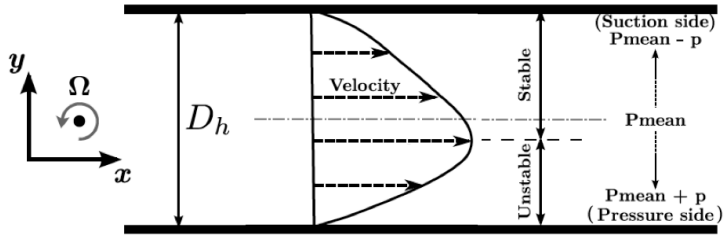

Figure 2.37: Scheme of a 2D rotating channel.

Adding ribs on the bottom side of the above discussed channel, turbulent flow in the vicinity of the ribs will be either further stabilized/destabilized when the channel is rotating in the negative/positive direction for the reasons detailed above but applied to an already turbulent flow. This behavior is illustrated on Fig. 2.38 that shows the Losses in Kinetic Energy (LIKE) given by

$$\phi = \overline{(\mu + \mu_t)\left(\frac{\partial \tilde{u}_i}{\partial x_j} + \frac{\partial \tilde{u}_j}{\partial x_i}\right)^2} \tag{2.4}$$

where μ and μ_t are the laminar and turbulent viscosities, $\tilde{u}$ is the resolved LES velocity field and $\overline{\cdot}$ is the temporal average operator. This quantity relies on irreversible dissipation of kinetic energy due to viscous friction in the fluid. In the static case, most of the dissipation occurs in the vicinity of the ribs (Fig. 2.38). Some dissipation occurs also on the smooth walls due to friction but its intensity is here found to be lower. On one hand, dissipation is higher in the near rib regions for the destabilized cases than in the static reference one. On the other hand, Fig. 2.38 shows that dissipation is lower in the near rib regions for the stabilized cases than in the static reference and destabilized cases. This observation confirms that the expected flow responses are reproduced by the respective simulation and that LIKE captures its impact.

Figure 2.39 illustrates that the LES approach used in this context is well suited to represent the flow field in adiabatic configurations [87, 102]. The axial velocity profiles between the 6th and 7th ribs are accurately predicted by the computations in the static, stabilizing, destabilizing regimes [102].

Figure 2.40 shows the impact of imposing an isothermal boundary condition on the ribs while keeping the other walls adiabatic for the static and the two rotation cases between ribs 6 and 7. When the channel is rotating, bigger differences appear between adiabatic condition and isothermal one than in the static case. For the positive rotation case, only the major recirculation zone after rib 6 is affected by the wall temperature change. When the ribs are heated, the recirculation gets stronger as the negative velocity under $y/h = 1$ is larger. The recirculation zone between the two ribs is also larger: for the adiabatic wall boundary condition the reattachment occurs between $x/h = 4$ and $x/h = 5$ while for the heated wall case, the recirculation remains still visible at $x/h = 9$. Note finally that no effective difference appears near the center of the channel at y/h above 1.5. For the negative rotation case, differences in axial velocity values can go up to 25%. The major differences appear over the ribs. When the flow is heated by the wall, the axial velocity above $y/h = 1$ is much smaller than with the adiabatic wall condition. This observation is consistant with the experimental results found

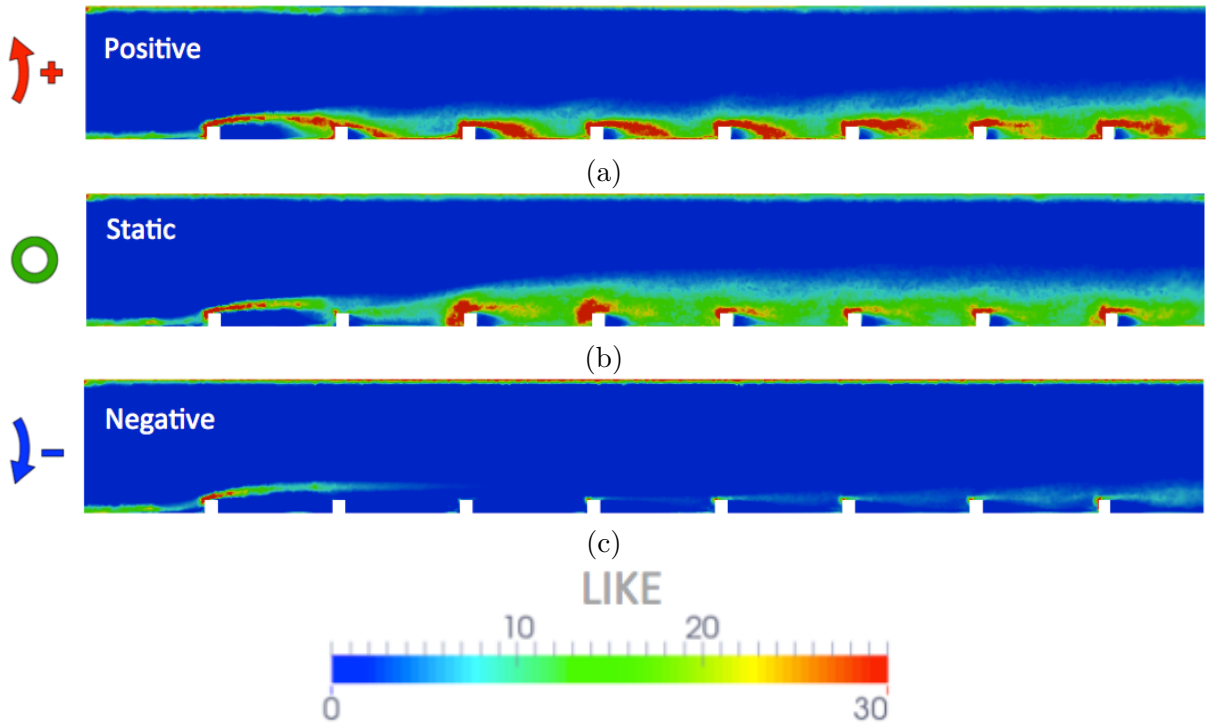

Figure 2.38: Contour of Loss in Kinetic Energy (Eq. 2.4) on the channel symmetry plane in positive rotation (a), static (b) and negative rotation (c) for adiabatic cases.

by Coletti *et al.* [36] and LES/experiments comparison is good [102]. As this case is more sensitive to thermal conditions, the mechanisms beyond these differences will be explained in more details. Figure 2.41 shows the flow development along the channel with the adiabatic and the isothermal wall conditions. The differences start after the third rib: the recirculation takes more space between the ribs with the heated wall but the main difference is the elevation of the high velocity zone of $u/U_0 > 1.2$ toward the smooth top wall of the channel. This leads to a decrease of the axial velocity in the near ribs region as noted on Fig. 2.40. This phenomenon was already seen experimentally by Coletti *et al.* [36] and the mechanism can by schematically represented on Fig. 2.42. First, the near-wall region is heated by the isothermal boundary condition. The heated fluid layer is then submitted to a centripetal buoyancy force that drags the fluid against the main flow direction. This leads to a recirculation zone that takes all the space between two ribs as visualized on the streamlines of Fig. 2.43. Second, the mixing layer going over the upstream rib cannot go anymore towards the wall between the ribs and goes directly over the downstream rib. The consequence is that the main flow is pushed away from the ribs by the mixing layer as evidenced on Fig. 2.41.

The impact of buoyancy can be quantified by the Buoyancy number Bo following the expression in Eq. 2.5,

$$Bo(r) = r\Omega^2 \frac{D_h}{U_0^2} \frac{T_w - T_0}{T_0}, \tag{2.5}$$

where $r\Omega^2$ is the centrifugal force, T_w the wall temperature while U_0 and T_0 are respectively the bulk velocity and bulk temperature. Looking at Eq. 2.5, the buoyancy is mainly driven by the temperature difference issued by the wall and the fluid but also by the rotation number. It was found experimentally that the heat transfer evolution changes for $Bo > 0.2$ [33, 270]. This was corroborated by the LES of Sewall *et al.* [243] who found that for $Bo < 0.25$, the recirculation zone is only growing but for $Bo > 0.25$ this recirculation takes all the inter-rib space, explaining differences in heat transfer. Note that Bo is a fonction of r and here $Bo = 0.2$ corresponds to the third rib location, where the flow topology begins to change. This study demonstrates that heat transfer and aerodynamics are strongly coupled in this ribbed channel configuration.

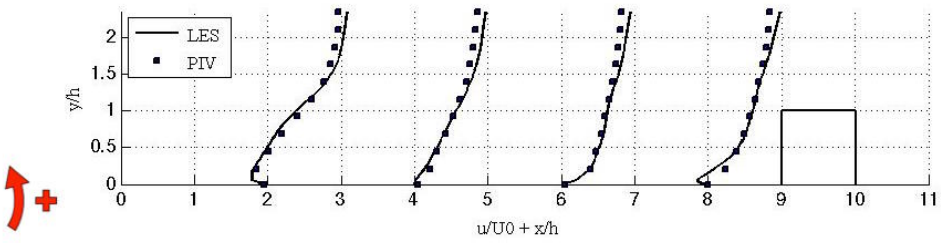

(a)

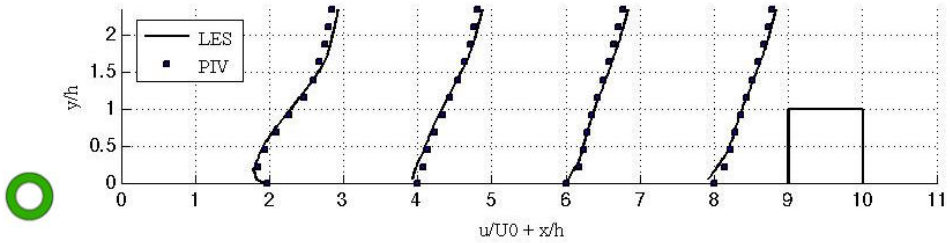

(b)

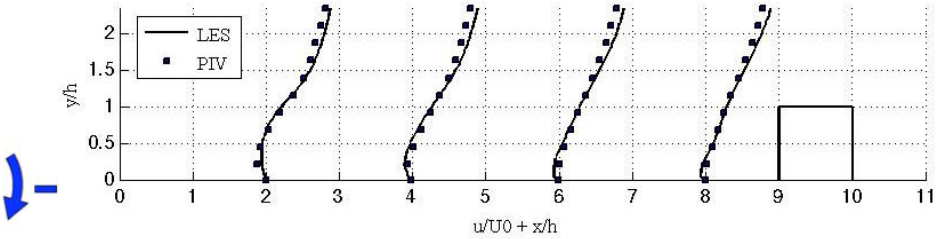

(c)

Figure 2.39: Comparison of mean axial velocity profiles on the symmetry plane from LES (lines) and PIV (symbols) between the 6th and 7th ribs: Positive rotation (a), static (b) and negative rotation (c).

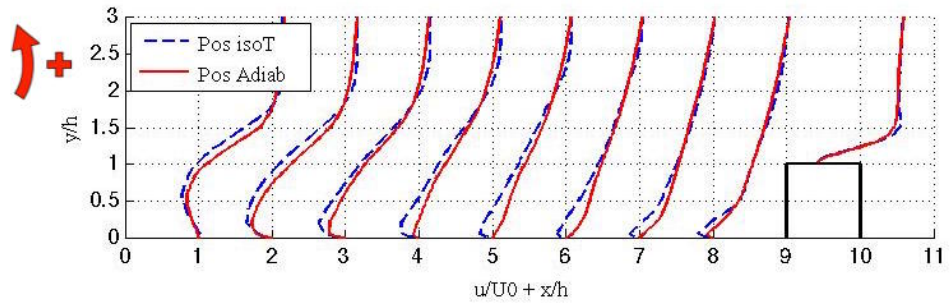

(a)

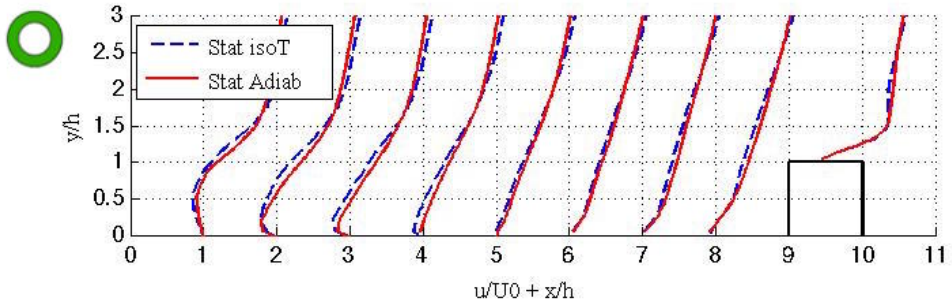

(b)

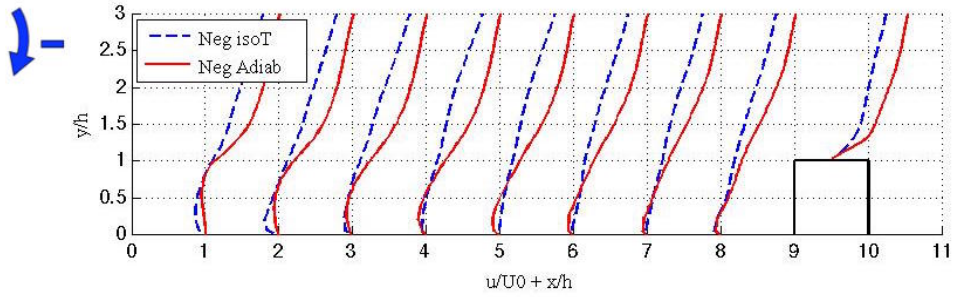

(c)

Figure 2.40: Comparison of mean axial velocity profiles on the symmetry plane from adiabatic LES (dashed-lines) and isothermal LES (lines) between the 6th and 7th ribs: Positive rotation (a), static (b) and negative rotation (c)..

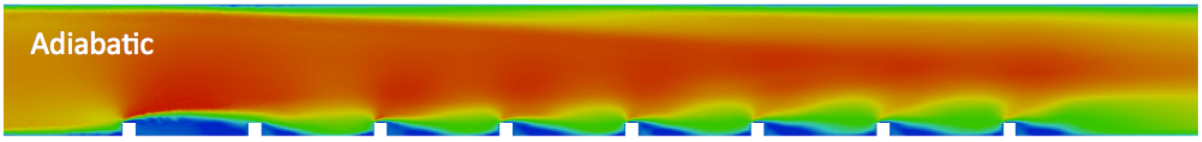

(a)

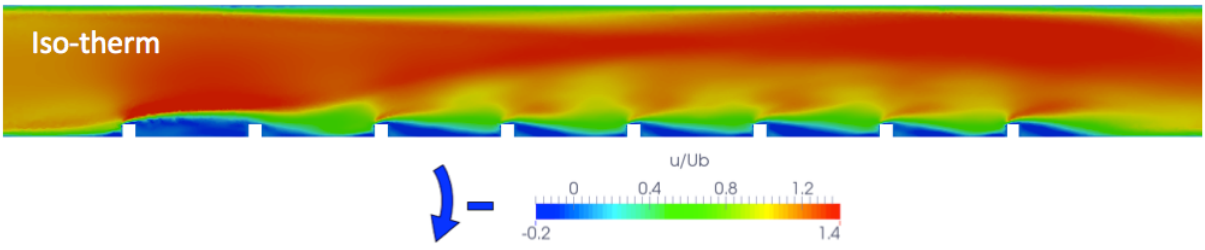

(b)

Figure 2.41: Non dimensional axial velocity on the symmetry plane of the channel with adiabatic (a) or isothermal (b) ribbed wall boundary condition.

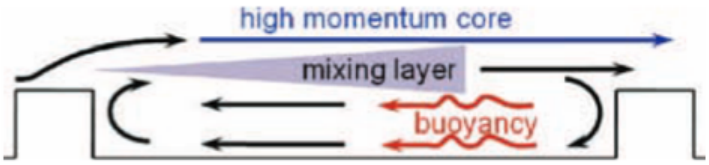

Figure 2.42: Schematic model for the mean flow by Coletti *et al.* [36].

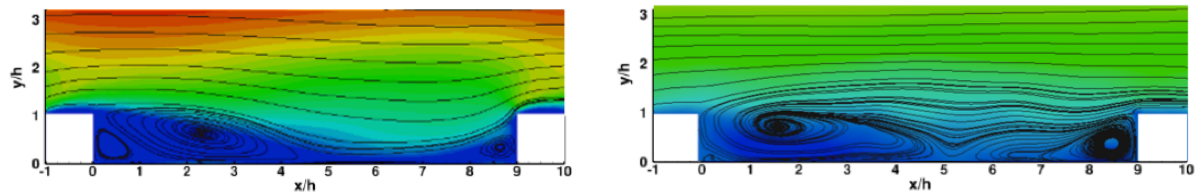

(a) (b)

Figure 2.43: Streamlines of velocity in the recirculation zones with adiabatic (a) or isothermal (b) ribbed wall boundary condition.

Laminar premixed flame stabilisation on bluff bodies

The stabilization process of laminar premixed flames on bluff bodies is largely influenced by wall temperature [82, 177, 134, 16, 26, 275]. To illustrate this point in a well controlled context where minimum modeling is introduced, several fluid-only simulations with different bluff-body wall temperatures are produced and discussed. These indeed allow to study the influence of the bluff-body uniform temperature on the flame stabilization pattern and flow fields. This work has been done during the PhD Thesis of Sandrine Berger and published at the ASME TurboExpo conference 2016 [16] as well as in Journal of Flow Turbulence and Combustion [15]. The geometrical configuration consists of a square cylinder placed in a laminar channel flow (Fig. 2.44). This bluff-body stabilized flame configuration is derived from the study of [134, 137, 135].

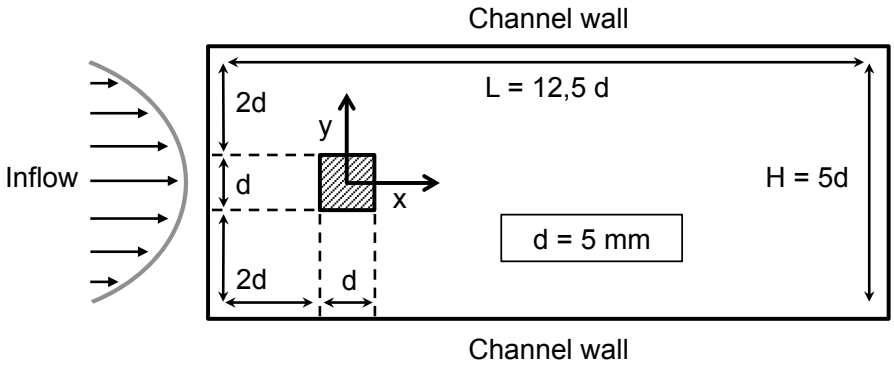

Figure 2.44: Schematic view of the square bluff body for flame stabilization computational domain.

The flow Reynolds number, based on the inflow quantities and the flame holder dimension, is $R_e = 500$. For combustion to proceed, a perfectly premixed mixture of methane and air is injected at the inflow at an equivalence ratio of $\phi = 0.7$. A two-step six species reduced kinetic scheme called 2S_CH4_BFER [88] is chosen. At the inflow, a fully-developed laminar parabolic profile is prescribed with a bulk velocity equal to $U_0 = 1.6\ m.s^{-1}$. Fresh gases enter the channel at a temperature $T_0 = 300\ K$. The outflow condition is set at atmospheric pressure $P = 1\ atm$.

For the regimes under investigation, the flame stabilizes symmetrically to the square bluff body thanks to a recirculation zone as presented on Fig. 2.45. The recirculation zone has various effects: it brings hot temperature burnt gases upstream, warming up and diluting the fresh gases and it provides a favorable aerodynamic region with very low velocity. The recirculation zone actions added to the heating/cooling effect of the flame holder wall result in flame stabilization. Naturally, acting on one of these processes could affect greatly the other parameters and hence the flame stabilization pattern. These observations are in full agreement with previous findings and are entry points for specific investigations. For example, Kedia *et al.* [134] investigate the effect of fuel composition, chemistry modeling and species differential diffusion on the near flame foot flow organisation and flame stabilization.

Depending on the wall temperature and for the specific initial flow condition, these computations evidence an upstream displacement of the flame foot as the wall temperature is increased and lead to the identification of three main stabilization regimes (Fig. 2.46). Indeed, the flow switches from a lifted flame (wall temperature in the range 600-1000 K) in which the recirculation zone provides the heat necessary to maintain the flame, to an anchored flame (wall temperature in the range 1100-18000 K) where fresh gas preheating is assured almost entirely by the walls or, for very hot temperatures, a bowed flame (stabilized ahead of the bluff-body for wall temperatures larger than the adiabatic flame temperature of about 1800 K) where combustion is sustained through a pseudo auto-ignition process. Heat flux distributions along the bluff-body walls are observed to be dictated by the flame stabilization process, illustrating the different mechanisms. An integration of these fluxes on the whole flame holder surface high-

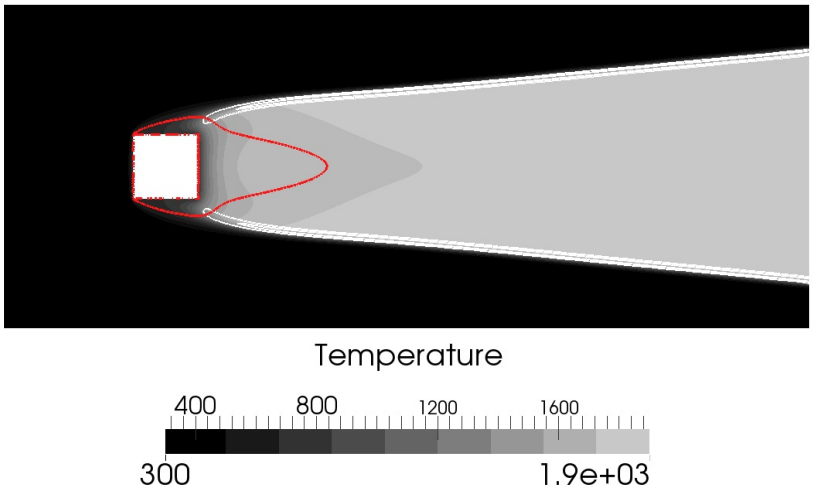

Figure 2.45: Temperature field with zero axial velocity contours (red) and heat release contours in white for the baseline flame stabilized on a square flame body ($T_w = 700\ K$).

lights a non-monotonous behavior as a function of flame holder wall temperature (Fig. 2.47). In particular, three equilibrium states (for which the curve crossed null integrated flux axis indicated by stars on Fig. 2.47) are evidenced for this configuration, suggesting that computation of more realistic cases including thermal conduction in the bluff-body solid could lead to different converged results depending on the initial thermal field.

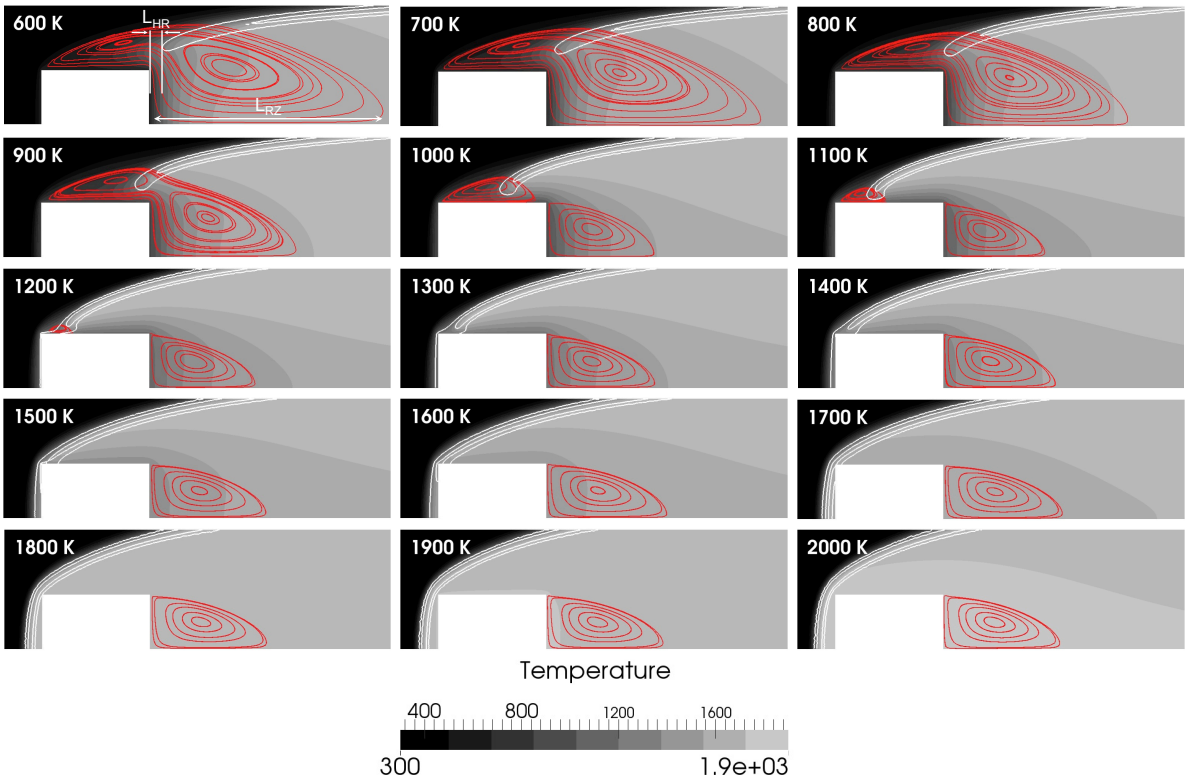

Figure 2.46: Temperature field with heat release contours in white and flow streamlines within the recirculation zone (red) in the vicinity of the flame holder on the top half of the domain. The temperature of the flame holder is imposed and varies from 600 to 2000K.

Flame stabilization mechanism is a main driver of combustion instabilities [136, 115, 177, 134, 183, 176]. As a result, thermal conditions on the flame holder walls appear to be of primary importance for the characterization of instabilities. In this context, the sensitivity of laminar

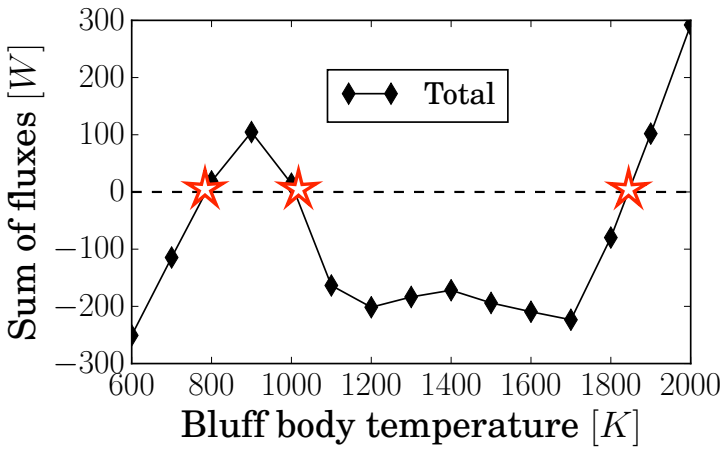

Figure 2.47: Integrated fluxes along the walls of the bluff-body for the different thermal conditions in the flame holder configuration from Fig. 2.44. Stars indicates potential thermal equilibrium states.

premixed methane/air flame responses to acoustic forcing has been investigated using direct numerical simulation to determine which parameters control their flame transfer function. In collaboration with IMFT and EM2C and published in Combustion and Flame [68], the delays τ of the flame transfer function (FTF) were computed for the axisymmetric flames of Boudy *et al.* [24] and the slot flames of Kornilov *et al.* [143] for different driving parameters introduced below. The simplest way to evaluate τ is to express it as the mean time necessary for a velocity perturbation to be convected from a given location to the effective position of concentrated heat release [73, 169]:

$$\tau = \frac{H_f}{\beta V_e} \tag{2.6}$$

where V_e is the convective velocity at the burner inlet, H_f is the flame height and β is a coefficient depending on the configuration. Values of β ranging from 1 to 3 are typically measured. Since the flame height depends on the flame speed s_L and on the convective velocity V_e, Eq. 2.6 suggests that τ changes only with s_L and V_e, hence that kinetic parameters (controlling s_L) but also temperatures of gas and walls (controlling V_e and s_L) must be important input data for τ.

FTFs of laminar premixed flames were computed using direct numerical simulation (DNS) to evaluate the influence of five critical input parameters (Fig. 2.48): (1) the flame speed s_L obtained by the kinetic scheme, (2) the shape of the domain characterized by its expansion angle α, (3) the inlet air temperature T_a, (4) the inlet duct temperature T_d and (5) the combustor wall temperature T_w. All these parameters have a direct effect on the FTF delay τ (or phase $\phi = \tau\omega$, ω begin the excitation frequency). The flame speed s_L obviously controls the flame length and therefore the delay of the flame to react to velocity changes. The shape of the domain determines the expansion of the burnt gases and the flow velocity, thereby also changing the FTF delay: here it is supposed to have a conical shape of angle α. The inlet air temperature T_a affects both the gas velocity and the flame speed whereas the inlet duct temperature T_d changes the temperature and velocity profiles at the burner inlet. The combustor walls temperature T_w determines the lift-off of the flame and can also control the FTF delay. Obviously, other uncertainties and phenomena can affect the FTF as radiation heat losses, geometric imperfections, inlet velocity profiles (steady and forcing parts), flame to flame interactions, three-dimensional effects or position of the reference point for the velocity measurement. Nevertheless, the study is restricted to these five parameters which are difficult to determine precisely, have an important impact on FTF, and are easily manageable with a CFD solver.

Both Boudy and Kornilov experiments are almost equally sensitive to input parameters. Certain parameters such as the combustor wall temperature T_w (which control the flame lift-off) have no influence at all in both cases and it is not worth spending time trying to determine them with precision. Flow expansion (α) also has a limited effect. The delay has a rather high

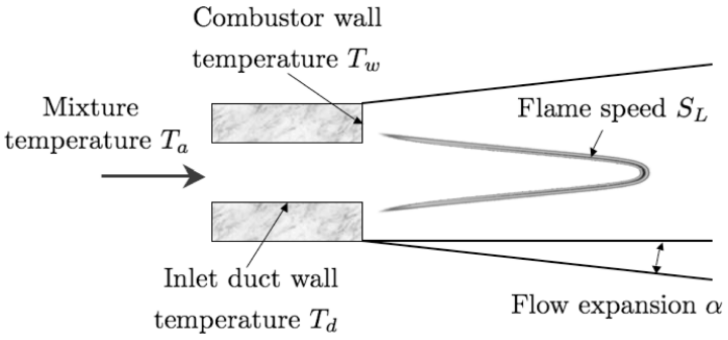

Figure 2.48: Parameters controlling the FTF of a laminar premixed flame.

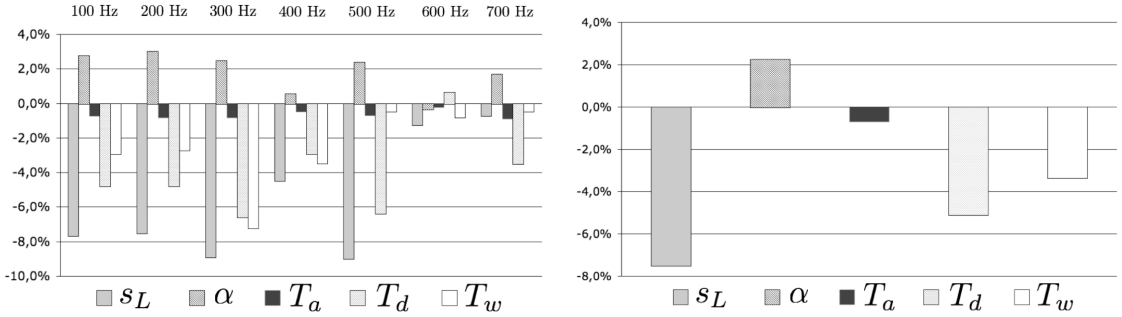

Figure 2.49: Relative errors on the phase ϕ of the Kornilov FTF versus computations parameters for several frequencies (left). Mean of relative errors on the phase ϕ of the Kornilov FTF over the frequency range $[100, 500]$ Hz (right).

sensitivity to inlet temperature but this quantity is usually well known, leading to small errors on the FTF phase. Figure 2.49 shows that the dominant role of the flame speed s_L controlled by the reduced kinetic used [88] and of the duct temperature T_d is obtained on the whole range of excitation frequency 100 Hz to 500 Hz. Beyond 600 Hz, the effect of the input parameters is largely reduced because of phase saturation [68]. Two parameters play a significant role:

- the flame speed s_L has a direct effect on the delay. Unfortunately, this is typically a quantity that is not well known and difficult to specify with precision. In the present computation, s_L is not specified directly because finite rate chemistry is used but it is a direct function of the pre-exponential constants used in the chemistry description. The main problem here is that experiments do not allow flame speed measurements within a 2 cm s^{-1} range for hydrocarbon flames so that it is difficult to adjust kinetic models for DNS.

- the duct wall temperature T_d induces significant errors on the FTF phase ϕ because it is difficult to evaluate precisely. For both cases, it is essential to know the wall temperature of the inlet duct to predict the phase correctly. Moreover for the present cases, the duct temperature was assumed to be the same everywhere: in practice, it could also vary with spatial position. The importance of the duct wall temperature comes from multiple facts. The premixed gas passing through the inlet duct is heated significantly by the hot walls: the gas velocity increases (because of the reduced density) and the local flame velocity also increases. These two factors modify the velocity field and the flame response to pulsations.

2.1.4 Intermediate conclusions

Simulations presented in this section have highlighted the ability of DNS and LES to provide high quality results on academic geometries where complex flows are encountered (stagnation,

	Square cylinder	Tandem of cylinders	Imping. jets	Ribbed channel	LPT	HPT BRITE	HPT T120	HPT LS89
Reynolds	22,050	16,000	23,000	15,000	158,088	2,800,000	390.000	1,150,000
Mach	0.108	0.105	0.1	0.01	0.116	0.79	0.87	0.927
Mesh	12.6	12	42	3.6	54.8	1.9	34	213
CPU	38,400	70,000	121,000	10,000	120,000	950	60,000	110,000

Table 2.7: Computational costs in CPU hours for the different cases presented in the heat transfer section. LPT: low pressure turbine, HPT: high pressure turbine. Mesh size is expressed in millions of cells. CPU costs are collected on different architectures and cannot be strictly compared.

mixing, massive separations, acoustics, laminar to turbulent boundary layer transition, shocks ...) It is worth mentioning that several developments of the solver have been requested to perform these simulations mainly for boundary conditions setup (total pressure and temperature inlet condition, turbulence injection, compliance of boundaries with rotation) and post-processing. Based on these experiences, we can propose methodologies to predict heat transfer with a high degree of fidelity with an unstructured LES solver in a wall-resolved context. It relies on:

- a hybrid mesh composed of prism layers at the wall and tetrahedra in the domain to resolve at a lower cost than a full tetrahedral mesh the boundary layers,
- a high-order numerical scheme (TTG family of schemes, at least third order accurate in time and space [37]),
- the Wall-Adapting Local Eddy-viscosity (WALE) sub-grid scale model that recovers the proper turbulent viscosity decrease at walls [193] or alternatively the σ model which is constructed to satisfy zero turbulent viscosity in pure shear and pure rotation as well as when there exists an isotropic or axisymmetric contraction/expansion [192]. WALE and σ models are good examples of CERFACS impact in the LES community: the models are used in almost all LES solvers today and results exposed in this manuscript confirm their efficiency.

The mesh capability and its associated CPU cost is obviously a main limitation in such strategy to address complex industrial configurations. Table 2.7 resumes CPU costs associated to the cases presented in this section along with Reynolds and Mach numbers as well as mesh sizes used for the simulations. Such resolutions are out of reach for industrial configurations and our results confirm that walls still are the weak limit part of LES. Alternative solutions for wall resolved strategies mush be found and the most advanced one is to use law of the wall approaches. An other difficulty comes from the mesh generation process for complex configurations. In this context, automatic mesh refinement in an interesting path to reduce human efforts [49]. Finally, numerical issues linked to multi-elements schemes naturally emerge as interface between prisms and tetrahedra can generate node to node oscillations (see PhD of L. Segui) as well as numerical closures in wall treatments [215, 158].

The last examples of this section have shown that in some situation, the *a priori* knowledge of wall temperatures is of primary importance to predict the flow physics. As a result, the solid temperature can become an unknown variable of the problem to solve as the flow depends on solid temperature and vice-versa. Such a coupled problem called Conjugate Heat Transfer is discussed in the next section.

2.2 Conjugate Heat Transfer methodologies and predictions

The joint resolution of the fluid and solid thermal fields requires the use of methodologies to assemble physics that have been separated for simplification purposes: convection, conduction and radiation. Indeed, each of this heat transfer process is very specific and has been studied

by dedicated scientific communities. Moreover, these specificities also imply different ways to solve them numerically. As a result, the combination of the convective, radiative and conductive heat transfer processes in a single numerical resolution implies to establish a computational methodology in line with the needs. This section introduces the methodology developed during this work based on the needs and existing solutions. Some applications are then presented.

2.2.1 Conjugate Heat Transfer Methodologies

When it comes to solve conjugate heat transfer problems, the first specificity arising is the large differences in time and length scales in the heat transfer processes. Radiation is a long distance instantaneous process while convection and conduction heat transfers are local phenomena with higher time-scales. Moreover, conduction time-scale is generally by several order longer than convection one. Hence, methodologies to solve a conjugate heat transfer depend on the type of time-scale targeted. To solve a fluid thermal transient, the solid environment can often be considered in a steady state while radiation follows the fluid evolution. The resolution of a thermal solid transient requires both the adaptation of the fluid and radiation states. To study both a fluid and a solid transient evolution, an initial steady thermal state of the coupled fluid/solid system must be determined. Such a determination is still today challenging with Large Eddy Simulation and is the scope of the work described here after. Note that conjugate heat transfer is not a new topic with first referenced publications in the Web Of Science in the last 1970 (Fig. 2.50). Thanks to computational fluid dynamics, the topic has exponentially attracted publication efforts addressing numerical resolutions of complex problems not solvable analytically.

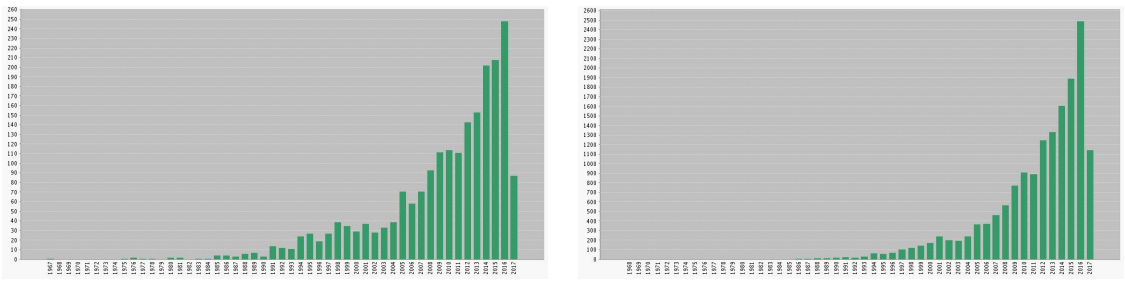

Figure 2.50: Published Items in Each Year (left) and Citations in Each Year (right) with the topic "Conjugate Heat Transfer" on Web of science, May 2017.

The objective of the computational process is to characterize a fluid/solid coupled system at a steady thermal state, *i.e.* at a given operating point. As the numerical treatment of radiation in the coupled systems of interest is rather straightforward [63, 277, 62, 13], only convection and conduction are considered in the following. To do so, initial guesses of solid and fluid solutions are combined at an initial time and after a transient phase, a statistically stationary regime is reached. Figure 2.51 presents a typical evolution of a local temperature at a fluid/solid interface in a thermally coupled system. The initial temperature T_I is linked to the ratio of effusivities $b = \sqrt{\lambda \rho C p}$ in the fluid (f) and the solid medium (s) as well as to local temperature T_f and T_s in these respective medium:

$$T_I = \frac{b_s T_s + b_f T_f}{b_s + b_f} \tag{2.7}$$

Then, the physical time τ_s requested to go through the transient phase is driven by the size of the solid medium L and its thermal diffusivity E_s:

$$\tau_s \approx \frac{L}{E_s} = L \frac{\rho_s C p_s}{\lambda_s} \tag{2.8}$$

Note that from the simplified diffusion theory, this time scale τ_s represents the delay needed to converge about 60% of the final temperature value while $5\tau_s$ is required to obtain a convergence

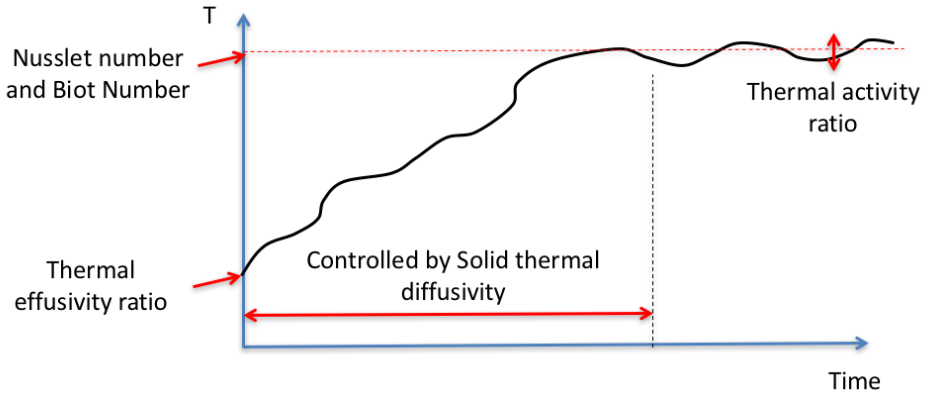

Figure 2.51: Typical convergence of fluid/solide interface temperature on at a given location in a CHT problem and main characteristic parameter of importance.

to 99% of the final value. After the transient phase the interface temperature oscillates around a mean state. The thermal equilibrium strongly depends on convection and diffusion competition in both mediums. Two non dimensional numbers are typically used in this context: the Nusselt number which compares the convection over diffusion in the fluid, as well as the Biot number characterizing the convection in the fluid with respect to the diffusion in the solid. Finally, for a given fluctuating heat flux, the amplitude of the temperature oscillations depend on the activity ratio K expressed as the ratio of the fluid and solid effusivities:

$$K = \sqrt{\frac{\lambda_f \rho_f C p_f}{\lambda_s \rho_s C p_s}} \tag{2.9}$$

as well as on the oscillation frequencies. The higher the activity ratio, the more important the temperature oscillations are. In the target configurations (steel walls in air or combustion products), the activity ratio is rather small ($K \approx 10^{-3}$) and wall temperature fluctuations are expected to be small enough to be neglected.

There are two basic approaches to solve CHT problems. The first one is a direct coupling where the different fields are solved simultaneously in a large system of equations by a monolithic solver [133, 107, 222, 171, 89]. The second approach consists in solving each set of field equations separately with dedicated solvers that exchange boundary conditions [113, 249, 205, 90, 21]. This solution has the advantage of using existing state-of-the-art codes to solve fluid and solid equations and of being able to exchange one solver with another easily [5]. The main drawback of this coupling methodology is that an adapted CHT framework is requested for the simulations especially on massively parallel machines. The performances of such a coupling framework are linked to (1) the strategy to couple the solvers in an accurate and stable way as well as (2) the exchange of information between the solvers in an efficient and scalable fashion when using a large number of processors [5]. The numerical approach to guaranty accurate and stable schemes depends on the type of solvers used, stationary or unsteady.

Stationary fluid and solid solvers

Historically, conjugate heat transfer computations have been done with steady fluid solvers such as RANS codes [113, 205, 90, 21]. In this context, the resolution of the coupled problem consists in a convergence loop over the sequential execution of the fluid and solid solvers transferring data until convergence of the thermal system. In most studies, a time-marching method is used for the fluid code and the solver convergence is not reached at each coupling iteration to lower the computational cost with the argument that it is not necessary to converge the fluid with a wrong (not converged) thermal boundary condition. As a result, intermediate pseudo-temporal

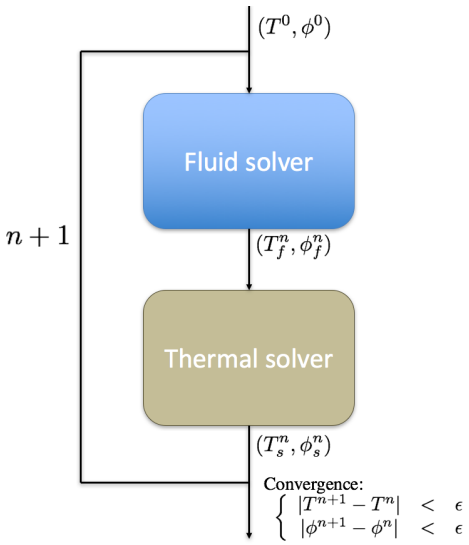

Figure 2.52: Typical convergence loop to solve a conjugate heat transfer problem with steady fluid and conduction solvers.

solutions are not physically meaningful. Natural physical informations to exchange between the solvers are based on heat flux ϕ and temperature T that are continuous at each location x of the fluid/solid interface:

$$\left\{ \begin{array}{rcl} T_s(x) & = & T_f(x) \\ \phi_s(x) & = & \phi_f(x) \end{array} \right. \tag{2.10}$$

An intuitive choice based on conventional boundary conditions of fluid and thermal solvers is to impose the temperature computed by the solid to the fluid interface with a Dirichlet condition and the heat flux computed by the fluid solver to the solid domain through a Neumann condition:

$$\left\{ \begin{array}{rcl} T_f^n(x) & = & T_s^{n-1}(x) \\ \phi_s^n(x) & = & \phi_f^n(x) \end{array} \right. \tag{2.11}$$

where n denotes the coupling iteration. This method referred as *flux forward temperature back* [58, 267] is often subject to numerical instabilities. For instance, in the extreme case where the solid is completely immersed in the fluid, the thermal diffusion problem in the solid is ill-posed. In such a case, the elliptic partial differential equation for the solid steady state has only Neumann boundary conditions and cannot be solved. As a result relaxation of the exchanged quantities from one coupling iteration to the other is mandatory to stabilise the convergence. A main drawback is that no theoretical framework exists to choose the relaxation parameters which are imposed based on experience [266, 117]. A common strategy is to use the convective heat transfer equation to impose the heat flux computed by the fluid solver to the solid one:

$$\left\{ \begin{array}{rcl} T_f^n(x) & = & T_s^{n-1}(x) \\ \phi_s^n(x) & = & h(x)\left(T_{ref}(x) - T_s(x)\right) \end{array} \right. \tag{2.12}$$

where $h(x)$ is the local heat transfer coefficient and $T_{ref}(x)$ is a local reference temperature of the fluid. Such formulation is commonly used to study heat loads in solids and has the advantage that the heat flux $\phi_s^n(x)$ automatically adjusts to the solid temperature $T_s(x)$. Nevertheless, it has the drawback to require the determination of two unknowns h and T_{ref} with only one equation at each coupling exchange:

$$h(x)\left(T_{ref}(x) - T_s^{n-1}(x)\right) = h(x)\left(T_{ref}(x) - T_f^n(x)\right) = \phi_f^n(x) \tag{2.13}$$

Different strategies exist to determine h and T_{ref}. The first category consists in imposing T_{ref} and deducting h from Eq. 2.13. The reference temperature can be estimated for example by:

- a global reference temperature of the system under study (such as an inlet static or total temperature),
- the local wall temperature obtained with an adiabatic simulation,
- the local temperature in the vicinity of x, *i.e.* in the surrounding wall mesh cell,
- the local recovery temperature in the case of compressible flows around turbine blades,
- ...

A major difficulty of this approach is to guaranty a positive value of the convective coefficient all over the solid domain as a negative value would make the conduction problem ill-posed. The second category consists in the imposition of h and determination of T_{ref} with Eq. 2.13. To do so, a usual method to proceed is to perform preliminary fluid flow simulations with different wall temperatures $T_w^1(x)$ and $T_w^2(x)$ and to extract h from the heat fluxes $\phi_w^1(x)$ and $\phi_w^1(x)$ resulting from the computations [266]:

$$h = \frac{\phi_w^1(x) - \phi_w^2(x)}{T_w^1(x) - T_w^2(x)} \tag{2.14}$$

Although often used in industry, the convective heat transfer equation is based on a strong hypothesis of linear relation between heat flux and the temperature difference between a reference state and wall temperature. The iterative process of the CHT allows to alleviate the impact of this relationship due to the convergence process of both interface temperature and flux. Nevertheless, different choices in the reference quantities can cause different predicted solid temperatures [112]. A typical example of interest for the present manuscript is encountered in combustion applications. Indeed, on one hand, flame stabilisation processes are strongly influenced by thermal conditions. On the other hand, flow fields induced by flame locations and dynamics directly dictate wall heat transfer.

An efficient way to enforce stability and convergence is to replace the standard Dirichlet and Neumann interface conditions by a general Robin transmission. It is a flexible approach enabling the introduction of simplified models in CHT, but also in fluid structure interaction [31, 194, 11]. Robin conditions are a weighted, linear combination of the Dirichlet and Neumann conditions:

$$\left\{ \begin{array}{rcl} T_f^n(x) & = & T_s^{n-1}(x) \\ \phi_s^n(x) & = & \phi_f^n(x) + \alpha_f(x) \left(T_f^n(x) - T_s(x) \right) \end{array} \right. \tag{2.15}$$

where $\alpha_f(x)$ is a relaxation parameter to set. Inspection of Eq. 2.15 shows that continuity of temperature and heat flux is obtained at convergence. The coupling coefficient is employed to increase stability and the convergence rate for steady state runs. The use of a Robin transmission may be interesting but choosing the relevant coefficients $\alpha_f(x)$ is critical [113, 189, 129]. Stability is the essential element in CHT procedures and even if Robin conditions have interesting properties, such benefits come at a price. Global over or under-relaxed coefficients can improve the numerical properties but not always significantly because they cannot adjust to local circumstances. In the context of a Robin transmission, it was shown recently using a one-dimensional aerothermal model problem that the temporal amplification factor of the coupled system is submitted to a transition between two contrasting modes, *i.e.* Neumann and Dirichlet types boundary conditions [79]. This transition that occurs at an absolute minimum of the amplification factor of the simplified coupled scheme has been derived from a normal mode stability analysis, and can be regarded as an optimal choice in terms of stability and convergence (Fig. 2.53). A study has been devoted to test the performance of several coupling coefficients in a simple aerothermal test case with particular emphasis put on the so-called "optimal coefficient" proposed by Errera and Chemin [79] in the context of steady CHT problems. The purpose of such an analysis is to know if a model problem based on a normal mode analysis can be relevant and directly applicable to more complex CHT problems. This work has been done in collaboration with Dr. Marc Errera from ONERA and leads to a journal paper in Journal of Computational Physics [78].

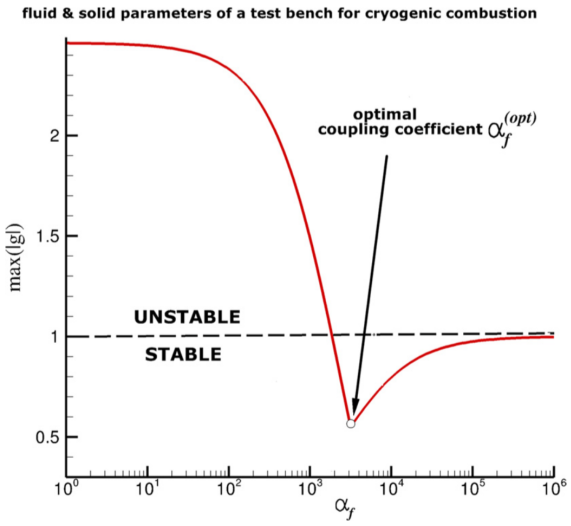

Figure 2.53: Example of an amplification factor with emphasis put on the optimal coefficient [79].

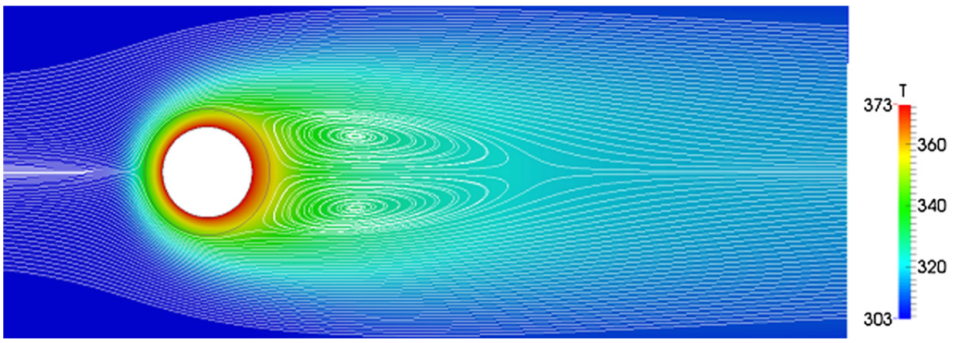

Figure 2.54: Temperature contours in the fluid-solid heated cylinder system along with streamlines in the fluid domain.

To gauge the ability of the simplified model of Errera and Chemin [79] to predict the stability and convergence properties of a realistic case, it is used on a steady laminar heated cylinder in a flow field test case (Fig. 2.54). A series of five coupling coefficients for three Fourier numbers D_f corresponding to coupling time-step sizes of the fluid solver are considered. These parameters are introduced into the model problem as data to compute the amplification factor and the stability limits. The stability and convergence properties predicted by the model problem are then compared to those obtained in the CHT computation.

Figure 2.55 plots the amplification factor of the 1D model problem corresponding to the heated cylinder configuration. There exists a singular point similar to a cusp. The left half-line which can be called the "Neumann branch" can be partly in the unstable zone. A coefficient located on this branch may speed up the rate of convergence but there is a risk of an instability. The right half-line, the Dirichlet branch, is always in the stable zone. A coefficient located on this branch will slow down the speed of convergence. The intersection corresponds to a transition brought to light recently by Errera and Chemin [79]. As mentioned above, it is a cross-over as the coupling coefficients increases and at this optimal point α_f^{opt}, the temporal amplification factor reaches its absolute minimum value and shares all the virtues of both branches: it is the most stable point of the unstable Neumann branch and simultaneously the fastest point of the slow Dirichlet branch. Figure 2.55 (right) shows a zoomed view of the 3 curves and on each of them, a point indicates the value employed in the coupled simulation. The intention is to investigate the most fundamental behaviors produced by 5 coupling coefficients strategically

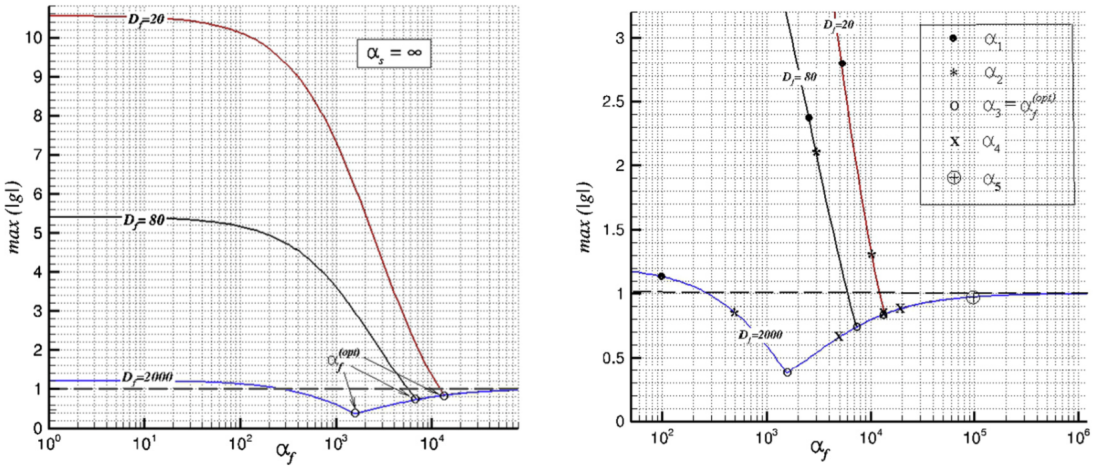

Figure 2.55: Amplification factor for the 3 Fourier numbers D_f considered in the heated cylinder test case.

	1D model	CHT	Location
α_1	Unstable	Unstable	Neumann branch
α_2	$D_f = 20$ unstable	Non-monotone convergence - stable	-
	$D_f = 80$ unstable	Non-monotone convergence - stable	-
	$D_f = 2000$ stable	Non-monotone convergence - stable	-
α_3	Stable	Monotone convergence - stable	Transition
α_4	Stable	Monotone convergence - stable	Dirichlet branch
α_5	Overstable	Over-stable convergence	-

Table 2.8: Comparison of stability characteristics between the simplified model and the CHT on the heated cylinder configuration.

located: a coefficient located on the Neumann branch, 3 coefficients in the optimal zone and a large coefficient clearly located on the Dirichlet branch:

- $\alpha_f < \alpha_f^{opt}$: Neumann branch:
  - $\alpha_f = \alpha_1$: coefficient clearly located on the Neumann branch
  - $\alpha_f = \alpha_2$: coefficient slightly lower than the optimal one
- $\alpha_f = \alpha_3 = \alpha_f^{opt}$: intersection of Neumann and Dirichlet branches: optimal coefficient
- $\alpha_f < \alpha_f^{opt}$: Dirichlet branch:
  - $\alpha_f = \alpha_4$: coefficient slightly larger than the optimal one
  - $\alpha_f = \alpha_5$: coefficient clearly located on the Dirichlet branch.

Table 2.8 compares the stability results obtained by the simplified model and the experimentation on the heated cylinder. This comparison shows an excellent overall agreement. Regardless of the fluid Fourier number D_f, the coupled simulations with α_1 are unstable, leading to divergent computations. In other words, the CHT computation produces oscillations that grow without bound. All the behaviors observed for α_2 are subject to oscillations (Fig. 2.56). These oscillations die out after 3/4 coupling periods when α_2 is located in the stable zone predicted by the 1D model or not too far away. When the amplification factor is much higher than one in the model problem, the oscillations are highly persistent and decay slowly due to convection that prevents the fluid sub-system from soaking up a lot of heat. When the coefficient is equal

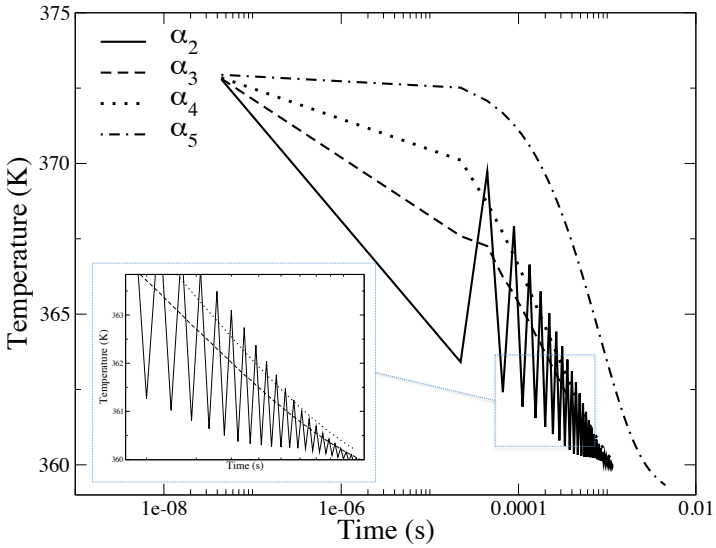

Figure 2.56: Pseudo-time history of average solid temperature highlighting the convergence of the thermal problem in the fluid time reference framework.

(α_3) or higher (α_4) than the optimal value, the convergence is always monotonic for all the Fourier numbers considered. The optimal coefficient α^{opt} appears to be an interesting choice as it provides a monotonic, stable and fast convergence of the coupled simulations. It is to be noted that the slope obtained in the CHT procedures becomes progressively steeper as D_f increases, exactly as predicted by the model problem. This would suggest that the one-dimensional normal mode analysis can provide relevant coefficients directly applicable to real CHT problems. Finally, for the largest values of the relaxation coefficient α_5, an over-stable convergence of the coupled system is observed leading to the largest CPU time to reach the steady state solution.

The use of such methodologies with a LES solver requires to converge the unsteady fluid solutions at each coupling loop to prevent the creation of undesirable oscillations of the thermal state during the convergence process due to large spatial and temporal spectral contents in the LES results. To avoid such convergence bias, the averaging time must contain several periods of the lowest frequency phenomena. As a result, computations rapidly become very costly with a lot of CPU hours wasted to converge the flow solutions on intermediate thermal states which are not physically representative of the system. Other solutions have to be proposed as discussed in the next section.

Unsteady fluid and solid solvers

The resolution of CHT problems with unsteady flow solvers such as LES is a rather new topic with first papers referenced in the Web Of Science database from 2003 (Fig. 2.57). Interestingly, Fig. 2.58 shows that the work produced at Cerfacs in this context is well positioned, 3 publications being in the 5 most cited papers in the field.

As mentioned in the previous section, it would be too CPU intensive to perform a complete LES resolution (eliminate transient phase due to boundary condition adjustment and simulate a sufficiently long physical time for averaging wall heat transfer quantities) at each iteration of a convergence loop as depicted on Fig. 2.52. Such a strategy will imply a CPU cost of about the number of convergence iteration loops times the cost of a unique LES of the non-coupled fluid system. To circumvent this issue, a strategy is to take advantage of the unsteady nature of the LES formalism and to form a coupled system where both solid and fluid domains are converged in a timeline together. As computing a solid transient phase to reach a steady state from an initial solution with a compressible LES solver is out of reach from a CPU resources point of view (and is also most of the time useless), an alternative is to modify the thermodynamical

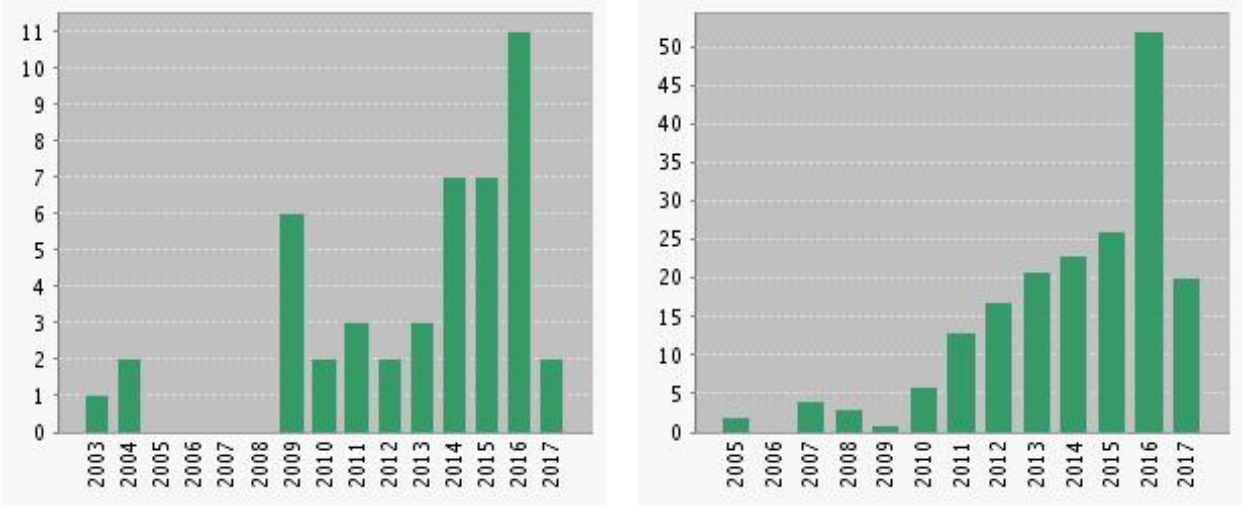

Figure 2.57: Published Items in Each Year (left) and Citations in Each Year (right) with the topics "Conjugate Heat Transfer" and "Large Eddy Simulation" on Web of science, May 2017.

		2013 ◀	2014	2015	2016	2017 ▶	Total	Average Citations per Year
Use the checkboxes to remove individual items from this Citation Report or restrict to items published between 1900 and 2017 Go		21	23	26	52	23	191	14.69
☐ 1.	**Development and assessment of a coupled strategy for conjugate heat transfer with Large Eddy Simulation: Application to a cooled turbine blade** By: Duchaine, F.; Corpron, A.; Pons, L.; et al. INTERNATIONAL JOURNAL OF HEAT AND FLUID FLOW Volume: 30 Issue: 6 Pages: 1129-1141 Published: DEC 2009	8	9	11	12	3	61	6.78
☐ 2.	**Computational study of conjugate heat transfer in T-junctions** By: Kuhn, Simon; Braillard, Olivier; Niceno, Bojan; et al. NUCLEAR ENGINEERING AND DESIGN Volume: 240 Issue: 6 Pages: 1548-1557 Published: JUN 2010	6	5	4	3	2	26	3.25
☐ 3.	**Conjugate heat transfer with Large Eddy Simulation for gas turbine components** By: Duchaine, Florent; Mendez, Simon; Nicoud, Franck; et al. Conference: 2nd INCA Workshop Location: CORIA, Rouen, FRANCE Date: OCT 23-24, 2008 COMPTES RENDUS MECANIQUE Volume: 337 Issue: 6-7 Pages: 550-561 Published: JUN-JUL 2009	2	3	3	3	1	16	1.78
☐ 4.	**k-l based hybrid LES/RANS approach and its application to heat transfer simulation** By: Zhong, BW; Tucker, PG INTERNATIONAL JOURNAL FOR NUMERICAL METHODS IN FLUIDS Volume: 46 Issue: 10 Pages: 983-1005 Published: DEC 10 2004	0	1	0	0	0	16	1.14
☐ 5.	**Large-Eddy Simulation and Conjugate Heat Transfer Around a Low-Mach Turbine Blade** By: Duchaine, Florent; Maheu, Nicolas; Moureau, Vincent; et al. JOURNAL OF TURBOMACHINERY-TRANSACTIONS OF THE ASME Volume: 136 Issue: 5 Article Number: 051015 Published: MAY 2014	0	3	2	5	0	10	2.50

Figure 2.58: Five most cited articles from the report with the topic "Conjugate Heat Transfer" and "Large Eddy Simulation" on Web of science, May 2017.

properties of the solid to reduce its characteristic time scale given by Eq. 2.8. For a simple heat transfer problem without fluctuation, the steady state is reached when the partial derivative of the temperature with respect to the time is null:

$$\rho_s Cp_s(x,t)\frac{\partial T(x,t)}{\partial t} = \frac{\partial}{\partial x_i}\left(\lambda_s(x,t)\frac{\partial T(x,t)}{\partial x_i}\right) \tag{2.16}$$

As a result, a modification of the density ρ_s or heat capacity Cp_s does not impact the steady state solution. A decrease of these quantities results in a decrease of the characteristic time scale of the solid medium. Such a manipulation is equivalent to desynchronizing the fluid and solid solvers, the solid solver simulating more physical time than the fluid one between two coupling events. As the increase of the heat diffusivity through the decrease of density and heat capacity increases the thermal activity ratio as well as increases the penetration depths of harmonique forcing on the solid, this strategy is to be used only to converge toward a steady thermal state and is not adequate to investigate temperature variances in the solid [142, 85]. An additional consequence of the over prediction of temperature fluctuation penetration in the solid concerns the prediction capability of the method. For example, when very thin solid materials surrounded by a flow on both sides are considered, the penetration over prediction may lead to an artificial thermal interaction between the fluids on the two sides of the solid. Such a feature may lead to inaccurate solutions of the coupled problem and care is required.

Based on a set of coupled 1D diffusion unsteady equations representative of a thermal fluid/solid interaction, Giles [93] has shown that the numerical stability is achieved when Neumann boundary condition is imposed to the structural code and a Dirichlet boundary condition to the fluid one. A major restrictive condition of the studies performed by Giles and other authors working on numerical stability of coupled thermal computations [34, 221, 225] is linked to the constraint of a meeting point between the solvers at each iteration with an equal time step in the solvers. Although Giles concludes that the methodology remains valid when different time steps are used, no demonstration and limitation of the method was proposed. To go beyond in this direction, a stability analysis based on the amplification matrix [114, 4] has been proposed for a 1D coupled diffusion model representative of a thermal fluid/solid interaction coupled with a Dirichlet/Robin interface (Eq. 2.15) [72]. In this study, the coupled solvers conserve their own time step based on stand-alone numerical stability criteria. Moreover, the solvers can integrate heat equation with different number iterations between two updates of interface conditions. Figure 2.59 presents a stability map in the space of the parameters α linked to the Robin condition ($D = \alpha \Delta x_s/\lambda_s$) and t^*, a normalized time between two coupling events corresponding to fraction of characteristic times of the heat transfer phenomena. When $t^* = 1$, the solvers exchange coupling data after a physical time corresponding to a convective time in the fluid domain and a diffusion time in the solid one. The heat flux $\phi_f^n(x)$ computed from the fluid is a time average heat flux on the coupling period t^*. Moreover, note that the use of such a definition for t^* corresponds to a unique desynchronization between the fluid and solid solver, or similarly to a unique modification of the solid heat capacity $\rho_s Cp_s$. As shown on Fig. 2.59, if the coupling is performed frequently ($t^* < 0.02$), the Neumann condition is stable. Then, until $t^* = 0.5$, the value of D that ensures numerical stability increases with t^* and remains approximatively constant above $t^* = 0.5$. The stability domain is also limited by an upper bound of D linked to the solid domain alone. As a result, for a given value of the coupling synchronization time parameter t^*, a range of relaxation parameter α allows numerical stability of the coupled scheme.

An important information not accessible from this stability analysis still misses: since the aim is to find a stationary thermal state of a coupled system in a reduced computational time, it is crucial to understand the effect of the parameters α and t^* on convergence. To investigate this point a real coupled turbine application is performed in Duchaine *et al.* [72] with the set of coupling parameters corresponding the symbols in Fig. 2.59. Two important aspects have to be underlined. The first one is that in 2008 during this study, the coupling software available was not as efficient as the one available in 2017 and data exchanges between solvers was costly. As a consequence, it was not possible to exchange data as often as requested to

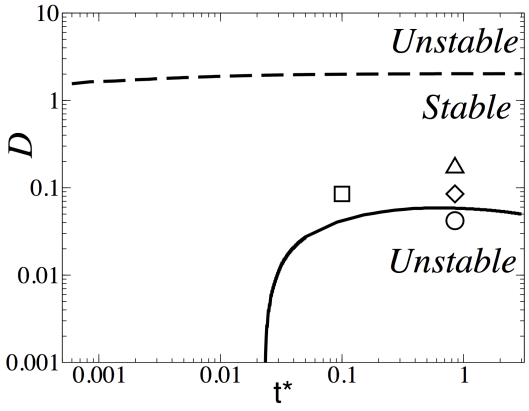

Figure 2.59: Stability map obtained for a 1D model of a coupled system [72].

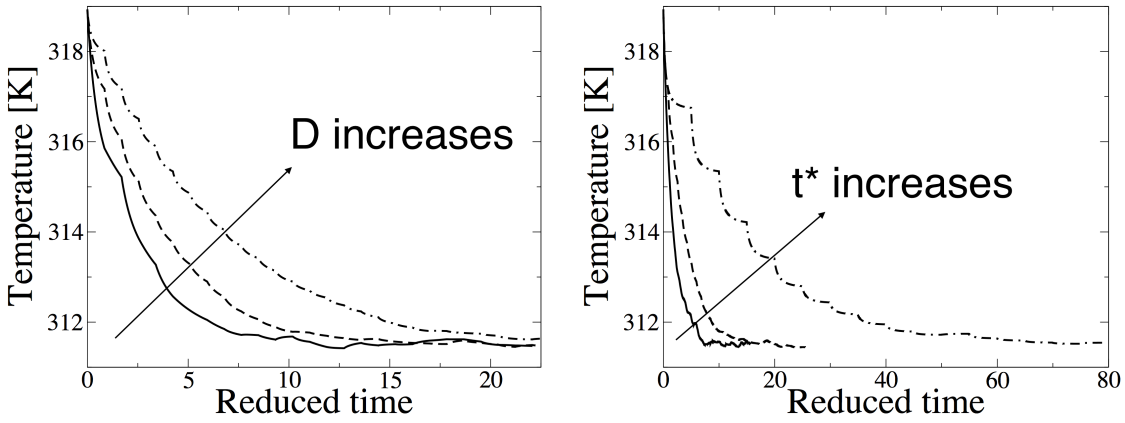

(a) (b)

Figure 2.60: Evolutions of the mean temperature in the solid of a coupled system as a function of reduced solid time for different coupling parameter D (a) and t^* (b) [72].

obtain a stable solution using $\alpha = 0$, *i.e.* a Neumann condition on the solid frontiers. Second, Eq. 2.59 shows that the predictions from the $1D$ problem are not directly applicable to the complex $3D$ CHT case: following the $1D$ analysis, 3 cases (triangle, square and diamond) over the 4 tested are stable while in the numerical experiment all the simulations are stable. This illustrate a point underlined in Errera and Duchaine [78] that convection terms probably help to stabilize the coupling process. Figure 2.60 depicts the evolutions of the mean temperature in the solid domain as a function of reduced solid time t_s/τ_s for these simulations. All the simulations converge towards the same mean temperature value. Due to the unsteady nature of the fluid solver resolving turbulence, at convergence, the temperature oscillates in time around the average solution. A time-averaging process of the solid temperature is thus necessary before exploitation [124]. The convergence rate is influenced by the choice of the coupling coefficient α : simulations converge faster for slower values of α as expected. Indeed from the highest value of D and the lowest one, the CPU time needed to reach a steady state is divided by approximatively 2.5. Fig. 2.60 shows that the choice of the time simulated between two coupling events t^* directly affects the convergence rate of the coupled simulations. Small values of t^* enhance the restitution times of the computations: high update frequencies of interface variables allow the computations to follow the steepest descent to converged state.

No generalization can be extracted from this precursor work. To complement this demonstration, ongoing numerical studies without a mathematical background have been performed on a 2D laminar tandem of heated cylinders in a cold flow at a Reynolds number of 100. This

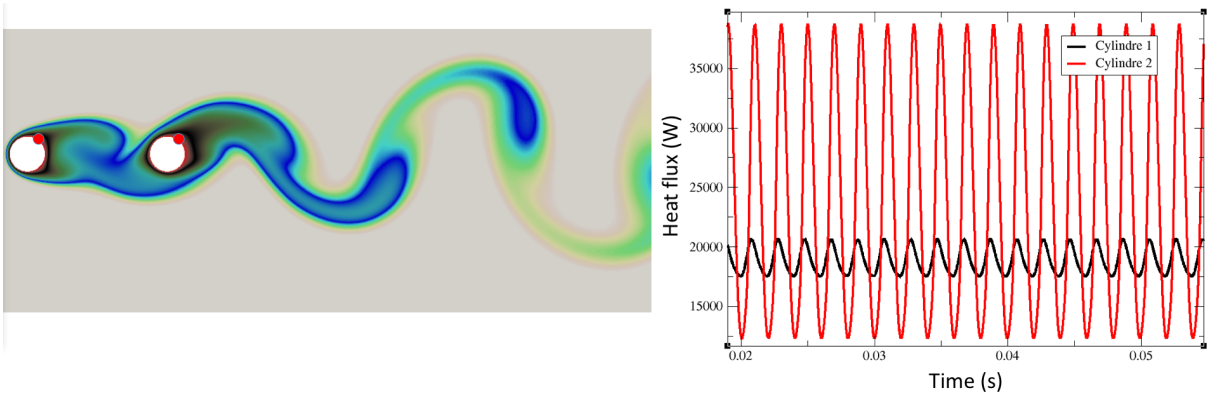

Figure 2.61: Heated cylinders in tandem: (left) view of the temperature field in the fluid domain, (right) temporal evolution of wall heat fluxes on probes located on the the upstream cylinder 1 and downstream cylinder 2.

Reynolds number is used to generate an harmonic signal of heat flux linked to the Karman street of vortices easier and cheaper to control and simulate than a 3D turbulent simulation (Fig 2.61).

For this tandem case, 6 simulations are compared for which Dirichlet/Neumann boundary are used without relaxation (Eq. 2.11):

- *Chaine*: corresponds to a chained loop between the fluid and solid solvers. The physical time τ_f computed by the fluid code before the coupling process corresponds to a period of vortex shedding and the physical time computed by the solid solver is the thermal characteristic time τ_s. Time-averaged heat flux over τ_f is transmitted from the fluid domain to the solid one while the skin temperature at the end of the τ_s period is given back from the solid to the fluid.

- *C41*: corresponds to a coupling process where both fluid and solid solvers are run together and exchange data every $0.04\tau_f$ (time-averaged heat flux on the coupling period) for the fluid solver and $0.01\tau_s$ for the solid one (final temperature).

- *C4025*: corresponds to a coupling process where both fluid and solid solvers are run together and exchange data every $0.04\tau_f$ (time-averaged heat flux on the coupling period) for the fluid solver and $0.0025\tau_s$ for the solid one (final temperature). The desynchronization (or equivalently the modification of the solid heat capacity $\rho_s Cp_s$) is thus 4 times less important than in case *C41*.

- *C1025*: corresponds to a coupling process where both fluid and solid solvers are run together and exchange data every $0.01\tau_f$ (time-averaged heat flux on the coupling period) for the fluid solver and $0.0025\tau_s$ for the solid one (final temperature). The desynchronization (or equivalently the modification of the solid heat capacity $\rho_s Cp_s$) is thus the same as in case *C41*.

- *C41Mean*: corresponds to a coupling process where both fluid and solid solvers are run together and exchange data every $0.04\tau_f$ (cumulative time-averaged heat flux over the whole simulation) for the fluid solver and $0.01\tau_s$ for the solid one (final temperature).

- *C11E*: this case has the particularity to be an ensemble fluid simulation coupled to the solid solver. To do so, 4 instances of the fluid solver run in parallel and are coupled with the solid solver. An arithmetic average is made on the heat fluxes provided by fluid codes on a period corresponding to $0.01\tau_f$ and the solid solver sends back the surface temperature each $0.01\tau_s$. The desynchronization (or equivalently the modification of the solid heat capacity $\rho_s Cp_s$) is thus 4 times more important than in case *C41*. The four fluid

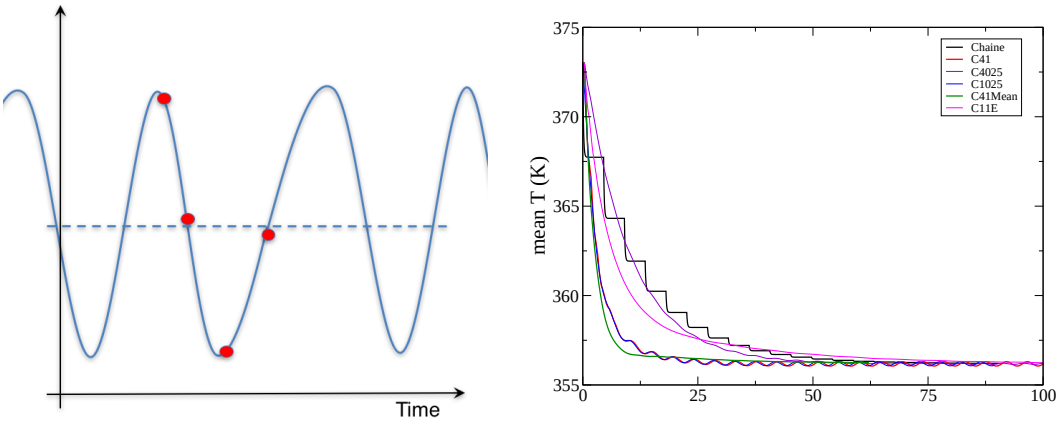

(a) (b)

Figure 2.62: (a) Distribution of the fluid simulations in the C11 case, (b) evolutions of the mean temperature in the solid for the tandem configuration as a function of a normalize time representative of the CPU cost of the simulation [72].

computations are uniformly distributed in the shedding period as depicted on Fig. 2.62-a leading to a good estimation of the mean heat fluxes at each coupling event.

Figure 2.62-b shows the convergence of spatial mean temperature of the solid for the six simulations. This representation gives a classification of the methods in terms of CPU costs considering the fluid solver as the greedy code. All the simulations converge toward the same mean steady thermal state except C41Mean for which a small overestimation of the temperature is observed due to the cumulative heat flux transmitted from the fluid to the solid. Coupled simulations converge more rapidly than the chained computation. Moreover, the more the desynchronisation (or equivalently the modification of the solid heat capacity $\rho_s Cp_s$) is important, the fastest the convergence is. As already mentioned, the counterpart of large modifications of solid heat capacity is to introduce large oscillations of temperature which can be detrimental to reach the good level of the thermal steady state. Simulations C41 and C1025 show that the same modification with different exchange frequencies leads to the same convergence history. The use of cumulative temporal integration of heat flux C41Mean is interesting to overcome the oscillation behavior but requires a sliding average to purge the convergence transient. For such case with a unique frequency, ensemble simulations are also interesting as they allow to increase the desynchronisation without creating numerical over-predictions of the temperature oscillation amplitude.

These demonstrations show that obtaining solid temperature with conjugate heat transfer in a LES context at a lower CPU cost than computing the full solid transient or chaining fluid and solid solver is feasible but remains an open field of investigation. An important output is that stability and convergence of the coupled system is enhanced by high frequency data exchange between solvers putting stress on the tool used to couple the codes (cf Chapter 4). In this context, main aspects remain to be studied: (1) the mathematical framework to provide generic guidelines for convergence acceleration, (2) the extension of the methodology to physically represent penetration depths of harmonic fluid forcing such as proposed by He and Fadl [110] in a URANS context and (3) energy conservation of the method [225, 142, 140]. Indeed, the method proposed is energy conserving at convergence of the system for stationary flow as the heat flux is and temperature at the interface converge toward the same value in the fluid and solid boundaries. Energy conservation is not strictly imposed but it statistically observed (in the sense of the temporal mean) in turbulent cases. Note that dealing with point (2) can be obtained by synchronized CHT simulations when steady state is reached. Finally, an important point which is rarely studied concerns the solution used to initialize the coupled system and its

impact on the converged steady state. The next section provides examples of conjugate heat transfer applications and illustrates on a reactive case the importance of initial conditions on the convergence history when fluid and solid states are deeply coupled.

2.2.2 Applications of Conjugate Heat Transfer

This section presents three applications using CHT in a LES context:

- the prediction of a low pressure blade temperature distribution,
- the estimation of the thermal environment of an industrial combustion chamber,
- flame stabilization on a square cylinder with CHT.

Temperature field predictions in a low pressure turbine cascade

The CHT computation performed to predict the temperature distribution in the low pressure blade introduced in section 2.1 (Fig. 2.16) is a good test case for CHT using LES. The results presented are extracted from a paper published in Journal of Turbomachinery [71]. Convective conditions are imposed in the 10 cooling holes inside the blade with convective temperatures and heat transfer coefficients provided by experimentalists. Exchanges are done every iteration of the thermal solver and after 10 iterations of the fluid one. In terms of physical time, the solid boundary conditions are updated each 20 ms while the surface temperature of the fluid is updated every 200 ns. This leads to a ratio of acceleration of the convergence of $t_s = 10^5\ t_f$, where t_s is the time spent in the solid and t_f in the fluid. The coupled system reaches a quasi steady state after 2 flow through times in the fluid solver corresponding to 2 characteristic times in the solid. Then, six flow through times are computed to converge and extract statistics for analysis leading to a total CPU cost of about 160 000 hours on 1024 cores of the BULL Sandy Bridge machine CURIE of the TGCC.

Figure 2.63-(a) presents the distribution of temperature obtained at convergence of the coupled simulation around the blade. The solution is far from an isothermal wall at 300 K. The warm fluid total temperature T_1^t is about 348 K: the wall temperature T_{wall} variations observed in Fig. 2.63-(a) lead to significant differences for the driving temperature difference $T_1^t - T_{wall}$, showing that assuming a constant wall temperature is not a good modeling option. The mean temperature of the profile is about $\overline{T}_{CHT} = 294.7$ K with a mean standard deviation of $\sigma_{\overline{T}_{CHT}} = 5.2$ K. The CHT results are in very good accordance with the experimental temperature profile both in terms of shape and level. Underestimations of convective heat transfer lead to under-predictions of the temperature levels. As for the heat transfer coefficient, the most important under-prediction takes place at the leading edge and seems to have an influence at the beginning of the suction side, shifting the profile to lower temperatures. An other important region of temperature underestimation is the large recirculation zone on the pressure side. Finally, the temperature in the transition region of the suction side (from s/C=1 to 1.25) seems to be under-predicted as well.

The convective heat transfer coefficients from the isothermal computation ($T_{wall}(s)$=300 K) and the coupled simulation are compared to the experimental ones in Fig. 2.63-(b). For the coupled case, the wall temperature $T_{wall}(s)$ is taken as the local temperature obtained by the CHT computation given in Fig. 2.63-(a). The results from the two simulations are superimposed on a large part of the profile. The main region of difference is the trailing edge on both suction and pressure sides where the coupled results improve the prediction of the heat transfer coefficient. The assumption of constant temperature at 300K to extract the convective coefficient is wrong in this region where the temperature is predicted to be higher. Having a good estimate of the temperature allows a better prediction of the correct heat flux. This trailing edge region is thus an example where Newton's law of cooling is not applicable, *i.e.* where a single heat transfer coefficient that does not vary significantly across the temperature-difference ranges covered during cooling and heating can be used.

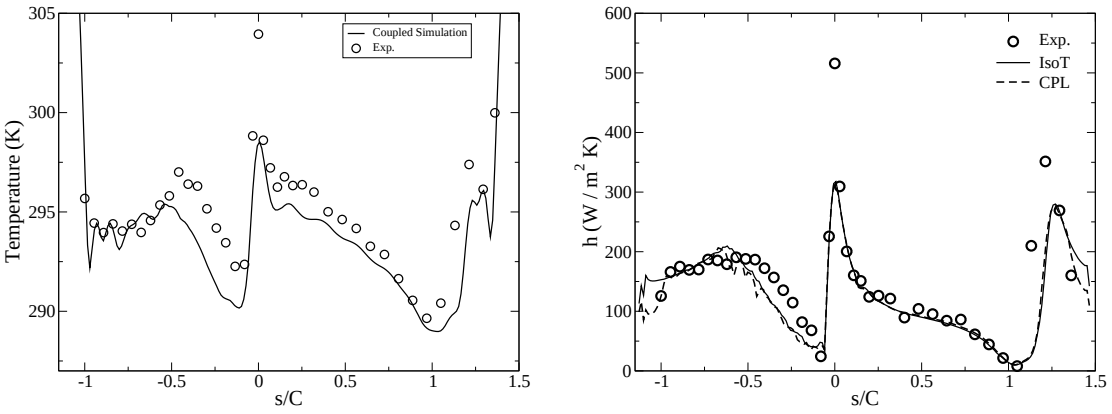

(a) (b)

Figure 2.63: (a) Mean temperature distribution around the low pressure blade from Fig. 2.16 obtained by CHT and (b) comparison of convective heat transfer coefficient obtained with an isothermal computation (Isot) and the coupled simulation (CPL). Suction side is represented on positive s/C and pressure side on negative s/C.

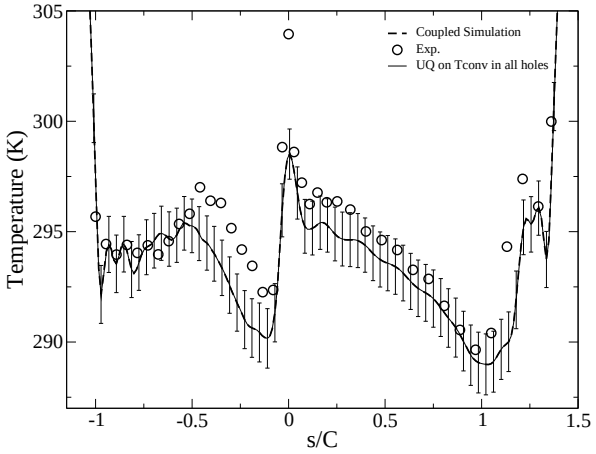

Figure 2.64: Mean and 95% confident interval of the temperature distribution around the blade with respect to uncertainty in convective conditions in all the holes.

The CHT simulation gives accurate distribution of heat transfer coefficient and temperature of the blade. The two main uncertain parameters of the solid model are the conductivity of the material as well as the convective conditions imposed in the cooling holes. To check the dependence of these two parameters on the temperature distribution inside the blade, uncertainty quantifications (UQ) studies were carried out [71]. Figure 2.64 presents the mean and 95% confidence interval of the temperature distribution around the blade resulting from a UQ analysis based on uncertainties in the cooling temperature in the blade holes. The temperature profile is largely affected by the knowledge of the cooling temperature: the standard deviation of the temperature ranges from 0.7 K near the trailing edge to 1.5K close the leading edge as well as in the separation zone on the suction side. The average value of the uncertainty is about 1.23 K representing almost 0.4% of the mean temperature $\overline{T}_{CHT}$ and 24% of the deviation $\sigma_{\overline{T}_{CHT}}$. Hence, the experimental measurements are included in the simulation error bars in most parts of the profile except at the leading edge and in the recirculation zone on the pressure side. This result illustrates that the flow and heat transfer are well captured on most of the blade except in these two regions.

Sensitivity of a helicopter combustor wall temperature to convective and radiative thermal loads

Combustion chamber wall temperatures are induced by complex interactions between convection, radiation and condution [185, 100, 141]. To investigate the sensitivity of an helicopter combustor thermal state, four main simulations are performed and presented:

1. Computation 1: a reference adiabatic fluid only turbulent combustion simulation. In this computation, the thermal losses and heat redistribution induced by radiation and conduction are not simulated. Moreover, such a simulation is unable to provide temperature distribution in the combustor walls.

2. Computation 2: a Conjugate Heat Transfer simulation including the fluid and solid domains. Such a simulation provides a wall temperature repartition that can be compared to experimental data. Moreover, it gives access to an estimation of global thermal losses of the Brayton cycle due to convection and conduction in the combustion chamber element.

3. Computation 3: a Radiation Fluid Thermal Interaction (RFTI) simulation where turbulent combustion is solved together with radiation. The heat redistribution in the flow fields due to radiation can be assessed as well as the convective and radiative fluxes at the wall can be compared. Radiation is computed with the Discret Ordinate Method (DOM) solver PRISSMA [213].

4. Computation 4: a fully coupled combustion/conduction/radiation simulation that gives access to wall temperature distribution with heat redistribution and losses due to all thermal mechanisms.

The results presented are extracted from the PhD Thesis of Sandrine Berger [13] and have been presented in the conference ASME TurboExpo 2015 [18] as well as published in Journal of Applied Thermal Engineering [17]

The simulations are performed on a single sector of an industrial annular combustion chamber that powers helicopters. The configuration being confidential, geometric data, material properties as well as operating points are not provided. Temperature fields are normalized by the fresh air temperature T_3 entering in the combustion chamber, chemical and radiative source terms by the nominal power P_n and fluxes by a reference flux Q_n based on the nominal power and the fluid-solid coupled surface. A schematic view in the mid-plane of the fluid and solid computational domain is given in Fig. 2.65. Both the reverse-flow Flame Tube (FT) and the casing (air feeding plenum) are included in the simulations. Air and fuel (considered for this work as purely gaseous) mix and burn in the primary zone. Primary holes are added on the internal side of the FT to inject air and help the combustion process. Then, the action of the dilution holes combined with the primary holes lowers the hot gas temperature in the dilution zone. Additional air is injected into the FT by cooling devices such as thin films and multiperforations. These cooling systems create protecting cold boundary layers along the chamber walls, preventing direct impingement of hot products onto the walls and extracting heat by convection.

First, a reference fluid-only adiabatic simulation is performed. To give an insight on the mean thermal flow behavior inside the chamber, Fig. 2.66 shows the temperature field along with contours of Heat Release (HR) in a cut plane following the engine axis. Denominations of each part of the chamber and the abbreviations (used in the following) are detailed on the figure. Hot products are mainly generated in the primary zone up to the end of the dilution region leading to a large zone of high temperature. This important hot region is challenging for the cooling devices to thermally protect the walls. Cooling systems create two strong cold boundary layers: the first one goes from the dome to the inner envelop (IV) while the second protects the major part of the outer elbow (OE) walls. A slight cold zone can also be seen in the outer envelop (OV). Although not visible on the figure, cooling systems are also installed in the inner elbow (IE). Finally, two non-cooled zones are visible in the OV, near the dome and at the end of the straight dilution zone where high temperatures are present near the walls.

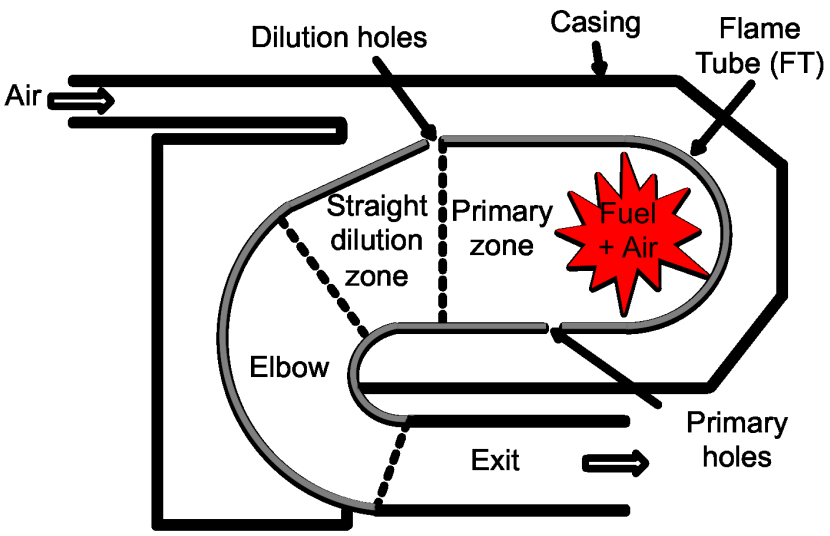

Figure 2.65: Schematic view of the helicopter combustion chamber

This adiabatic fluid field will help the comprehension of the following analyses: the temperature repartition in the liner walls obtained by computations 2 and 4 as well as the the radiative heat fluxes (computations 3 and 4).

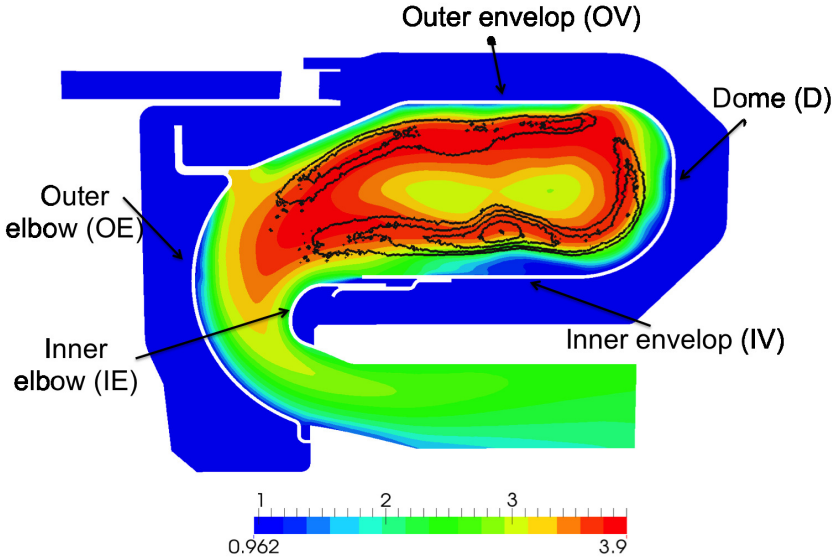

Figure 2.66: Normalized mean fluid temperature field with heat release iso-contours (black lines) on a cut plane following the engine axis. Results from computation 1: adiabatic fluid-only simulation.

Then, the steady solid thermal state is obtained by coupling the LES combustion code and the solid conduction solver without taking into account radiative effects (Computation 2). Figure 2.67 shows the temporal evolution of the spatially averaged and maximum temperatures over the solid domain as well as the evolution of the energy budget on the whole solid surface. First, the simulation goes through a numerical transient phase: both solvers adapt to the boundary conditions imposed by each other. The initially cold solid is globally heated due to the hot surrounding flow and fluxes applied by the fluid to the solid decrease. A thermal equilibrium between the two domains is reached slightly after 20 s in the solid time scale. Still, large oscillations are observed once the limit cycle is reached due to the unsteady nature of the two solvers. Because of such a feature, the solid stationary solution is deduced by averaging in time the unsteady solutions over a time period sufficiently large to cover several fluid characteristic

periods.

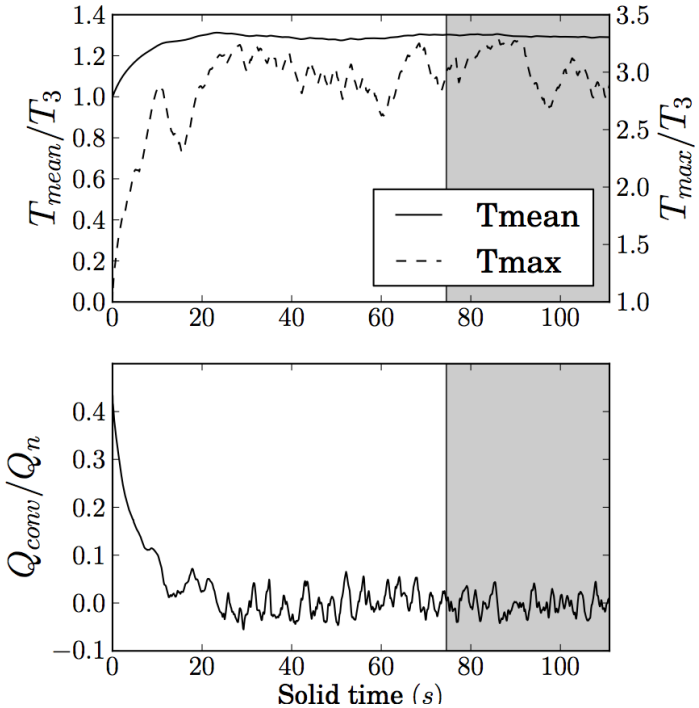

Figure 2.67: Time evolutions of solid spatially-averaged and maximal temperature (up) and sum of heat fluxes around the solid (down). Positive flux values corresponds to heat flux entering the solid domain. Results from solid CHT simulation (computation 2). The grey zone corresponds to the averaging window used to compute statistics.

From these mean predictions, the relative difference between the adiabatic fluid-only and the CHT fluid temperature fields is shown in Fig. 2.68 in the same axial cut than Fig. 2.66. The flow field exhibits some local changes of small amplitude. Peak differences are close to 20% in the whole FT. Moreover, a spatial integration along the engine mean abscissa confirmed that the coupling process does not affect significantly the global fluid features.

The solid mean temperature field shows no visible differences between the FT side and the casing side of the liner, which is in agreement with the low thickness (< 1 mm) and high conductivity of the liner leading to a low Biot number. Figure 2.69 presents the time averaged temperature map on the chamber liner obtained with CHT. Strong spatial thermal variations are clearly evidenced. Looking at the fluid temperature distribution Fig. 2.66 allows to better understand this temperature distribution within the solid parts. Powerful cooling systems installed along the dome and the first part of the IV lead to low solid temperatures in the nearby regions. The same phenomenon is observed with a slightly decreased amplitude in the OE of the FT. Conversely, strong heating of the chamber walls coincides with a decrease in the cooling efficiency of the IE. Finally, relatively hot zones can be observed on the solid OV near the dome and at the end of the straight dilution zone, where no cooling device is installed to cool down the fluid and hot gases approach the wall.

To assess the validity of the CHT computation 2, solid temperatures are compared to experimental data obtained with thermocolor tests. The comparison is performed along two profiles, located on the OV, on the casing side of the liner. Figure 2.70 presents the two distinct lines A and B following the engine axis in the mid-plane and along the periodic boundary of the computational domain, respectively. Results are shown on Fig.2.71 where experimental data are presented with error bars that states for the temperature range corresponding to each color. Overall comparisons between the numerical predictions and the thermocolor test temperature shows good global trends. Numerical predictions are in good agreement all along the two profiles with however a slight under-estimation of the temperature decrease towards the OE on line A

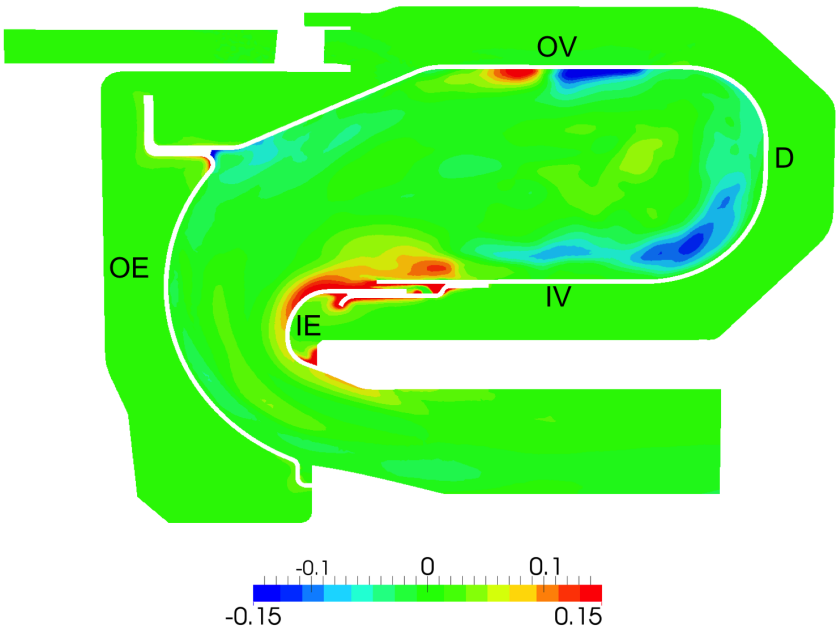

Figure 2.68: Relative difference between CHT (computation 2) and adiabatic fluid only (computation 1) temperature fields on a cut plane following the engine axis.

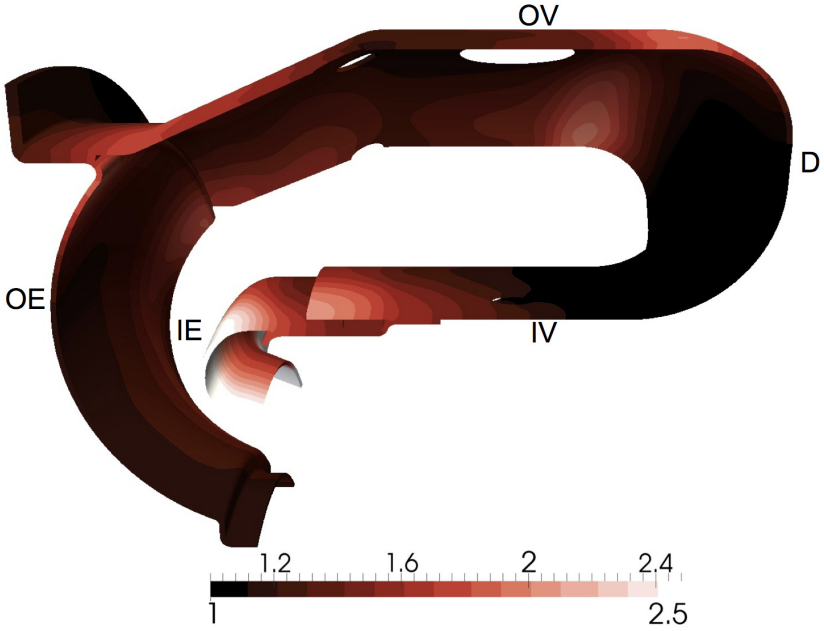

Figure 2.69: Normalized solid mean temperature field. Results from solid CHT simulation 2.

and an under-estimation of the temperature right after the dilution hole location towards the dome on line B.

The next step is to evaluate the contribution of the radiative effect onto the thermal state of this burner. To reach this goal, the LES solver and the radiative DOM code are coupled (computation 3). The temporal evolution of spatially-averaged normalized temperature, heat release and radiative source term for this period are shown on Fig. 2.72. Radiative source term and temperature signals are strongly correlated while the heat release oscillates at a higher frequency. The radiative source term values range is approximatively 100 times smaller than the heat release one, indicating a limited global effect of radiation on the fluid fields. This is confirmed by the absence of significant changes in the mean temperature field compared to the adiabatic one with peak differences lower than 15%.

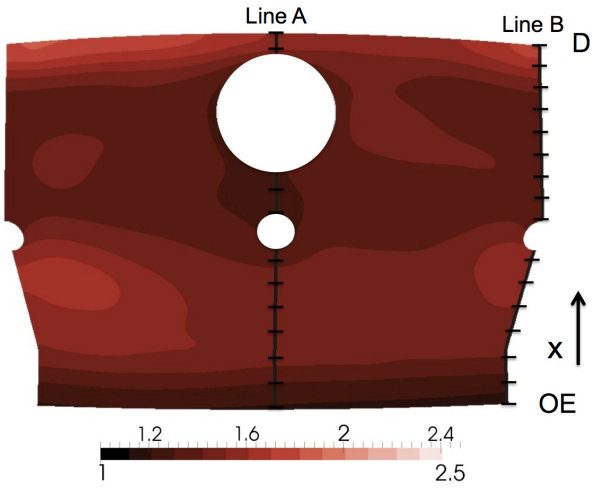

Figure 2.70: Normalized solid mean temperature field on the outer part of the primary and straight dilution zone on the casing side of the liner. Results from solid CHT simulation 2.

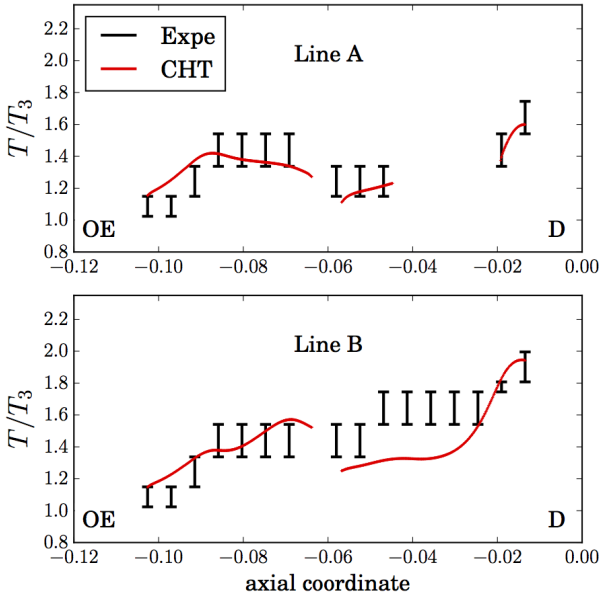

Figure 2.71: Comparison between simulation and experiment temperatures on line A (upper fig) and line B (lower fig) following the engine axis. Numerical results from solid CHT simulation 2.

To compare the radiative wall fluxes to the convective ones, the fluxes of an instantaneous DOM evaluation are compared to the mean convective heat fluxes obtained with the CHT computation 2. Figure 2.73 displays each flux on the liner surfaces. All fluxes are oriented towards the solid: positive fluxes correspond to heating of the solid parts. First, convective fluxes exhibit large values both on the FT and the casing sides of the liner whereas radiative fluxes are only significant on the FT side. Indeed, in the casing, only fresh gases (which are considered as radiatively transparent) are present, hence no interaction occurs between the gas and the walls. On the casing side, convective fluxes are purely negative, indicating the natural cooling of the solid walls. On the FT side, convective fluxes cover a large area extending from the dome to the beginning of the IV with an amplitude close to zero coherent with previous observations. Besides, fluxes of both signs and of rather low amplitude are observed in the OV or the OE with no clear pattern. Strong positive fluxes can be seen at the beginning and at the end of the OE, in the IE as well as at the very end of the IE where the flame and hot products approach the walls. Radiative fluxes depict wider patterns. Hot gases are relatively spread all over the combustion chamber and since the wall emissivity is homogeneous, the radiative flux repartition

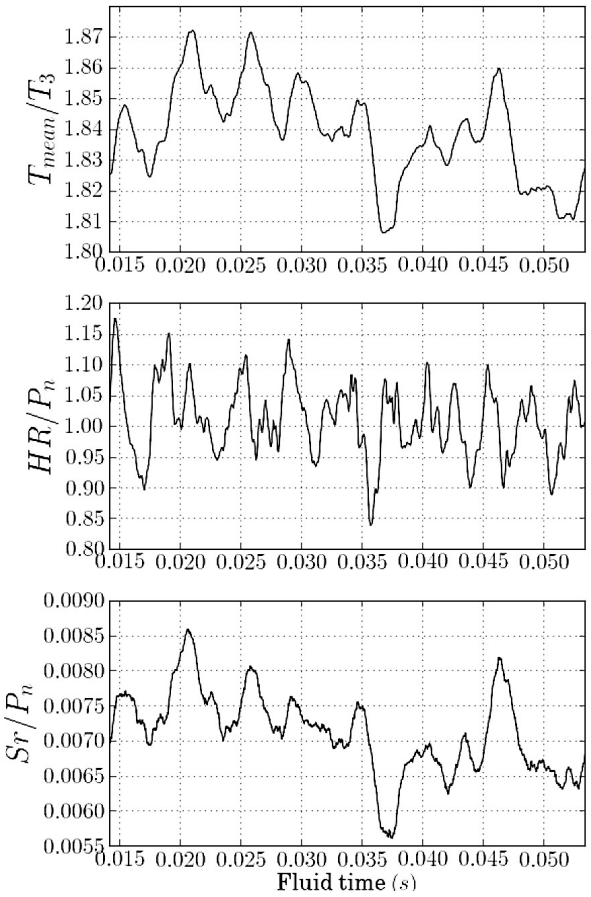

Figure 2.72: Time evolutions of spatially-averaged normalized temperature, heat release and radiative source term on the averaging window. Results from flow RFTI simulation 3.

is mainly driven by the solid temperature distribution. Most of the liner encounters positive fluxes. Negative ones are strongly restricted and correspond to locations where strong positive convective fluxes are observed. The explanation for this observation is illustrated in Fig. 2.74. A scatter plot of normalized convective flux versus normalized radiative flux for all points of the liner flame tube side is presented. Each point is colored by the corresponding solid temperature at that location. A large amount of points exhibits fluxes of opposite signs. Indeed, strong local positive convective fluxes lead to high solid temperatures. As a result, since the radiative effect redistributes energy from hot to cold zones, such regions experience strong negative radiative fluxes. On the contrary, many low temperature regions exhibit negative convective fluxes and positive radiative ones. Finally, a significant amount of points present positive values for both fluxes. These correspond to the outer envelop and the outer elbow, where convective fluxes exhibit small patterns of both signs and radiative ones are globally positive.

Finally, when integrated over the entire liner, convective fluxes are low, due to the necessary balance between both sides of the liner (note that the integrated value is not zero since some parts of the solid walls such as the injection device are not included) while the radiative flux gets close to the total radiative heat lost by the gas (not equal for the same reason). This evaluation confirms that it appears necessary to integrate radiation wall fluxes in computations to determine accurately combustion chamber wall temperatures.

For the last simulation, computation 4, the steady solid thermal state is obtained by coupling the LES combustion code with the solid conduction solver while taking into account the radiation each 7500 meeting points of the CHT resolution. The initial condition of the computation is the converged solution obtained by the CHT simulation 2. Figure 2.75 shows the convergence of the solid spatially averaged temperature and maximal temperature as well as the sum of heat fluxes along all the solid boundaries for both the CHT (white area) and the fully coupled (grey

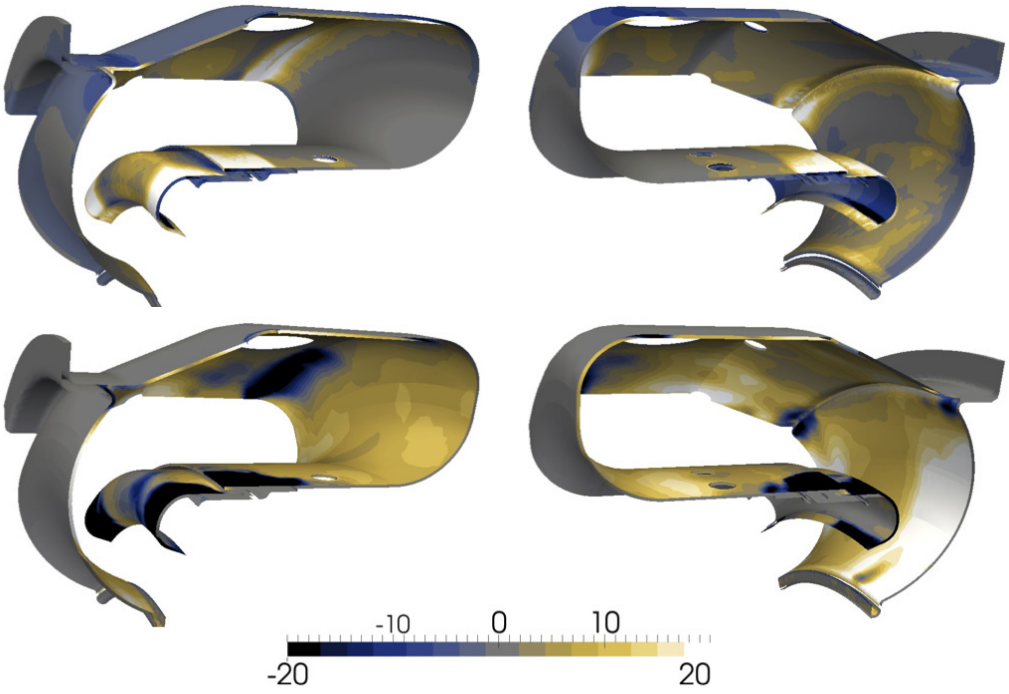

Figure 2.73: Normalized mean convective fluxes (upper fig) and instantaneous radiative fluxes (lower fig) fields on the liner surfaces coupled with the solid. Results from computation 3.

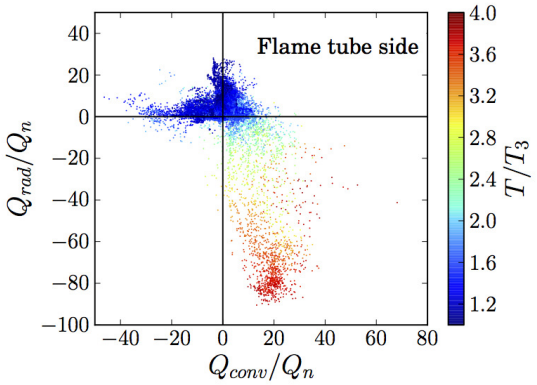

Figure 2.74: Scatterplot of convective fluxes versus radiative fluxes on the FT side of the liner surfaces coupled with the solid colored by solid temperature. Results from computation 3.

Integrated quantities	Q_{conv}/Q_n	Q_{rad}/Q_n
Liner casing side	-8.89×10^{-2}	-1.66×10^{-3}
Liner flame tube side	8.64×10^{-2}	8.34×10^{-2}
Both liner sides	-2.48×10^{-3}	8.17×10^{-2}

Table 2.9: Normalized convective and radiative fluxes integrated on the liner. Results from computation 3.

area) simulations. Due to the low radiative heat loss, no peak is evidenced in the sum of heat fluxes at the initialization of computation 4. However, an increase of the spatially averaged solid temperature is observed as well as a sharp decrease of the maximum temperature. Indeed, radiation redistributes energy between hot and cold regions of the solid, hence decreasing the extremes while globally heating the solid due to the positive radiative heat loss. Just like for the CHT simulation and due to the unsteady nature of the fluid and solid solvers, the fluid and solid stationary solutions are deduced by averaging the instantaneous solutions over a time period covering $40ms$ for the fluid and over the corresponding period of time in the solid reference time

unit (*i.e.* 36 *s*).

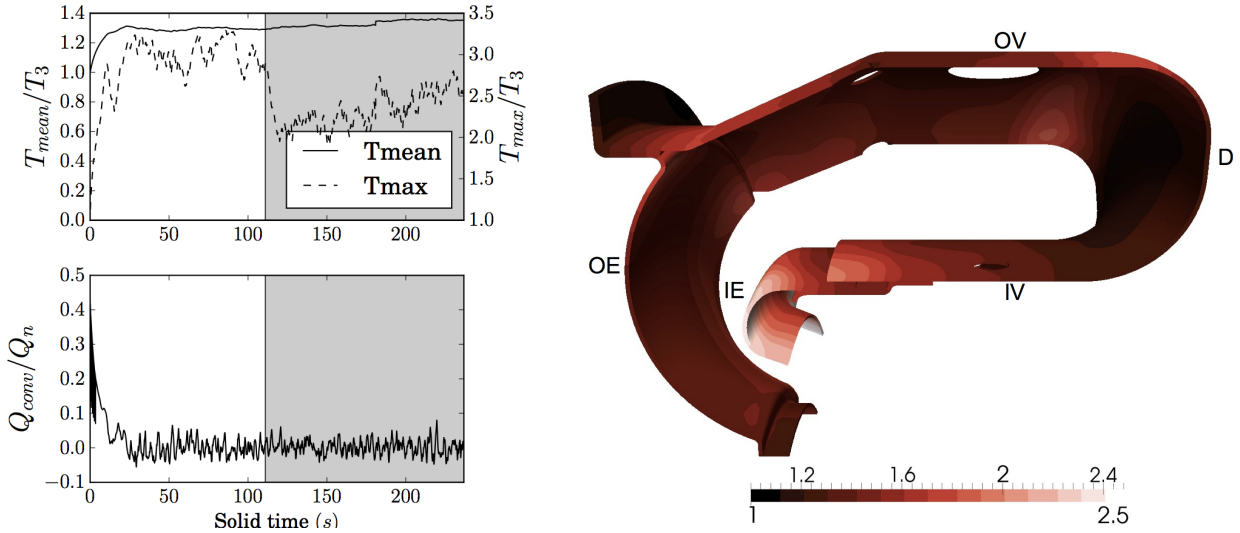

(a) (b)

Figure 2.75: (a) Time evolutions of solid spatially-averaged and maximal temperature (up) and sum of heat fluxes around the solid (down). Positive flux values corresponds to heat flux entering the solid domain. Results from solid CHT simulation (white zone) followed by the fully coupled simulation (grey zone). (b) Normalized solid mean temperature field. Results from solid fully coupled computation 4.

As already seen in the CHT case (computation 2), the solid mean temperature field shows no visible differences between the FT side and the casing side of the liner. Figure 2.75 presents the time averaged temperature distribution on the chamber liner obtained with this fully coupled simulation to be compared with the CHT one (Fig. 2.69). As evidenced by Fig. 2.75, the solid mean temperature obtained by the fully coupled simulation is higher than the one of the CHT case indicating a global heating of the walls by the hot regions of the fluid by radiation. In addition, all the changes of temperature correspond well with the previously discussed instantaneous radiative fields with a cooling of hot solid regions such as in the IE and a heating of cold areas such as between the IV and the dome. As a consequence, the maximum temperature in the solid domain in lower in computation 4 than in computation 2 (Fig. 2.75). Besides, variations of temperature reach 25% of the CHT solid temperature in extreme cases, indicating a strong impact of radiative heat transfer.

To assess the validity of the fully coupled computation 4, solid numerical results are compared to experimental data obtained with thermocolor tests on Fig. 2.76. As illustrated by the comparisons of temperature distributions between computation 2 (Fig. 2.69) and 4 (Fig. 2.75), including radiation wall fluxes in the simulation impacts the results. On line A, while the CHT solid temperature is under-predicted in the dilution hole region compared to the experiments, the fully coupled computation provides improved results in this zone. On the other hand, although the overall trends are respected on line B, the fully coupled simulation still tends to under-estimate the temperature level right after the dilution hole location.

These simulations demonstrate that CHT with LES is affordable in an industrial context and provide useful informations for designers. Moreover, radiation has an important effect on heat redistribution in the combustion chamber and need to be taken into account. Finally, an important point not discussed here concerns the modeling of multiperforated plate that cannot be resolved by actual meshes due to sub-millimeter hole sizes (PhD Thesis of Dorian Lahbib [155, 156] and Romain Bizzari).

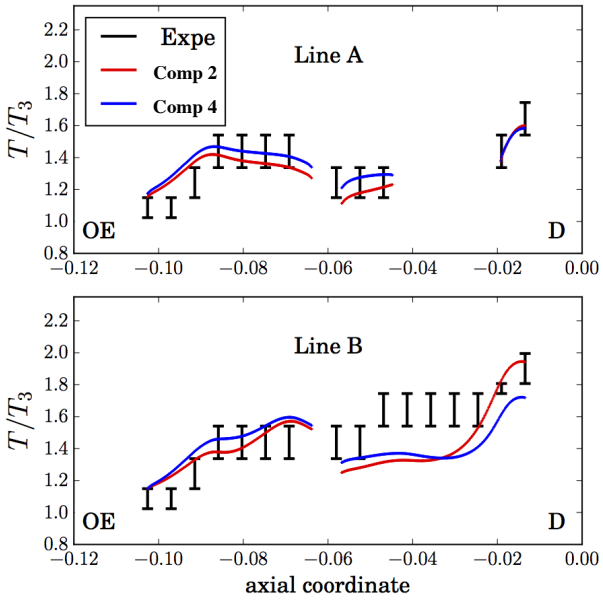

Figure 2.76: Comparison between the CHT (computation 2) and fully coupled simulation (computation 4) with experiment temperatures on line A (upper fig) and line B (lower fig) following the engine axis.

Bluff-body thermal property and initial state effects on a laminar premixed flame anchoring pattern

This section, extracted from the PhD Thesis of Sandrine Berger [13] and presented in two conferences [16, 14] as well as published in Journal of Flow Turbulence and Combustion [15], aims at illustrating the sensitivity of CHT converged results to initial solutions in reactive flows, an element rarely discussed. To analyze the physical relevance of the three potential equilibrium states outlined by the fixed temperature computations in the case of the bluff body stabilized laminar flames presented in section 2.1, CHT simulations are performed with various initial conditions. The latter are inherited from the previously detailed fluid-only fixed temperature computations. Indeed, each of the fluid converged solutions obtained for $T_w \in [600; 2000]$ K are used to initialize the fluid domain of the different CHT computations. For all these coupled simulations, the solid initial field is homogeneous and at the corresponding fluid wall temperature. The various simulations discussed here are therefore identified through this initial condition: $T_{init} = T_w \in [600; 2000]$ K. For brevity reasons only 7 of the 15 simulations performed are presented in this section. These correspond to the initial conditions $T_{init} = T_w$(at the initialization) = 700, 900, 1000, 1100, 1400, 1700, 2000 K.

A first set of simulations is performed for solid properties corresponding to those of a ceramic bluff-body simulated by Kedia *et al.* [134]. The thermal conductivity taken as a constant not evolving with the local temperature is $\lambda_A^s = 1.5$ $W.m^{-1}K^{-1}$. Interface physical fields are set with Dirichlet-Neumann conditions. Only the stationary solution is pursued here, thus allowing the use of a desynchronization technique to enhance the simulations convergence rate. The fluid and solid solvers are therefore physically desynchronized by a factor of the order of $O(10^4)$. Additional simulations have been performed for different desynchronization factors and evidenced the exact same results but naturally different associated CPU costs to reach a converged state.

Two different converged end states of the joint problems originating from the various initial conditions of the CHT simulations are obtained. For $T_{init} \in [700,\ 900\ K]$, the coupled fluid-solid system converges towards a 'cold' case for which the flame stabilized in the flame holder wake. For this case, the solid spatially averaged temperature is $T^s_{ave} = 878\ K$. For $T_{init} \in [1000,\ 2000\ K]$, fresh gases preheating achieved both by the flame and the solid walls allows the flame to move upstream. At convergence, the solid domain temperature is homogeneous and equals the adiabatic flame temperature $T^s = T_{adia} = 1844\ K$.

Within each category ($T_{init} \in [700,\ 900\ K]$ and $T_{init} \in [1000,\ 2000\ K]$), the converged thermal states obtained from any initial condition are strictly equivalent. These two states are presented in Fig. 2.77. The spatially averaged solid temperature is indicated in white at the top left of the plot to allow an easier identification of the various cases. The 'cold' and 'hot' converged states fall respectively into the lifted and bowed regimes evidenced by the fixed temperature computations. As could be expected, the stabilization pattern of the $T^s_{ave} = 878\ K$ case in terms of flame foot location, recirculation zone shape and length as well as fluid temperature field lies between the patterns observed for the fluid-only isothermal cases $T_w = 800\ K$ and $T_w = 900\ K$. The same conclusion can be drawn for the $T^s_{ave} = 1844\ K$ case whose fields are in between those of the $T_w = 1800\ K$ and $T_w = 1900\ K$ fluid-only solutions. Note that in Kedia *et al.* [134] the CHT simulations were initialized from non-reactive states and hence only a solution similar to the $T^s_{ave} = 878\ K$ case was obtained.

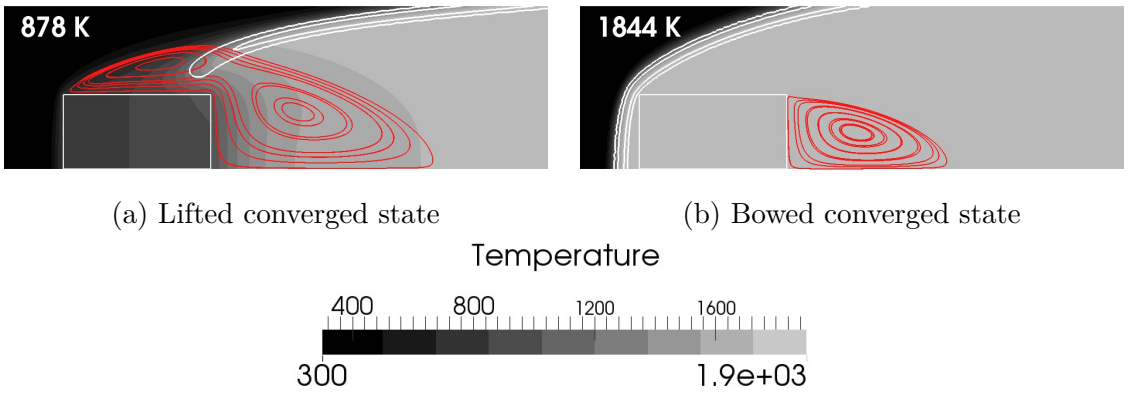

(a) Lifted converged state (b) Bowed converged state

Figure 2.77: Temperature field of the two CHT converged states in both fluid and solid domains with heat release contours at $HR = 10^8\ J.m^{-3}.s^{-1}$ (outer flame contour) and $HR = 10^9\ J.m^{-3}.s^{-1}$ (inner most flame contour) in white and flow streamlines within the recirculation zone (red) in the vicinity of the flame holder on the top half of the domain. The solid domain is indicated with the white square. For (a), initial solid temperature is $T_{init} \in [700,\ 900\ K]$ and for (b) $T_{init} \in [1000,\ 2000\ K]$.

The low conductivity of the material leads to large thermal heterogeneities in the solid domain for the lifted converged case as observed in Fig. 2.77. In addition, the low conductivity is also responsible for the significant difference between the actual spatially averaged solid temperature and the theoretical equilibrium state predicted by the fixed temperature case in Fig. 2.47 (theoretical equilibrium obtained for a temperature slightly below $T_w = 800\ K$). Indeed, the isothermal condition imposed at the wall in the fluid-only simulations corresponds, in terms of physics, to an hypothesis of infinite conductivity and uniform solid temperature. The conductivity is particularly low and hence far from this hypothesis. Finally, an interesting result lies in the fact that only two cases from the three theoretical equilibrium states identified earlier seem actually achievable with CHT computations. Even the case with an initial wall temperature at $T_{init} = 1000\ K$ initially very close to the third theoretical equilibrium state does not converge towards this pseudo solution but instead converges to a bowed flame. To further investigate the physical relevance of the third equilibrium state, additional simulations are performed for increased solid conductivities, and thus for cases closer to the infinite conductivity hypothesis.

Two additional sets of CHT simulations are performed: the various initial conditions remain

the same than for the previous computations, the solid conductivity being however multiplied by a factor 10 and 100. The previous and new sets of results are denoted as **Cases A**, **B** and **C** and correspond hence to solid conductivities respectively equal to: $\lambda_A^s = 1.5\ W.m^{-1}K^{-1}$, $\lambda_B^s = 15\ W.m^{-1}K^{-1}$ and $\lambda_C^s = 150\ W.m^{-1}K^{-1}$. Similarly to the previous observations these 21 computations converge towards only two stable states: the lifted and bowed regimes. Interestingly, depending on the conductivity, the bifurcation between these two states is either between $T_{init} = 900\ K$ and $T_{init} = 1000\ K$ for **Case A** or $T_{init} = 1000\ K$ and $T_{init} = 1100\ K$ for **Cases B** and **C**. Although all the converged bowed regime solutions are strictly equivalent whatever the initial conditions or the solid conductivity, the lifted converged regimes are impacted by the conductivity of the material. Indeed, changes in conductivity result in different thermal equilibria of the coupled fluid-solid system. Therefore, the lifted flame thermal fields obtained for the three conductivities differ which is evidenced by the different spatially averaged temperature of the solid. The higher the conductivity, the most homogeneous the solid temperature is and the lower is the spatially averaged solid temperature. Indeed as the conductivity increases and gets closer to the infinity hypothesis, the spatially averaged solid temperature gets closer to the value at which the integrated heat flux of the isothermal computations crosses zero (Fig. 2.47). More importantly, it appears that even for very high conductivity, the anchored regime is not a physical stable regime. Figure 2.78 presents the three lifted converged states corresponding to **Cases A**, **B** and **C** along with the bowed converged regime identical for all three solid conductivities. The spatially averaged solid temperature T_{ave}^s indicated in the top left of each figure.

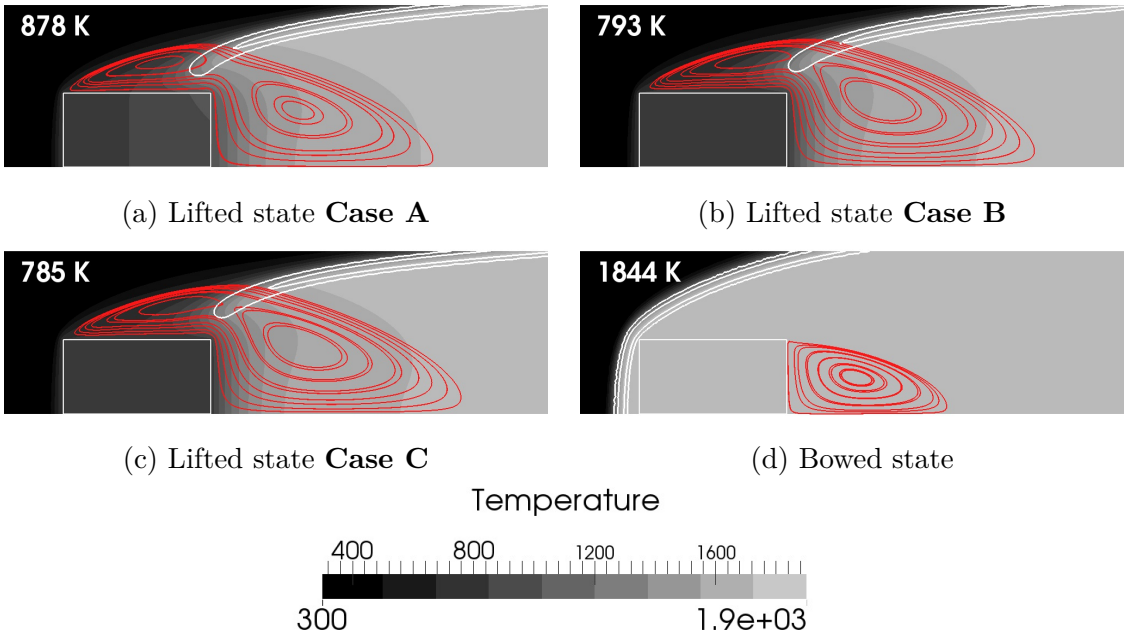

(a) Lifted state **Case A**

(b) Lifted state **Case B**

(c) Lifted state **Case C**

(d) Bowed state

Figure 2.78: Temperature field of the four CHT converged states in both fluid and solid domains with heat release contours at $HR = 10^8\ J.m^{-3}.s^{-1}$ (outer flame contour) and $HR = 10^9\ J.m^{-3}.s^{-1}$ (inner most flame contour) in white and flow streamlines within the recirculation zone (red) in the vicinity of the flame holder on the top half of the domain. The solid domain is indicated with the white square.

Although the solid conductivity is multiplied by the same factor 10 between **Cases A** and **B** or **Cases B** and **C**, significant modifications of the solid and fluid fields are observed when comparing Fig. 2.78(a) and 2.78(b), while Fig. 2.78(b) and 2.78(c) are very similar. Such important variations between **Cases A** and **B** are also evidenced through the solid spatially averaged temperature. Indeed, this quantity differs by 85 K for **Cases A** and **B** while only 8 K differentiates **Cases B** and **C**.

The decrease of the spatially averaged steady solid temperature with increased conductivity

observed for lifted cases in Fig 2.78 can be explained with a simple analytic model. Indeed on the basis of the observed quasi one-dimensional solid thermal fields simplifications can be introduced. For this analysis, the domain of interest is hence reduced to a solid of thickness d in the axial direction and infinite in the other direction and submitted to convective fluxes on both left and right surfaces respectively denoted ϕ_1 for the fresh gas side and ϕ_2 for the fully burnt gas side. These thermal conditions are then expressed as:

$$\phi_1 = h_1(T_w^1 - T_0) \quad and \quad \phi_2 = h_2(T_w^2 - T_{adiab}), \tag{2.17}$$

where h_1 and h_2 are the convective heat transfer coefficients respectively for the left and right surfaces T_w^1 and T_w^2 stand for the wall temperatures on both sides, and T_0 and T_{adiab} are the fresh gas temperature and the adiabatic flame temperature respectively. Since only the steady state is considered here, fluxes are equal and one can get the expression of the wall temperatures at steady state as function of the two corresponding Biot numbers: *i.e.* on the fresh side, $Bi_1 = h_1 d/\lambda_s$ and the hot gas side, $Bi_2 = h_2 d/\lambda_s$:

$$\begin{cases} T_w^1 = \frac{(1\ +\ 1/Bi_2)\ T_0\ +\ 1/Bi_1\ T_{adiab}}{1\ +\ (1/Bi_1\ +\ 1/Bi_2)} \\ T_w^2 = \frac{T_{adiab}\ +\ 1/Bi_2\ T_w^1}{1\ +\ 1/Bi_2} \end{cases} \tag{2.18}$$

Two limit cases appear:

- If $Bi \longrightarrow \infty$ or $\lambda_s \longrightarrow 0$

$$T_w^1 = T_0 \quad and \quad T_w^2 = T_{adiab} \tag{2.19}$$

  Temperature is strongly heterogeneous within the solid which behaves as adiabatic.

- If $Bi \longrightarrow 0$ or $\lambda_s \longrightarrow \infty$

$$T_w^1 = T_w^2 = \frac{h_1\ T_0\ +\ h_2\ T_{adiab}}{h_1\ +\ h_2} \tag{2.20}$$

  Temperature is homogeneous in the solid and governed by the respective values of the convective coefficients on each side of the solid (*i.e.* for the bluff-body case, by the respective upstream and downstream aerodynamic fields since the lateral faces have been neglected).

The spatially averaged temperature in the solid T_{ave} can then be deduced for these two extreme cases:

$$\underset{\lambda_s \longrightarrow 0}{T_{ave}} = \frac{T_w^1 + T_w^2}{2} = \frac{T_0 + T_{adiab}}{2} \tag{2.21}$$

and

$$\underset{\lambda_s \longrightarrow +\infty}{T_{ave}} = \frac{T_w^1 + T_w^2}{2} = T_w^1 = \frac{h_1\ T_0\ +\ h_2\ T_{adiab}}{h_1\ +\ h_2} \tag{2.22}$$

As a result, the larger the conductivity, the higher is the impact of the ratio h_1/h_2 on T_{ave}. Whether the solid spatially averaged temperature increases or decreases with increased conductivity therefore depends on the value of the convective heat transfer coefficients ratio compared to one (i.e. whether h_1 is superior or inferior to h_2).

Based on these relations, a theoretical solid spatially averaged temperature for the three converged lifted regimes can be obtained as long as the convective heat transfer coefficients on the flame holder front and back faces are known. For this analysis, they are extracted from Eq. 2.17, where T_w^1 and T_w^2 are obtained by spatially averaging the temperature over the corresponding face. Results are given in Tab. 2.10 where T_{ave}^{th} stands for the theoretical solid spatially averaged temperature, T_{ave}^{simu} is the corresponding temperature obtained in the CHT simulations and $\Delta T_{rel} = (T_{ave}^{th} - T_{ave}^{simu})/T_{ave}^{simu}$ is the relative difference between these two temperatures.

Table 2.10 indicates a small variability of the ratio h_1/h_2 between the three cases which lies around 2.5. As a result, since T_0 is naturally inferior to T_{adiab}, the solid spatially averaged temperature decreases when the solid conductivity increases. T_{ave}^{th} slightly underestimates the

Case	h_1 $[Wm^{-2}K^{-1}]$	h_2 $[Wm^{-2}K^{-1}]$	h_1/h_2 $[-]$	T_{ave}^{th} $[K]$	T_{ave}^{simu} $[K]$	ΔT_{rel} $[-]$
A	120	48	2.5	775	878	11.7%
B	122	50	2.4	755	793	4.8%
C	122	50	2.4	750	785	4.5%

Table 2.10: Quantities deduced from the three converged lifted regimes.

solid spatially averaged temperature of the simulations, by 5% for **Cases B** and **C** and 12% for **Case A**. For the latter case, the flame foot is closer to the flame holder walls, Fig. 2.78, inducing more interactions with the flame on the lateral surface. As a consequence, the one-dimensional hypothesis is erroneous for this case and hence can induce larger differences with the model, justifying the need for CHT for accurate predictions for specific regimes. Nevertheless, the model allows to idenfity the physical phenomena responsible for the decrease of the spatially averaged solid temperature and provides a fairly good first approximation of this temperature.

This study illustrates that in cases where thermal fields strongly influence the fluid dynamics and vice versa, as it is often the case in combustion application, the initial state used to start the CHT computation can have an impact on the converged solution indicating a non-unique solution of the problem. Note that the method proposed by Errera and Duchaine [78] has been tested on this case and provide the same bifurcations [13].

2.3 Partial Conclusions

Compressible LES in a wall-resolved context can provide high fidelity heat transfer results on a wide number of cases ranging from low Reynolds and Mach numbers to high Reynolds and Mach numbers. A main conclusion is that large meshes are necessary to properly resolve main flow features as well as boundary layers. As a consequence high performance computers are required to reduce restitution times. Some numerical issues are still under investigation to ensure oscillation free solutions close to walls (not discussed here - PhD of Luis Segui). An interesting point of LES more and more exploited in recent computations is the use of high order statistics than mean and root mean square to analyse the flow fields and relation with thermal fields (PhD Thesis of Charlie Koupper, Pierre Aillaud and Martin Thomas). This is a direct consequence of the use of HPC systems coupled with recent tool developments inside and outside the AVBP solver to extract informations on dedicated locations reducing the deluge of data which ease storing and exploitating solutions. When addressing complex industrial configurations, wall modeling is still necessary to provide acceptable CPU cost. The investigations not discussed in this manuscript concern wall laws for high temperature differences (PhD Thesis of Dario Maestro and Luc Potier) as well as effusion cooling modeling (PhD Thesis of Dorian Lahbib [155, 156] and Romain Bizzari). As thermal aspect is a key point in many industrial systems, new applications emerge (in the field of propulsion or not) such as the coupling of acoustic and heat transfer in acoustic treatments that equip fan duct liners [65]. Concerning conjugate heat transfer, performant tools and methodologies are available. Applications on academic cases and industrial configurations show interesting results (PhD Thesis of Stéphan Jauré and Sandrine Berger). Some work is still needed to propose more general guidelines in the context of LES. Finally the coupling of massively parallel LES solvers with thermal codes (conduction and radiation) raises the issue of High Performance Code Coupling (HPCC). Indeed, as the methodologies proposed for CHT require high frequency data exchange between the codes, an important stress exists on the process use to exchange informations (PhD Thesis of Stéphan Jauré). Discussed in Chapter 4, HPCC aims at providing solutions to hide as far as possible coupling step CPU times with respect to time consuming physical system resolutions.

Chapter 3

Combustion chamber / Turbine interaction

Gas turbine optimization targets increased reliability and efficiency, together with lower pollutant and noise emission. It is a complex multi-physics problem which has long been based on engineering intuition and expensive experiments and tests. Until now gas turbines have been designed following individual pathways for each component (for the primary flux: compressor, combustor and turbine). Analyses and testing are done component by component. Components are then assembled and the resulting engine is tested. One major practical problem encountered by gas turbine manufacturers, is that the individual behavior of the components can be very different from their behavior when mounted together in an engine. This may seriously affect the engine performance and reliability. Another practical problem is the limited access to measurements during engine operation. On the other hand gas turbine experts commonly acknowledge today that computer simulations are the most promising path for optimization. Therefore the numerical simulation of the entire engine with all physics involved is a key element for scientific progress and innovation. This would allow to analyse the behavior of the assembled components prior to any expensive and time consuming engine test. More importantly, it would give access to the details of the interaction between the components and the different physics, and bring new and informative material for the optimized design of the whole engine. Developing numerical tools and methodologies to simulate the entire gas turbine with all physical effects is a new challenge and constitutes an objective of Cerfacs in an attempt to create *digital twins* of real engines and minimize the necessary experimental effort.

3.1 Towards integrated simulations

Performing CFD of the entire primary flux of a gas turbine is challenging because of the very different nature of the flow field in the combustor (high swirl, combustion process, turbulence, low-Mach flow) and in the turbine as well as compressor stages (high Reynolds number, highly compressible and sensitive to the boundary layer flow). High-fidelity simulation methods are accessible for each individual component and physics: RANS or URANS for the turbomachinery parts and LES for the combustion chamber. To the author knowledge, the only study published about a tentative to perform a fully integrated simulation of the flow in a whole gas turbine has been performed by the Center for Turbulence Research at Stanford University [232, 233, 265, 234]. The strategy was to use a compressible URANS solver for the compressor and turbine stages and an incompressible LES solver for the combustor. Although interesting from a scientific point of view, the methods and framework used to couple the codes was complex. As a consequence, the integrated flow simulation of the whole engine failed to produce physical results.

Additionally, several tentatives have been made by coupling either RANS or LES solvers for the combustion chamber and Unsteady-RANS for the turbine [232, 229, 118, 120]. Nonetheless, these approaches lead to strong hypotheses on the data transferred from one code to the other,

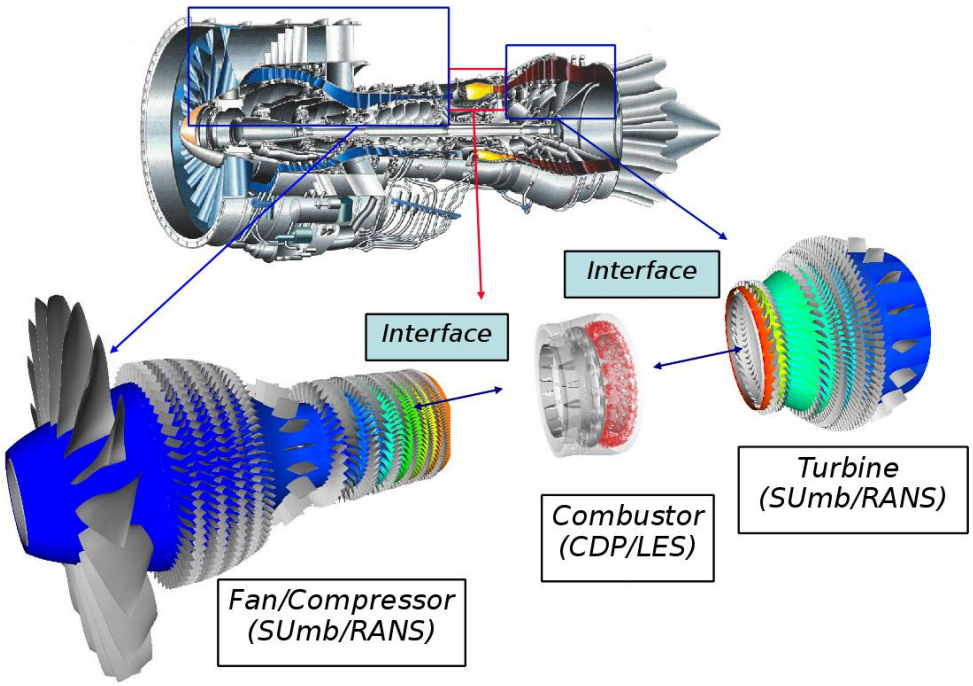

Figure 3.1: Flow simulation of a whole gas turbine (Pratt & Whitney engine, courtesy of Stanford University - https://ctr.stanford.edu/integrated-hybrid-ransles-realistic-gas-turbine-engine-0).

implying approximations on the mass flow rate, total energy and turbulent quantities. Using a compressible LES solver to solve the full system constitutes a high potential solution as such an approach is now recognized to deal well with the highly unsteady turbulent flow in the combustion chamber [92, 187], while allowing to compute the wall-bounded high velocity flow within the turbomachinery stages [260, 204]. The application of LES to turbomachinery stages is less mature, due to its higher cost and the inherent complexity of the flow, driven by wall flow behaviors and domains in relative motions. Nevertheless recent studies tend to show the benefit of such simulations over existing RANS computations, still widely used in industry [257, 197, 175, 96, 97, 191, 186]. According to Tucker *et al.* [258, 259], the two most important features to make CFD a predictive and reliable tool for gas turbine flows are the influence of real geometry (boundary conditions) and the wall modeling (transition, separation, etc.). As a result, the extension of the compressible unstructured LES solver AVBP to treat turbomachinery applications appears very promising. The extension of AVBP to treat turbomachinery stages is first presented along with two examples of applications: a high pressure turbine and a multistage high pressure compressor. Then, an integrated combustion chamber / high pressure turbine stage is shown as thermal interaction between combustion chamber and turbine stages is of primary importance for designers. Finally, some collateral computations using the extension of AVBP are briefly introduced.

3.2 Large Eddy Simulations of turbomachinery stages

Although some attempts have been made to couple LES and (U)RANS in the PhD Thesis of Elena Collado [38], this strategy has rapidly been considered as less interesting than performing the integrated simulation with the same compressible unstructured LES solver, *i.e.* AVBP, for two main reasons:

- LES in turbomachinery stages, compressors or turbines, is a new scientific topic where numerous issues concerning methodologies and applications can be explored,
- the use of a unique solver to treat all the components simplifies the integrated simulation setup as well as the computational workflow.

In this section, the method used to extend AVBP for the simulation of turbomachinery stages is presented. Then, applications to a high pressure turbine stage and a multi-stage high pressure compressor are exposed.

3.2.1 Extension of AVBP to simulate turbomachinery flows

It is not possible to start the description of the method used to extend AVBP for the simulation of turbomachinery stages without giving some words about the main investigator in charge of the developpement: Gaofeng Wang, now professor at Zhejiang University. We started to perform coupled computations between two instances of AVBP through boundary conditions with E. Collado [38] to mimic a (U)RANS/LES coupling and anticipate some potential problems. Coupling by boundary conditions of course introduces a bias in the different waves traveling across the domain (acoustic, entropic and vortical) as well as shocks [199, 200] as compared to the simulation directly performed on the whole domain. It was thus decided to test a coupling of two AVBP instances via numerical fluxes on a common interface between two sub-domains as done for mesh partitioning paradigm. Pr. Wang, post-doctoral fellow at Cerfacs at that time (RTRA funding), contributed strongly to this task in terms of computational science, coding, testing and debugging. He tested several methods and was a wonderful source of propositions, the retained one being his idea (MISCOG for Multi Instance Solver Coupled through Overlapping Grids) as well as the name of the resulting tool, *i.e.* TurboAVBP. Note that external coupling of two instances is used to limit modifications in the AVBP solver in terms of data structure, enabling to easily test very different approaches.

To describe the tested methods, some details about the numeric in AVBP are mandatory. The filtered LES unsteady compressible Navier-Stokes equations that describe the spatially filtered mass, momentum and energy $(\rho, \rho\mathbf{U}, \rho E)$ conservations, can be written in the following conservative form:

$$\frac{\partial \mathbf{W}}{\partial t} + \nabla \cdot \mathcal{F} = 0, \tag{3.1}$$

where $\mathbf{W}$ is the vector containing the conservative variables $(\rho, \rho\mathbf{U}, \rho E)^T$ and $\mathcal{F}$ is the flux tensor. For convenience, this flux is usually divided into two components:

$$\mathcal{F} = \mathcal{F}^C(\mathbf{W}) + \mathcal{F}^V(\mathbf{W}, \nabla\mathbf{W}), \tag{3.2}$$

where $\mathcal{F}^C$ is the convective flux depending on $\mathbf{W}$ and $\mathcal{F}^V$ is the viscous flux depending on both $\mathbf{W}$ and its gradients $\nabla\mathbf{W}$. The contributions of Sub-Grid Scale (SGS) turbulence models are included in the viscous flux through the addition of the so called turbulent viscosity ν_t [214, 228].

Two main types of numerical schemes are used in the present studies. First, the Lax-Wendroff scheme (LW) [161] is a 2^{nd}-order finite volume scheme in time and space, which corresponds to the accuracy of most commercial codes as well as most turbomachinery CFD tools available today. Secondly, the two-step Taylor-Galerkin finite element schemes TTG (C or 4A) (3^{rd} and 4^{th}-order in time and 3^{rd}-order in space) provides improved LES quality on unstructured grids [240, 37]. All schemes are expressed in the cell-vertex numerical discretization approach, for its compactness and effectiveness on parallel architectures. The cell-based residuals, *i.e.* the spatially dependent terms of the equations on each control volume Ω_j, are then calculated by integrating the fluxes over the cell as:

$$\mathbb{R}_{\Omega_j} = \frac{1}{V_{\Omega_j}} \int_{\partial\Omega_j} \mathcal{F} \cdot n \, dS, \tag{3.3}$$

where V_{Ω_j} is the cell volume and $\partial\Omega_j$ its boundary with normal vector n. Since the integration is obtained around a vertex, a distributed version of these cell-based residuals $\mathbb{R}_k$ is constructed via distribution matrices. One can hence express Eq. (3.1) into the semi-discrete scheme

$$\frac{d\mathbf{W}_k}{dt} = \mathbb{R}_k = -\frac{1}{V_k} \sum_{j|k\in\Omega_j} D^k_{\Omega_j} V_{\Omega_j} \mathbb{R}_{\Omega_j}, \tag{3.4}$$

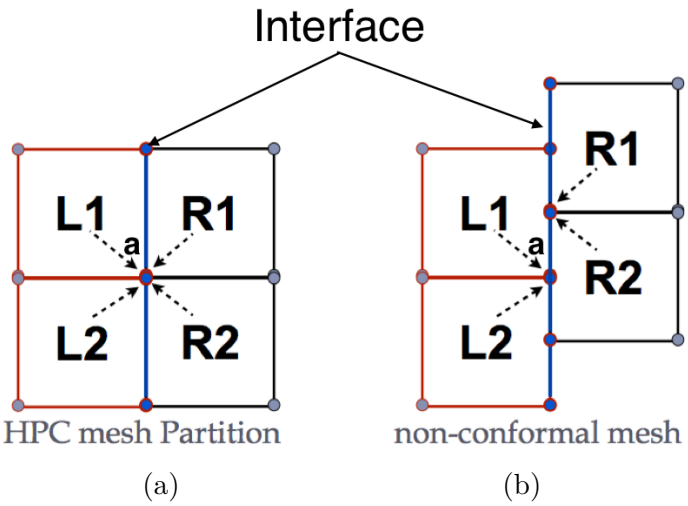

(a) (b)

Figure 3.2: (a) Domain decomposition method for cell-vertex schemes used in parallel computations and (b) non-conformal issue raised by a translating interface.

where V_k is a control volume associated with a node k and $D^k_{\Omega_j}$ is the distribution matrix that weights the cell residual from the cell center Ω_j to node k [59, 158].

In static (with stationary mesh element) parallel computations, the computational domain is divided into several individual vertices-shared partitioned domains each of which is attributed to one processor using Domain Decomposition Methods (DDM) [256]. Figure 3.2(a) illustrates the conventional DDM static coupling process for a cell-vertex scheme. The cells $(\mathbf{L_{1,2}}, \mathbf{R_{1,2}})$ are grouped into two domains respectively denoted by $\mathbf{L}$ and $\mathbf{R}$ and contribute to the common node $\mathbf{a}$ cell residual. Indeed in cell-vertex schemes, the cell-based residuals are computed locally (*i.e.* for all individual cells, $\mathbf{L_{1,2}}, \mathbf{R_{1,2}}$) and scattered to the belonging vertices. Vertex $\mathbf{a}$ that is located at the interface therefore needs all the contributions from the neighboring partitions for the nodal residual to be evaluated following Eq. (3.4). In conventional approaches of static massively parallel codes, this is simply done through network communications.

The problem for the rotor/stator coupling is similar to the DDM problem described above except that the two domains $\mathbf{L}$ and $\mathbf{R}$ are moving (translating or rotating) relatively to each other. Non-conformal vertices (shown in Fig. 3.2b) are hence present at a given instant and along the interface. Additional evaluations at every iteration are therefore needed if compared with static DDM. Numerically, several coupling methods are possible for such problems, all of which introduce the notion of interpolation for information reconstruction around or on the interface. Rotor/stator interface treatment may be introduced at various steps of the numerical scheme. Coupling fluxes before computing the cell-based residuals of Eq. (3.3) has the benefit of involving only the interface nodes limiting the number of unknowns and potential manipulations. Within such a context, the computed fluxes should be interpolated on the 2D coupled interface for a 3D computation as performed in the traditional sliding mesh approach for example [223]. An alternative is to couple nodal residuals. In this approach, the nodal residuals $\mathbb{R}^L_a$, $\mathbb{R}^R_b$ and $\mathbb{R}^R_c$ are calculated by counting the contributions of all sub-domain local cells using Eq. (3.4) first. The contributions of each missing domain (*i.e.*: $\mathbf{R}_2$ residual contribution to node $\mathbf{a}$ for example) are then estimated by introducing an additive interpolation $\mathfrak{L}$ to obtain the vertex $\mathbf{a}$ residual at the interface for example,

$$\mathbb{R}_a = \mathbb{R}^L_a + \mathfrak{L}(\mathbb{R}^R_b, \mathbb{R}^R_c). \tag{3.5}$$

With this approach, the difficulty comes from the rotation terms added in the transport equations of the moving domain that are not compliant with the static part of the configuration. As a result such a scheme was found to be unstable in the case of a rotating domain coupled to a static domain if using simple linear interpolation schemes. Note also that cell volumes V_{Ω_j} must be exchanged to comply with Eq. 3.4 which can be complex and increases the CPU cost of the simulation.

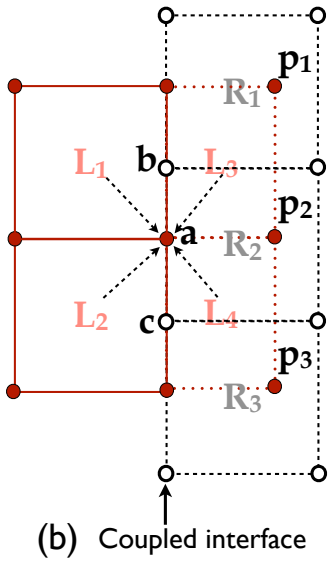

Figure 3.3: Proposed method for rotor/stator interface. $\mathbf{L_{1,2,3,4}}$ (composed of: solid lines - edges and filled symbols for the vertices) and $\mathbf{R_{1,2,3}}$ (composed of: dashed lines - edges and open symbols for vertices) denote the cells on the left and right sides of a partitioned domain, respectively. In the case of a moving fluid boundary, points $\mathbf{a}$ of domain $\mathbf{L}$ and points $\mathbf{b}, \mathbf{c}$ of domain $\mathbf{R}$ are the vertices to be coupled at the interface. Points $\mathbf{p_{1,2,3}}$ and $\mathbf{L_{3,4}}$ are additional vertices involved in the coupling when the overlapping method is introduced.

The solution retained to overcome these difficulties consists in reconstructing the residuals using an overset grid method that directly exchanges the multi-domain conservative variables by interpolation. As shown in Fig. 3.3, overset grids are introduced relying on extended domains $\mathbf{L}$ by two $\mathbf{L_{3,4}}$ or more ghost cells in the normal direction of the interface so that the nodal residual of vertex $\mathbf{a}$ can be computed from available sub-domain cell-based residuals of $\mathbf{L_{1,2,3,4}}$. Note that $\mathbf{L_{1,2,3,4}}$ is obtained using the interpolated conservative variables within the overlap region to evaluate the right-hand side of Eq. (3.3). Note finally that cells $\mathbf{L_{3,4}}$ are geometrically overlapped with the domain $\mathbf{R}$ with points located in cells $\mathbf{R_{1,2,3}}$. In the more generic cases, the extent and topology of the duplicated cells will not coincide. The unknown conservative variables of the overset vertices $\mathbf{p_{1,2,3}}$ are hence approximated through an interpolation from the information of cells $\mathbf{R_{1,2,3}}$. The same procedure is used to compute the nodal residuals of $\mathbf{b}, \mathbf{c}$ in domain $\mathbf{R}$ that is also extended onto mesh $\mathbf{L}$ by two or more cells, since it is a two-way coupling. This third approach is selected here as it is easily implemented externally from any base CFD code and yields high-order accuracy if used in conjunction with high order interpolation [54, 242, 244, 166, 20, 47].

In terms of methodology and overall strategy, external code coupling is preferred over an internal implementation to extend the available LES solver so that it can deal with rotor/stator simulations. Hence two or more copies of the same LES solver (namely AVBP) each with its own computational domain and static DDM algorithm executing a given partitioning with a given target number of processes, are coupled through the parallel coupler OpenPALM [70]. The detailed implementation of such coupling includes: (1) find the enclosed cell; (2) calculate the local coordinates in the cell; (3) calculate the interpolation coefficients using a shape function; (4) calculate the interpolated value. Figure 3.4 shows a typical communication framework for a rotor/stator coupling approach using the MISCOG method described above. For this case, the whole flow domain should initially be divided into static (AVBP01) and rotating parts (AVBP02). For rotating parts, the code uses the moving-mesh approach in the absolute frame of reference while the remaining unit simulates the flow in the stationary part in the same coordinate system [190]. The interfaces between the two units involving rotating and non-rotating parts are coupled with the overset grids by interpolating and then exchanging the

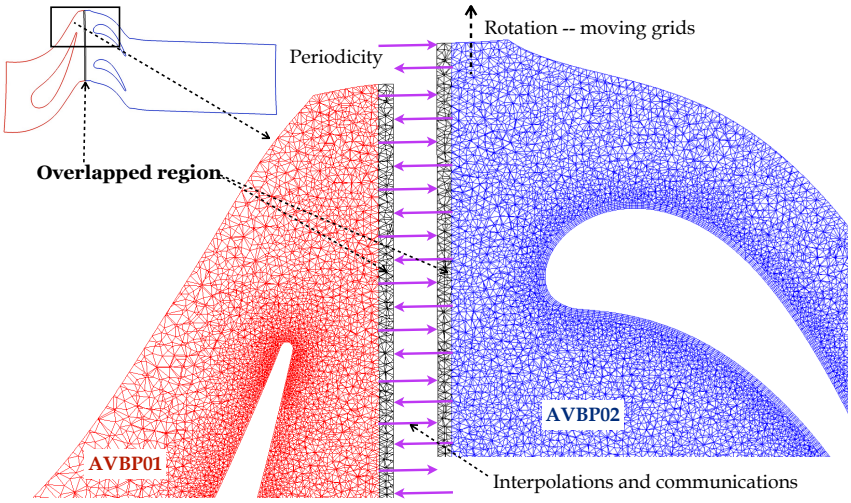

Figure 3.4: Communication framework of coupling rotor/stator interface.

conservative variables wherever needed. To do so, an efficient distributed search algorithm is implemented in the coupler OpenPALM to locate the points in parallel partitioned mesh blocks. This coupling algorithm updates the information and carries the interpolation from one sub-MPI world to the next and vice-versa. The numerical stability of the coupled solution and the convergence of this coupled problem are directly linked to the size of the overlapped region and the stencil of the numerical schemes as studied during the PhD Thesis of Elena Collado [38]: the TTGC scheme with is third order in time and space requires a larger overlapping region than the LW scheme, second order in time and space.

Prior to the application of the proposed solution to rotor/stator problems, many validation cases have been conducted focusing on acoustic wave propagation, convection of inviscid and viscous vortices and rotating boundaries. These test cases were performed by post-doctoral fellows (Gaofeng Wang and Jérôme de Laborderie) funded by RTRA and a national program supported by Safran called CN2020[1] and lead to two publications in Journal of Computational Physics [273, 50]. The primary objectives are to qualify and quantify errors introduced by the coupling approach with respect to known solutions or solutions obtained with a unique computational domain. The main outputs of these various tests are the following:

- accurate transfer of flow variables across the interfaces is essential to limit dissipative and dispersive errors on the vortical, acoustic and entropic waves typically found in LES. That is the reason why a third-order interpolation method has been introduced in TurboAVBP. This interpolation relies on 1D Hermite interpolators and has been implemented for various types of 2D and 3D elements. The high-order interpolation keeps the global accuracy of the AVBP schemes, even in the most detrimental case: non-matching cells at the interface, coarsened cells in all directions and moving interface.

- the computations of wave propagations through moving overlapping regions of MISCOG raise interesting fundamental questions similar to the treatment of boundary conditions studied by Vichnevetsky and Bowles [268] or Sengupta [241]. Analytical studies and tests performed with MISCOG showed that three types of spurious waves can be generated at the interface, representing a numerical discontinuity for the flow. They consist of physical waves, *i.e.* acoustic waves, numerical waves, *i.e.* Nyquist frequency waves, and waves only present with a moving interface since they are caused by the temporally evolving spatial interpolation error. The high-order interpolation has been shown to drastically reduce these waves respectively to the second-order accurate interpolation method available in

[1] In the CN2020 program, AVBP was compared to many other high-order codes (including spectral differences and Discontinuous Galerkin methods) and confirmed the high performances obtained with AVBP and MISCOG.

OpenPALM.

- dealing with viscous flows, the study of velocity derivatives through the interface has shown that a high-order interpolation is required to properly transfer diffusive fluxes, whatever the convective scheme. Indeed a second-order interpolation method systematically yields discontinuities of velocity derivatives at the interface.

- The overset grid method is known to be not globally conservative by nature. This represents a limitation for its application to turbomachinery flows, for which mass flow conservation is expected. To guarantee minimal losses on conservation, homogenous sizes of donor and receptor cells are recommended to be used along with third-order interpolation. For all cases (including real compressor and turbine cases), the relative difference in mass flow observed in TurboAVBP is negligible (less than 0.01%).

Since its first runs during spring 2012, TurboAVBP has been used to study different configurations of rotor/stator stages such as fans [168, 195], compressors [271, 51, 50] and turbine flows [273, 204] providing good predictions in flow fields as compared to available experimental data. Two examples are given, the first one dealing with a high pressure turbine stage and the second one with a 3.5 stages high pressure compressor. Due to the high Reynolds and Mach number of the configurations, wall-modeled LES are performed.

3.2.2 Large Eddy Simulation of a high pressure turbine stage

In an attempt to provide guidelines for LES of rotor/stator, several LES of the high-pressure experimental rotor /stator turbine stage MT1 have been performed using different sub-grid scale models in conjunction with a wall model: the classic Smagorinsky model [248], the Wall Adapting Local-Eddy viscosity (WALE) model [193], and the recent σ model [192]. Results presented in this section are extracted from the PhD Thesis of Dimitrios Papadogiannis and have been published in Journal of Turbomachinery [204]. While modeling the unresolved scale effects on the filtered field, SGS operators may not follow certain universal turbulent flow properties and erroneously introduce additional turbulent viscosity when unnecessary. A primary and highly desirable property of SGS models is that since turbulence is damped near walls, turbulent viscosity should follow the same behavior (hereafter denoted as property P1). Two other desired properties are that turbulent viscosity should be zero in pure shear and pure rotation (property P2) as well as when there exists an isotropic or axisymmetric contraction/expansion (property P3) [192]. Satisfying property P1 is essential in wall-resolved LES. It is less constraining with a law-of-the-wall approach since no attempt is made for the SGS model to provide the wall shear-stress. Note nonetheless that interactions between the SGS model and the law-of-the-wall in the matching region and outer part of the boundary layer can affect the predictions [19]. This difficulty inherent to wall-modeled LES is here of specific importance. Indeed, the P1 property is expected to yield a better near-wall boundary layer flow and SGS blending with a law-of-the-wall. This is of importance since wall-modeled LES is today the only affordable approach able to deal with real turbine flows. Table 3.1 summarizes which of the desired properties are satisfied by the three SGS models and corresponding LES of interest in this work.

The first mesh M1 investigated is composed of 8.1 million cells for the stator domain and 10.5 million cells for the rotor domain. Prisms are preferred at end-walls to ensure reasonable wall resolution while tetrahedra are used in the vanes. First nodes off the blade walls are placed in the logarithmic region of the turbulent boundary layer to allow proper use of a wall function with prisms having a low aspect ratio: *i.e.* $\Delta x^+ \approx \Delta z^+ \approx 4\Delta y^+$. Finally and to maintain an acceptable time-step the rotor tip region is meshed with $6-7$ cell layers. Note that in wall units and despite the poor tip region discretization, the maximum values of y^+ measured around the blade is approximately 130. The average value of y^+ across the stator and rotor blades (including the tip) is 60.

Despite modeling changes, all the important flow characteristics and secondary flow features are revealed by all three simulations (Fig. 3.5). Additionally, overall mean flow results show

Mesh M1	**Case 1**	**Case 2**	**Case 3**
Mesh M2	**Case 4**	**Case 5**	**Case 6**
	Smagorinsky	WALE	σ
P1	NO	YES	YES
P2	NO	NO	YES
P3	NO	NO	YES

	Nb. cells stator	Nb. cells rotor	Averaged y^+
M1	8.1 M	10.5 M	60
M2	40 M	74 M	12

Table 3.1: Summary of the three sub-grid scale models, their constants and whether they satisfy the desired properties. Main properties of the 2 meshes used for the MT1 turbine computations.

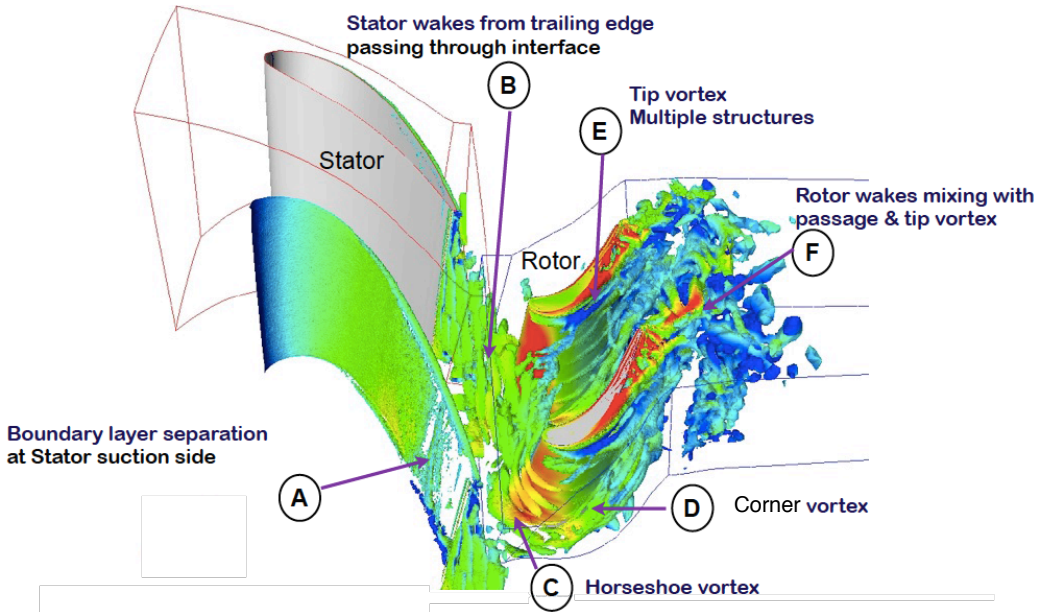

Figure 3.5: Q criterion of an instantaneous LES solution within the turbine stage obtained the Smagorinsky model.

qualitative and quantitative agreements with the experiments performed at the Oxford Turbine Research facility and for all cases. Figure 3.6 shows the time averaged isentropic Mach number on the stator vane for the three SGS models (Case 1: Smagorinsky model, case 2: WALE model and case 3 σ model) and at three radial positions: 10, 50 and 90% of the vane span. All three models predict similar behaviors on both the pressure and suction sides of the blade. Small differences exist near the trailing edge at 10% span, where a hub corner vortex exists (Fig. 3.5) and the models predict slightly different locations of the separation point. At the other radial locations, minor differences are related to discrepancies in the shock structures on the suction side. Reasons for such changes are differences in the boundary layer thicknesses as well as matching region behaviors amplified by the outer boundary layer flow unsteady content potentially interacting with the wall-law model [19]. Typically Case 1 produces much stronger shock structure within the stator that are not present for Cases 2 and 3. Similar findings are observed for the rotor, Fig. 3.7, when looking at pressure profiles across the blade at mid-span.

The unsteady behavior of the flow is be very sensitive to the SGS modeling, providing different shock structures and more importantly different unsteady contents. Using SGS models adapted to wall-bounded flows results in flows with higher unsteadiness and higher effective turbulent Reynolds numbers, hence flow fields likely to be more realistic. As expected, the basic Smagorinsky model proves to be too dissipative for these flows. Looking at an instantaneous

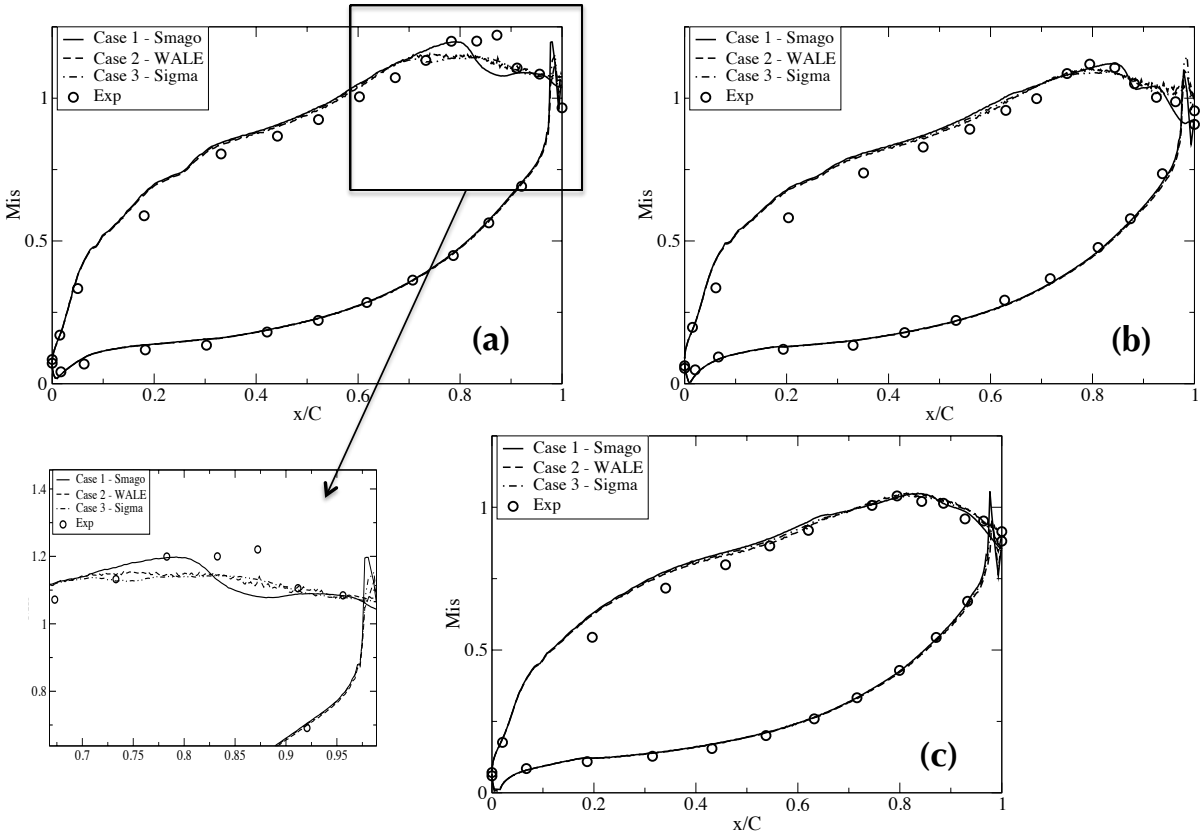

Figure 3.6: Isentropic Mach number across the MT1 stator at 10% (a), 50% (b) and 90% (c) span.

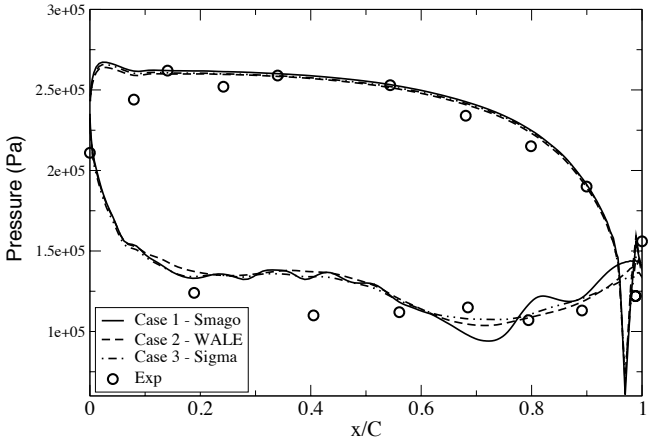

Figure 3.7: Static pressure across the rotor blade of MT1.

density gradient at mid-span and across the flow field for the 3 cases, Fig. 3.8, allows evaluating the unsteady content of the simulations. Aside from the acoustic waves that propagate and impact neighboring blades, all flow patterns are affected by the SGS models. Shock locations and strength differ although Cases 2 & 3 converge to the same solution which differ from Case 1. Stator wakes are also affected as evidenced by the FFT's of pressure signals on probes located in the vane wake, Figs. 3.8: multiple peaks appear with amplitudes depending on the SGS model. For this operating condition the rotor blade passing frequency (BPF) is 9.5 kHz. For all three cases, the highest peak relates to the passing rotors and is particularly clear. Higher harmonics

are present but can be altered by the modeling. Another potentially expected peak relates to the Vortex Shedding (VS) from the trailing edge of the stator. For Cases 1 and 3 it approaches 42 kHz. Case 2 shows a much weaker VS peak with a wider range of impacted frequencies accompanied by a particularly strong peak at the 5th harmonic of the rotor-BPF. The strong peaks related to the VS indicate that the stator wake appears to be experiencing coherent vortex shedding potentially developing into a turbulent shear layer.

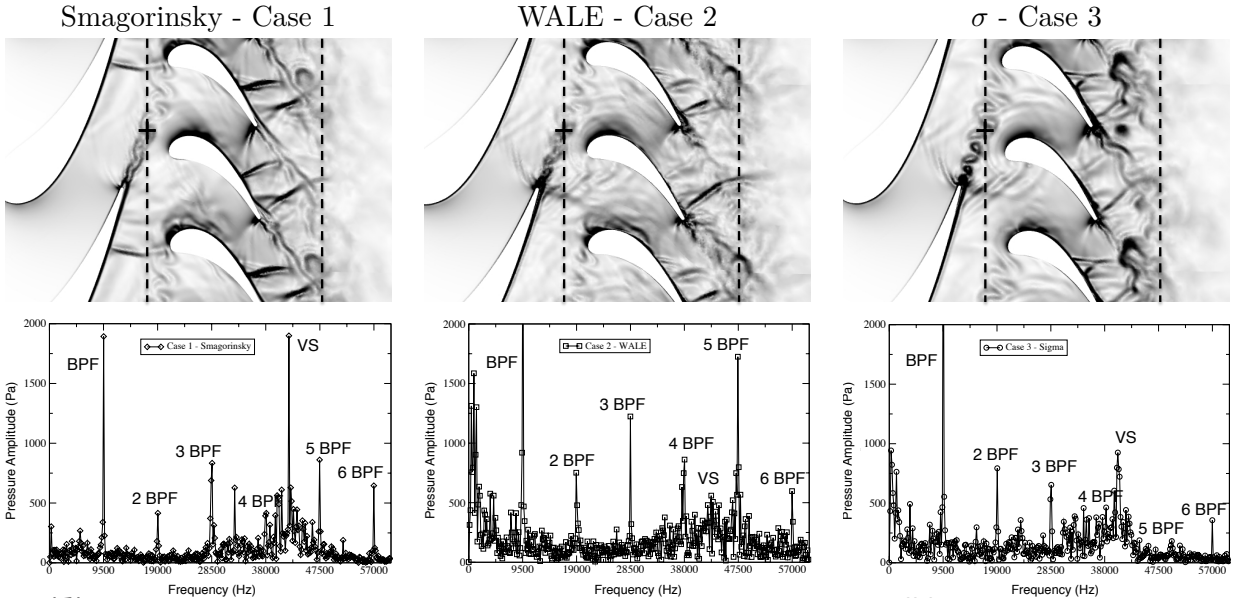

Figure 3.8: Instantaneous views of $\frac{||\nabla\rho||}{\rho}$ at mid-span (top) and FFT's of the pressure signal for the identified probe (bottom) for the three SGS models case 1, 2 and 3.

Looking at the energy distribution across the frequency spectrum in logarithmic scales at the same probe location thanks to a Power Spectral Density of axial velocity (Fig. 3.9), the $-5/3$ internal slope is captured for all cases. On top of this broadband activity, peaks relate to the vortex shedding from the stator trailing edge and their harmonics, highlighting the coherent vortex shedding and the effect of SGS modeling on this instability. Cases 2 and 3 have a larger amplitude and a larger range of frequencies with a linear slope, hence a higher effective Reynolds number. The Smagorinsky model, on the other hand, appears to be too dissipative with a cut-off at lower frequency and a narrower inertial subrange. Such changes in spectra indicate that the energetic flow content issued by the three different SGS models are potentially very different.

In depth analysis of the different LES predictions based on triple decomposition of the velocity field at different stations proved SGS modeling to be of critical importance especially at the exit of the stage where not only are the deterministic parts affected but so are the stochastic components [204]. Such diagnostics also evidence the complexity of the rotor flow which is affected by the stator exit unsteady flow content. Transfers as well as sources among the various components of such decompositions are seen to be accessible through LES predictions and should be of interest to better understand rotor / stator interactions.

A higher resolution mesh has been tested (mesh M2), containing 40 million cells in stator domain and 74 million in the rotor one, leading to a maximum y^+ of about 12 [202]. Looking at the density gradient for case 4 (Smagorinsky model with refined mesh), cases 5 (WALE model with refined mesh) and Cases 6 (σ model with refined mesh), Fig. 3.10, to be compared to the coarse cases in Fig. 3.8, allows a quick overview of the unsteady activity across the turbine stage. With the refined mesh M2 a much richer flow is revealed throughout with finer structures and increased acoustics. Results with WALE and σ models in particular reveal the strongest activity. A first notable difference is the evolution of the boundary layer where a much finer boundary layer appears compared to the coarse cases as well as with the Smagorinsky case on the refined

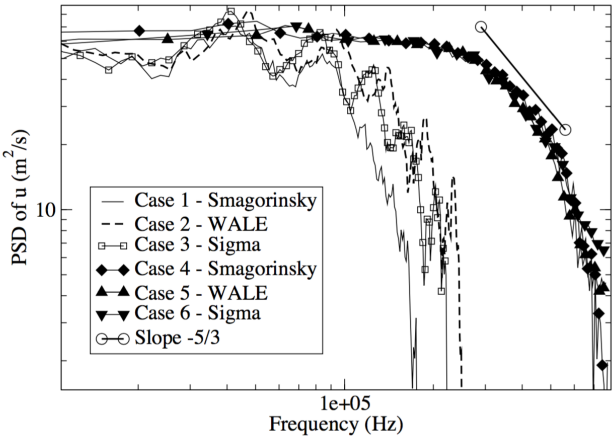

Figure 3.9: Power spectral density of the temporal axial velocity signal of a probe in stator's wake

mesh. Clearly, the satisfaction of property P1 by the WALE and σ SGS models changes the boundary layer prediction. Differences are observed also in the stator wake and shock structures. The coherent vortex shedding depicted in Fig. 3.8 has been replaced by turbulent vortex shedding with vortices quickly braking up downstream. The trailing edge shock structure in the stator passages is also altered, with a very pronounced shock visible for Cases 5 & 6 that interacts with the passing rotor blades. Finally the shock structures in the rotor passages are drastically changed as discussed in the PhD Thesis of Papadogiannis [202].

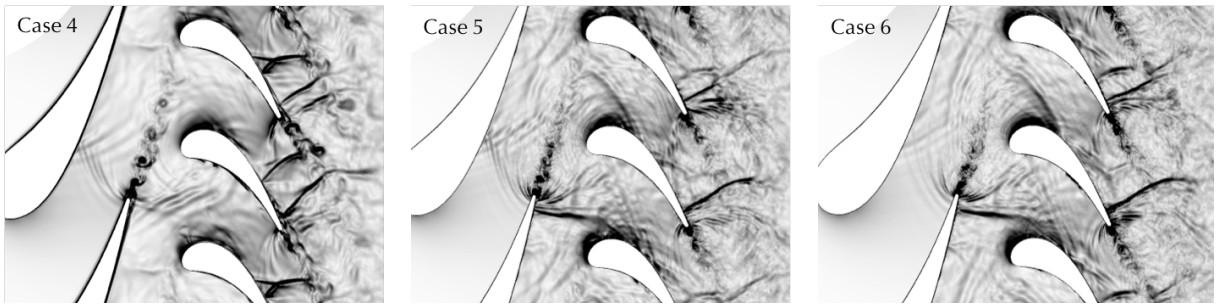

Figure 3.10: Instantaneous views of $\frac{||\nabla\rho||}{\rho}$ at mid-span for the three SGS models (case 4: Smagorinsky, case 5: WALE and case 6 σ) with the refined mesh.

Comparisons of the turbulent content of the flow can be useful to establish the changes in the turbulence cascade and turbulent production. To this end, a Power Spectral Density (PSD) is evaluated for the axial velocity component signals recorded from probes located in the stators wake (Fig. 3.9). Compared to the coarse mesh simulations 1-3, the refined Cases 4-6 results are very different. The cut-off frequency of the refined mesh is almost double the one of the coarse cases and a pronounced turbulent cascade is visible. No particular peak appears, highlighting the broadband nature of vortex shedding at this position. Another finding is the good agreement between these high-resolution Cases 4-6 for which the effect of the SGS model is less pronounced.

All these observations confirm that wall-modeled LES of turbomachinery flows do raise issues that need to be addressed carefully. Apart from the grid and near-wall modeling sensitivity of such simulations, these analyses cannot be separated from an evaluation of the impact of SGS modeling: a tight coupling occurs between these models resulting in distinct energetic distributions or equivalently distinct LES instantaneous behaviors despite the fact that mean global statistics are all similar and in agreement with experimental findings. Nonetheless, such simulations can give relevant informations for designers and scientists. As an example, based on

the coarser mesh, indirect combustion noise generation has been evaluated with LES of this 3D high-pressure turbine stage subjected to a constant-frequency entropy wave train pulsation [203] (Fig. 3.11).

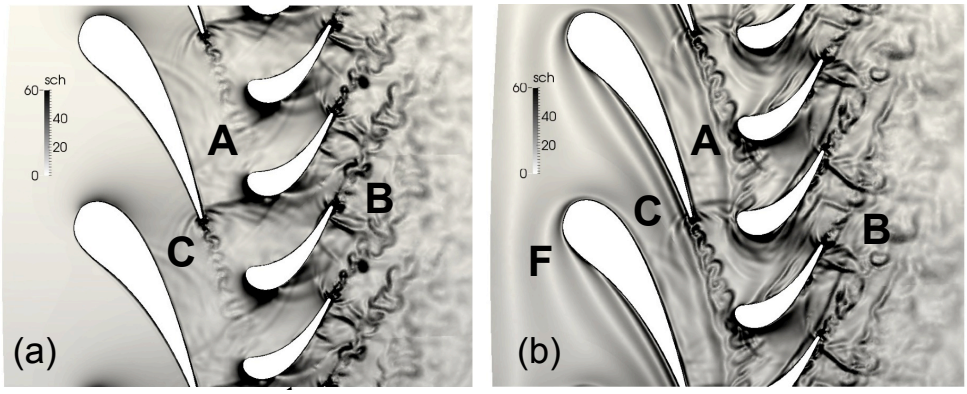

Figure 3.11: Instantaneous views of $\frac{||\nabla\rho||}{\rho}$ at mid-span for the steady inflow (a) and pulsed cases (b).

To simplify the data processing, the flow field and the generated noise were analyzed through the Dynamic Mode Decomposition of instantaneous snapshots at several positions across the turbine and the results are compared with a steady inflow case. Entropy wave injection generates a distinctive high-amplitude mode at the pulsation frequency, as well as interaction modes with the blade passing frequency. Despite the presence of broadband turbulence and non-linear interactions, the blade passing frequency and pulsation modes are shown to be the most important. For the forced frequency, a detailed analysis of the 3D LES predictions is performed and the results are compared with the compact theory of Cumpsty and Marble [45] as well as 2D simulations of a similar turbine configuration [76, 75]. While the compact theory over-predicts the noise levels, the 3D LES of the choked transonic high pressure turbine reveals that the entropy waves become highly distorted (Fig. 3.11). The 3D entropy waves are transmitted even less efficiently to downstream stages than 2D simulations and the compact theory and thus are unlikely to generate any additional indirect noise (Fig. 3.12-c); the transmitted acoustic waves, however, remain strong and contribute to the indirect noise as in 2D (Fig. 3.12-b). The reflected acoustic waves are slightly weaker than in 2D and far less than in the compact theory, and will therefore not amplify any potential acoustic instabilities in the combustion chamber (Fig. 3.12-a).

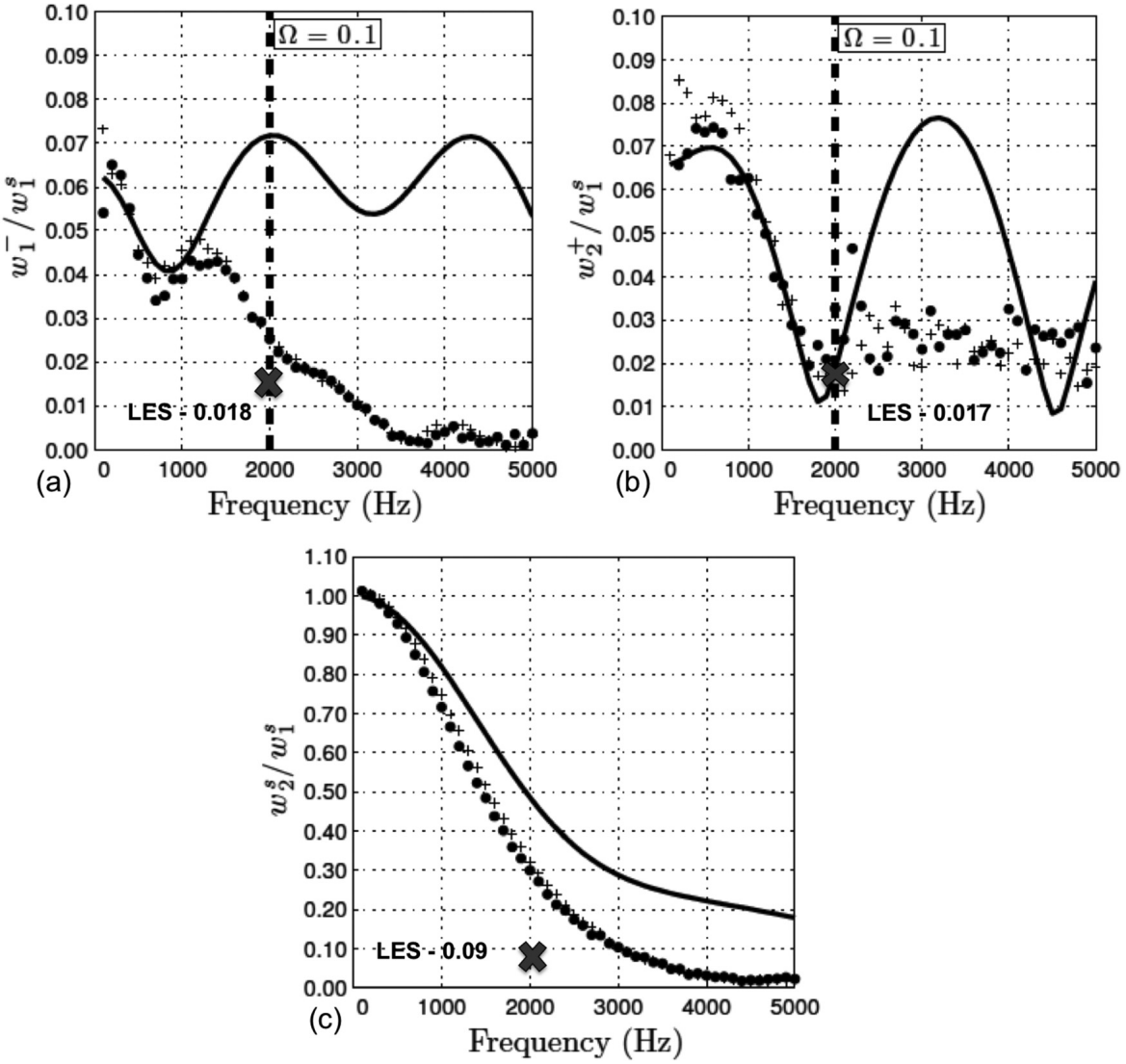

Figure 3.12: Comparisons of the evaluated transmission coefficients using 3D LES ($\times$), 2D predictions ($+$ and $\circ$) and the compact theory (-) for: (a) reflected acoustic wave, (b) transmitted acoustic wave and (c) transmitted entropy wave.

3.2.3 Large Eddy Simulation of a multi-stage high pressure compressor

The most challenging computation performed with TurboAVBP is a Large Eddy Simulation of the high-pressure multistage axial compressor CREATE [198, 179, 180, 41], with realistic technological effects such as the tip clearances and a hub cavity. This challenging simulation has been performed by Jérôme de Laborderie during its post-doctoral fellow at Cerfacs and leads to two contributions in international conferences [51, 50] as well as to a journal paper under preparation. Using the natural periodicity of CREATE, only a 22.5 degree sector of the machine is simulated (Fig. 3.13). Three grids are generated, from 88 to 1032 millions cells (Tab. 3.2)[2]. Note that with more than one billion cells, the M3 grid agrees with the expected order of magnitude of a LES grid for industrial compressors at Re $\approx 10^6$ [261]. For M3, the maximum y^+ value is less than 40 over the whole set of blades. This is in agreement with recommendations for wall-modeled LES [228, 99]. In the M2 grid, y^+ is globally less than 100 on the blades, still allowing a relevant use of a law of the wall. The order of magnitude of the y^+ value in M1 is around 500 thus no accurate near-wall flow physics are expected in this case. For the most refined mesh, a particular effort has been conducted to properly resolve the gaps at the tip of the rotor blades, with 20 layers of cells (see Tab. 3.2) and to accurately resolve the flow in these regions as it drives the performances and the stability of the whole compressor [99].

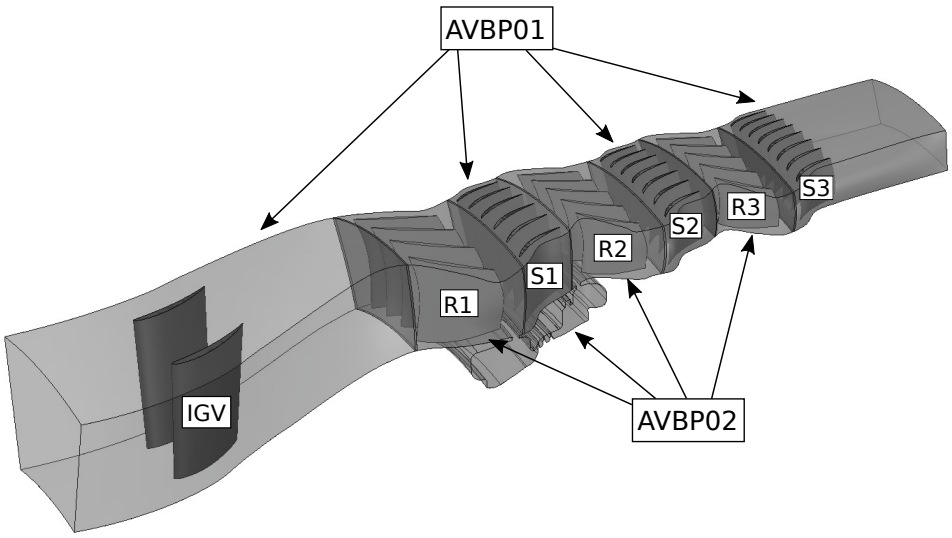

Figure 3.13: Computational domain of the axial compressor CREATE.

Grids	M1	M2	M3
Nb. cells stator ($\times 10^6$)	57	124	523
Nb. cells rotor ($\times 10^6$)	31	70	509
Nb. prisms layers on blades	0	3	10
Nb. cells layers in rotor tip gaps	3	6	20
Time step (s)	4×10^{-8}	2×10^{-8}	5.4×10^{-9}
CPU cost per revolution (kh)	17	165	2020

Table 3.2: Main properties of the 3 grids used for the multi-stage CREATE configuration. CPU costs obtained on Intel Xeon Haswell processors (2.6 GHz).

[2]The CREATE simulation was the ultimate test of the CN2020 program which aimed at comparing solvers for LES of turbomachinery and included Cerfacs, CORIA, ONERA and Cenaero codes. TurboAVBP was the only one which passed this test with success, all other solvers failing to run or were unable to run long enough.

Figure 3.14 compares the entropy fields at mid-height of the duct for M2 and M3 grids. Entropy being an indicator of losses produced within the flow, it highlights the shear flows and the wakes. First the grid resolution effect is clearly seen, since the M2 grid predicts larger blades wakes than the M3 grid, with less turbulent structures. For the M3 grid, the first rotor wakes are thin and mostly result from the turbulent structures developing in the rear part of the blades suction sides. These wakes are then convected with the mean flow through the first stator passage, and are visible in all the vane channels. Downstream of mid-chord, these boundary layers present higher entropy values than on the first rotor, as the flow is detaching and contains large eddies. For second and third stator passages, complementary studies show that the transition of the suction side boundary layers is triggered by a laminar separation followed by a reattachment. The boundary layers and wakes are thinner on rotor blades 2 and 3.

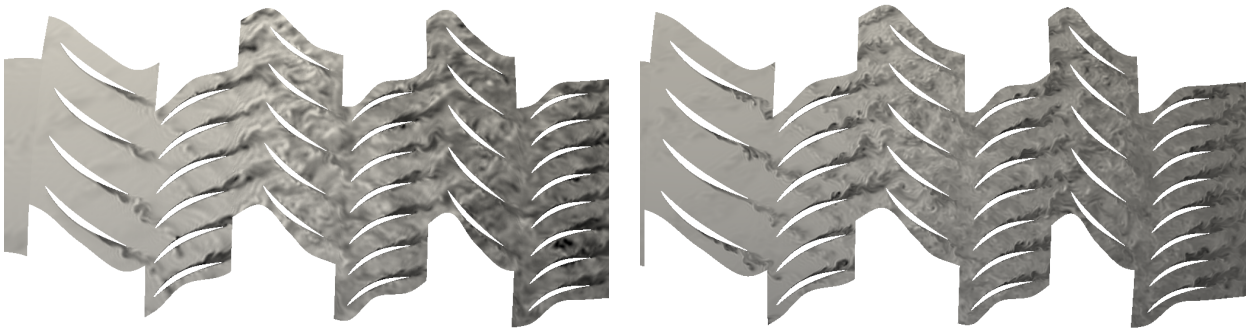

Grid M2 Grid M3

Figure 3.14: Instantaneous flow field colored by entropy at mid-height of the duct.

Figure 3.15 presents the instantaneous flow in the sections downstream rotor blade 1 and stator vane 1 (Fig. 3.13). For each sub-figure, the axial velocity is normalized by its average on the surface. Downstream of the first rotor, the wakes of the four blades are indicated by a deficit of axial velocity. They are rather thin compared to the main flow passage, and tend to enlarge from the hub to the casing. Whereas the grid M2 predicts a larger structure above mid-span, the grid M3 gives a turbulent wake all over the duct height. Close to the tip casing, the low momentum fluid zone resulting from the mixing of the casing boundary layer, the rotor wakes and the tip leakage vortex is clearly described by the M3 grid. The latter yields a better flow prediction in the tip region than M2 grid as discussed latter. Below the main duct passage, the region with a weak negative axial velocity corresponds to the cavity and to the slot through which the flow is re-injected upstream of S1. Downstream of stator vane 1, the comparison again highlights the improved resolution of the 6 vane wakes with the M3 grid. As no clearance exists between the vane tip and the casing, the flow in the vane channels is rather homogeneous along the whole span. The section downstream the first stator row again passing through the cavity, the flow entering the slot and going in the upstream direction is visible.

Figure 3.16 presents the performance curve of CREATE at nominal speed in terms of total pressure ratio as a function of mass flow rate. The values are normalized by the experimental quantities at the nominal point, denoted A in the figure. LES results, represented with circles for M1, squares for M2 and triangle for M3, are post-processed consistently with measured data. As the computational cost for simulations on M1 and M2 grids is affordable, several operating conditions have been simulated. These points in Fig. 3.16 are obtained by varying the pressure imposed at the outlet. Shapes and levels of both M1 and M2 curves are rather close to the experimental iso-speed line up to a normalized mass flow of 0.96. Further reducing mass flow rate shows that M2 better predicts the measured operating points than M1, including the last stable point denoted C. The grid refinement effort from M1 to M2 mainly concerns near-wall regions of blades and tip clearances of rotors. An improved prediction of the flow dynamics and losses is thus expected in these zones that are critical for global performance prediction. The lowest mass flow rate operating point for M1 has been obtained for a variation of 3.2% of back pressure relatively to nominal conditions. It has furthermore been verified that an increase of

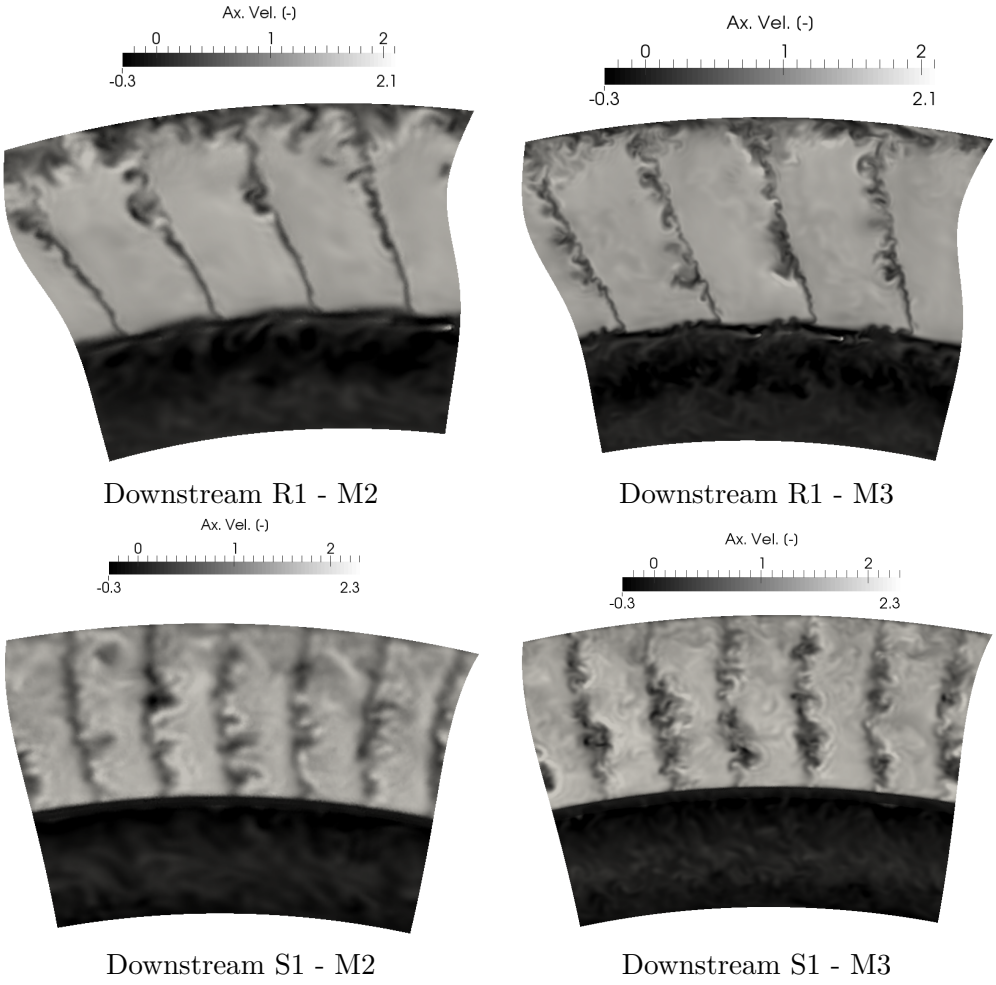

Figure 3.15: Instantaneous normalized axial velocity at constant axial sections inside the duct. S1: stator 1, R1: rotor 1.

0.3% of back pressure from this M1 last point leads to mass flow reversal and to surge. For M2 grid, the lowest mass flow rate conditions correspond to a variation of 5.3% of outlet pressure with respect to nominal conditions. The grid refinement is thus crucial to get stable operating conditions at lower mass flow rates, approaching the experimental stability limit. Only one operating point has been simulated with the M3 grid. The resulting mass flow rate is around 4% higher than for M1 and M2 at this pressure ratio value. This slight gap is caused by the mass flow rate convergence, not yet strictly reached. Experimental point B in Fig. 3.16 corresponds to operating conditions for which the database used in this study is available. In the following, only the three simulations circled in the figure will be compared to measurements as they correspond to an operating point close to the nominal regime of the compressor.

Figure 3.17 shows the time and azimuthally averaged radial distributions of total pressure and total temperature, downstream of rotor 1 (R1) and downstream of rotor 2 (R2). All values are normalized by the radially averaged experimental data at each section. At the outlet of R1, the maximal difference between the measured and predicted total pressure is 3% and 5% for M1 and M2, whereas it is less than 2% for M3. Moreover only the latter gives the correct shape of the profile, especially in the upper part of the duct. Concerning the total temperature, the differences between experimental and numerical data are relatively small (max. 2%), but only M3 is able to yield less than 1% of error. More specifically, Fig. 3.17 shows that mesh refinement is necessary to avoid the over-prediction of total temperature close to the casing seen in M1 and M2. At the outlet of R2, M3 predicts a total pressure profile shape close to experimental data, especially regarding the variation of total pressure in the last 20% of duct height caused by the tip leakage vortex. In terms of total temperature, M2 and M3 show similar

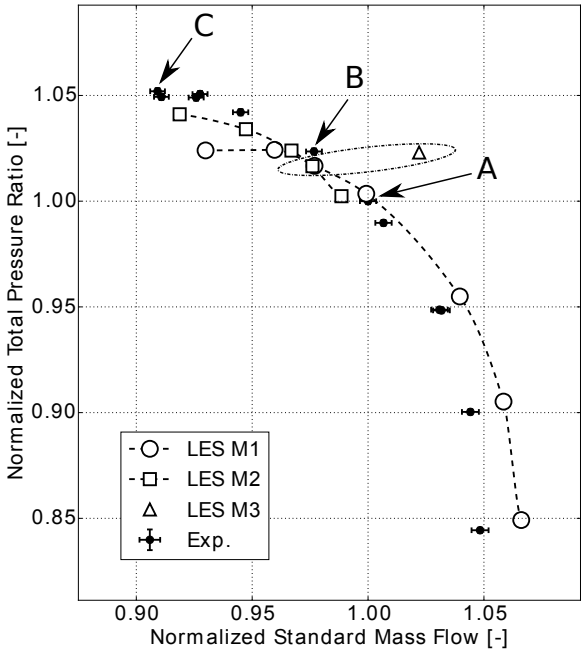

Figure 3.16: Aerodynamic performance curve of CREATE. Comparison of LES predictions with experimental data [198].

results, except that the radial position of the minimal temperature is shifted for M3. Thus, contrary to the global performances plotted in Fig. 3.16, Fig. 3.17 clearly shows that the finest grid provides the most accurate results relatively to the two coarser grids. It is particularly highlighted that a sufficient mesh density is needed in the tip region to capture the averaged pressure and temperature profiles. This is consistent with the results reported on the MT1 transonic turbine stage [204]. Note that thermal transfers at the hub and tip casings should improve the prediction of temperature profiles close to these walls.

Beyond the feasibility demonstration of wall-modeled LES of multistage compressors, this study indicates the required grid refinement according to the expected fidelity of the results. An intermediate grid indeed allows correctly reaching the performance curve at low mass flow rate as well as main flow features such as wakes and losses within the main passage of the duct. For a precise description in the rotor tip region, a grid refinement similar to M3 with 20 layers of cells appears necessary (Fig. 3.18). This allows capturing the complex flow structures developing in these regions. It then gives access to a large flow database that can be exploited for improving understanding of physical phenomena. In the future, in collaboration with Safran, these LES will be compared with state-of-the-art RANS and URANS data, to provide recommendations on the use of wall-modeled LES for compressor design.

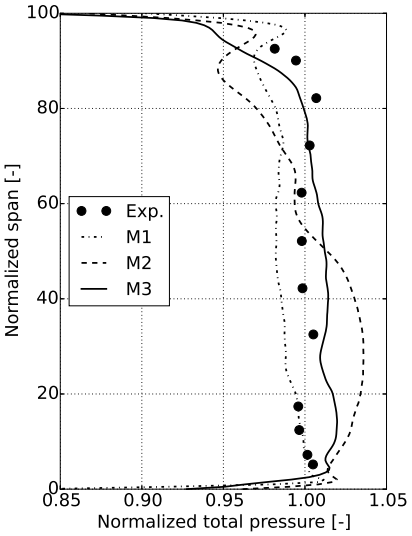

Total pressure, downstream R1

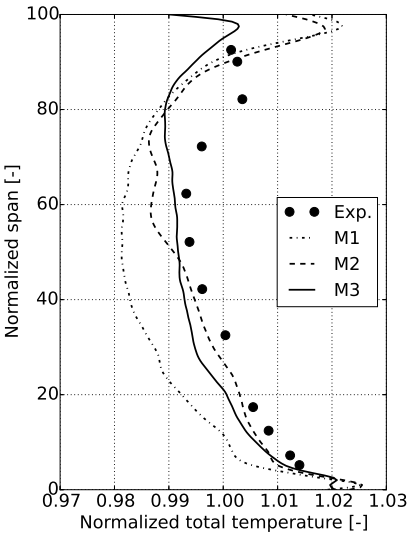

Total temperature, downstream R1

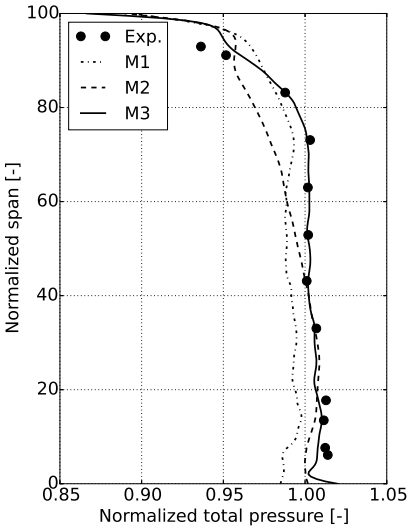

Total pressure, downstream R2

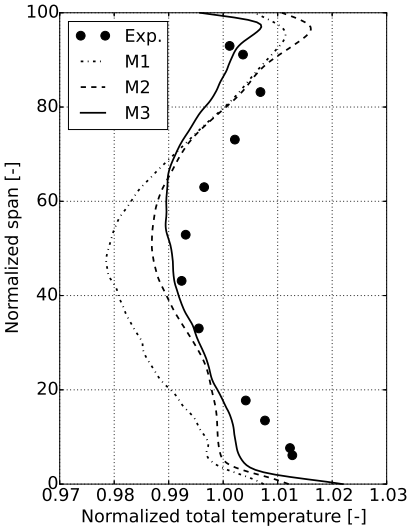

Total temperature, downstream R2

Figure 3.17: Radial distribution of time and azimuthally averaged quantities downstream rotors 1 (R1) and 2 (R2).

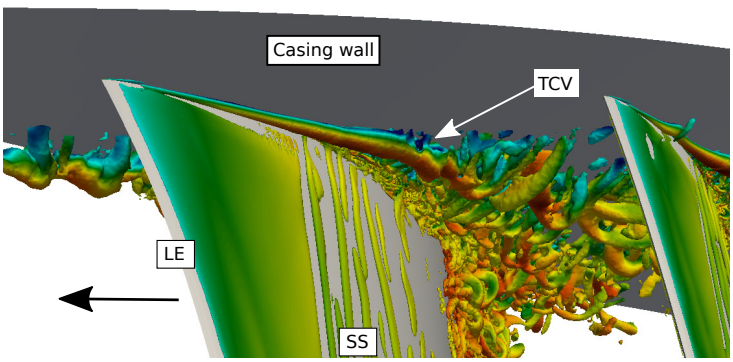

Figure 3.18: Instantaneous Q-criterion iso-surface colored by Mach number within a blade passage of rotor 1, close to the tip casing, obtained in grid M3. Black arrows indicate the rotational direction. LE: Leading Edge, SS: Suction Side and TCV: Tip Clearance Vortex

3.3 Large Eddy Simulations of integrated combustion chamber and turbine

Since the 80s, turbine designers have investigated the influence of the combustor exit flow on the turbine [61, 218], as high and non-uniform turbulence levels, length-scales, residual swirl as well as temperature heterogeneities may significantly impact the turbine life [119]. All these experimental and numerical findings were obtained relying on the assumption that the performance of the combustor and turbine modules is identical in their assembled and dis-assembled versions. This modular approach allows to design chamber and turbine almost independently. Experiments are usually obtained with non engine-representative combustor simulators, while Computational Fluid Dynamics (CFD) in the turbine is almost always performed using time and spatially-averaged profiles imposed at the combustor-turbine interface [77]. When it comes to analyzing the flow in the turbine, one possibly suffers from the intrinsic assumptions of having a combustor-turbine interface. From a numerical point of view, a possible solution to tackle such organization induced limitations is to go to an integrated simulation where the chamber and the turbine are computed as one single element, removing the interface plane.

Performing CFD of this entire device is however challenging because of the very different natures of the flow field in the combustor (high swirl, combustion process, turbulence, low-Mach flow) and in the turbine (highly compressible and sensitive to the boundary layer flow). Several tentatives have been made by coupling either RANS (Reynolds Averaged Navier Stokes) or LES (Large-Eddy Simulation) solvers for the combustion chamber and Unsteady-RANS for the turbine [232, 229, 118, 120]. Nonetheless, these approaches lead to strong hypotheses on the data transferred from one code to the other, implying approximations on the mass flow rate, total energy and turbulent quantities. Using a compressible LES solver to resolve the full system constitutes a high potential solution as such an approach is now recognized to deal well with the highly unsteady turbulent flow in the chamber [92, 187], while allowing to compute the wall-bounded high velocity flow within the turbine stages [260, 204]. In collaboration with Safran Helicopter Engine, we have simulated the combustor-turbine interactions by performing wall-modeled LES of an axial combustor fitted with a turbine stage. This work have been recently published in Computers and Fluids [69]. Although not accurate enough to reproduce specific wall features such as separation and transition, wall-modeled LES is used with the goal to capture macro phenomenon at a reduced cost as compared to wall-resolved simulations. One focuses here on the special case of Lean Burn combustors that produce higher levels of swirl, turbulence and more marked hot streaks as compared to the previous combustor generation. Considering this new context, the non-reactive axial combustor simulator together with a 1.5 high pressure turbine stage developed within the European project FACTOR (Full Aerothermal Combustor-Turbine interactiOns Research) serves as basis of this study. FACTOR is not a true combustion chamber / turbine experiment because the combustion in the chamber is mimicked by injecting non reacting hot gases into a chamber cooled by multiperforated plates. It is however an excellent prototype to validate integrated simulation methods. Three sets of simulations were compared to investigate the interactions of chamber and turbine stages (Fig. 3.19):

- Case A: the full geometry which involves the chamber and the turbine stage,
- Case B: the turbine stage starting at plane 40, the combustor/turbine interface with a 2D mean inlet boundary condition extracted from case A,
- Cases B_1, B_2 and B_3: the turbine stage starting at plane 40 with a 2D mean inlet boundary condition extracted from case A with three different turbulence injections.

As free stream turbulence has a strong impact on the flow field development in both turbine and compressors, inlet turbulence injection is an active topic for LES of turbomachinery components. Several recent works report effects of inlet turbulence on losses in compressor cascades [238], as well as low pressure turbine cascades [127, 184, 43, 44] and high pressure turbine cascades [39, 139, 274, 125, 207, 239] where wall-resolved LES are affordable. Among these studies, Jacobi *et*

al. [120] investigate unsteady flow phenomena caused by a combustor flow with swirl on a high pressure vane with LES. Results highlight that unsteady features emanating from the combustor influence the unsteady flow structures developing in the vane leading to non negligible differences in the flow topologies when compare to a RANS prediction of the vane with mean quantities extracted from the combustor exit. Probably due to high computational costs, from the author knowledge no study exists on the analysis of turbulence injection on a high pressure turbine stage.

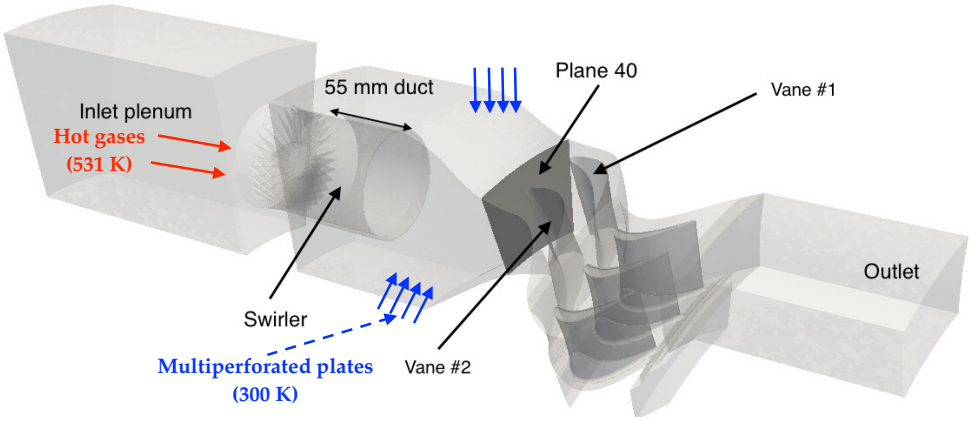

Figure 3.19: Numerical domain of the integrated chamber and turbine stage simulation.

The numerical domain comprises a single periodic sector of the FACTOR test section (18°), featuring a CFD-friendly count of one combustor simulator for two vanes and three rotor blades (Fig. 3.19). The flow within the combustor simulator is representative of a lean burn chamber, with 65% of air mass flow in the mainstream and 35% used for effusion cooling. After crossing an inlet plenum, the hot air stream (531 K) goes through an axial swirler followed by a duct to confine and preserve the hot spot as intense as possible in the chamber. The Reynolds number of the swirler is about 111.000 with a Mach number of about 0.112. Cooling at 300 K is only provided by effusion systems, which are located on the inner and outer liners of the combustor simulator. The exit of the chamber (plane 40) has been largely investigated experimentally and numerically [10, 146, 7, 147]. Such comparisons highlighted the good predictions of LES in the combustor simulator and are thus not further detailed here. The mean Mach number in the combustor exit plane is about 0.14 while the temperature distortion is contained within +10% and −30% of the mean value, which is representative of typical aero-engines [145, 218]. The vanes are specifically positioned so that the hot streak exiting the swirler impacts the leading edge of vane # 1 (Fig. 3.19). Because of the count ratio between the vanes and the swirler, one vane over two is impacted by a hot streak. The vane inlet Reynolds number based on the vane axial chord and inlet velocity is about 106.000 while the outlet vane Reynolds number is about 424.000 for a Mach number of 0.96. The geometry of the rotor blades contains the upstream and downstream cavities around the blade's hub where cold air at 300 K is injected. Note that the tip of the rotor blade includes a squealer. The absolute and relative rotor blade exit Reynolds number based on the axial blade chord and exit velocity are 247.000 and 135.000 respectively. Corresponding Mach number are 0.8 and 0.44 respectively. No experimental data is available to validate now the flow predictions in the turbine stage, making the study purely numerical.

Numerical integration is performed using a two-step Taylor Galerkin numerical scheme TTG4A [60]. The Smagorinsky model [248] is used to account for the sub-grid scale contribution. The mesh is a 3D hybrid grid to handle the turbulent flow field in the chamber and turbine stage as well as the rotor/stator interface while satisfying LES requirements. Mesh dependency on the chamber has been performed in a previous study [146]. State-of-the-art methodologies are used for the turbine stage mesh [273, 204]: prisms are used on the stator and rotor blades to ensure reasonable wall resolution while tetrahedra are used in the domain. First nodes off the

blade walls are placed in the logarithmic region of the turbulent boundary layer to allow proper use of a wall function with prisms having a low aspect ratio: *i.e.* $\Delta x^+ \approx \Delta z^+ \approx 5\Delta y^+$. Finally and to maintain an acceptable time-step, the rotor blade tip region is meshed with 10 cell layers. The wall friction Reynolds number y^+ associated with the mesh on the vane and rotor blade walls remains below 30. With this mesh and a law of the wall treatment, a fine resolution of boundary layer state is out of reach. However, the target of the simulations is to capture first order effects of inlet conditions on the flow field and to clarify them. The final mesh of case A is composed of 32, 42 and 44 million cells for the the chamber, stator vanes and rotor blades, respectively. Case B is composed of the domains of the stator vanes and rotor blades only.

The inlet and outlet boundary conditions follow the Navier-Stokes Characteristic Boundary Condition (NSCBC) formulation [211]. A mass flux is imposed at the inlets of case A while a 2D map of total pressure, total temperature and velocity angle extracted from simulation A is imposed at the inlet of case B. In a first part, no turbulent fluctuation is imposed at the inlet of case B. Then, a parametric study on the turbulent fluctuations injected at the stage inlet is performed. The method used to inject turbulence is the synthetic approach proposed by Guezennec *et al.* [103]. The parametric study is based on the variation of the integral length-scale Le and turbulent intensity Tu based on estimations performed on simulations A. The base configuration B_1 consists in imposing at the turbine inlet the mean quantities measured on plane 40 on case A ($\overline{Tu_{40}}$, $\overline{Le_{40}}$). Cases B_2 and B_3 aim at evaluating the flow sensitivity to turbulence intensity and length-scale respectively in the limits observed in plane 40, *i.e.* ($2\overline{Tu_{40}}$, $\overline{Le_{40}}$) for case B_2 and ($\overline{Tu_{40}}$, $2\overline{Le_{40}}$) for case B_3. Static pressure is imposed at the outlet of both configurations, where the NSCBC treatment naturally allows the radial equilibrium to establish as shown in the PhD Thesis of Charlie Koupper and published in AIAA Journal [148]. All walls are considered adiabatic and treated with a wall-law [235]. Regarding the effusion cooling systems, an adiabatic homogeneous injection model [178] is used to account for the momentum injection. The rotational speed of the rotor blades is imposed at 8 500 turns per minute.

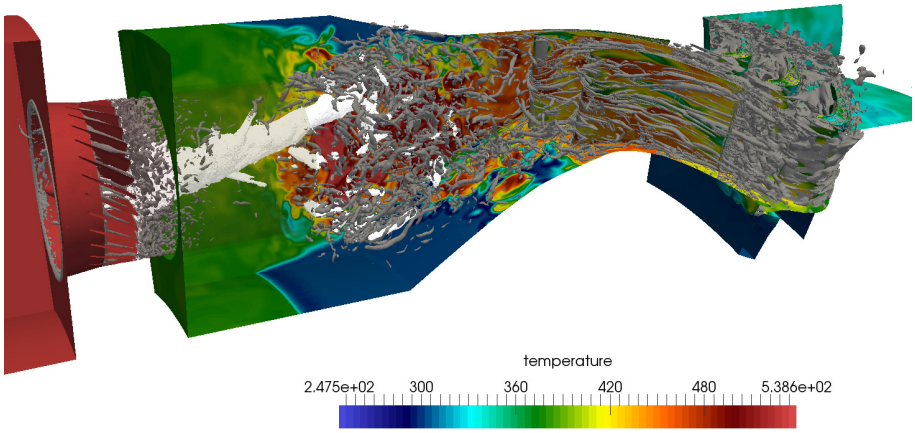

Figure 3.20: Instantaneous view of the turbulent activity in simulation A: precessing vortex core in white (iso-surface of low pressure), turbulent eddies in grey (iso-surface of Q-criterion) and temperature field on walls and periodicity.

To illustrate the organisation of coherent deterministic flow structures and turbulence in the configuration, Fig. 3.20 presents an instantaneous view of results obtained with case A. An iso-surface of low pressure allows to identify a precessing vortex core (PVC) which originates close to the swirler and breaks down shortly after leaving the duct. The PVC rotates at a frequency of about 510 Hz. The same frequency is found at the combustor chamber / turbine interface with dynamic mode decomposition of the pressure field indicating the impact of the

PVC at the turbine stage inlet [254]. Figure 3.20 also highlights turbulent structures thanks to an iso-surface of Q-criterion. Coherent structures are generated by the swirler as well as in the region of the PVC break down. These eddies are then convected in the vane passages where they are elongated due to the flow acceleration. Then, the interaction with the rotor blades leads to complex flow structures.

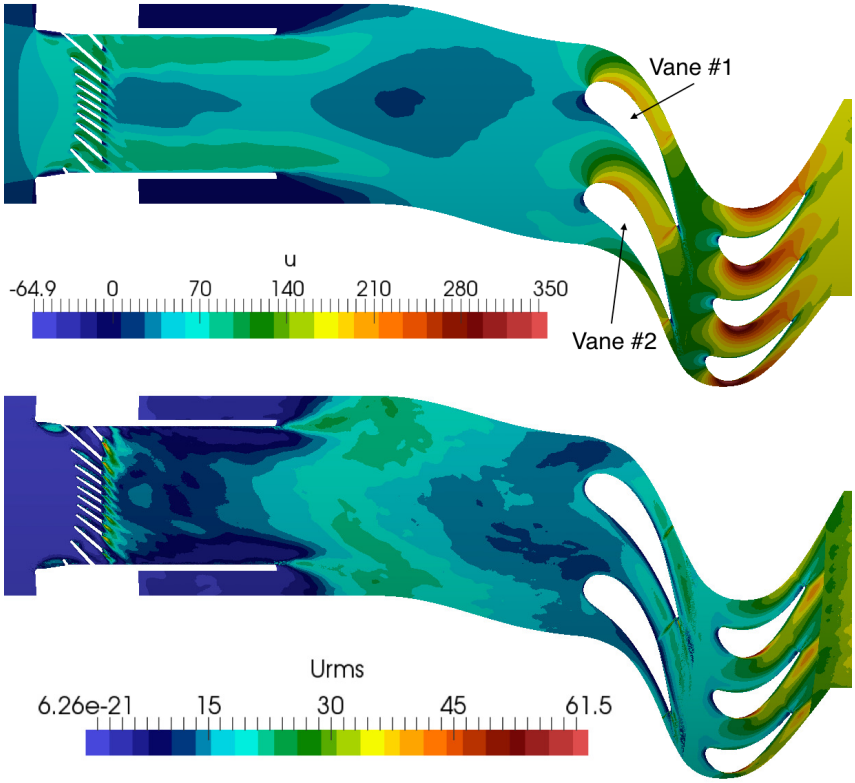

Figure 3.21: Time-averaged axial velocity [m/s] field (top) and associated RMS fields [m/s] (bottom) in case A on a cut at the vane leading edge midspan position.

Figure 3.21 and 3.22 present the mean flow features in the integrated simulation A in terms of axial velocity and temperature, respectively. The hot flow from the plenum enters the chamber though the swirler resulting in an important rotating stream (Fig. 3.21). Confined by the duct at the chamber inlet, the flow topology is characteristic of swirling flows with a sudden expansion of the jet and a large central recirculation zone. Due to the confinement duct, the recirculation zone extends over a long distance in the chamber. The velocity field at the turbine stage inlet is not homogeneous and characteristic of a lean burn combustor with an important swirl motion [146, 147]. The flow then accelerates as it enters the turbine stage and expands. As reported in the literature [106], accelerations are more important on both the vanes and rotor blades suction sides than on the pressure sides. The row of vanes is transonic with a weak shock located near the trailing edge of the stator suction side. The main aerodynamics flow features in the stator vanes seem to be independent of the position with respect to the swirler. On the other hand, aerodynamics are similar in all the rotor blades. In terms of unsteady motions, the wakes of swirler blades induce turbulence which remains local due to the confinement effets of the duct and the recirculation zone (Fig. 3.21). The important sources of unsteadiness in the chamber are thus the shear layer induced by the end of the duct lip as well as the surrounding shear layer of the recirculation zone. On plane 40, the RMS profiles are heterogeneous with an average turbulence intensity of about 28% [146]. Turbulence is then convected in the turbine stage where it interacts with secondary flows in both stator and rotor rows. Small differences in the RMS are observed from one stator vane to the other while the flow fields in all rotor blades remain identical.

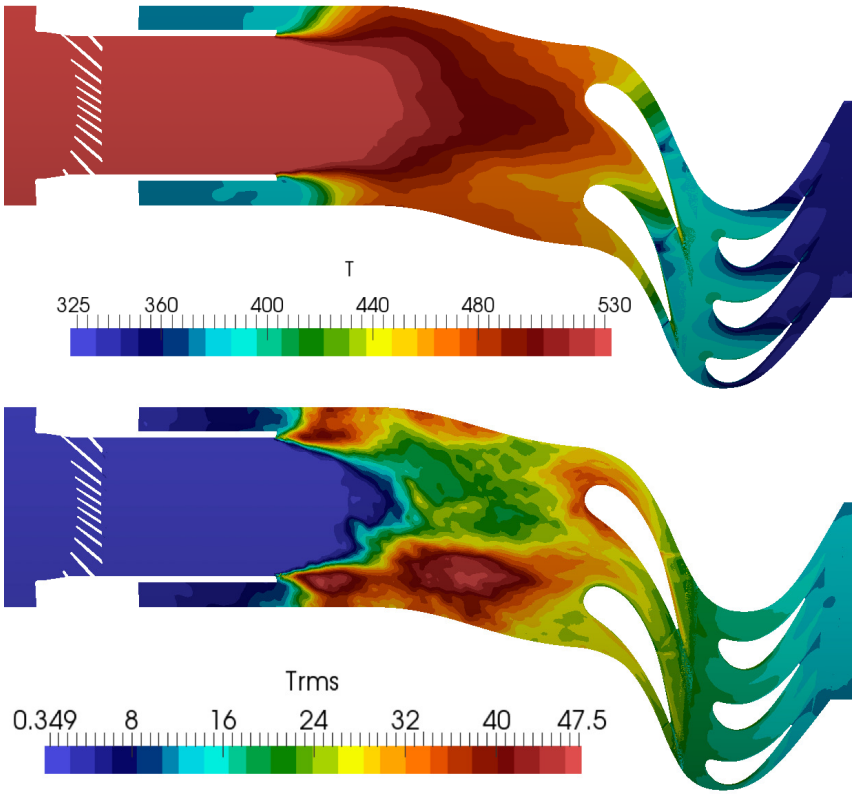

Figure 3.22: Time-averaged temperature field [K] (top) and associated RMS fields [K] (bottom) in case A on a cut at the vane leading edge midspan position.

In terms of temperature distribution, Fig. 3.22 illustrates the mixing between the hot stream from the swirler with the colder flow injected in multi-perforated plates. The aerodynamics in the chamber leads to a hot spot at the turbine inlet representative of a lean burn combustor [145]. The hot spot is centered on vane #1 leading edge. It directly hits the vane leading edge, wraps around it and remains in contact with its surface. The impact of the hot streak on the vane in conjunction with the flow acceleration seems to promote mixing as the temperature decreases almost homogeneously through the row of blades [144]. Due to rotation, the rotor blades are exposed to an azimuthally homogeneous temperature field. Linked to the acceleration in the rotor passages, the temperature decreases from the inlet to the outlet. Fluctuations of temperature in the chamber are mainly located in the shear layers of the duct lip and recirculation zones identified previously. At the turbine stage inlet, the profile of temperature fluctuations is highly heterogeneous leading to non uniform distributions in the stator. On the contrary, due to the rotation effect, the azimuthal distribution of temperature fluctuations remains rather constant at the rotor passages inlet at the given radius of the surface cut.

The temporal mean total pressure, total temperature and velocity angles on plane 40 from this integrated chamber and turbine simulation (case A) have been extracted and imposed as 2D maps inlet conditions for the turbine stage simulation (case B). It has been checked that the pressure ratio between inlet and outlet in both configurations remains the same meaning that the same operating point is computed. Comparisons between the integrated computation (case A) and the simulation of a stage alone (case B) without turbulence injection provide similarities as well as important differences. Both simulations give similar predictions in the global aerodynamics of both the stator vanes (Fig. 3.23) and the rotor passages (Fig. 3.24) in terms of flow expansion and secondary flows. As expected, the main differences seem to be attributed to the unsteady flow features such as deterministic eddies and turbulence coming from the chamber in case A that are not injected in the stage alone simulation B. They concern first the turbulent activities in the stator. The aerodynamic fluctuations in the rotor passages are

mainly driven by secondary flows and few differences are observed. On the other hand, important differences are seen in the range of temperatures in both stator vanes and rotor passages: with turbulent fluctuations at the inlet of the turbine stage, case A shows more mixing and thus less segregation of temperature. Contrarily, since the inlet condition is steady in case B, more coherent patterns are predicted with a higher range of temperatures (both lower and higher).

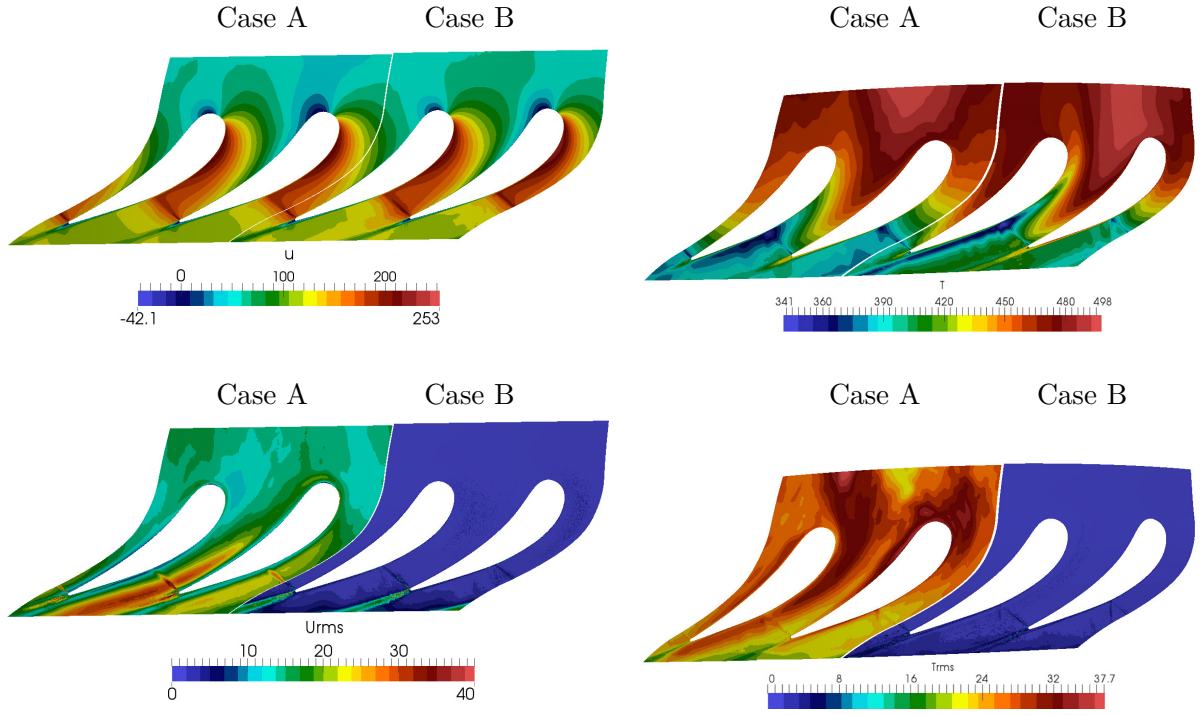

Figure 3.23: Time-averaged axial velocity [m/s] and temperature [K] (top) as well as associated fluctuations [m/s] (bottom) at mid-span of the stators for cases A and B.

The different migrations of the hot spot and coolant flow from case A and B significantly impact the adiabatic wall temperature of the vanes (Fig. 3.25). The hot streak is more spread in simulation A and its impact with vane # 1 leads to a larger hot region which is more mixed and thus colder and less coherent than in case B. Mixing is faster in simulation A than in simulation B, leading to different segregation patterns of wall temperature.

Concerning adiabatic rotor wall temperature, simulations A and B show similar behaviors (Fig. 3.26). The hot spot impinges the blades at mid radius and spreads on almost the whole radial extend on the pressure side of both cases. Due to secondary flows (tip, induced and passage vortices) the hot spot signature on the suction side is restricted to a narrow region centered at about 60% of the radius. As far as RMS temperature are concerned, both simulations show high levels near the tip due to the incoming temperature heterogeneities as well as in the region of secondary flows near the casing (tip and induced vortices) and hub (passage vortices). This illustrates how secondary vortices participate in the mixing of the hot streak with colder streams (at the casing with fresh air from the chamber and at the hub with fresh air from the cavities) and generate important temperature fluctuations in the shear layers. Then, concerning differences, RMS temperature variations are stronger in case B than in case A (Fig. 3.26). Moreover, the hot streak seems to be located at lower radii in case A than in case B. Finally, the temperature fluctuations are more important and more spread in case A illustrating a more turbulent simulation (Fig. 3.26).

To assess the role of inlet conditions, three simulations with synthetic turbulence injections were performed with different parameters: spatial mean turbulent intensity and length scale obtained from case A (case B_1), extreme turbulent intensity and spatial mean length scale obtained from case A (case B_2), spatial mean turbulent intensity and extreme length scale obtained from case A (case B_3). Although some improvements are observed, none of the conditions used allows

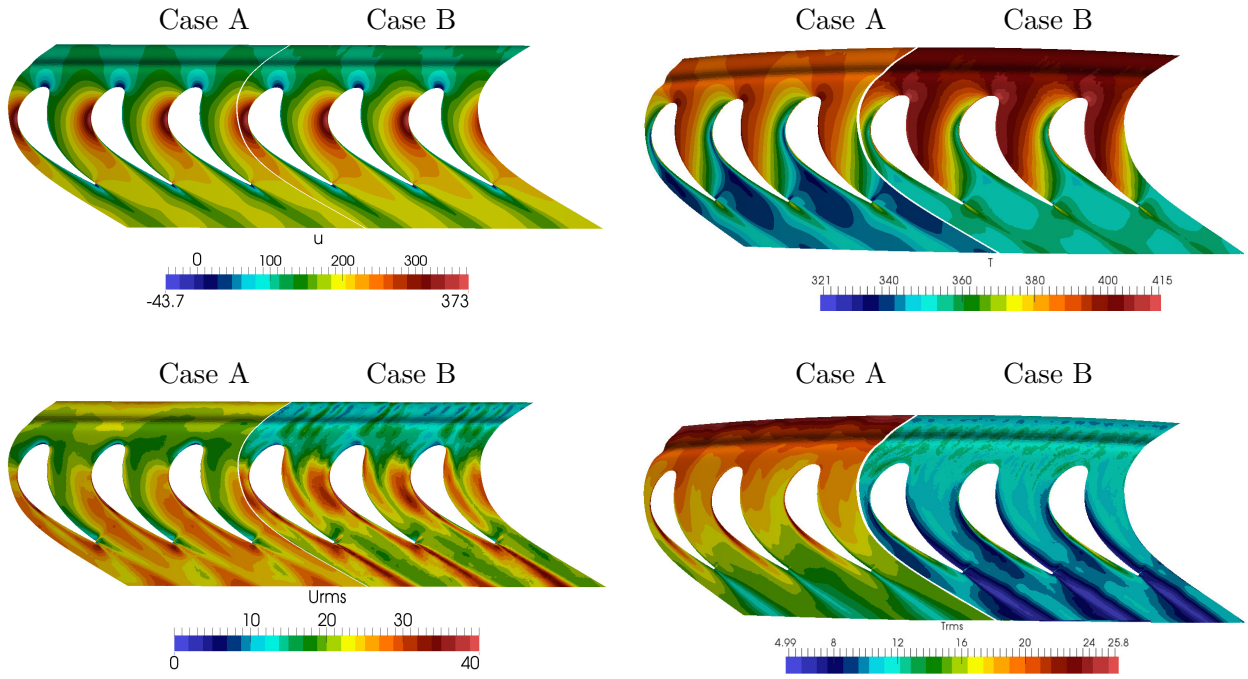

Figure 3.24: Time-averaged axial velocity [m/s] and temperature [K] (top) as well as associated fluctuations [m/s] (bottom) at mid-span of the rotor passages for cases A and B.

to recover the turbulent activity in the stator passages as well as the temperature fluctuations of the integrated simulation (Figs. 3.27 and 3.28). The simulations of case B with turbulence injected at the inlet show that the mean aerodynamics is almost insensitive to the incoming velocity fluctuations in the range of operation tested. The turbulence injection model is not able to reproduce the temperature fluctuations observed at the inlet of the stage from case A. Indeed, as no temperature fluctuation is prescribed at the inlet boundary condition, the RMS of temperature naturally develops from the mixing of hot and cold regions induced by the turbulence. Small levels of the order of 4-7 K at the inlet and 3-5 K at the stator leading edges are obtained as compared to 40 K at the inlet and 30 K at the stator leading edges in case A. As compared to case B, injecting turbulence leads to an enhanced mixing on the suction side of vane #2. This mixing is increased from case B_1 to B_3, with increasing levels of temperature RMS (Fig. 3.28). Nevertheless, the temperature fluctuations are less pronounced than in case A where incoming fluctuations play a key role in the distribution and levels of RMS.

None of the conditions tested for inlets in case B allows to recover the turbulent activity in the stator passages as well as the temperature fluctuations. Two explanations are possible and constitute paths of studies for the future. The first one concerns the turbulence spectrum generated by the combustor simulator which is neither isotropic not spatially homogeneous at the combustor exit. Preliminary studies have been performed to compute maps of timescales on plane 40 based on the axial velocity [146]. These timescales have been used here in the present study to inject isotropic turbulence. Turbulence anisotropy as well as impact of deterministic coherent eddies such as PVC must be quantified and the effect of the spatial heterogeneity of the turbulence intensity, integral length-scale and anisotropy on the stage flow field development has to be also investigated. The second path of study consists in the analysis of the temperature fluctuations on plane 40. As shown with simulation A, plane 40 is subject to strong temperature fluctuations. Moreover, Koupper *et al.* [147] have shown that for the present configuration, the temporal distributions of temperature are not Gaussian, with regions where the most probable temperature largely differs from the mean temperature. The analysis of higher order moments (skewness and kurtosis) explains such differences indicating strongly segregated regions of cold or hot fluid in the chamber. Additionally, in this context, it would be of interest to investigate the correlation between velocity and temperature fluctuations. Injecting such complex temperature

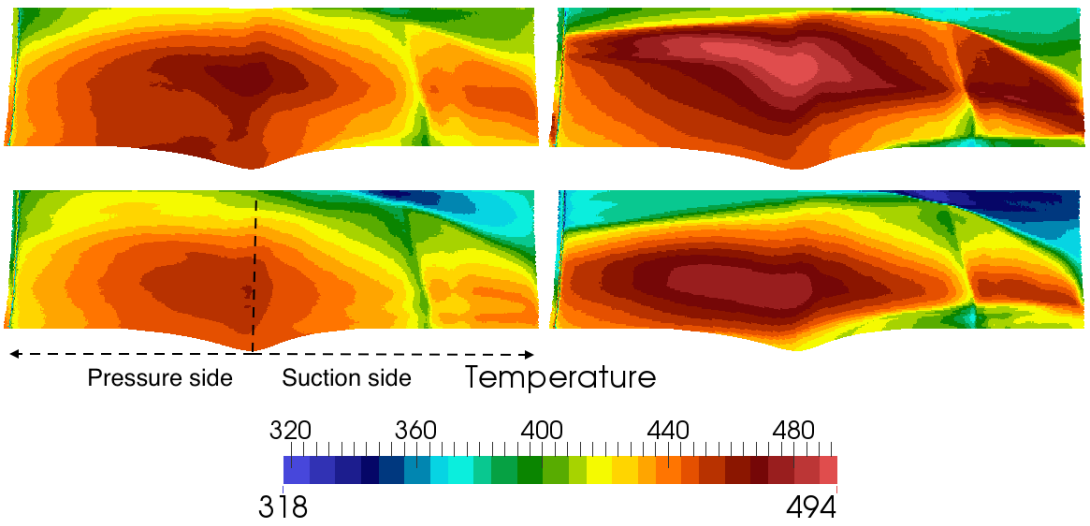

Figure 3.25: Adiabatic wall temperature [K] on vane #1 (Top) and 2 (bottom) for case A (left) and B (righ) .

distributions in a Large Eddy Simulation of a turbine stage is a theoretical challenge to work on.

On the long term, these results demonstrate the power of an integrated simulation such as case A: event if its cost s larger than stage only simulation (as case B), it totally suppresses the questions linked to the generation of the correct inlet boundary condition for the turbine simulation. This is obviously the path to go and this is what is done at Safran: Dr. Jérôme Dombard recently performed at Cerfacs such an integrated simulation on an industrial configuration for Safran Aircraft Engine. Beyond the demonstration of the tool capacity to deal with a highly complex industrial geometry, very useful (confidential) information has been extracted from these simulations.

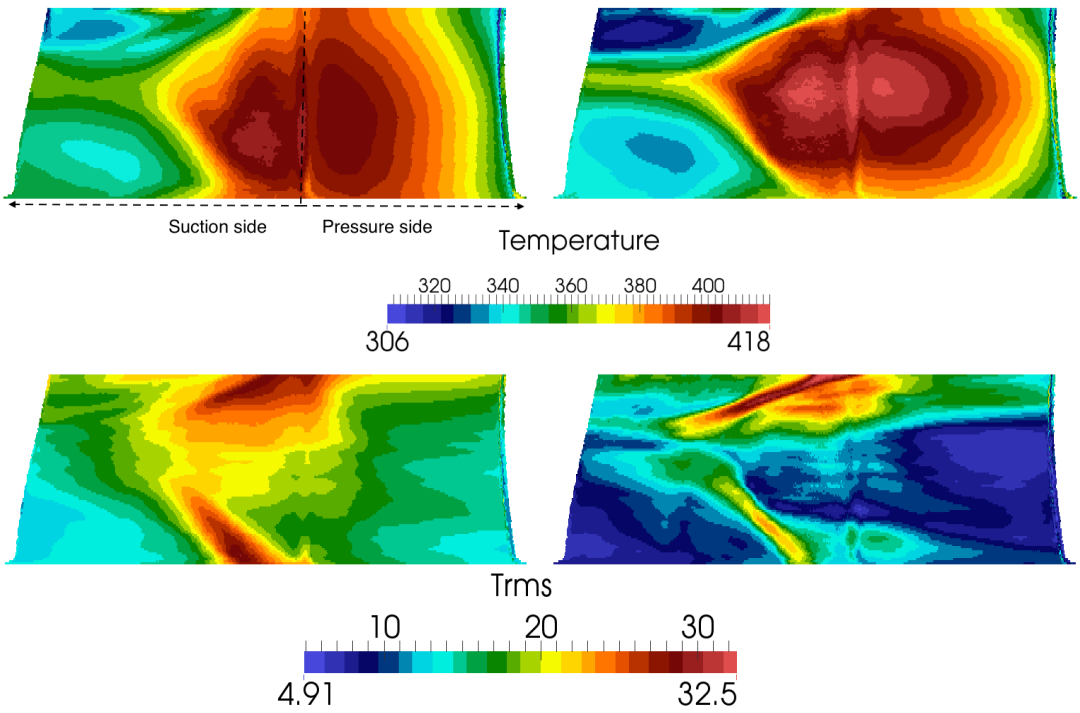

Figure 3.26: Adiabatic wall temperature [K] in the rotor blade wall (Top) and associated RMS fields (bottom) for cases A (left) and B (righ).

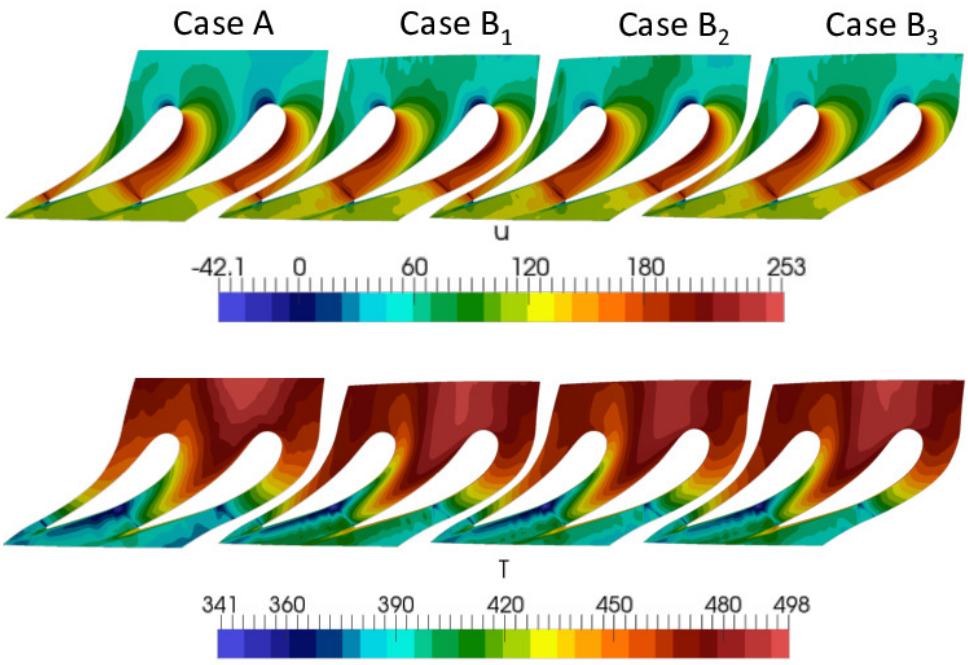

Figure 3.27: Time-averaged axial velocity [m/s] (top) and time-averaged temperature [K] (bottom) at mid-span of the stators for Cases A, B_1, B_2 and B_3.

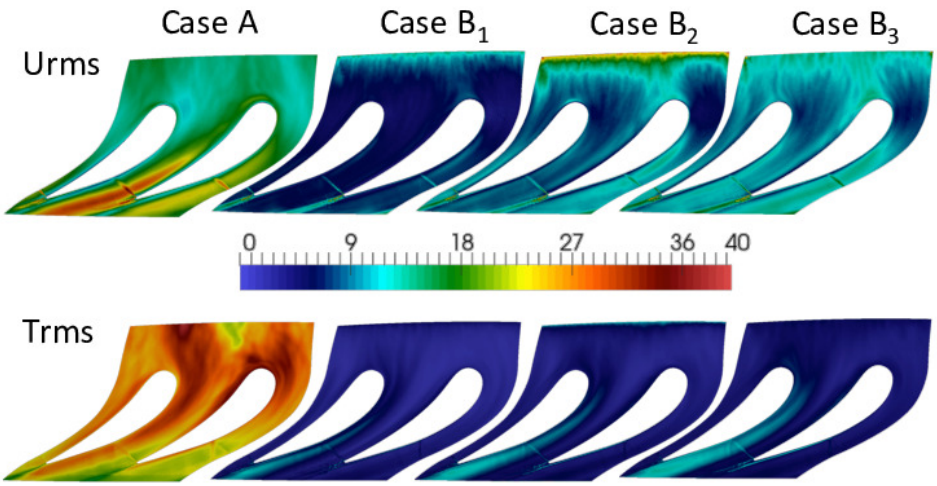

Figure 3.28: RMS of axial velocity [m/s] (top) and temperature [K] (bottom) at mid-span of the stators for Cases A, B_1, B_2 and B_3.

3.4 Collateral actions

The first stable version of TurboAVBP was able to simulate a turbine stage during spring 2012. The interest for the method to couple different instances of AVBP has rapidly disseminated in the lab as well as in other institutions such as IMFT. As a result, two challenging applications started to use the tool: (1) the prediction of chemistry in the wake of a solid rocket booster jet and (2) the simulation of turbulent flows in fan-stirred closed vessels. These two *heroic* (reviewer terminology) cases are briefly introduced along with a third one dealing with the analysis of a constant volume combustion chamber. I have assisted the PhD students who performed these three simulations for all questions linked to TurboAVBP (Adèle Poubeau and Laure Labarrère at Cerfacs and Adrien Bonhomme at IMFT).

3.4.1 Reduction of the CPU cost for the simulation of solid rocket booster jet on a long distance

To improve predictions of the impact of a solid-rocket booster on atmospheric ozone, a booster jet has to be accurately modeled on a long computational domain to initialize atmospheric models on larger scales. This study has been published in AIAA Journal [217]. Large Eddy Simulations of such a configuration are computationally very expensive. The objective of the the work of Adèle Poubeau at Cerfacs was to overcome this issue by applying and validating a new local-time-stepping method to LES of a solid rocket booster jet, in order to compute the flow through the nozzle down to 400 nozzle exit diameters downstream with a reduced computational cost (Fig. 3.29). In this application, the nozzle domain has a time step which is smaller than the atmosphere domain by an order of magnitude because the mesh must be refined in the nozzle to capture the transition of the jet. Thus, performing 10 iterations in the first domain while the second one performs only one iteration reduces the computational effort by reducing the number of operations done on the whole domain. This can be achieved

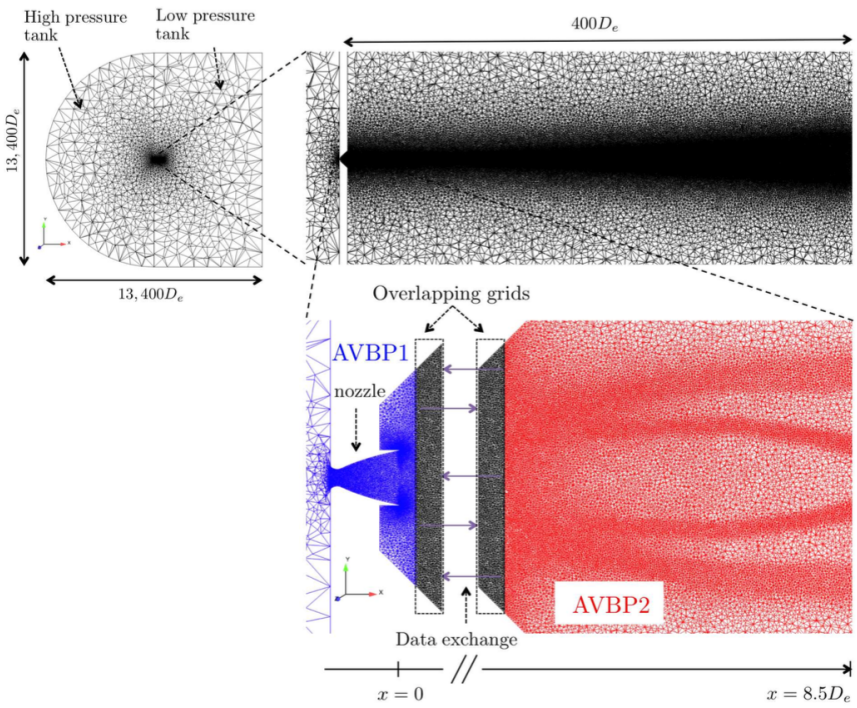

Figure 3.29: Cuts of the meshes (case B): full domain (top left), jet zone (top right), overlapping grids (bottom).

by using the MISCOG approach and splitting the domain in two parts: (1) the nozzle region

and (2) the wake region. MISCOG is used here on fixed meshes with very different time steps. Its application made it possible to reduce the computational cost by a factor of 5, and Adèle Poubeau shown that it did not introduce significant error in the vicinity of the coupling zone. To confirm the accuracy of the results, turbulence statistics including mean flow and Reynolds stresses were analyzed and compared to previous results in literature (Fig. 3.30). The analysis and validation of the dynamics properties of this simulation are a fundamental step towards the use of the MISCOG methodology for Large Eddy Simulation of a reactive solid booster jet. Then, knowing the composition of the jet and its dynamics and turbulence properties, it will be possible to carry out improved atmospheric simulations whose objective would be to obtain more precise evaluation of environmental impact of solid fuel stages in flight conditions [216].

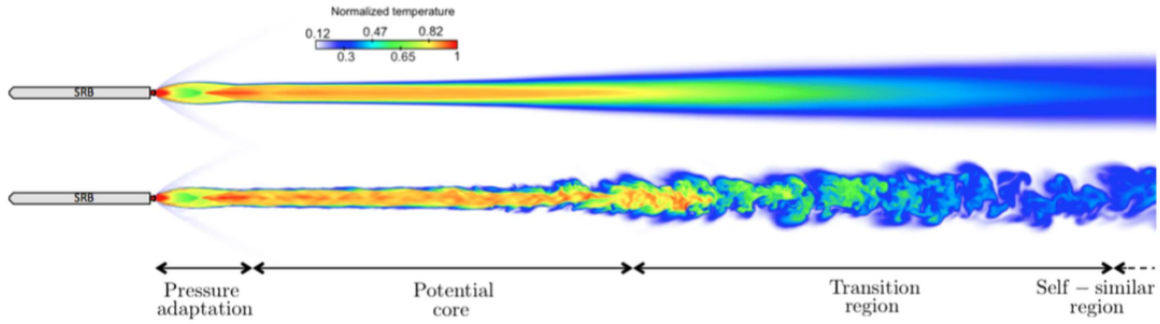

Figure 3.30: Cut of the jet up to $180D_e$ behind the nozzle showing instantaneous (bottom) and mean (top) normalized temperature.

3.4.2 Simulation of turbulent flows in fan-stirred closed vessels

The PhD study of Adrien Bonhomme at IMFT focused on the computation of a spherical vessel stirred by six fans [23]. This configuration corresponds to an experiment conducted at the PRISME laboratory in Orléans to study the propagation of turbulent premixed flames in homogeneous isotropic turbulence (Fig. 3.31). In this work, only the non-reacting flow were

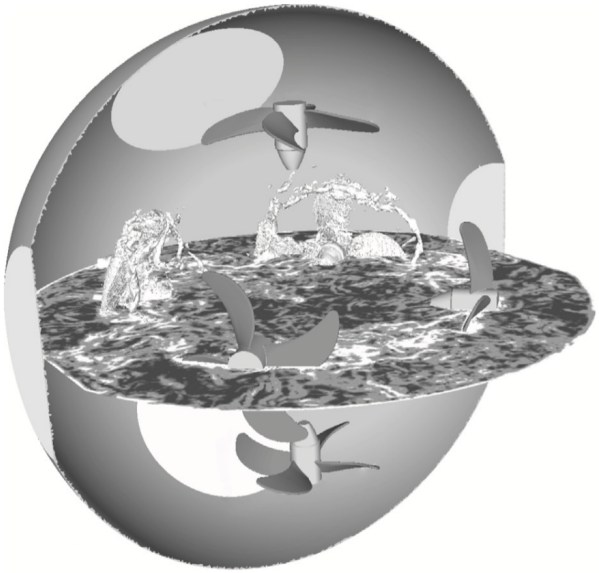

Figure 3.31: Sketch of the fan-stirred vessel.

studied, just before ignition. At this instant, the Reynolds number associated to the fans is

60,000 while the Reynolds number based on the integral length and RMS speed is of the order of 600 at the bomb center. The MISCOG methodology has been adapted here to handle six fans inside the vessel. The parallel efficiency of MISCOG applied to seven instances of AVBP (one for the bomb volume itself and six for the fans) has been discussed. Average and fluctuating fields match experimental data reasonably well. Finally the structure of the turbulence has been studied and it has been shown that turbulence is almost homogeneous and isotropic at the bomb center. The budget of mean turbulent kinetic energy were closed too and showed that turbulence is not convected from fans to the bomb center but diffused since the average velocities are near zero at this location. Interestingly, the trace of the blade passage frequency disappears near the bomb center. The setup of this heroic simulation has been facilitated by the use of TurboAVBP which also offers a high level of fidelity for the resolution of the flow around the fans. This work has been published in Computers and Fluids [23]. Other methods such as Immersed Boundaries (IB) were tested by Adrien Bonhomme and performed less well than the body-fitted method employed in MISCOG. Indeed, the mesh in the blade had to be very fine something difficult to ensure with an IB approach.

3.4.3 Simulation of a constant volume combustion chamber with rotating inlet and outlet valves

Based on the extension of MISCOG to treat more than one rotating body, a Constant Volume Combustion chamber where gases are injected with 2 rotating valves and exhausted through a second set of valves has been simulated during the PhD of Laure Labarrère [152] (Fig. 3.32). Like

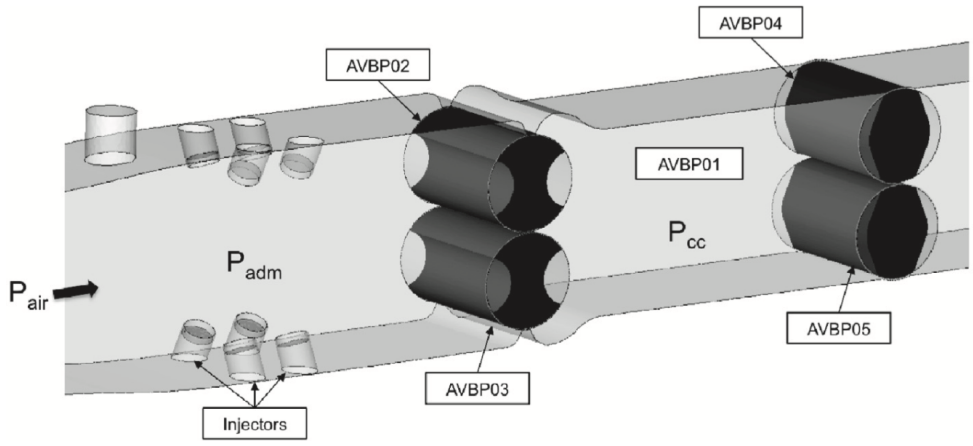

Figure 3.32: The MISCOG method for moving objects applied to a CVC chamber. Five instances of the LES code are used: one for the inlet, chamber and outlet domain and four others for each valve.

piston engines, CVC combustion raises multiple questions linked to the volumetric efficiency of the valves, the heat losses to the chamber walls, the ignition in a strongly turbulent flow, the influence of residual gases. These issues can compromise the potential gains associated to constant volume combustion. They have been investigated in an experimental setup from PPRIME (Prof. Marc Bellenoue, Poitier) and compared to LES performed with TurboAVBP. A major conclusion of the study is the existence of significant cyclic variations which are observed in the experiment and analyzed in the LES: the local flow velocity at spark timing and the level of residuals are the major factors leading to cyclic variations (Fig. 3.33). Cycles also appear to be coupled: combustion during cycle N directly affects cycle (N+1), more than in a piston engine. Once again, TurboAVBP offers a high fidelity framework as well as allow to easily setup such a complex simulation. This work was published in Combustion and Flame [153].

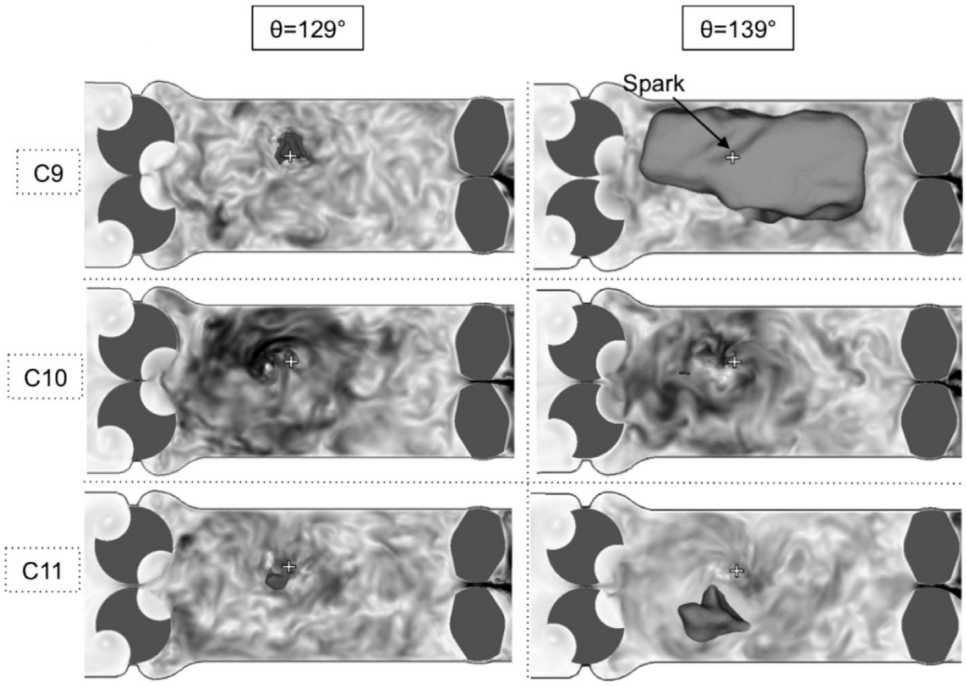

Figure 3.33: Comparison of the flame propagation (isosurface of temperature: T = 1800 K) between three cycles (C9: fast ignition, C10: ignition fails, C11: slow ignition) superimposed to the field of velocity (velocity magnitude from 0 to 60 m/s) for two angles in the cycle: Left: $\theta = 129°$, Right: $\theta = 139°$.

3.5 Partial Conclusions

From 2012 to 2017, AVBP has been extended to simulate turbomachinery flows thanks to an external coupling of several instances of AVBP through an overlapping method. Several applications on fans, compressors and turbine stages have been studied. Due to high Reynolds and Mach numbers of these cases, wall-modeled LES were performed. The role of sub-grid models as well of the mesh refinement used has been investigated. As expected, finest meshes (both at the wall, tip gap and in the passages) provide better results as compared with available experimental data. On the other hand, although used with wall models, sub-grid models that takes into account near-wall decrease of turbulent viscosity such as WALE and σ give better agreements with experiments. Beyond the unavoidable benchmarking work, TurboAVBP has been used in turbomachinery applications to predict noise generation on fan [168] by extracting high order statistic such as turbulence length scales [195] as well as combustion noise [203, 272]. Moreover, first integrated simulations have been performed both on academic configuration and industrial engines including combustion chamber and the first stage of the high pressure turbine. Results highlight the importance of the stage inlet condition in a LES context which is naturally provided in an integrated simulation and need careful reconstructions in a classical modular framework. Interesting work is needed on the specific topic of data extraction at a combustor exit simulated with LES to properly construct an inlet condition for the LES of a turbine stage. Tools such as Proper Orthogonal Decomposition and Dynamic Mode Decomposition are currently tested to address this issue (PhD of Martin Thomas). Amazingly, since its beginning, TurboAVBP has attracted a lot of attention for different types of applications where no performant method were available. Finally, a point not yet addressed concerns the performance of the methodology on massively parallel architectures. The external coupling methodology has to be as transparent as possible with respect to the CPU time requested by the resolution of the Navier-Stokes equations by the AVBP instances and to scale on actual and future big machines. This point is discussed in next chapter.

Chapter 4

High Performance Code Coupling

One key of the success of the coupled simulations discussed previously is *external code coupling*. External code coupling allows to use existing validated and efficient solvers and to make them work in a coupled mode without merging them of modifying them significantly. This strategy requires to use a tool that manages code execution, data exchanges between the codes as well as numerical aspects of the interface treatments. Such tool if often called a coupler, *i.e.* a library of functionalities that facilitate the scheduling of existing components execution sequentially or concurrently as well as the exchange of data between these components. This is achieved in part via a collection of primitives that are called in the codes as well as with more complex mechanisms for application scheduling. Many coupling libraries exist (see reviews in [48, 101]). The main coupler used in this work is OpenPALM, co-developed by ONERA and Cerfacs [224, 70]. OpenPALM is a general tool allowing to easily integrate high performance computing applications in a flexible and evolutive way proposing an optimal compromise between performance, software reuse and numerical accuracy. OpenPALM is mainly composed of three complementary components:

- the PALM[1] library [27, 206],
- the CWIPI[2] library [224]
- the graphical interface PrePALM [27, 206].

Code coupling is an appealing method to develop multiphysics and multicomponent applications. However if it is done incorrectly it can become a performance pitfall and annihilate the efforts invested to optimize each individual code. There are at least two important aspects to take into account to manage efficient code coupling in a HPC context (Fig. 4.1): (1) reducing the overhead of data transfer between the solvers and (2) maintaining a global processor idle time low, unless both codes have perfectly equal CPU per iteration times, the fastest code will have to wait the others. Having a good load balancing is the key to maintain a low idle time and thus reduce CPU waste. The first point requires the most attention and a direct point to point communication between each solver's processors is proposed [124]. This phase also requires the development of accurate parallel interpolation since the grids used by the coupled codes are generally different. The algorithm consists of two parts: the initialization or setup phase, *i.e.* where the communication routes and the interpolation coefficients are computed, and the run-time phase, or how inter code synchronization is actually executed. The first phase is done just once per coupled simulation except if the geometries are mobile.

The first part of this chapter gives an overview of OpenPALM. The second part reports performance analysis on large-scale systems complemented by paths to improvements.

[1] Projet d'Assimilation par Logiciel Multiméthodes
[2] Coupling With Interpolation Parallel Interface

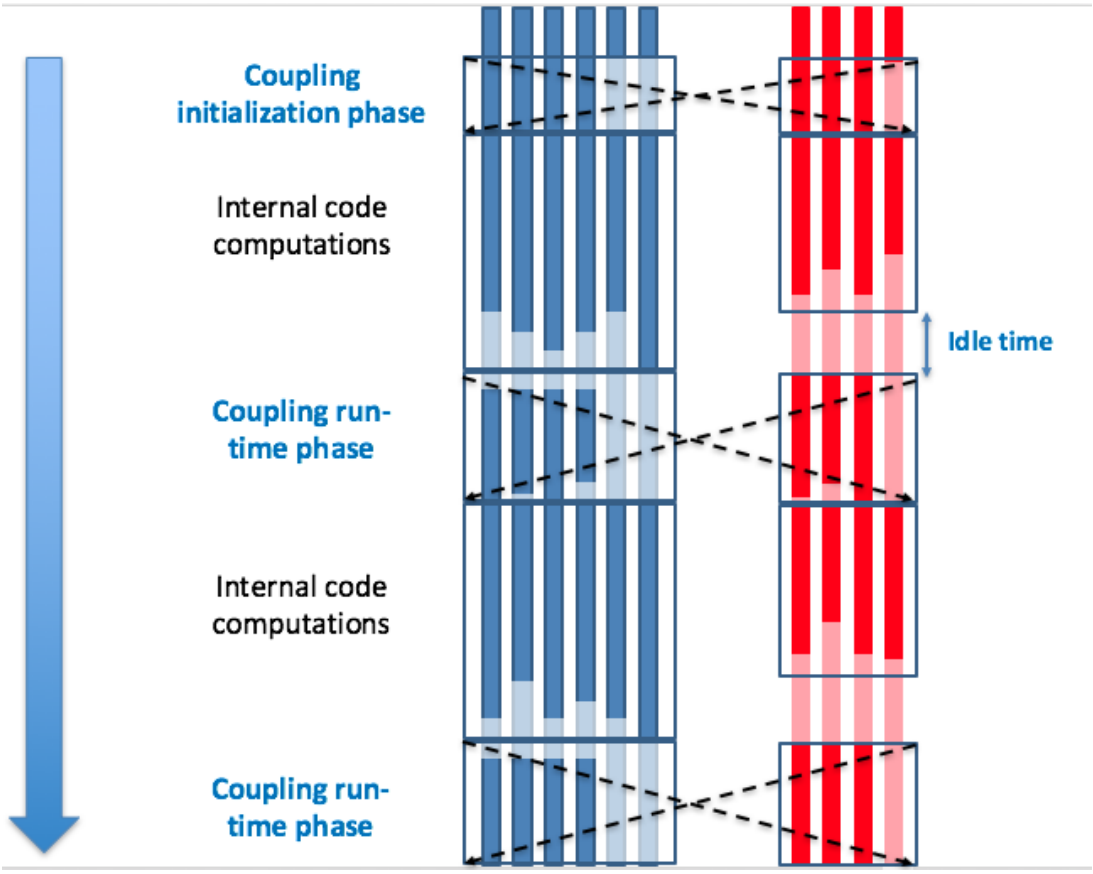

Figure 4.1: Time line corresponding to a coupled simulation including two codes.

4.1 The OpenPALM code coupler

OpenPALM is mainly composed of 3 complementary components, (1) the PALM library, (2) the CWIPI library and (3) the graphical interface PrePALM. As the application programming interface is available in Fortran and C/C++, OpenPALM can couple codes written in different languages.

4.1.1 The PALM library

PALM has originally been designed for oceanographic data assimilation algorithms, but its application domain extends to all scientific applications [27, 206]. In the framework of PALM, applications are split into elementary components that can exchange data though MPI communications. The main features of PALM are the dynamic launching of the coupled components, the full independence of the components from the application algorithm, the parallel data exchanges with redistribution and the separation of the physics from the algebraic manipulations performed by the PALM algebra toolbox. It can be defined as a dynamic coupler for its ability to deal with situations where the component execution scheduling and the data exchange patterns cannot be entirely defined before execution.

4.1.2 The CWIPI library

Based on the BFT and FVM libraries [86], CWIPI [80, 224] aims at providing a fully parallel communication layer for mesh based coupling between several parallel codes with MPI communications. Like most existing coupling libraries for multi-executables paradigm [128, 53, 123, 264], CWIPI is a static coupler in the sense that all the components of the simulations are started at the beginning, exchange data during the run phase and finish together at the end. Cou-

pling is made through 1D, 2D or 3D exchange zones that can be discretized in different ways in the coupled codes. The library takes into account all types of geometrical elements (polygon, polyhedral) with an unstructured description. CWIPI functionalities involve the construction of the communication graph between distributed geometric interfaces through geometrical localization, interpolation on non coincident meshes, exchange of coupling fields for massively parallel applications as well as visualization file building. For the description of these phases, let us consider that solvers A and B are linked by a coupling through their respective discretized coupled interface I_A and I_B.

Inter-code communication scheme determination

The communication routes construction, Inter-code communication scheme (ICCS) determination, consists in projecting the discretized interface I_A on I_B and vice-versa to prepare the communication phase. To maintain full scalability, coupling massively parallel applications has to remain a distributed process not only during the run-time part, but also the initialization part. Furthermore distributing the workload in the initialization improves the capacity of the coupled application to handle large simulations (which is a key for future applications as illustrated in the PhD Thesis of Stéphan Jauré [122, 124]).

Connecting the interfaces I_A and I_B means being able to perform geometrical searches from a computational domain into the other to locate the degrees of freedom of I_A in I_B and vice-versa. To keep the data distribution, the geometrical searches are performed in a parallel way by avoiding data centralization and sequential treatments. This objective faces a clear difficulty: in massively parallel CFD applications or heat transfer solvers the meshes are partitioned into sub-domains which are processed by different processors. This partitioning also applies to the coupling interfaces. As the partitioning algorithm is usually not aware of the coupling process, the different distributions have no reason to match, leading to complex associations between interface processors of both solvers. To address these specific difficulties the CWIPI algorithm is composed of an optimized three levels location method (Algo. 1): the first level is the partition number of the mesh, the second one is the cell number in the selected partition, and the next one is the mean values computed in the selected cell.

As the process is fully symmetric, let us consider that code A is the source code (where the data is localized for the interpolation) and code B is the target code. The corresponding interfaces I_A and I_B are partitioned on processes, leading to n_A sub-interfaces noted I_A^n and n_B sub-interfaces I_B^m with $n \in [1, n_A]$ and $m \in [1, n_B]$. It is worth noting that the number of sub-interfaces n_A (respectively n_B) is lower than or equal to the total number of total partition of the code A (respectively B). Only the processes which contain a sub-interface are involved in the projection algorithm. In his PhD Thesis, Stéphan Jauré [122] has proposed an alternative method with a higher degree of parallelism thanks to hash-tables which has been published in Journal of Computation Science and Discovery [124].

The location algorithm is parametrized to adjust the size of the bounding box around the source process sub-interface I_A^n for step #2 as well as around the source cells for step #4. This parameter takes the form of a tolerance: increasing it leads to helping locating points when geometries are not exactly matching. Note however that increasing tolerance results in an increase of the time requested by the location algorithm to converge.

Communication phase

The communication phase consists in the interpolation of the fields and the exchange of the data between the solvers. The data can be stored either at the center of the cells for cell-centered solvers or at the nodes for cell-vertex solvers. Interpolation is done directly by the source solver via linear methods, *i.e.* barycenter interpolation with $\mathbb{P}_1$ element (triangular in 2D and tetra in 3D), implying an order of 2. Note that users can customize the interpolation with call-back definition. To ensure communication scalability the communication scheme between each solver is based on direct point to point communications between the processors which share a common

Algorithm 1 Inter-code communication scheme (ICCS) determination algorithm

Step0:
- Each partition n of the source code defines its discretized source sub-interface I_A^n to the coupler (nodes coordinates & connectivity of the cells).
- Each partition m of the target code defines its discretized target sub-interface I_B^m to the coupler (nodes coordinates & connectivity of the cells)

Step1: Each process of the the source code defines a surrounding box of its partition I_A^n

Step2: Each process of the source code checks for geometrical intersections of its surrounding box of sub-partition I_A^n with target nodes of the different target sub-interface I_B^m
return Determination of a reduce number of target nodes per source process n
return Construction a first communication graph between source and target processes

Step3: Each process of the source code classifies the previous target nodes in an octree structure to optimize the next research step
return Octree structure containing the target nodes

Step4: Each source process defines a sub-box per mesh element of its sub-interface I_A^n

Step5: Each source process checks the intersection between each source cell sub-box of I_A^n and the target nodes classified in the octree
return Determination of a limited number of candidate target nodes per source cell

Step6: For each target node, the source process identifies the closest element of the source sub-interface I_A^n and defines the final communication graph
return Final communication graph from the source processes to the target ones

interface following the communication graph ICCS setup in the previous phase. Each processor generally has several counter parts, which have to provide a portion of its data field.

Two communication schemes exist in the library: (1) synchronous and (2) asynchronous. In the synchronous mode, each process of code A that treats a sub-interface I_A^n is involved in a loop of communications with processes of code B that share partially this sub-interface. The bounds of this loop are obtained thanks to the inter-code communication scheme determination phase and follow the natural order of the process numbering. The exchanges are based on the MPI_Sendrecv primitive so that they can be mono or bi-directional. This primitive is a blocking one implying that an exchange between process n of code A with process m of code B has to be finished before starting the exchange between n and $m+1$. This method is not well optimized when a very large number of cores is involved in the coupling. Concerning the asynchronous mode, the exchanges are based on loops around the primitives MPI_Issend for the sending and MPI_Irecv for reception. The completion monitoring of the exchanges is achieve thanks to loops around primitives MPI_Wait. In this mode, the communication times can overlap in a fully transparent way. As a result, asynchronous communications are more performant than the synchronous ones providing a better scaling as the number of cores of coupled applications increases. The other advantage of the method is its potential to overlap the communication times with other treatments in the code that doesnot affect the exchanged fields.

4.1.3 The graphical interface PrePALM

The Graphic User Interface, called PrePALM, is a portable Tcl/Tk application. The user describes the execution scheduling, the parallel sections, the data exchange patterns and the algebraic treatments, entirely from the user interface. It ends up providing the input file for the coupler executable and the source code for the wrappers of the coupled component that take entirely care of the set-up of the communication context with no need of change in the component sources. The same graphic tool can be used at run-time to monitor the simulation status and to provide post-mortem some statistics on the memory and CPU time resources used by the different components. Both PALM and CWIPI libraries can be used under the control of

PrePALM providing a very complete and mature coupler.

4.2 In situ observations and paths for performance improvements

Results presented this section have been obtained mainly during performance tests performed on the CURIE supercomputer (TGCC / CEA) up to 12,288 cores as well as on the TITAN supercomputer (Oak Ridge National Laboratory. No. 1 system of Top500 in November 2012) up to 132 000 cores. Both conjugate heat transfer and turbomachinery coupled simulations have been tested. Analyzes of the scaling response underline the impact of imbalanced repartition of cores among the codes, imbalance repartition of the sub-interface among the coupling cores on each solver, as well as the complex communication schemes with a lot of connections between processes of the solvers on coupling overhead [70, 66]. These points are independent from the coupler and can be addressed by incorporating the knowledge of the coupling in the preprocessing step of the solvers with methods such as constraint and co-partitioning tested in the PhD of Maria Predari at INRIA [220, 219].

Figure 4.2 presents the time requested for the initialization and the run-time phases for a turbomachinery application [51, 50] performed on Titan up to 132 000 cores. Globally, a decrease of both times is observed as the number of cores involved in the coupling increases. Interestingly, there are two orders of magnitude difference between the two phases, the initialization being the more time consuming. These times are affected by the location algorithms, machine performances and characteristics as well as by the way external communications between solvers are handled (communication algorithm, interface partitioning as discussed in the PhD Thesis of Sandrine Berger). For turbomachinery applications where the initialization phase is repeated several times due to relative motion of meshes, reducing the time requested by the localization phase is thus essential to ensure the scalability of the simulations. Two methods have been tested:

- save and reused: most of the configurations treated with TurboAVBP are periodic in space meaning that localizations performed on the first phase can be stored and reuse for the following ones. A brute force method has been implemented and tested where all the localization informations are stored (either in memory or on disc). The method works very well for small to moderate simulations in terms of mesh size. Nonetheless, the stored information rapidly grows and reaches several terabytes for daily applications making the implementation not usable for real cases. Optimization are thus required to store only the data expensive to recompute.

- re-localization: in the original implementation of TurboAVBP, the localization time performed when meshes are in relative motion doesnot take advantage from previous localization. The process described in Algo. 1 is done for each coupling cells and nodes. As from one iteration to the other, several nodes are still located in the same cell, it is not necessary to re-locate them. This possibility has been implemented in CWIPI allowing a reduction of the localization process of about 50% on small test cases and 30% on real applications.

Other methods inherited from Lagrangian particule tracking in flows for example can also be of interest to increase the performances of the coupler.

Focusing on the communication time (run-time phase), Fig. 4.3 shows the exchange time as a function of the ratio between the number of cores allocated to the fluid and those allocated to the solid (in abscissa) as well as the total number of cores involved in the exchange (which increases with the bubbles size) in the case of a CHT computation on Curie [70]. The total number of exchanging cores (indicated by the bubble size) does not have a leading role in the variation of the communication times. Instead Fig. 4.3 highlights that when the ratio of cores increases, the communications become more expensive. This points out that important unbalance in the

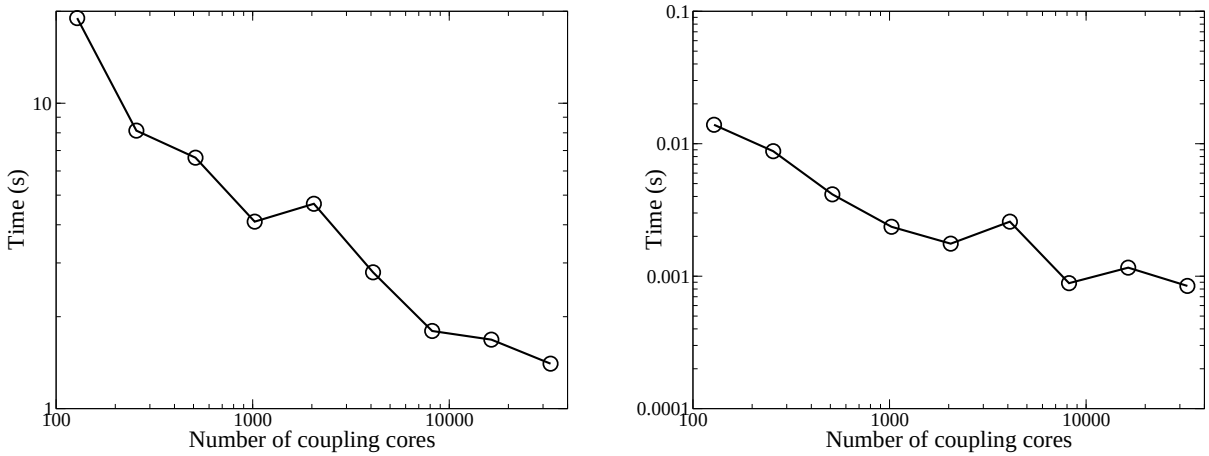

Figure 4.2: Time requested for the initialization (a) and the run-time (b) phases as a function of the number of cores involved in the coupling process for a turbomachinery application [51] performed on Titan.

core distribution between the solvers (which may be requested to synchronize the solvers to avoid waiting as illustrated on Fig. 4.1) can be detrimental for exchange the time optimization. Interestingly, two points (colored in red in Fig. 4.3) exhibit very close core ratios with very different communications times. Neither this switching of ratio nor the corresponding total number of cores can explain by themselves the differences in the communication time between the two cases. The differences observed between the two red circles on Fig. 4.3 is simply due to the difference of total amount of data per coupling core which is reduced from the smallest circle to the biggest one. As more cores are involved in the coupling, there are less data per core to exchange leading to a decrease of the exchange time (as far as the core ratio between the solvers is the same). Such behavior can be mathematically modeled based on architecture parameters as proposed in the PhD of Sandrine Berger [13]. The analyses also bring to the conclusion that the minimization of exchange times between coupled components can be performed by process placement on the parallel architecture [66]. Such placement algorithm must take into account internal exchanges in the parallel models to minimize the impact on the standalone model performances.

4.3 Partial conclusions

The coupler OpenPALM exhibits a very good behavior on actual HPC systems implying that the use of parallel computing can drastically reduce the restitution time of coupled applications for industrial design with high fidelity solvers. When increasing the number of cores, the time taken by coupling operations tend to reduce but slower than the iteration time of typical solvers [70]. Reductions in data exchange time can be achieved by co-partitioning strategies as demonstrated during the PhD Thesis of Maria Predari [219]. Many orders of magnitude higher than the communication time, the time requested by the interconnection process between coupled solvers also depends on several parameters such as core distribution between the coupled components. Nevertheless, the real gain to decrease its CPU cost relies on interconnection algorithms and thus on further development in coupling libraries rather than on the global management of the coupling environment. This is especially true for configurations with moving bodies such as fluid/structure interactions or turbomachinery.

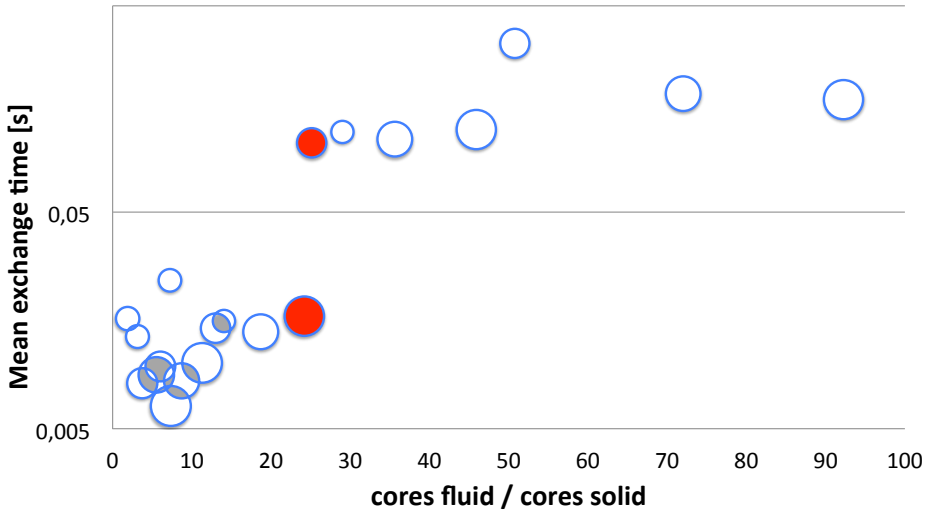

Figure 4.3: Evolution of the exchange time as a function of the ratio between the number of cores allocated to the fluid and the number of cores allocated to the solid (abscissa) and the total number of cores involved in the exchange (increasing with the bubbles size). Data extracted from [70].

Chapter 5

Perspectives

The main driver of my research activities is the use of Large Eddy Simulation (LES) in a coupled context. As shown in the different chapters of this manuscript, LES based on unstructured meshes is a powerful numerical tool to predict, understand and help in the design of canonical as well as industrial configurations. High Performance Computing allows the possibility to complexify the simulated models through different ways: increase the spatial and temporal resolutions, add more physics thanks to better modeling closures and multiphysics coupling, and finally break the frontiers of components in gas turbine thanks to integrated simulations. Based on my background constructed along my career as a researcher, my research perspectives are built on the continuity of present studies, the extension to new fields and opening to new topics:

- **Continuity of present studies:** predicting and understanding turbulent flows still is a challenge. Cerfacs has developed powerful tools for the prediction of gas turbine component flows and an important part of my future activities will consist in continuing in this direction with strong collaborations with Safran and Airbus as industrial supports and providers of applications as well as with many academic partners (Laboratoire de Mécanique des Fluides et d'Acoustique de Lyon, Institut de Mécanique des Fluides de Toulouse, Supérieur de l'Aéronautique et de l'Espace, Sherbrooke University, CentraleSupélec, von Karman Institute, Center for Turbulence Research, COmplexe de Recherche Interprofessionnel en Aérothermochimie, Barcelona Supercomputing Center ...). On one hand, the studies will concern aerothermal simulations to extract relevant physical informations, understand complex phenomena and propose guidelines for industrial usage in terms of Large Eddy Simulations best practices as well as low order modeling. On the other hand, efforts will also continue in the field of LES of turbomachinery flows, firstly concerning combustion chamber/turbine interaction. An important aspect deals with the characterization of combustion chamber outlet (deterministic and non deterministic disturbances) to generate adequate inlet conditions for LES of turbine stages. Integrated simulations will play a key role in this study especially to analyse how disturbances influence the turbine flows and how geometrical features typical of turbine stages (tip gaps, cavities, cooling systems, ...) interact with mean flow structures and turbulence. An other field of application is the analysis of acoustic sources in fan stages as well as acoustic treatment in fan ducts [65].

- **Extension to new fields:** TurboAVBP has shown to be very versatile and has opened many new potential applications. Firstly, the simulation of new propulsion concepts such as Constant Volume Combustion and Rotative Detonation Engine is of particular interest due to the tight coupling between the combustion chamber and the compressor and turbine components. Indeed, in such systems, the combustion is driven by highly unsteady processes of first importance for the turbomachinery operation. The noise created by these engines will also be a major issue: here, TurboAVBP with the MISCOG methodology will be mandatory to compute the combustion chamber, the turbine but also the acoustic waves

propagating through both components. An other subject of interest for industrial purposes with many scientific challenges is the coupling between a disperse phase and a turbulent rotating flow. Such coupling arises when sand enters compressors of aircraft and helicopter engines. It is also the leading mechanism in all systems dedicated to air-oil separation by centrifugation. In the first situation, mechanical impact of sand on compressor blades can damage the structure and thus the performances of the engine. The objective of the second type of system is to extract as much as possible oil to reuse it in the engine. The main challenges to address concern the coupling between the disperse phase and turbulence in a rotating frame, the impact of particules on walls, the potential generation of liquid films as well as re-atomisation.

- **Opening to new topics:** the major part of the new topics I intend to work on in the near future deal with LES and code coupling. The first one concerns solutions to decrease the CPU costs induced by LES of high Reynolds and Mach number turbomachinery stages. Classical methods used in URANS such as phase lag have recently been extended to LES [191] with questionable success. Other solutions also emerge in the community such as the two-scale method where URANS and LES are jointly used [111]. Search for methods to address this problem is challenging as it involves physical, algorithmic, computational and coupling issues. Then, an important research topic for the future lies in the coupling of fluid flow solvers dedicated to treat specific phenomena: it is hardly possible to build a unique solver able to deal with the wide variety of situations encountered in fluid dynamics. As a result, coupling specialized fluid solvers to include different complex physics is a promising way. A typical application is fuel injection in aeronautical combustion chambers. The turbulent combustion process has been shown to be well captured by compressible unstructured LES methods such as in AVBP. Nonetheless, fuel atomisation processes need very accurate high order numerical schemes to be finely resolved, as demonstrated by the DyJeat code [278]. Using a code such as DyJeat to simulate a whole combustion chamber would be inappropriate due to high CPU cost induced as well as the need to integrate combustion models. On the other hand, including atomisation in AVBP would require to use adequate numerics and develop surface tracking methods. Coupling both codes is then an attracting path which will allow to use efficient existing codes putting pressure on the method to couple to solvers. Finally, I plan to study several open issues on coupling methodologies which is a general subject of interest for Cerfacs, not only in the field of Large Eddy Simulation but also in Climate sciences where many models are coupled or in hydraulics where 1D, 2D and 3D models interact.

More than code coupling and Large Eddy Simulation, all the research perspectives cannot be treated without dealing with Numerics, High Performance Computing and Big Data. Numerics are of primary importance for the spatial and temporal discretization of the equations and competences in this field are essential to produce reliable tools. To address complex problems, the tools developed must benefit from state of the art High Performance Computing as well as anticipate future big machines such as Exascale systems. Cerfacs is a perfect place to continue to develop this competence and have decisive contacts with HPC labs or vendors. Finally, Big Data and associated methods become more and more a topic of interest to produce tools able to extract pertinent information from the deluge of data generated by the solvers on HPC systems. As a researcher at Cerfacs, an important part of the studies is dedicated to address industrial problems and a major goal is to transfer the tools and methods to industry. Finally, all this work is performed with PhD and post-doctoral students: Cerfacs is organized in such a way that every permanent researcher leads at least four or five students. Supervising students already is and will become more and more a central part of my work, explaining why I apply for an HDR diploma.

Bibliography

[1] P. Aillaud, F. Duchaine, and L.Y.M. Gicquel. Les of a round impinging jet: investigation of the link between nusselt secondary peak and near-wall vortical structures. In *Proceedings of ASME Turbo Expo 2016: Turbine Technical Conference and Exposition*, number GT2016-56111, Seoul, South Korea, June 14-17 2016.

[2] P. Aillaud, F. Duchaine, L.Y.M. Gicquel, and S. Didorally. Secondary peak in the nusselt number distribution of impinging jet flows: A phenomenological analysis. *Physics of Fluids*, 28(9):095110–1– 095110–22, 2016.

[3] P. Aillaud, F. Duchaine, L.Y.M. Gicquel, and S. Didorally. Characterization of the surface curvature effect using les for a single round impinging jet. In *Proceedings of ASME Turbo Expo 2017: Turbine Technical Conference and Exposition GT2017*, number GT2017-64159, Charlotte, NC, USA, 2017.

[4] G. Allaire and A. Craig. *Numerical Analysis and Optimization: An Introduction to Mathematical Modelling and Numerical Simulation.* Oxford University Press, 2007.

[5] J. J. Alonso, S. Hahn, F. Ham, M. Herrmann, G. Iaccarino, G. Kalitzin, P. LeGresley, K. Mattsson, G. Medic, P. Moin, H. Pitsch, J. Schluter, M. Svard, E.V. der Weide, D. You, and X. Wu. Chimps: a high-performance scalable module for multi-physics simulation. In *42nd AIAA/ASME/SAE/ASEE Joint Propulsion Conference & Exhibit*, number AIAA-Paper 2006-5274, 2006.

[6] L. Andrei, C. Carcasci, R. Da Soghe, B. Facchini, F. Maiuolo, L. Tarchi, and S. Zecchi. Heat Transfer Measurements in a Leading Edge Geometry With Racetrack Holes and Film Cooling Extraction. *Journal of Turbomachinery*, 135(3):031020, 2013.

[7] A. Andreini, B. Facchini, M. Insinna, L. Mazzei, and S. Salvadori. Hybrid RANS-LES modeling of a hot streak generator oriented to the study of combustor-turbine interaction. In *ASME Turbo Expo 2015: Turbine Technical Conference and Exposition*, number GT2015-42402, 2015.

[8] T. Arts, M. Lambert de Rouvroit, and A. W.Rutherford. Aero-thermal investigation of a highly loaded transonic linear turbine guide vane. In *Technical Note, Von Karman Institute*, 1990.

[9] S. Ashforth-Frost and K. Jambunathan. Effect of nozzle geometry and semi-confinement on the potential core of a turbulent axisymmetric free jet. *International Communications in Heat and Mass Transfer*, 23(2):155–162, 1996.

[10] T. Bacci, G. Caciolli, B. Facchini, L. Tarchi, C. Koupper, and J.-L. Champion. Flowfield and temperature profiles measurements on a combustor simulator dedicated to hot streaks generation. In *ASME Turbo Expo 2015: Turbine Technical Conference and Exposition*, number GT2015-42217, 2015.

[11] S. Badia, F. Nobile, and C. Vergara. Fluid–structure partitioned procedures based on robin transmission conditions. *J. Comput. Phys.* , 227(14):7027 – 7051, 2008.

[12] J. W. Baughn and S. Shimizu. Heat Transfer Measurements From a Surface With Uniform Heat Flux and an Impinging Jet. *Journal of Heat Transfer*, 111:1096–1098, 1989.

[13] S. Berger. *Implementation of a coupled computational chain to the combustion chamberÂŕs heat transfer*. Phd thesis, Université de Toulouse, INPT, 6 2016.

[14] S. Berger, F. Duchaine, and L.Y.M. Gicquel. Influence des conditions aux limites thermiques sur la stabilisation d'une flamme laminaire prémélangée. In *Congrés Français de Thermique 2016*, Toulouse, France, 5 2016.

[15] S. Berger and F. Duchaine L.Y.M Gicquel. Bluff-body thermal property and initial state effects on a laminar premixed flame anchoring pattern. *Flow Turbulence and Combustion*, 2017.

[16] S. Berger, S. Richard, F. Duchaine, and L.Y.M. Gicquel. Variations of anchoring pattern of a bluff-body stabilized laminar premixed flame as a function of the wall temperature. In *ASME Turbo Expo 2016*, pages GT2016–56473, Seoul, South Korea, June 14-17 2016.

[17] S. Berger, S. Richard, F. Duchaine, G. Staffelbach, and L.Y.M. Gicquel. On the sensitivity of a helicopter combustor wall temperature to convective and radiative thermal loads. *Applied Thermal Engineering*, 103(25):1450–1459, 2016.

[18] S. Berger, S. Richard, G. Staffelbach, F. Duchaine, and L.Y.M. Gicquel. Aerothermal prediction of an aeronautical combustion chamber based on the coupling of large eddy simulation, solid conduction and radiation solvers. In *ASME Turbo Expo 2015*, pages GT2015–42457, Montreal, Canada, 6 2015.

[19] S. Bocquet, P. Sagaut, and J.-C. Jouhaud. A compressible wall model for large-eddy simulation with application to prediction of aerothermal quantities. *Physics of Fluids*, 24(June):65103, 2012.

[20] D.J. Bodony, G. Zagaris, A. Reichert, and Q. Zhang. Provably stable overset grid methods for computational aeroacoustics. *Journal of Sound and Vibration*, 330(17):4161 – 4179, 2011.

[21] D. Bohn, J. Ren, and K. Kusterer. Systematic investigation on conjugate heat transfer rates of film cooling configurations. *International Journal of Rotating Machinery*, 2005(3):211–220, 2005.

[22] M. Boileau, F. Duchaine, T. Poinsot, and Y. Sommerer. Large eddy simulation of heat transfer around a square cylinder. *AIAA Journal* , 51(2):372–385, 2013.

[23] A. Bonhomme, F. Duchaine, G. Wang, L. Selle, and T. Poinsot. A parallel multidomain strategy to compute turbulent flows in fan-stirred closed vessels. *Comput. Fluids* , 101(C):183–193, September 2014.

[24] F. Boudy, D. Durox, T. Schuller, G. Jomaas, and S. Candel. Describing function analysis of limit cycles in a multiple flame combutor. In GT2010-22372, editor, *ASME Turbo expo*, Glasgow, UK, June 2010.

[25] P. Bradshaw. The analogy between streamline curvature and buoyancy in turbulent shear flow. *Journal of Fluid Mechanics*, 36(01):177, 1969.

[26] M. Brebion, D. Mejia, P. Xavier, F. Duchaine, B. Bédat, L. Selle, and T. Poinsot. Joint experimental and numerical study of the influence of flame holder temperature on the stabilization of a laminar methane flame on a cylinder. *Combustion and Flame*, 172:153–161, 2016.

[27] S. Buis, A. Piacentini, and D. Déclat. Palm: A computational framework for assembling high performance computing applications. *Concurrency and Computation: Practice and Experience*, 18(2):231–245, February 2006.

[28] R. S. Bunker. Gas turbine heat transfer: 10 remaning hot gas path challanges. In *Procceedings of GT2006. ASME Turbo Expo 2006*, 2006.

[29] F Cadieux, JA Domaradzki, T Sayadi, S Bose, and F Duchaine. Dns and les of separated flows at moderate reynolds numbers. In *Bulletin of the American Physical Society*, volume 57, 2012.

[30] Laurent Cambier, Sébastien Heib, and Sylvie Plot. The onera elsa cfd software: input from research and feedback from industry. *Mechanics and Industry*, 14(3):159–174, 2013.

[31] P. Causin, J.F. Gerbeau, and F. Nobile. Added-mass effect in the design of partitioned algorithms for fluid–structure problems. *Computer Methods in Applied Mechanics and Engineering*, 194(42-44):4506 – 4527, 2005.

[32] I. Celik, A. Smirnov, and J. Smith. Appropriate initial and boundary conditions for LES of a ship wake. In *Proceedings of the 3rd ASME/JSME Joint Fluids Engineering Conference*, volume FEDSM99-7851, San Francisco, California, USA, 1999.

[33] S. W. Chang and W. D. Morris. Heat transfer in a radially rotating square duct fitted with in-line transverse ribs. *International Journal of Thermal Sciences*, 42(3):267–282, 2003.

[34] S. Chemin. *Étude des Interactions Thermiques Fluides-Structure par un Couplage de Codes de Calcul*. PhD thesis, Université de Reims Champagne-Ardenne, 2006.

[35] M. Choi, H. S. Yoo, G. Yang, J. S. Lee, and D. K. Sohn. Measurements of impinging jet flow and heat transfer on a semi-circular concave surface. *International Journal of Heat and Mass Transfer*, 43:1811–1822, 2000.

[36] F. Coletti, D.L. Jacono, I. Cresci, and T. Arts. Turbulent flow in rib-roughened channel under the effect of Coriolis and rotational buoyancy forces. *Physics of Fluids*, 26(4), 2014.

[37] O. Colin, F. Ducros, D. Veynante, and T. Poinsot. A thickened flame model for large eddy simulations of turbulent premixed combustion. *Phys. Fluids* , 12(7):1843–1863, 2000.

[38] E. Collado. *Impact of the unsteady aerothermal environment on the turbine blades temperature*. PhD thesis, Université de Toulouse - Institut National Polytechnique de Toulouse - Energétique et Transferts, 2012. PhD.

[39] E. Collado Morata, N. Gourdain, F. Duchaine, and L.Y.M. Gicquel. Effects of free-stream turbulence on high pressure turbine blade heat transfer predicted by structured and unstructured les. *International Journal of Heat and Mass Transfer*, 55(21-22):5754 – 5768, 2012.

[40] C. Cornaro, A. S. Fleischer, and R. J. Goldstein. Flow visualization of a round jet impinging on cylindrical surfaces. *Experimental Thermal and Fluid Science*, 20(2):66–78, 1999.

[41] N. Courtiade and X. Ottavy. Experimental study of surge precursors in a high-speed multistage compressor. *J. Turbomach.* , 135, 2013.

[42] T. J. Craft, A. V. Gerasimov, H. Iacovides, and B. E. Launder. Progress in the generalization of wall-function treatments. *Int. J. Heat Fluid Flow* , 23(2):148–160, 2002.

[43] J. Cui, V.N. Rao, and P. Tucker. Numerical investigation of contrasting flow physics in different zones of a high-lift low-pressure turbine blade. *Journal of Turbomachinery*, 138(1):011003–011003–10, 2016.

[44] J. Cui, V.N. Rao, and P. Tucker. Numerical investigation of secondary flows in a high-lift low pressure turbine. *International Journal of Heat and Fluid Flow*, 63:149–157, 2017.

[45] N. A. Cumpsty and F. E. Marble. The interaction of entropy fluctuations with turbine blade rows; a mechanism of turbojet engine noise. *Proc. R. Soc. Lond. A* , 357:323–344, 1977.

[46] T. Dairay, V. Fortuné, E. Lamballais, and L.-E. Brizzi. Direct numerical simulation of a turbulent jet impinging on a heated wall. *Journal of Fluid Mechanics*, 764:362–394, feb 2015.

[47] F. Daude, J. Berland, T. Emmert, P. Lafon, F. Crouzet, and C. Bailly. A high-order finite-difference algorithm for direct computation of aerodynamic sound. *Comput. Fluids* , 61:46–63, 2012.

[48] Lois C McInnes Carol Woodward William Gropp Eric Myra Michael Pernice John Bell Jed Brown Alain Clo Jeffrey Connors Emil Constantinescu Don Estep Kate Evans Charbel Farhat Ammar Hakim Glenn Hammond Glen Hansen Judith Hill Tobin Isaac Xiangmin Jiao Kirk Jordan Dinesh Kaushik Efthimios Kaxiras Alice Koniges Kihwan Lee Aaron Lott Qiming Lu John Magerlein Reed Maxwell Michael McCourt Miriam Mehl Roger Pawlowski Amanda P Randles Daniel Reynolds Beatrice Rivière Ulrich Rüde Tim Scheibe John Shadid Brendan Sheehan Mark Shephard Andrew Siegel Barry Smith Xianzhu Tang Cian Wilson Barbara Wohlmuth David E Keyes. Multiphysics simulations challenges and opportunities. *The International Journal of High Performance Computing Applications*, 27(1), 2013.

[49] G. Daviller, M. Brebion, P. Xavier, G. Staffelbach, J.D Muller, and T. Poinsot. A mesh adaptation strategy to predict pressure losses in les of swirled flows. *Flow, Turbulence and Combustion*, 99(1):93–118, 2017.

[50] J. de Laborderie, F. Duchaine, and L.Y.M. Gicquel. Analysis of a high-pressure multistage axial compressor at off-design conditions with coarse large eddy simulations. In EUROTURBO, editor, *12th European Conference on Turbomachinery Fluid Dynamics & Thermodynamics*, pages Paper ID: ETC2017–125, Stockholm, Sweden, 2017.

[51] J. de Laborderie, F. Duchaine, O. Vermorel, L.Y.M. Gicquel, and S. Moreau. Application of an overset grid method to the large-eddy simulation of a high speed multistage axial compressor. In *ASME Turbo Expo 2016*, pages GT2016–56344, Seoul, South Korea, June 14-17 2016.

[52] C. Carton de Wiart, K. Hillewaert, L. Bricteux, and G. Winckelmans. Implicit les of free and wall-bounded turbulent flows based on the discontinuous galerkin/symmetric interior penalty method. *International Journal for Numerical Methods in Fluids*, 78(6):335–354, 2015. fld.4021.

[53] D. DeCecchis, L.A. Drummond, and J.E. Castillo. Design of a distributed coupling toolkit for high performance computing environment. *Mathematical and Computer Modelling*, 2011.

[54] G. Desquesnes, M. Terracol, E. Manoha, and P. Sagaut. On the use of a high order overlapping grid method for coupling in cfd/caa. *J. Comput. Phys.*, 220(1):355–382, December 2006.

[55] A. Dewan, R. Dutta, and B. Srinivasan. Recent Trends in Computation of Turbulent Jet Impingement Heat Transfer. *Heat Transfer Engineering*, 33(4-5):447–460, 2012.

[56] N.S. Dhamankar, G.A. Blaisdell, and A.S. Lyrintzis. An overview of turbulent inflow boundary conditions for large eddy simulations. In *22nd AIAA Aviation*, Dallas, 2015. AIAA 2015-3213.

[57] A. Di Sante, R. Theunissen, and R. Van Den Braembussche. A new facility for time-resolved PIV measurements in rotating channels. *Experiments in Fluids*, 44(2):179–188, 2008.

[58] E. Divo, E. Steinthorsson, F. Rodriguez, A.J. Kassab, and J.S. Kapat. Glenn-ht/bem conjugate heat transfer solver for large-scale turbomachinery models. Technical Report CR 212195, NASA, 2003.

[59] J. Donea. Taylor-galerkin method for convective transport problems. *Int. J. Numer. Meth. Fluids* , 20(1):101–119, 1984.

[60] J. Donea, L. Quartapelle, and V. Selmin. An analysis of time discretization in the finite element solution of hyperbolic problems. *J. Comput. Phys.* , 70:463–499, 1987.

[61] D. J. Dorney, K. L. Gundy-Burlet, and D. L. Sondak. A survey of hot streak experiments and simulations. *International Journal of Turbo and Jet Engines*, 16(1):1–15, 1999.

[62] R. Goncalves dos Santos, S. Ducruix, O. Gicquel, and D. Veynante. A study of three-dimensional les of turbulent combustion with radiative heat transfer. *Journal of the Brazilian Society of Mechanical Sciences and Engineering*, 38(1):33–48, 2016.

[63] R. Gonçalves dos Santos, M. Lecanu, S. Ducruix, O. Gicquel, E. Iacona, and D. Veynante. Coupled large eddy simulations of turbulent combustion and radiative heat transfer. *Combust. Flame*, 152(3):387–400, 2008.

[64] P. Druault, S. Lardeau, J.P. Bonnet, F. Coiffet, J. Delville, E. Lamballais, J.F. Largeau, and L. Perret. Generation of three-dimensional turbulent inlet conditions for large-eddy simulation. *AIAA Journal*, 42(3):447–456, 2004.

[65] F. Duchaine. Sensitivity analysis of heat transfer in a honeycomb acoustic liner to inlet conditions with large eddy simulation. In *Proceedings of ASME Turbo Expo 2017: Turbine Technical Conference and Exposition GT2017*, number GT2017-63243, Charlotte, NC, USA, 2017.

[66] F. Duchaine, S. Berger, G. Staffelbach, and L.Y.M. Gicquel. Partitioned high performance coupling applied to cfd. In *JARA HPC Symposium*, Aachen, Germany, 2016. Jîlich Aachen Research Alliance (JARA), October 4-5.

[67] F. Duchaine, M. Boileau, Y. Sommerer, and Th. Poinsot. Large eddy simulation of the flow and heat transfer around two square cylinders in a tandem arrangement. *Journal of Heat Transfer*, 136(10), 2014.

[68] F. Duchaine, F. Boudy, D. Durox, and T. Poinsot. Sensitivity analysis of transfer functions of laminar flames. *Combust. Flame*, 158(12):2384–2394, 2011.

[69] F. Duchaine, J. Dombard, L.Y.M Gicquel, and C. Koupper. On the importance of inlet boundary conditions for aerothermal predictions of turbine stages with large eddy simulation. *Computers & Fluids*, 154:60–73, 2017.

[70] F. Duchaine, S. Jauré, D. Poitou, E. Quémerais, G. Staffelbach, T. Morel, and L. Gicquel. Analysis of high performance conjugate heat transfer with the openpalm coupler. *Journal of Computational Science and Discovery*, 8:015003, 2015.

[71] F. Duchaine, N. Maheau, V. Moureau, G. Balarac, and S. Moreau. Large eddy simulation and conjugate heat transfer around a low-mach turbine blade. *J. Turbomach.* , 136(5), 2013.

[72] F. Duchaine, S. Mendez, F. Nicoud, A. Corpron, V. Moureau, and T. Poinsot. Conjugate heat transfer with large eddy simulation application to gas turbine components. *C. R. Acad. Sci. Mécanique*, 337(6-7):550–561, 2009.

[73] S. Ducruix, D. Durox, and S. Candel. Theoretical and experimental determinations of the transfer function of a laminar premixed flame. *Proc. Combust. Inst.* , 28(1):765–773, 2000.

[74] M.G. Dunn. Convective heat transfer and aerodynamics in axial flow turbines. *J. Turbomach.* , 123:637–686, 2001.

[75] I. Duran. *Prediction of combustion noise in modern aero-engines combining large eddy simulations and analytical methods - th/cfd/13/83*. PhD thesis, Université de Toulouse - Institut National Polytechnique de Toulouse, MEGeP, 2013.

[76] I. Duran and S. Moreau. Study of the attenuation of waves propagating through fixed and rotating turbine blades. In *18th AIAA/CEAS Aeroacoustics Conference (33rd AIAA Aeroacoustics Conference)*, number AIAA2012-2133 paper, Colorado Springs, USA, June 4-6 2012.

[77] T. E. Dyson, D. B. Helmer, and J. A. Tallman. Large-scale simulation of the clocking impact of 2d combustor profile on a two stage high pressure turbine. In *ASME Turbo Expo 2014: Turbine Technical Conference and Exposition*, number GT2014-25883, 2014.

[78] M. Errera and F. Duchaine. Comparative study of coupling coefficients in dirichlet–robin procedure for fluid–structure aerothermal simulations. *Journal of Computational Physics*, 312(1):218–234, 2016.

[79] M-P Errera and S. Chemin. Optimal solutions of numerical interface conditions in fluid–structure thermal analysis. *Journal of Computational Physics*, 245:431–455, 2013.

[80] M.P. Errera, E. Quémerais, and B. Baqué. Approche mutli-physique par couplage de codes. application en aérothermique. In *Premier colloque international francophone d'énergétique et mécanique*, number ART-2-126, Saly, Sénégal, 2010.

[81] V. Eswaran and S. B. Pope. Direct numerical simulations of the turbulent mixing of a passive scalar. *Phys. Fluids* , 31:506, 1988.

[82] A. Fan, J. Wan, K. Maruta abd H. Yao, and W. Liu. Interaction between heat transfer, flow field and flame stabilization in a micro-combustor with a bluff body. *Int. J. Heat and Mass Transfer* , 66:72–79, 2013.

[83] M. Fenot, E. Dorignac, and J. J. Vullierme. An experimental study on hot round jets impinging a concave surface. *International Journal of Heat and Fluid Flow*, 29(4):945–956, 2008.

[84] M. Fenot, J. J. Vullierme, and E. Dorignac. Local heat transfer due to several configurations of circular air jets impinging on a flat plate with and without semi-confinement. *International Journal of Thermal Sciences*, 44(7):665–675, 2005.

[85] C. Flageul, S. Benhamadouche, E. Lamballais, and D. Laurence. On the discontinuity of the dissipation rate associated with the temperature variance at the fluid-solid interface for cases with conjugate heat transfer. *International Journal of Heat and Mass Transfer*, 111:321–328, 2017.

[86] Y. Fournier, J. Bonelle, C. Moulinec, Z. Shang, A.G. Sunderland, and J.C. Uribe. Optimizing Code_Saturne computations on Petascale systems. *Computers & Fluids*, 45(1):103 – 108, 2011.

[87] R. Fransen, L. Vial L.Y.M., and Gicquel. Large eddy simulation of rotating ribbed channel. In *ASME Turbo Expo 2013*, San Antonio, USA, June 2013.

[88] B. Franzelli, E. Riber, M. Sanjosé, and T. Poinsot. A two-step chemical scheme for Large-Eddy Simulation of kerosene-air flames. *Combust. Flame*, 157(7):1364–1373, 2010.

[89] V. Ganesan. Non-reacting and reacting flow analysis in an aero-engine gas turbine combustor using cfd. In *SAE 2007 World Congress*, number 2007-01-0916, Detroit, Michigan, USA, April 2007.

[90] V.K. Garg. Heat transfer research on gas turbine airfoils at NASA GRC. *Int. J. Heat Fluid Flow* , 23(2):109–136, April 2002.

[91] C. Gau and C. M. Chung. Surface Curvature Effect on Slot- Air-Jet Impingement Cooling Flow and Heat Transfer Process. *Journal of Heat Transfer*, 113(4):858–864, 1991.

[92] L. Y. M. Gicquel, G. Staffelbach, and T. Poinsot. Large eddy simulations of gaseous flames in gas turbine combustion chambers. *Prog. Energy Comb. Sci.* , 38(6):782 – 817, 2012.

[93] M.B. Giles. Stability analysis of numerical interface conditions in fluid-structure thermal analysis. *Int. J. Numer. Meth. Fluids* , 25(4):421–436, 1997.

[94] R. A. Gomes and R. Niehuis. Film cooling effectiveness measurements with periodic unsteady inflow on higly loaded blades with mean flow separation. In *Proceedings of the ASME Turbo Expo 2009: Power for Sea, Land and Air*, Orlando, Florida, USA, 2009.

[95] N. Gourdain. *High-performance computing of gas turbine flows: current and future trends.* PhD thesis, Ecole Centrale de Lyon, 2011.

[96] N. Gourdain. Prediction of the unsteady turbulent flow in an axial compressor stage. part 1: Comparison of unsteady rans and les with experiments. *Computers & Fluids*, 106:119–129, 2015.

[97] N. Gourdain. Prediction of the unsteady turbulent flow in an axial compressor stage. part 2: Analysis of unsteady rans and les data. *Computers & Fluids*, 106:67–78, 2015.

[98] N. Gourdain, F. Duchaine, E. Collado, and L. Gicquel. Advanced numerical simulation dedicated to the prediction of heat transfer in a highly loaded turbine guide vane. In GT2010-22793, editor, *ASME Turbo expo*, Glasgow, UK, June 2010.

[99] N. Gourdain, F. Sicot, F. Duchaine, and L.Y.M. Gicquel. Large eddy simulation of flows in industrial compressors: a path from 2015 to 2035. *Phil. Trans. R. Soc. A*, 372(20130323), 2014.

[100] S. Govert, D. Mira, M. Zavala-Ake, J.B.M. Kok, M. Vazquez, and G. Houzeaux. Heat loss prediction of a confined premixed jet flame using a conjugate heat transfer approach. *International Journal of Heat and Mass Transfer*, 107:882–894, 2017.

[101] D. Groen, S.J. Zasada, and P.V. Coveney. Survey of multiscale and multiphysics applications and communities. *Computing in Science & Engineering*, 16(2):34–43, 2014.

[102] T. Grosnickel, F. Duchaine, L.Y.M Gicquel, and C. Koupper. Large-eddy simulations of static and rotating ribbed channels in adiabatic and isothermal conditions. In *Proceedings of asme turbo expo 2017: turbine technical conference and exposition*, Charlotte, NC, USA, June 26 - 30 2017.

[103] N. Guezennec and T. Poinsot. Acoustically nonreflecting and reflecting boundary conditions for vorticity injection in compressible solvers. *AIAA Journal* , 47:1709–1722, 2009.

[104] T.F. Guiberti, D. Durox, P. Scouflaire, and T. Schuller. Impact of heat loss and hydrogen enrichment on the shape of confined swirling flames. *Proceedings of the Combustion Institute*, 35(2):1385 – 1392, 2015.

[105] M. Hadžiabdić and K. Hanjalić. Vortical structures and heat transfer in a round impinging jet. *Journal of Fluid Mechanics*, 596:221–260, 2008.

[106] J.C. Han, S. Dutta, and S.V. Ekkad. *Gas Turbine Heat Transfer and Cooling Technology*. Taylor & Francis, New York, NY, USA, 2000.

[107] Z. X. Han, B. Dennis, and G. Dulikravich. Simultaneous prediction of external flow-field and temperature in internally cooled 3-d turbine blode material. *Int. J. Turbo Jet-Eng.* , 18:47–58., 2001.

[108] M. Harnieh, L.Y.M. Gicquel, and F. Duchaine. Sensitivity of large eddy simulations to inflow condition and modeling if applied to a transonic high-pressure cascade vane. In *ASME Turbo Expo 2017: Turbine Technical Conference and Exposition*, number GT2017-64686, Charlotte, NC, USA, June 26 - 30 2017.

[109] A. Hashiehbaf, A. Baramade, Amit Agrawal, and G.P. Romano. Experimental investigation on an axisymmetric turbulent jet impinging on a concave surface. *International Journal of Heat and Fluid Flow*, 53:167–182, 2015.

[110] L. He and M. Fadl. Multi-scale time integration for transient conjugate heat transfer. *International Journal for Numerical Methods in Fluids*, 83(12):887–904, 2017.

[111] L. He and J. Ji. Two-scale methodology for urans/large eddy simulation solutions of unsteady turbomachinery flows. *Journal of Turbomachinery*, 139:101012–1, 2017.

[112] A. Heselhaus. A hybrid coupling scheme and stability analysis for coupled solid/fluid turbine blade temperature calculations. In *ASME 1998 International Gas Turbine and Aeroengine Congress and Exhibition*, Stockholm, Sweden, June 2-5 1998.

[113] A. Heselhaus and D. T. Vogel. Numerical simulation of turbine blade cooling with respect to blade heat conduction and inlet temperature profiles. In *ASME, SAE, and ASEE, Joint Propulsion Conference and Exhibit, 31st*, number AIAA-1995-3041, San Diego, CA, USA, July 1995.

[114] C. Hirsch. *Numerical Computation of Internal and External Flows*. John Wiley, New York, 1988.

[115] Seunghyuck Hong, Santosh J. Shanbhogue, Kushal S. Kedia, and Ahmed F. Ghoniem. Impact of the flame-holder heat-transfer characteristics on the onset of combustion instability. *Combust. Sci. Technol.* , 185(10):1541–1567, 2013.

[116] T. Igarashi. Heat transfer from a square prism to an air stream. *International journal of heat and mass transfer*, 28(1):175–181, 1985.

[117] J.B. Illingworth, N.J. Hills, and C.J. Barnes. 3d fluid–solid heat transfer coupling of an aero engine pre-swirl system. In *ASME Turbo Expo 2005: Turbine Technical Conference and Exposition*, number GT2005-68939, Reno-Tahoe, Nevada, June 6–9 2005.

[118] M. Insinna. *Investigation of the Aero-Thermal Aspects of Combustor/Turbine Interaction in Gas Investigation of the aero-thermal aspects of combustor/turbine interaction in gas turbine*. PhD thesis, Energetica e Tecnologie Industrali ed Ambientali Innovative, 2014.

[119] P. T. Ireland and G. Dailey. Aerothermal performance of internal cooling systems in turbomachines. In *Internal Cooling in Turbomachinery, VKI Lecture Series*, volume 2010-05, 2010.

[120] S. Jacobi, C. Mazzoni, B. Rosic, and K. Chana. Investigation of unsteady flow phenomena in first vane caused by combustor flow with swirl. *Journal of Turbomachinery*, 139(4):041006–041006–12, 2017.

[121] K. Jambunathan, E. Lai, M. A. Moss, and B. L. Button. A review of heat transfer data for single circular jet impingement. *International Journal of Heat and Fluid Flow*, 13(2):106–115, 1992.

[122] S. Jauré. *Méthodologies pour le couplage Simulation aux Grandes Echelles/Thermique en environnement massivement parallèle - TH/CFD/12/114*. PhD thesis, Université de Toulouse - Ecole doctorale : Mécanique, Energétique, Génie civil, Procédés - Dynamique des Fluides - December, 13, 2012. phd.

[123] S. Jauré, F. Duchaine, and L. Gicquel. Comparisons of coupling strategies for massively parallel conjugate heat transfer with large eddy simulation. In *In IV International Conference on Computational Methods for Coupled Problems in Science and Engineering*, Kos Island, Greece, 2011.

[124] S. Jauré, F. Duchaine, G. Staffelbach, and L.Y.M Gicquel. Massively parallel conjugate heat transfer solver based on large eddy simulation and application to an aeronautical combustion chamber. *Comput. Sci. Disc.*, 6, 2013.

[125] S. Jee, J. Joo, and G. Medic. Large-eddy simulation of a high-pressure turbine vane with inlet turbulence. In *ASME Turbo Expo 2016*, number GT2016-56980, Seoul, South Korea, June 14-17 2016.

[126] J. P. Johnston, R. M. Halleen, and D. K. Lezius. Effects of spanwise rotation on the structure of two-dimensional fully developed turbulent channel flow. *Journal of Fluid Mechanics*, 56:533–557, 1972.

[127] R. Johnstone, L. Chen, and R.D. Sandberg. A sliding characteristic interface condition for direct numerical simulations. *Computers & Fluids*, 107(31):165–177, 2015.

[128] W. Joppich and M. Kürschner. Mpcci - a tool for the simulation of coupled applications. *Concurrency and Computation: Practice and Experience*, 18(2):183–192, 2006.

[129] O. Joshi and P. Leyland. Stability analysis of a partitioned fluid–structure thermal coupling algorithm. *Journal of Thermophysics and Heat Transfer,*, 28(1):59 – 67, 2014.

[130] G. Kalitzin, G. Medic, and J. A. Templeton. Wall modeling for LES of high Reynolds number channel flows: what turbulence information is retained? *Comput. Fluids* , 37(7):809–815, August 2008.

[131] Y. Kallinderis, A. Khawaja, and H. McMorris. Hybrid prismatic/tetrahedral grid generation for viscous flows around complex geometries. *AIAA Journal*, 34(2):291–298, 1996.

[132] Y. Kallinderis and S. Ward. Prismatic grid generation for three-dimensional complex geometries. *AIAA Journal*, 31(10):1850–1856, 1993.

[133] K. H. Kao and M. S. Liou. Application of chimera/unstructured hybrid grids for conjugate heat transfer. *AIAA Journal* , 35(9):1472–1478, 1997.

[134] K. S. Kedia and A.F. Ghoniem. The anchoring mechanism of a bluff-body stabilized laminar premixed flame. *Combust. Flame*, 161(9):2327–2339, 2014.

[135] K. S Kedia and A.F. Ghoniem. The response of a harmonically forced premixed flame stabilized on a heat-conducting bluff-body. *Proceedings of the Combustion Institute*, 35(1):1065–1072, 2015.

[136] K.S. Kedia, H.M. Altay, and A.F. Ghoniem. Impact of flame-wall interaction on premixed flame dynamics and transfer function characteristics. *Proc. Combust. Inst.* , 33:1113–1120, 2011.

[137] K.S. Kedia and A.F. Ghoniem. The blow-off mechanism of a bluff-body stabilized laminar premixed flame. *Combust. Flame*, 162(4):1304–1315, April 2015.

[138] M. K. Kim, D. K. Kim, S. H. Yoon, and D. H. Lee. Measurements of the flow fields around two square cylinders in a tandem arrangement. *Journal of Mechanical Science and Technology*, 22(2):397–407, 2008.

[139] J.E. Kopriva, G.M. Laskowski, and M. R.H. Sheikhi. Computational assessment of inlet turbulence on boundary layer development and momentum/thermal wakes for high pressure turbine nozzle and blade. In *ASME 2014 International Mechanical Engineering Congress and Exposition*, Montreal, Quebec, Canada, November 14–20 2014.

[140] C. Koren, R. Vicquelin, and O. Gicquel. An acceleration method for numerical studies of conjugate heat transfer with a self-adaptive coupling time step method: Application to a wall-impinging flame. In *ASME Turbo Expo 2017: Turbine Technical Conference and Exposition*, number GT2017-64224, Charlotte, NC, USA, June 26 - 30 2017.

[141] C. Koren, R. Vicquelin, and O. Gicquel. High-fidelity multiphysics simulations of confined premixed swirling flame combining large-eddy simulation, wall heat conduction and radiative energy transfer. In *ASME Turbo Expo 2017: Turbine Technical Conference and Exposition*, number GT2017-64844, Charlotte, NC, USA, June 26 - 30 2017.

[142] C. Koren, R. Vicquelin, and O. Gicquel. Self-adaptive coupling frequency for unsteady coupled conjugate heat transfer simulations. *International Journal of Thermal Sciences*, 118:340–354, 2017.

[143] V. Kornilov, R. Rook, J. ten Thije Boonkkamp, and L. de Goey. Experimental and numerical investigation of the acoustic response of multi-slit bunsen burners. *Combust. Flame*, pages 1957–1970, 2009.

[144] C. Koupper, L. Bonneau, L.Y.M. Gicquel, and F. Duchaine. Large-eddy simulation of the combustor turbine interface: study of the potential and clocking effects. In *ASME Turbo Expo 2016*, pages GT2016–56443, 2016.

[145] C. Koupper, G. Caciolli, L. Gicquel, F. Duchaine, G. Bonneau, L. Tarchi, and B. Facchini. Development of an engine representative combustor simulator dedicated to hot streak generation. *Journal of Turbomachinery*, 136(11), 2014.

[146] C. Koupper, L. Gicquel, F. Duchaine, T. Bacci, B. Facchini, A. Picchi, L. Tarchi, and G. Bonneau. Experimental and numerical calculation of turbulent timescales at the exit of an engine representative combustor simulator. *Journal of Engineering for Gas Turbines and Power*, 138(2):021503–021503, 09 2015.

[147] C. Koupper, L. Gicquel, F. Duchaine, and G. Bonneau. Advanced combustor exit plane temperature diagnostics based on large eddy simulations. *Flow, Turbulence and Combustion*, 95(1):79–96, 2015.

[148] C. Koupper, T. Poinsot, L. Gicquel, and F. Duchaine. Compatibility of characteristic boundary conditions with radial equilibrium in turbomachinery simulations. *AIAA Journal*, 52(12):2829–2839, 2014.

[149] R.H. Kraichnan. Diffusion by a random velocity field. *Phys. Fluids* , 13:22–31, 1970.

[150] R. Kristoffersen and H. Andersson. Direct simulations of low-Reynolds-number turbulent flow in a rotating channel. *Journal of Fluid Mechanics*, 256:163–197, 1993.

[151] Tay-Wo-Chong L and Polifke W. Large eddy simulation-based study of the influence of thermal boundary condition and combustor confinement on premix flame transfer functions. *ASME. J. Eng. Gas Turbines Power*, 135(2):021502–021502–9, 2013.

[152] L. Labarrère. *Etude théorique et numérique de la combustion à volume constant appliquée à la propulsion*. Phd thesis, Université de Toulouse - Ecole doctorale MEGeP, 3 2016.

[153] L. Labarrère, T. Poinsot, A. Dauptain, F. Duchaine, M. Bellenoue, and B. Boust. Experimental and numerical study of cyclic variations in a constant volume combustion chamber. *Combustion and Flame*, 172:49–61, 2016.

[154] H. Ladisch, A. Schulz, and H.-Jorg Bauer. Heat transfer measurements on a turbine airfoil with pressure side separation. In *ASME Turbo Expo 2009 : Power for Land, Sea, and Air*, Orlando, Florida, USA, 2009.

[155] D. Lahbib. *Modélisation aérodynamique et thermique des multiperforations en LES*. Phd thesis, Université de Montpellier - Ecole doctorale: Information, Structures et Systèmes (I2S), 12 2015.

[156] D. Lahbib, A. Dauptain, F. Duchaine, and F. Nicoud. Large-eddy simulation of conjugate heat transfer around a multi-perforated plate with deviation. In *ASME Turbo Expo 2016*, pages GT2016–56442, Seoul, South Korea, June 14-17 2016.

[157] B. Lakshminarayana. *Fluid Dynamics and Heat Transfer of Turbomachinery*. Wiley, 1996.

[158] N. Lamarque. *Schémas numériques et conditions limites pour la simulation aux grandes échelles de la combustion diphasique dans les foyers d'hélicoptère*. Phd thesis, INP Toulouse, 2007.

[159] E. Lamballais, M. Lesieur, and O. Métais. Effects of spanwise rotation on the vorticity stretching in transitional and turbulent channel flow. *International Journal of Heat and Fluid Flow*, 17(3):324–332, 1996.

[160] B. E. Launder, G. J. Reece, and W. Rodi. Progress in the development of a reynolds stress turbulence closure. *J. Fluid Mech.* , 68(3):537–566, 1975.

[161] P. D. Lax and B. Wendroff. Difference schemes for hyperbolic equations with high order of accuracy. *Commun. Pure Appl. Math.* , 17:381–398, 1964.

[162] D. H. Lee, Y. S. Chung, and S. Y. Won. The effect of concave surface curvature on heat transfer from a fully developed round impinging jet. *International Journal of Heat and Mass Transfer*, 42:2489–2497, 1999.

[163] J. Lee and S-J. Lee. Stagnation region heat transfer of a turbulent axisymmetric jet impingement. *Experimental Heat Transfer*, 12:137–156, 1999.

[164] S. Lee, S. Lele, and P. Moin. Simulation of spatially evolving turbulence and the applicability of taylor's hypothesis in compressible flows. *Phys. Fluids A*, 4(7):1521–1530, 1992.

[165] A. H. Lefebvre. *Gas Turbines Combustion*. Taylor & Francis, 1999.

[166] F. Lekien and J. Marsden. Tricubic interpolation in three dimensions. *Int. J. Numer. Meth. Eng.* , 63(3):455–471, 2005.

[167] T. Leonard, L.Y.M. Gicquel, N. Gourdain, and F. Duchaine. Steady/unsteady reynolds averaged navier-stokes and large eddy simulations of turbine blade at high subsonic outlet mach number. *Journal of Turbomachinery*, 137(4):041001–1: 041001–10, 2015.

[168] T. Leonard, M. Sanjosé, S. Moreau, and F. Duchaine. Large eddy simulation of a scale-model turbofan for fan noise source diagnostic. In *22nd AIAA/CEAS Aeroacoustics Conference*, Lyon, France, 30 May - 1 June 2016.

[169] T. Lieuwen. Modeling premixed combustion-acoustic wave interactions: A review. *J. Prop. Power* , 19(5):765–781, 2003.

[170] C.-H. Liu and J. M. Chen. Observations of hysteresis in flow around two square cylinders in a tandem arrangement. *Journal of Wind Engineering and Industrial Aerodynamics*, 90(9):1019–1050, 2002.

[171] J. Luo and E. H. Razinsky. Conjugate heat transfer analysis of a cooled turbine vane using the v2f turbulence model. *J. Turbomach.* , 129(4):773–781, 2007.

[172] D. A. Lyn and W. Rodi. The flapping shear layer formed by flow separation from the forward corner of a square cylinder. *J. Fluid Mech.* , 267:353–376, 1994.

[173] N. Maheu, V. Moureau, P. Domingo, F. Duchaine, and G. Balarac. Large-eddy simulations of flow and heat transfer around a low-mach number turbine blade. In Center for Turbulence Research, NASA Ames/Stanford Univ., editor, *Proc. of the Summer Program* , 2012.

[174] P. D. McCormack, H. Welker, and M. Kelleher. Taylor-Goertler vortices and their effect on heat transfer. *Journal of Heat Transfer*, 92(1):101–112, 1970.

[175] W.A. McMullan and G.J. Page. Towards large eddy simulation of gas turbine compressors. *Prog. in Astronautics and Aeronautics* , 52(0):30 – 47, 2012.

[176] D. Mejia, M. Brebion, A. Ghani, T. Kaiser, F. Duchaine, L. Selle, and T. Poinsot. Influence of flame-holder temperature on the acoustic flame transfer functions of a laminar flame. *Combustion and Flame*, Accepted, 2017.

[177] D. Mejia, L. Selle, R. Bazile, and T. Poinsot. Wall-temperature effects on flame response to acoustic oscillations. *Proc. Combust. Inst.* , 35(3201-3208):3, August 2014.

[178] S. Mendez and F. Nicoud. Adiabatic homogeneous model for flow around a multiperforated plate. *AIAA Journal* , 46(10):2623–2633, 2008.

[179] M. Mersinligil, J.-F. Brouckaert, N. Courtiade, and X. Ottavy. A high temperature high bandwith fast response total pressure probe for measurements in a multistage axial compressor. *J. Eng. Gas Turb. and Power* , 134, 2012.

[180] M. Mersinligil, J.-F. Brouckaert, N. Courtiade, and X. Ottavy. On using fast response pressure sensors in aerodynamic probes to measure total temperature and entropy generation in turbomachinery blade rows. *J. Eng. Gas Turb. and Power* , 135, 2013.

[181] D. E. Metzger and R. S. Bunker. Local Heat Transfer in Internally Cooled Turbine Airfoil Leading. *Journal of Turbomachinery*, 112:459–466, 1990.

[182] D. E. Metzger, T. Yamashita, and C. W. Jenkins. Impingement Cooling of Concave Surfaces With Lines of Circular Air Jets. *Journal of Engineering for Power*, 91(3):149–155, 1969.

[183] D. Michaels, S.J. Shanbhogue, and A.F. Ghoniem. The impact of reactants composition and temperature on the flow structure in a wake stabilized laminar lean premixed ch4/h2/air flames; mechanism and scaling. *Combustion and Flame*, 176:151–161, 2017.

[184] V. Michelassi, L. Chen, R. Pichler, and R.D. Sandberg. Compressible direct numerical simulation of low-pressure turbines—part ii: Effect of inflow disturbances. *Journal of Turbomachinery*, 137(7)::071005–071005–12, 2015.

[185] D. Mira, M. Vazquez, G. Houzeaux, S. Govert, J.W.B Kok, E.I Mahiques, and L. Panek. Study of the wall thermal condition effect in a lean-premixed downscaled can combustor using large-eddy simulation. In *Proceedings of ASME Turbo Expo 2016: Turbine Technical Conference and Exposition*, number GT2016-58016, Seoul, South Korea, June 14-17 2016.

[186] V. Moenne-Loccoz, I. Trébinjac, E. Benichou, S. Goguey, and B. Paoletti. An experimental description of the flow in a centrifugal compressor from al- ternate stall to surge. *Journal of Thermal Science*, 4:289–296, 2017.

[187] P. Moin and S. V. Apte. Large-eddy simulation of realistic gas turbine combustors. *AIAA Journal* , 44(4):698–708, 2006.

[188] L. Momayez, P. Dupont, and H. Peerhossaini. Some unexpected effects of wavelength and perturbation instability strength on heat transfer enhancement by Gortler instability. *International Journal of Heat and Mass Transfer*, 47:3783–3795, 2004.

[189] A. Montenay, L. Paté, and J. M. Duboué. Conjugate heat transfer analysis of an engine internal cavity. In *Proceedings of ASME Turbo Expo 2000*, number ASME Paper 2000-GT-282, Munich, Germany, May 2000.

[190] V. Moureau, G. Lartigue, Y. Sommerer, C. Angelberger, O. Colin, and T. Poinsot. Numerical methods for unsteady compressible multi-component reacting flows on fixed and moving grids. *J. Comput. Phys.* , 202(2):710–736, 2005.

[191] G. Mouret, N. Gourdain, and L. Castillon. Adaptation of phase-lagged boundary conditions to large eddy simulation in turbomachinery configurations. *Journal of Turbomachinery*, 138(4):041003, 2016.

[192] F. Nicoud, H. Baya Toda, O. Cabrit, S. Bose, and J. Lee. Using singular values to build a subgrid-scale model for large eddy simulations. *Phys. Fluids* , 23(8):085106, 2011.

[193] F. Nicoud and T. Poinsot. Dns of a channel flow with variable properties. In *Int. Symp. On Turbulence and Shear Flow Phenomena.*, Santa Barbara, Sept 12-15., 1999.

[194] F. Nobile and C. Vergara. An effective fluid-structure interaction formulation for vascular dynamics by generalized robin conditions. *SIAM Journal on Scientific Computing*, 30(2):731 – 763, 2008.

[195] N. Odier, F. Duchaine, L.Y.M Gicquel, G. Dufour, and N. García-Rosa. Comparison of les and rans predictions with experimental results of the fann of a turbofan. In *12th European Conference on Turbomachinery Fluid dynamics & Thermodynamics*, Stockholm, Sweden, April 3-7 2017.

[196] T.S. O'Donovan and D.B. Murray. Jet impingement heat transfer – Part I: Mean and root-mean-square heat transfer and velocity distributions. *International Journal of Heat and Mass Transfer*, 50:3291–3301, 2007.

[197] T. O'Mahoney, N. Hills, and J. Chew. Sensitivity of les results from turbine rim seals to changes in grid resolution and sector size. *Progress in Aerospace Sciences*, 52:48–55, 2012.

[198] X. Ottavy, N. Courtiade, and N. Gourdain. Experimental and computational methods for flow investigation in high-speed multistage compressor. *J. Prop. Power* , 28(6):1141–1155, 2012.

[199] X. Ottavy, I. Trébinjac, and A. Vouillarmet. Analysis of the interrow flow field within a transonic axial compressor: Part 1—experimental investigation. *ASME. J. Turbomach.*, 123(1):49–56, 2001.

[200] X. Ottavy, I. Trébinjac, and A. Vouillarmet. Analysis of the interrow flow field within a transonic axial compressor: Part 2—unsteady flow analysis. *ASME. J. Turbomach.*, 123(1):57–63, 2001.

[201] R. Paoli and K. Shariff. Turbulent condensation of droplets: direct simulation and a stochastic model. *J. Atmos. Sci.* , DOI 10.1175/2008JAS2734.1, 2008.

[202] D. Papadogiannis. *Coupled large eddy simulations of combustion chamber-turbine interactions.* PhD thesis, Université de Toulouse - Ecole Doctorale MEGeP, 5 2015.

[203] D. Papadogiannis, F. Duchaine, L. Gicquel, G. Wang, S. Moreau, and F. Nicoud. Assessment of the indirect combustion noise generated in a transonic high-pressure turbine stage. *Journal of Engineering for Gas Turbines and Power-Transactions of the ASME*, 138(4):0415030 (8 pp.), 2015.

[204] D. Papadogiannis, F. Duchaine, L.Y.M. Gicquel, G. Wang, and S. Moreau. Effects of subgrid scale modeling on the deterministic and stochastic turbulent energetic distribution in large-eddy simulations of a high-pressure turbine stage. *Journal of Turbomachinery*, 138(9):091005–091005–10, 2016.

[205] E. Papanicolaou, D. Giebert, R. Koch, and A. Schultz. A conservation-based discretization approach for conjugate heat transfer calculations in hot-gas ducting turbomachinery components. *Int. J. Heat and Mass Transfer* , 44:3413–3429, 2001.

[206] A. Piacentini, T. Morel, A. Thevenin, and F. Duchaine. Open-palm: an open source dynamic parallel coupler. In *In IV International Conference on Computational Methods for Coupled Problems in Science and Engineering*, 2011.

[207] R. Pichler, J. Kopriva, G. Laskowski, V. Michelassi, and R. Sandberg. Highly resolved les of a linear hpt vane cascade using structured and unstructured codes. In *ASME Turbo Expo 2016*, number GT2016-57189, Seoul, South Korea, June 14-17 2016.

[208] U. Piomelli. Wall-layer models for large-eddy simulations. *Prog. Aerospace Sci.* , 44(6):437–446, 2008.

[209] U. Piomelli, E. Balaras, H. Pasinato, K. D. Squires, and P. R. Spalart. The inner–outer layer interface in large-eddy simulations with wall-layer models. *Int. J. Heat Fluid Flow* , 24(4):538–550, August 2003.

[210] T. Poinsot. Prediction and control of combustion instabilities in real engines. *Proc. Combust. Inst.* , pages –, 2016.

[211] T. Poinsot, T. Echekki, and M. G. Mungal. A study of the laminar flame tip and implications for premixed turbulent combustion. *Combust. Sci. Technol.* , 81(1-3):45–73, 1992.

[212] T. Poinsot and S. Lele. Boundary conditions for direct simulations of compressible viscous flows. *J. Comput. Phys.* , 101(1):104–129, 1992.

[213] D. Poitou, J. Amaya, and F Duchaine. Parallel computation for the radiative heat transfer using the dom in combustion applications: direction, frequency, sub-domain decomposition and hybrid methods. *Numerical Heat Transfer, Part B Fundamentals*, 62(1):28–49, 2012.

[214] S. B. Pope. *Turbulent flows.* Cambridge University Press, 2000.

[215] M. Porta. *Développement, vérification et validation des outils LES pour l'étude du bruit de combustion et de l'interaction combustion/acoustique/turbulence - TH/CFD/07/46.* PhD thesis, Institut National Polytechnique de Toulouse, France - Dynamique des Fluides, CERFACS - CFD Team, Toulouse, 2007.

[216] A. Poubeau. *Simulation des émissions dÂťun moteur à propergol solide : vers une modéisation multi-échelle de lÂťimpact atmosphérique des lanceurs*. Phd thesis, SDUEE : Océan, Atmosphère et Surfaces Continentales, 2 2015.

[217] A. Poubeau, R. Paoli, A. Dauptain, F. Duchaine, and G. Wang. Large-eddy simulations of a single-species solid rocket booster jet. *AIAA Journal*, 53:1467 – 1491, 2015.

[218] T. Povey and I. Qureshi. Developments in hot-streak simulators for turbine testing. *Journal of Turbomachinery*, 131(3):1–15, 2009.

[219] M. Predari. *Load balancing for parallel coupled simulations*. PhD thesis, Ecole Doctorale de Mathematiques et d'informatique de l'Université de Bordeaux, 2016.

[220] M. Predari and A. Esnard. Coupling-aware graph partitioning algorithms: Preliminary study. In *IEEE International Conference on High Performance Computing*, Goa India, December 2014.

[221] E. Radenac. *Développement et validation d'une méthode numérique pour le couplage fluide structure en aérothermique instationnaire*. PhD thesis, Université Paul Sabatier - Toulouse, 2006.

[222] F. Rahman, J. A. Visser, and R. M. Morris. Capturing sudden increase in heat transfer on the suction side of a turbine blade using a navier-stokes solver. *J. Turbomach.* , 127(3):552–556, 2005.

[223] Man Mohan Rai. Navier-stokes simulations of rotor/stator interaction using patched and overlaid grids. *Journal of Propulsion and Power*, 3(5):387–396, 1987.

[224] A. Refloch, B. Courbet, A. Murrone, P. Villedieu, C. Laurent, P. Gilbank, J. Troyes, L. Tessé, G. Chaineray, J.B. Dargaud, E. Quémerais, and F. Vuillot. Cfd platforms and coupling - cedre software. *The Onera Journal Aerospace Lab*, (2), 2011.

[225] B. Roe, R. Jaiman, A. Haselbacher, and P. H. Geubelle. Combined interface boundary condition method for coupled thermal simulations. *Int. J. Numer. Meth. Fluids* , 57(3):329–354, 2008.

[226] S. Roux, M. Fénot, G. Lalizel, L.-E. Brizzi, and E. Dorignac. Experimental investigation of the flow and heat transfer of an impinging jet under acoustic excitation. *International Journal of Heat and Mass Transfer*, 54(15-16):3277–3290, 2011.

[227] P. Sagaut. *Large Eddy Simulation for incompressible flows*. Scientific computation series. Springer-Verlag, 2000.

[228] P. Sagaut. *Large eddy simulation for incompressible flows*. Springer, 2002.

[229] S. Salvadori, R. Giovanni, M. Insinna, and F. Martelli. Analysis of combustor/vane interaction with decoupled and loosely coupled approaches. In *ASME Turbo Expo 2012: Turbine Technical Conference and Exposition*, number GT2012-69038. ASME, 2012.

[230] R. Schiele and S. Wittig. Gas turbine heat transfer: Past and future challenges. *J. Prop. Power* , 16(4):583–589, July 2000.

[231] H. Schlichting. *Boundary-layer Theory*. McGraw-Hill Book Company, 7th edition, 1979.

[232] J. Schlüter, S. Apte, G. Kalitzin, E. van der Weide, J. J. Alonso, and H. Pitsch. Large-scale integrated LES-RANS simulations of a gas turbine engine. In *Annual Research Briefs* , pages 111–120. Center for Turbulence Research, NASA Ames/Stanford Univ., 2005.

[233] J. Schluter, X. Wu, E. v. d. Weide, S. Hahn, M. Herrmann, J. J. Alonso, and H. Pitsch. A python approach to multi-code simulations: Chimps. In *Annual Research Briefs* , pages 97–110. Center for Turbulence Research, NASA Ames/Stanford Univ., 2005.

[234] J. Schlüter, X. Wu, E. van der Weide, S. Hahn, J. Alonso, and H. Pitsch. Integrated les-rans of an entire high-spool of a gas turbine. In *44th AIAA Aerospace Sciences Meeting and Exhibit*, paper 0897, 2006.

[235] P. Schmitt, T. Poinsot, B. Schuermans, and K. P. Geigle. Large-eddy simulation and experimental study of heat transfer, nitric oxide emissions and combustion instability in a swirled turbulent high-pressure burner. *J. Fluid Mech.* , 570:17–46, 2007.

[236] S. Scholl, T. Verstraete, F. Duchaine, and L.Y.M Gicquel. Conjugate heat transfer of a rib-roughened internal turbine blade cooling channel using large eddy simulation. *International Journal of Heat and Fluid Flow*, 61(B):650 – 664, 2016.

[237] S. Scholl, T. Verstraete, J. Torres-Garcia, F. Duchaine, and L.Y.M. Gicquel. Influence of the thermal boundary conditions on the heat transfer of a rib-roughened cooling channel using les. *Proceedings of the Institution of Mechanical Engineers Part A-Journal of Power and Energy*, 229(5):498–507, 2015.

[238] A.D. Scillitoe, P.G. Tucker, and P. Adami. Numerical investigation of three-dimensional separation in an axial flow compressor: The influence of freestream turbulence intensity and endwall boundary layer state. *Journal of Turbomachinery*, 139(2):021011–021011–10, 2017.

[239] L.M. Segui, L.Y.M. Gicquel, F. Duchaine, and J. de Laborderie. Les of the ls89 cascade: influence of inflow turbulence on the flow predictions. In *12th European Conference on Turbomachinery Fluid dynamics & Thermodynamics*, Stockholm, Sweden, April 3-7 2017.

[240] V. Selmin. Third-order finite element schemes for the solution of hyperbolic problems. Technical Report 707, INRIA report, 1987.

[241] T. K. Sengupta. *Fundamentals of Computational Fluid Dynamics.* Universities Press, Hyderabad (India), 2004.

[242] Tapan K. Sengupta, V.K. Suman, and Neelu Singh. Solving navier-stokes equation for flow past cylinders using single-block structured and overset grids. *Journal of Computational Physics*, 229(1):178 – 199, 2010.

[243] Evan a Sewall and Danesh K Tafti. Large Eddy Simulation of Flow and Heat Transfer in the Developing Flow Region of a Rotating Gas Turbine Blade Internal Cooling Duct With Coriolis and Buoyancy Forces. *ASME Conference Proceedings*, 130, 2008.

[244] Scott E. Sherer and James N. Scott. High-order compact finite-difference methods on general overset grids. *J. Comput. Phys.* , 210(2):459 – 496, 2005.

[245] F. Shum Kivan, F. Duchaine, and L.Y.M. Gicquel. Large-eddy simulation and conjugate heat transfer in a round impinging jet. In *Proceedings of asme turbo expo 2014: turbine technical conference and exposition*, Dusseldorf, Germany, 2014.

[246] C.H. Sieverding, D. Ottolia, C. Bagnera, A. Comadoro, J.-F. Brouckaert, and J.-M. Desse. Unsteady turbine blade wake characteristics. *J. Turbomach.*, 126:551–559, 2004.

[247] C.H. Sieverding, H. Richard, and J.-M. Desse. Turbine blade trailing edge flow characteristics at high subsonic outlet mach number. *Transaction of the ASME*, 125:298–309, 2003.

[248] J. Smagorinsky. General circulation experiments with the primitive equations: 1. the basic experiment. *Mon. Weather Rev.* , 91:99–164, 1963.

[249] D. L. Sondak and D. J. Dorney. Simulation of coupled unsteady flow and heat conduction in turbine stage. *J. Prop. Power* , 16(6):1141–1148, 2000.

[250] D. B. Spalding. A single formula for the "Law of the Wall". *J. Appl. Mech.* , pages 455 –458, September 1961.

[251] W. Sturm and L. Fottner. The high-speed cascade wind-tunnel of the german armed forces university munich. In *8th Symposium on Measuring Techniques for Transonic and Supersonic Flows in Cascades and Turbomachines*, Genova, Italy, October 1985.

[252] G. I. Taylor. The spectrum of turbulence. *Proc. R. Soc. London Ser.*, A 164, 476, 1938.

[253] H. Tennekes and J. L. Lumley. *A first course in turbulence.* M.I.T. Press, Cambridge, 1972.

[254] M. Thomas, L.Y.M. Gicquel, F. Duchaine, and C. Koupper. Advanced statistical analysis estimating the heat load issued by hot streaks and turbulence on a high-pressure vane in the context of adiabatic large eddy simulations. In *ASME Turbo Expo 2017: Turbine Technical Conference and Exposition*, number GT2017-64648, Charlotte, NC, USA, June 26 - 30 2017.

[255] R. Toe, A. Ajakh, and H. Peerhossaini. Heat transfer enhancement by Gortler instability. *International Journal of heat and fluid flow*, 23:194–204, 2002.

[256] Andrea Toselli and Olof Widluhd. *Domain Decomposition Methods - Algorithms and Theory*, volume 34. Springer Series in Computational Mathematics, 2004.

[257] I. Trébinjac, P. Kulisa, N. Bulot, and N. Rochuon. Effect of unsteadiness on the performance of a transonic centrifugal compressor stage. *J. Turbomach.* , 131(4):041011–041011–9, 2009.

[258] P. Tucker, S. Eastwood, C. Klostermeier, R. Jefferson-Loveday, J. Tyacke, and Y. Liu. Hybrid LES approach for practical turbomachinery flows - part 1: hierarchy and example simulations. *J. Turbomach.*, 134(2), 2012.

[259] P. Tucker, S. Eastwood, C. Klostermeier, H. Xia, P. Ray, J. Tyacke, and W. Dawes. Hybrid LES approach for practical turbomachinery flows - part 2: further applications. *J. Turbomach.*, 134(2), 2012.

[260] P.G. Tucker. Computation of unsteady turbomachinery flows: Part 1 progress and challenges. *Prog. Aerospace Sci.* , 47(7):522 – 545, 2011.

[261] P.G. Tucker. Computation of unsteady turbomachinery flows: Part 2 LES and hybrids. *Prog. Aerospace Sci.* , 47(7):546 – 569, 2011.

[262] M. J. Tummers, J. Jacobse, and S. G. J. Voorbrood. Turbulent flow in the near field of a round impinging jet. *International Journal of Heat and Mass Transfer*, 54:4939–4948, 2011.

[263] S. Vagnoli, T. Verstraete, B. Mateos, and C.H. Sieverding. Prediction of the unsteady turbine trailing edge wake flow characteristics and comparison with experimental data. *Journal of Power and Energy*, 2015.

[264] S. Valcke, V. Balaji, A. Craig, C. DeLuca, R. Dunlap, R. W. Ford, R. Jacob, J. Larson, R. O'Kuinghttons, G. D. Riley, , and M. Vertenstein. Coupling technologies for earth system modelling. *Geosci. Model Dev. Discuss.*, 5:1987–2006, 2012.

[265] E. van der Weide, G. Kalitzin, J. Schluter, and J. J. Alonso. Unsteady turbomachinery computations using massively parallel platforms. In *44th AIAA Aerospace Sciences Meeting and Exhibit*, paper 0421, 2006.

[266] J.A. Verdicchio, J.W. Chew, and N.J. Hills. Coupled fluid/solid heat transfer computation for turbine discs. In *ASME Turbo Expo*, paper 2001-GT-0205, 2001.

[267] T. Verstraete and S. Scholl. Stability analysis of partitioned methods for predicting conjugate heat transfer. *International Journal of Heat and Mass Transfer*, 101(852-869), 2016.

[268] R. Vichnevetsky and J. B. Bowles. *Fourier analysis of numerical approximations of hyperbolic equations*. SIAM Studies in Applied Mechanics, Philadelphia, 1982.

[269] R. Viskanta. Heat transfer to impinging isothermal gas and flame jets. *Experimental Thermal and Fluid Science*, 6(2):111–134, 1993.

[270] J. H. Wagner, B V. Johnson, R. a. Graziani, and F. C. Yeh. Heat Transfer in Rotating Serpentine Passages With Trips Normal to the Flow. *Journal of Turbomachinery*, 114:847–857, 1992.

[271] G. Wang, S. Moreau, F. Duchaine, and L.Y.M. Gicquel. Les investigation of aerodynamics performance in an axial compressor stage. In *22nd annual conference of the cfd society of canada*, University of Toronto, Canada, 2014.

[272] G. Wang, M. Sanjosé, S. Moreau, D. Papadogiannis, F. Duchaine, and L.Y.M. Gicquel. Noise mechanisms in a transonic high-pressure turbine stage. *International Journal of Aeroacoustics*, 15(1-2):144–161, 2016.

[273] Gaofeng Wang, Florent Duchaine, Dimitrios Papadogiannis, Ignacio Duran, Stephane Moreau, and Laurent Y M Gicquel. An overset grid method for large eddy simulation of turbomachinery stages. *Journal of Computational Physics*, 274:333–355, October 2014.

[274] A.P.S. Wheeler, R.D. Sandberg, N.D. Sandham, R. Pichler, V. Michelassi, and G. Laskowski. Direct numerical simulations of a high pressure turbine vane. *Journal of Turbomachinery*, 138(7):071003–071003–9, 2016.

[275] P. Xavier, A. Ghani, D. Mejia, M. Brebion, M. Bauerheim, L. Selle, and T. Poinsot. Experimental and numerical investigation of flames stabilised behind rotating cylinders : interaction of flames with a moving wall. *Journal of Fluid Mechanics*, (127-151), 813.

[276] S.Y. Yoo, J.H. Park, C.H. Chung, and M.K. Chung. An Experimental Study on Heat/Mass Transfer From a Rectangular Cylinder. *Journal of Heat Transfer*, 125:1163, 2003.

[277] J. Zhang, O. Gicquel, D. Veynante, and J. Taine. Monte carlo method of radiative transfer applied to a turbulent flame modeling with les. *Comptes Rendus Mécanique*, 337(6–7):539–549, 2009.

[278] D. Zuzio, J-L Estivalezes, and B. DiPierro. An improved multiscale eulerian–lagrangian method for simulation of atomization process. *Computers & Fluids*, (In press), 2016.

Part II

Administrative elements

Chapter 6

Curriculum Vitae

Florent DUCHAINE
Senior Researcher in Fluid Dynamics
CERFACS, France

Research interests:

- Computational Fluid Dynamics
- Conjugate Heat Transfer
- Combustion instabilities
- Code coupling
- Massively parallel computations
- Large Eddy Simulations
- Optimization

Phone num.: 06 83 81 97 51
E-mail: florent.duchaine@cerfacs.fr
Url:
`http://www.cerfacs.fr/~duchaine`

CERFACS
42 avenue Gaspard Coriolis
31 057 Toulouse Cedex 01. France.

Nationality: French
37 years old
2 children

Professional Background

2010 – ... **Senior Researcher at CERFACS**
→ *Multi-physic and multi-component simulations*
- Conjugate heat transfer in gas turbine components with LES
- LES of turbomachinery stages
- LES of combustion chamber/turbine interactions

→ *Software development*
- TurboAVBP: extension of AVBP solver for turbomachinery simulations
- OpenPALM coupler: development, installation and test on massively parallel architectures
- Thermal solver AVTP and radiation solver PRISSMA
- Identification of coupling strategies for computations on massively parallel architectures

→ *Coordination of coupling activities for multi-physics and multi-composants simulations in the CFD Team of CERFACS*
→ *Setting up, coordination and execution of PRACE projects*
→ *Setting up, coordination and execution of European and national projects*

2009 – 2010 **Postdoctoral fellow at Institut de Mécanique des Fluides de Toulouse in PSC Team**
Advisor: Dr. Laurent Selle, IMFT (French project ANR SIGLE)
→ *Eulerian models for turbulent spray combustion with polydispersity*: Investigations in droplets coalescence in a LES framework
→ *Numerical investigations of combustor wall temperature effect on Flame Describing Functions (FDFs)*:
• Thermal coupling of a solid conduction solver and a reactive LES fluid code,
• Acoustic forcing of a laminar flame and determination of corresponding FDFs,
• Comparisons with experimental results.

2007 – 2009 **Postdoctoral fellow at CERFACS in CFD-Combustion group**
Advisor: Prof. Thierry Poinsot, IMFT
→ *Numerical investigations of conjugate heat transfer in gas turbines*:
• Thermal coupling of a solid conduction solver and a LES fluid code,
• Researches in coupling strategies,
• Applications to gas turbine components.

→ *Collaboration with Airbus on Large Eddy Simulations for heat transfer problems*
• Assessment of LES in academic flows with experimental and RANS comparisons,
• CHT in an experimental model of an aero engine nacelle cooling.

2006 **Automatization of a multi-physic framework for the prediction of combustion chamber walls temperature. SNECMA Moteur (France)**
Iterative loop based on 3D solvers: reactive multiphase flows / radiative / conduction in solid media.

2004 – 2007 **Ph.D. at CERFACS (preceded by a 7-month training period)**
Advisors: Prof. Thierry Poinsot, Institut de Mécanique des Fluides de Toulouse and Dr. L. Gicquel, CERFACS
Ph.D. funded by the European project INTELLECT-DM (contract of the FP6)
→ *Multi-objective Shape Optimization on Parallel Architectures with Meta-models and Couplers. Application to Aeronautical Combustion Chambers.*
Development of a fully parallel optimization tool based on a CFD reactive RANS code:
• Researches and developments in design optimization and code coupling applied to CFD,
• Implementation of the design tool on massively parallel architectures,
• Shape optimization of a combustion chamber.

2004 – 2005 Teaching in numerical fluid dynamics for Undergraduate students for Masters Degree in energetics engineering. ENSEEIHT (France)

2003 **Research training (6 months) at Institut de Mécanique des Fluides et des Solides de Strasbourg**
Advisor: Prof. Pierre Comte, IMFS Strasbourg
→ *Toward noise prediction of 3D turbulent jets.*
• Implementation and validation of characteristic boundary conditions in a LES solver,
• Simulations of 3D compressible round jets.

Education

2004 – 2007 **Ph.D. in Fluid Dynamics**
Institut National Polytechnique de Toulouse (France)

2003 – 2004 **Mastère Spécialisé (label CGE) in Numerical Fluid Dynamics**
Ecole Nationale Supérieure d'Electrotechnique, d'Electronique, d'Informatique, d'Hydraulique et des Télécomunications (ENSEEIHT) de Toulouse (France)

2002 – 2003 **Masters of Science in Mechanics and Energetics**
Institut National Polytechnique de Lorraine (France)

1998 – 2003 **Masters Degree in Engineering: Fluid Mechanics and Thermals**
Ecole Supérieure des Sciences et Technologies de l'Ingénieur de Nancy (ESSTIN - France)

Languages and Computer skills

Languages *French:* Native
English: Fluent conversational and written

Computer *Massively parallel computations:* C3I label from GENCI (`http://c3i.genci.fr`)
Programming: Fortran 90, MPI-1, HTML

Awards

2015 Teratech/Usine Digitale - Meilleure collaboration dans la simulation numérique

2013 Most Innovative Industrial HPC End-User Application in Europe

Activities and Interests

Reviewer *Scientific Journals*: Computers and Fluids, Journal of Heat and Mass Transfer, Combustion and Flame, Symposium of Combustion Institute, Journal of Applied Thermal Engineering et Journal of Aerospace Science and Technology, Journal of Applied Energy, Journal of Simulation Modeling Practice and Theory, International Journal of Numerical Methods in Fluid, Journal of Computational Physics and AIAA Journal.
French funding agency: Agence Nationale pour la Recherche (ANR) - evaluation of research projects

Capoeira President of the association *Capoeiragem* that promotes Brazilian arts (Toulouse)
Graded student entitled to give lessons

Chapter 7

Supervision, Collaboration, Animation

7.1 Supervision of students

I am involved in the supervision of different trainees, PhD student as well as post-docs. The following lists give the PhD for whom I was/am the official co-advisor as well as trainees and post-docs with whom I had/have a direct supervision role.

7.1.1 PhD students (all registered at MEGEP/INPT)

- Stéphan Jauré (2009-2012): CIFRE SNECMA, Conjugate heat transfer in gas turbine combustion chamber. Identification of coupling strategies for massively parallel computations.
- Charlie Koupper (2011-2014): CIFRE Turbomeca / EU Projet FACTOR, Towards the unsteady multi-physic simulations of aeronautical gas turbine combustion chamber and turbine components.
- Dimitrios Papadogiannis (2011-2014): Marie Curie action COPA-GT, large eddy simulation in turbine stage and interaction with combustion chamber.
- Sandrine Berger (2012-2016): CIFRE Turbomeca, Aerothermal predictions in aeronautical combustion chambers by coupling Large Eddy Simulation, radiation and conduction.
- Luis Segui Troth (2013-2017): Marie Curie action COPA-GT, wall modeling for heat transfer in LES.
- Thomas Grosnickel (2014-2017): Conjugate heat transfer in blade cooling channels.
- Pierre Aillaud (2014-2017): Heat transfer in high pressure stators: impinging jets and trailing edge flows.
- Luc Potier (2014-2017): CIFRE SNECMA, Heat transfer analysis in liquid boosters.
- Mael Harnieh (2015-2018): PIA project CASCADE, aerothermal predictions of high pressure stator with LES.
- Martin Thomas (2015-2018): CIFRE Turbomeca, LES of combustion chamber and turbine interactions.
- Soizic Esnault (2017-2020): DGA project OPTIMA, Heat transfer in liner acoustic treatment in aeronautical engine with LES.

7.1.2 Trainees

- Karine Minatchi (2005 - SNECMA): Determination of an industrial combustor wall temperature by code coupling.
- Matthieu Tarillon (2006 - SNECMA): Determination of an industrial combustor wall temperature by code coupling.
- Thomas Leonard (2006): Comparison between AVBP and elsA for turbomachinery applications.
- Pierre Trespeuch (2011): Comparison between OASIS and OpenPALM.
- Francis Shum Kivan (2013): Large Eddy Simulation and heat transfer of impinging jets.
- Yamina Boumediene (2014): Comparison of OASIS-MCT and OpenPALM HPC performances.
- Thomas Grosnickel (2014): Conjugate heat transfer in gas turbine ribs.
- Gauthier Le Chenadec (2016): Large eddy simulation of an aeronautic acoustic liner.
- Nikolaos Simiriotis (2016): Large eddy simulation of heat transfer around a shaped hole.
- Maxime Perini (2017): Investigation of phase lag approaches for Large Eddy Simulation.

7.1.3 Post-docs

- Jorge Amaya (2010): Unsteady coupled convection, conduction and radiation simulations on parallel architectures for combustion applications.
- Damien Poitou (2009-2011): FRAE Project STRASS, Analysis of the interaction between turbulent combustion and thermal radiation using unsteady coupled LES/DOM simulations.
- Gaofeng Wang (2011-2013): RTRA COFFECI project (Couplage Fluide/Fluide entre Codes Instationnaires) dealing with the simulation of a whole gas turbine by use of fuid/fluid coupling.
- Jérome de Laborderie (2013-2015): RTRA COFFECI project (Couplage Fluide/Fluide entre Codes Instationnaires) dealing with the simulation of a whole gas turbine by use of fuid/fluid coupling.
- Nicolas Odier (2015-2017): RTRA SIMACO3FI project dealing with the simulation of a whole gas turbine by use of fuid/fluid coupling.

7.2 Review activities

I am a reviewer for the following peer-review journals: Computers and Fluids, Journal of Heat and Mass Transfer, Combustion and Flame, Symposium of Combustion Institute, Journal of Applied Thermal Engineering et Journal of Aerospace Science and Technology, Journal of Applied Energy, Journal of Simulation Modeling Practice and Theory, International Journal of Numerical Methods in Fluid, Journal of Computational Physics et AIAA Journal.

Moreover, I am involved in the review of PRACE and INCITE projects as well as in expertises of ANR projects.

7.3 Contractual activities and collaborations

Since my PhD work, my research activities are linked to several national or international projects (ANR, FRAE, RTRA, FUI, PIA, DGA or European). The following list gives the main projects in which I have been involved, quoting my role in terms of execution, participation in the set-up and management.

- European projects:
  - INTELLECT DM (2004 - 2007): execution
  - FACTOR (2010 - 2015): execution
  - TECC-AE (2008 - 2013): execution
  - COPA-GT (2012 - 2015): participation in the set-up, execution
- FUI projects:
  - COSMOS+ (2012 - 2015) : participation in the set-up, involved in the management of a work package, execution
  - ICARUS (2017-2020) : participation in the set-up, execution
- ANR/FRAE projects:
  - SIGLE (2008 - 2012): execution
  - STRASS (2009 - 2012): participation in the set-up, execution
  - TIMBER (2014 - 2017) : participation in the set-up, involved in the management of a work package, execution
  - SIMUMOPS (2017-2020) : participation in the set-up, management of the project, execution
- PIA projects:
  - ELCI (2014 - 2017) : participation in the set-up, execution
  - CASCADE (2014 - 2017) : participation in the set-up, execution
- RTRA projects:
  - COFFECI (2011 - 2014): participation in the set-up, execution
  - SIMACO3FI (2014 - 2017): participation in the set-up, management of the project, execution
- DGA projects:
  - OPTIMA (2016 - 2019) : participation in the set-up, execution

To obtain larger quota of CPU hours that can provide the GENCI programs, I have been involved in the building of PRACE projects on identified scientific issues:

- 2012 - 2013 : SIMAC - Simulation of ignition mechanisms in annular multi-injector combustors and comparison with experiments
- 2013 - 2014 : Simulation of thermal environment of industrial combustors and comparison with experiments
- 2015 - 2016 : Large Eddy Simulation for FACTOR

Additionally, I participated to two *Grands challenges Scientifiques* during the test period of two GENCI supercomputers:

- 2012: CURIE - TGCC/GENCI: Aerothermal simulations of aeronautical combustion chambers.
- 2015: OCCIGEN - CINES/GENCI: Large Eddy Simulations of an axial multi-stage compressor.

For the different research subjects I address, I have regular and sustainable collaborations with many national and international labs. The following list sum-up the more important ones with a classification by theme that are not exhaustif and fix:

- Combustion, conjugate heat transfer and radiation:
  - EM2C
  - CORIA
  - IMFT
  - Institut Von Karman (Belgique)
  - I3M - University of Montpellier
  - CETHIL
- Turbomachinery flows:
  - University of Sherbrooke (Québec - Canada)
  - LMFA
  - ISAE
  - Cenaero (Belgique)
- Informatical and numerical aspects of code coupling:
  - INRIA
  - ONERA

Additionally, the European Climate Community has organized around several European projects (IS-ENES, IS-ENES2, `https://is.enes.org`) a working group on code coupling technics. More global reflexion and prospective actions have emerged from this group around a series of workshops involving international researchers from different fields (Coupling Technologies for Earth System Modeling : Today and Tomorrow). As a developer and user of the OpenPALM coupler on large number of cores, I participate to these actions. Similarly, I was involved in the panel of experts of the European project EESI2 (European Exascale Software Initiative 2 - `http://www.eesi-project.eu`) that aims to elaborate an evolutive European vision and roadmap and to propose recommendations to address the challenges of Extreme Data and Extreme Computing on the new generation of Exascale computers expected in 2020.

Every two years, the Center for Turbulence Research at Stanford organizes a Summer Program where worldwide researchers are invited to submit projects in many different field of fluid mechanics. I had the opportunity to participate to the last four ones being involved in different project in collaboration with different national and international labs leading to co-publications as listed:

- 2008 :
  - Coupling heat transfer solvers and Large Eddy Simulations for combustion applications : collaboration with Turbomeca and University of Montpellier.
- 2010 :
  - Sensitivity of flame transfer functions of laminar flames : collaboration with EM2C / Centrale Paris.

- 2012 :
  - Large-Eddy Simulations of flow and heat transfer around a low-Mach number turbine blade : collaboration with CORIA and LEGI
  - Stabilization mechanisms of a supercritical hydrogen / oxygen flame : collaboration with IMFT
  - DNS and LES of Separated Flows at Moderate Reynolds Numbers : collaboration with CTR/Stanfrod and university of Southern California
- 2014 :
  - Assessment of the indirect combustion noise generated in a transonic high-pressure turbine stage : collaboration with University of Sherbrooke, University of Montpellier and University of Minnesota

Considering relations with industries, the main partners I am working with are Cerfacs partners:

- SAFRAN Group (Turbomeca, SNECMA, Herakles, SNECMA Vernon, SAFRAN TECH)
- AIRBUS Group
- CNES

I am also involved in lab/industry networks such as:

- INCA : Initiative en Combustion Avancée
- HAIDA : cHAllenges aérothermIques et aéroDynAmiques
- CIRT : Consortium Industrie Recherche en Turbomachines

7.4 Animation activities and Teaching

Since my arrival at Cerfacs in October 2010, I am in charge of coupling activities in the CFD Team. The objectives are to organize collaborative meeting as well as centralize and mutualize methods and tools to ease technic and scientific growth of the team on these activities. Within this context, I became responsible since 2014 of the Cerfacs transverse axe *Coupling and interface*. My role is to coordinate discussions and reflexions on common prospects concerning Cerfacs couplers (OASIS-MCT and OpenPALM), define development strategies and more generally exchange about physical and informatics issues of code coupling for climate and fluid mechanic communities.

Computing activities realized at Cerfacs in the CFD team require a large amount of CPU time that cannot be achieved only with internal means. External ressources such as GENCI (from France), PRACE (from Europe) and INCITE (from United States) are thus mandatory. For the last four years, I managed a GENCI project for the Combustion activities in the CFD group. To do so, I am in charge every year to built the request proposal of CPU hours, to manage project execution (management of logins, CPU consomption, on the fly hour requests) and finally to provide to GENCI an annual activity report.
Since October 2014 I am involved in the CINES user committee (C4 - *Comité des Chercheurs Calculant au CINES*) in the fluid mechanics sections (CT2a and CT2b). C4 is a forum for exchange between CINES and its users. Our role is to give technical opinions on the guidelines for equipments, the choice of software applications, the quality and the evolution of the services on the new needs of the user community, etc.

As far as international scientific animation is concerned, I have participated to the following actions:

- I have co-organized with Dr L. Gicquel (Cerfacs) a mini-symposium on *High fidelity coupled simulation of reacting systems* during the 15th International Conference on Numerical Combustion (April 19-22 2015, Avignon).
- I was the co-chairman with Dr. A.M. Briones (University of Dayton Research Institute), of the *Combustion Modeling / Combustor Simulation* session of the ASME TurboExpo 2015 (June 15-19 2015 Montreal).
- In collaboration with researchers from ONERA (Prof. G. Casalis, Prof. B. Aupoix, Dr. J.L. Estivalezes and Dr. S. Deck) and from Cerfacs (Prof. T. Poinsot and J.F. Boussuge), we have organized the third edition of the MUSAF colloquium (Multiphysics and Unsteady Simulations for Aeronautical Flows) that taked place at Toulouse en September 2016 ((`http://musaf2016.onera.fr`).

Finally, in terms of teaching I participate to training sessions organized at Cerfacs: about two training sessions per year on the code coupler OpenPALM and one training session per year on turbomachinery. During my PhD, I gave tutorials to engineer students (ENSEEIHT) in 2005 and 2006. Since I arrived at Cerfacs, I dedicated my working time to code developments, researches and animations of different teams in the lab and preferred not to give external classes to focus my scientific activities. As teaching is an exercice I appreciate (in my private life, I am a teacher of Capoeira), I will make this choice evolves in future.

Finally, since 2011, I belong to the Cerfacs *Comité d'entreprise* board, with the role of treasurer.

7.5 Scientific vulgarization

I participated to the redaction of two vulgarization articles published by *The Conversation* (`http://theconversation.com/`). The first one concerns the importance of conjugate heat transfer to predict accurately physical phenomenon. The second one deals with the world *première* capability of being able to jointly simulate a combustion chamber and a high pressure turbine with Large Eddy Simulation.

Multiphysique, une discipline pour mieux prédire et comprendre les phénomènes complexes

1 mars 2017, 22:34 CET

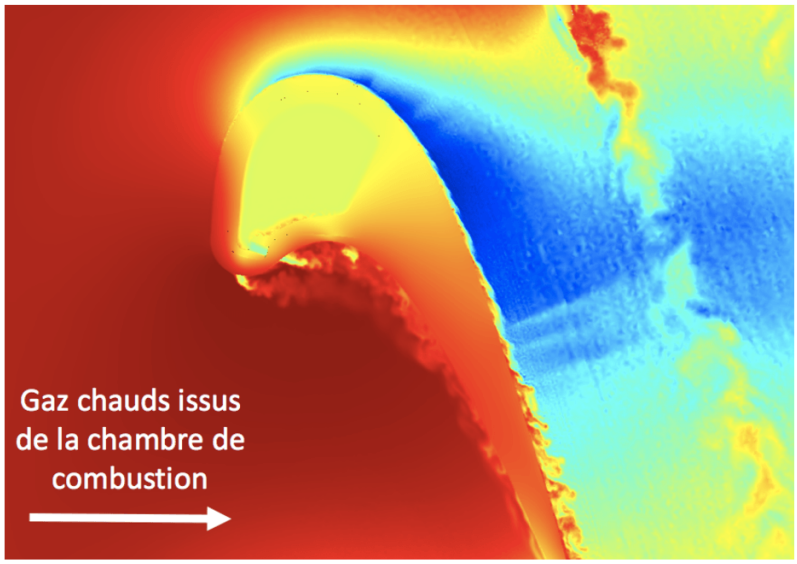

Champs de température issu d'une simulation jointe aérodynamique et thermique du solide d'une aube de turbine refroidie d'un moteur aéronautique. Cerfacs, Duchaine et coll., 2009, Author provided

Simulation intégrée : un nouvel outil au service de l'aéronautique

17 avril 2017, 20:40 CEST

Turboréacteur d'un avion de ligne. Cristianalkido/ Pixabay

Auteurs

Florent Duchaine
Chercheur senior, dynamique des fluides numérique, multiphysique, Cerfacs

Laurent GICQUEL
Chercheur, dynamique des fluides computationnelle, Centre Européen de Recherche et de Formation Avancée en Calcul Scientifique, Cerfacs

Déclaration d'intérêts

Les équipes de recherche du Cerfacs ont reçu des financements de l'Europe et du RTRA-STAE.

Les équipes de recherche du Cerfacs ont reçu des financements de l'Europe et du RTRA-STAE.

Partenaires

CERFACS

Cerfacs apporte un financement en tant que membre adhérent de The Conversation FR.

Voir les partenaires de The Conversation France

Part III

Publications

Chapter 8

List of publications

8.1 Papers in refereed journals

1. F. Duchaine, T. Morel and L.Y.M. Gicquel. Computational-Fluid-Dynamics-Based Kriging Optimization Tool for Aeronautical Combustion Chambers. AIAA Journal, 47(3):631-645, 2009

2. F. Duchaine, S. Mendez, F. Nicoud, A. Corpron, V. Moureau, and T. Poinsot. Conjugate heat transfer with large eddy simulation. Application to gas turbine components. In C.R.A.S. Mécanique, 2009. 337(6-7), 550-561

3. N. Gourdain, L. Gicquel, G. Staffelbach, O. Vermorel, F. Duchaine, J-F. Boussuge and T. Poinsot. High performance parallel computing of flows in complex geometries - part 2: applications, Computational Science & Discovery 2(1): 015004, 2009

4. F. Duchaine, A. Corpron , V. Moureau , F. Nicoud , T. Poinsot. Development and assessment of a coupled strategy for conjugate heat transfer with Large Eddy Simulation. Application to a cooled turbine blade. International Journal of Heat and Fluid Flow, 30(6): 1129-1141, 2009

5. F. Duchaine, F. Boudy, D. Durox and T. Poinsot. Sensitivity analysis of transfer functions of laminar flames. Combustion and Flame, 158(12):2384-2394, 2011

6. D. Poitou, J. Amaya and F. Duchaine. Parallel computation for the radiative heat transfer using the DOM in combustion applications: direction, frequency, sub-domain decomposition and hybrid methods. Numerical Heat Transfer, Part B Fundamentals, 62-1, 2012

7. E. Collado Morata, N. Gourdain, F. Duchaine, L.Y.M. Gicquel. Effect of free-stream turbulence on high pressure turbine blade heat transfer using structured and unstructured LES. International Journal of Heat and Mass Transfer, 55(21-22):5754-5768, 2012

8. M. Boileau, F. Duchaine, J.-C. Jouhaud and Y. Sommerer. Large Eddy Simulation of of heat transfer around a square cylinder using unstructured grids. AIAA Journal, Vol. 51, No. 2 (2013), pp. 372-385

9. F. Duchaine, N. Maheu, V. Moureau, G. Balarac and S. Moreau. Large Eddy Simulation and Conjugate Heat Transfer Around a Low-Mach Turbine Blade. Journal of Turbomachinery 136(5), 2013

10. S. Jauré, F. Duchaine, G. Staffelbach and L.Y.M. Gicquel. Massively parallel conjugate heat transfer solver based on Large Eddy Simulation and application to an aeronautical combustion chamber. Journal of Computational Science and Discovery, 6:015008, 2013.

11. C. Koupper, T. Poinsot, L. Gicquel and F. Duchaine. On the ability of characteristic boundary conditions to comply with radial equilibrium in turbomachinery simulations. AIAA Journal. Vol. 52, No. 12 (2014), pp. 2829-2839.

12. G. Lecocq, D. Poitou, I. Hernandez, F. Duchaine, E. Riber and B. Cuenot. A methodology for soot prediction including thermal radiation in complex industrial burners. Flow Turbulence and Combustion, 92(4):947-970. 201. 2014

13. A. Bonhomme, G. Wang, L. Selle, F. Duchaine and T. Poinsot. A parallel multidomain coupled strategy to compute turbulent flows in fan-stirred bombs. Computers and Fluids, 101:183-193. 2014

14. G. Wang, F. Duchaine, D. Papadogiannis, I. Duran, S. Moreau and L.Y.M Gicquel. An overset grids method for large eddy simulation of turbomachinery stages. Journal of Computational Physics, 274:333-355. 2014

15. F. Duchaine, M. Boileau, Y. Sommerer and T. Poinsot. Large Eddy Simulation of the flow and heat transfer around two square cylinders in a tandem arrangement. Journal of Heat Transfer. 2014. 136(10), 101702

16. N. Gourdain F. Sicot, F. Duchaine and L. Gicquel. Large Eddy Simulation of flows in industrial compressors: a path from 2015 to 2035. Philosophical Transactions A. 2014. 372(2022):20130323

17. C. Koupper, G. Bonneau, G. Caciolli, B. Facchini, L. Tarchi, L.Y.M. Gicquel and F. Duchaine. Development of an Engine Representative Combustor Simulator Dedicated to Hot Streak Generation. Journal of Turbomachinery. 2014. 136(11), 111007

18. T. Leonard, N. Gourdain, L. Gicquel and F. Duchaine. Steady / Unsteady Reynolds Averaged Navier-Stokes and Large Eddy Simulations of Turbine Blade at High Subsonic Outlet Mach Number. Journal of Turbomachinery. 2014. 137(4), 041001

19. C. Koupper, L. Gicquel, F. Duchaine and G. Bonneau. Advanced combustor exit plane temperature diagnostics based on Large Eddy Simulations. Flow, Turbulence and Combustion. 2015. 95(1):79-96

20. A. Poubeau, R. Paoli, A. Dauptain, F. Duchaine and G. Wang. Large Eddy Simulation of a solid rocket booster jet: towards a better prediction of the impact of solid-fuel launchers on the atmosphere. AIAA Journal. 2015. Vol. 53, No. 6, pp. 1477-1491

21. S. Scholl, T. Verstraete, J. Torres-Garcia, F. Duchaine and L. Y. M. Gicquel. Influence of the Thermal Boundary Conditions on the Heat Transfer of a Rib-Roughened Cooling Channel using LES. Proceedings of the Institution of Mechanical Engineers, Part A: Journal of Power and Energy. 2015. 229(5), 498-507

22. F. Duchaine, S. Jauré, D. Poitou, E. Quémerais, G. Staffelbach, T. Morel and L. Gicquel. Analysis of High Performance Conjugate Heat Transfer with the OpenPALM Coupler. Journal of Computational Science and Discovery. 8:015003, 2015

23. D. Papadogiannis, F. Duchaine, L.Y.M. Gicquel, G. Wang, S. Moreau and F. Nicoud. Assessment of the indirect combustion noise generated in a transonic high-pressure turbine stage. ASME. J. Eng. Gas Turbines Power. 2015;138(4):041503-041503-8

24. C. Koupper, T. Bacci, B. Facchini, A. Picchi, L. Tarchi, L. Gicquel, F. Duchaine and G. Bonneau. Experimental and numerical calculation of turbulent timescales at the exit of an engine representative combustor simulator. Journal of Engineering for Gas Turbines and Power. 2015;138(2):021503-021503-10

25. G. Wang, M. Sanjose, S. Moreau, D. Papadogiannis, F. Duchaine and L.Y.M Gicquel. Noise mechanisms in a transonic high-pressure turbine stage. International Journal of Aeroacoustics, 0(0) 1Ð18, 2016

26. M.P. Errera and F. Duchaine. Comparative study of coupling coefficients in Dirichlet-Robin precedure for fluid-structure aerothermal simulations. Journal of Computational Physics. 2016. 312:218Ð234

27. D. Papadogiannis, F. Duchaine, L. Gicquel, G. Wang and S. Moreau. Effects of Sub-Grid-Scale modeling on the deterministic and stochastic turbulent energetic distribution in LES of a high pressure turbine stage. Journal of Turbomachinery. 138(9), 091005. 2016

28. R. Mari, J.P. Rocchi. F. Duchaine, L. Selle and B. Cuenot. Effect of pressure on Hydrogen/Oxygen coupled flame-wall interaction. Combustion and Flame. 168:409-419. 2016

29. S. Berger, S. Richard, F. Duchaine, G. Staffelbach and L. Gicquel. On the sensitivity of a helicopter combustor wall temperature to convective and radiative thermal loads. Applied Thermal Engineering. 103(25):1450-1459. 2016

30. L. Labarrere, T. Poinsot, A. Dauptain, F. Duchaine, M. Bellenoue and B. Boust. Experimental and numerical study of cyclic variations in a Constant Volume Combustion Chamber. Combustion and Flame. 172:49-61, 2016

31. M. Brebion, D. Mejia, P. Xavier, F. Duchaine, B. Bedat, L. Selle and T. Poinsot. Joint experimental and numerical study of the influence of flame holder temperature on the stabilization of a laminar flame on a cylinder. Combustion and Flame. 172:153-161, 2016

32. S. Scholl. T. Verstraete, F. Duchaine and L. Gicquel. Large Eddy Simulation and conjugate heat transfer of a rib-roughened internal turbine blade cooling channel. International Journal of Heat and Fluid Flow. Vol 61 - Part B, pp 650-664, 2016.

33. P. Aillaud, F. Duchaine, L.Y.M Gicquel and S. Didorally. Secondary peak in the Nusselt number distribution of impinging jet flows: A phenomenological analysis. Physics of Fluids. 28(9):, 2016.

34. F. Duchaine, J. Dombard, L.Y.M Gicquel and C. Koupper. On the importance of inlet boundary conditions for aerothermal predictions of turbine stages with Large Eddy Simulation. Computers and Fluids. 154, pp60-73, 2017

35. D. Mejia, M. Miguel-Brebion, A. Ghani, T. Kaiser, F. Duchaine, L. Selle, T. Poinsot. Influence of flame-holder temperature on the acoustic flame transfer functions of a laminar flame. Combustion and Flame. 188:5-12, 2018

36. S. Berger, F. Duchaine and L.Y.M. Gicquel. Bluff-body thermal property and initial state effects on a laminar premixed flame anchoring pattern. Accepted in Flow, Turbulence and Combustion.

37. P. Aillaud, L. Y. M. Gicquel, and F. Duchaine. Jet impingement onto flat and concave surfaces: A detailed comparison of flow dynamics and heat transfer. Accepted in Phys. Rev. Fluids.

38. J. de Laborderie, F. Duchaine and L.Y.M. Gicquel. Numerical Analysis of a High-Order Unstructured Overset Grid Method for Compressible Large Eddy Simulation. Submitted to Journal of Computational Physics.

8.2 Book Chapters

1. G. Dufour, N. Gourdain, F. Duchaine, O. Vermorel, L. Gicquel, J-F. Boussuge and T. Poinsot. Large Eddy Simulation Applications. VKI Lecture Series Numerical Investigations in Turbomachinery: the State of the Art, Rhodes-St-Genese (Belgique), Sept. 21-25, 2009.

2. Gicquel L.Y.M., Vermorel O., Duchaine F., Riber E., Dauptain A., Staffelbach G., Cuenot B., and Poinsot T. J. ERCOFTAC - Best Practice Guidelines in Computational Fluid Dynamics of Turbulent combustion, Chapter 4: Gas Turbine and Industrial Burners. 2013.

3. F. Duchaine, S. Berger, G. Staffelbach and L. Gicquel. Partitioned High Performance Code Coupling Applied to CFD. In LNCS, Theoretical Computer Science and General Issues High-Performance Scientific Computing. First JARA-HPC Symposium, JHPCS 2016, Aachen, Germany, October 4-5, 2016, Di Napoli, E., Hermanns, M.-A., Iliev, H., Lintermann, A., Peyser, A. (Eds.)

8.3 Invited lectures

1. F. Duchaine, M. Garcia, P. Wolf, G. Staffelbach, M. Boileau, M. Leyko, B. Enaux and T. Poinsot. Massively Parallel simulation of combustion engines. CScADS Workshop on Scientific Data Analysis and Visualization for Petascale Computing, Tahoe City, (CA, USA), Aug. 3-6, 2009.

2. F. Duchaine and T. Poinsot. Prédictions aérothermiques par couplage de codes de simulations aux grandes échelles et de thermique. CRCT - Centre de Recherche sur la Combustion Turbulente, IFP, Rueil-Malmaison (France), March 30, 2010

3. T. Poinsot, T. Leonard, F. Duchaine, V. Moureau, L. Pons, J. Amaya, E. Collado and B. Cuenot. LES and multi-physics for engine computations on massively parallel machines. MUSAF - Multiphysics and Unsteady Simulations for Aeronautical Flows, CERFACS, Toulouse (France), Sept. 27-29, 2010

4. A. Piacentini, T. Morel, A. Thévenin and F. Duchaine. The dynamic parallel PALM coupler. Workshop on "Coupling Technologies for Earth System Modelling : Today and Tomorrow", CERFACS, Toulouse (France), Dec. 15-17, 2010.

5. T. Poinsot and F. Duchaine. Simulations of fame/wall interactions and effects on combustion instabilities. First International Workshop on Near-Wall Reactive Flows, Lufthansa Center, Darmstadt/Seeheim-Jungenheim (Allemagne), Nov. 18-19, 2010.

6. L.Y.M. Gicquel, B. Cuenot, G. Staffelbach, O. Vermorel, E. Riber, A. Dauptain, F. Duchaine, and T. Poinsot. LES modeling and sensitivity issues - implications on the prediction and flame dynamics - Invited conference. In GE Global Research Symposium on LES of Turbulent Reacting Flows for GT Design, Niskayuna, NY, USA, 2011.

7. F. Duchaine and G. Staffelbach. Large Eddy Simulation and Muti-physics for Engine computations on Massively Parallel Machines. Toward petaflop numerical simulation on parallel hybrid architectures, CEA-EDF-INRIA summer school, INRIA, Sophia Antipolis (France), June 6-10, 2011

8. F. Duchaine, D. Mejia, L. Selle, T. Poinsot, F. Boudy and D. Durox. Couplage entre thermique et instabilitées de combustion. CRCT - Centre de Recherche sur la Combustion Turbulente, Centrale Paris, Chatenay-Malabry (France), March 29, 2011

9. L.Y.M. Gicquel, B. Cuenot, G. Staffelbach, O. Vermorel, E. Riber, A. Dauptain, F. Duchaine, N. Gourdain, F. Sicot and T. Poinsot. CERFACS State-of-the-art and recent investigations for temperature predictions in Turbo-machineries - Invited conference. In GE Global Research Symposium on High Fidelity Simulations of Combustion Turbine Systems, Niskayuna, NY, USA, 2012.

10. A. Thevenin, Th. Morel, F. Duchaine, A. Piacentini, M. Kirmse, S.Valcke and L. Coquart. OASIS3-MCT and Open-PALM: 2 open source codes couplers. In Advanced Dynamical Core Modeling for Atmospheric and Oceanic Circulations, Pradesh, India, 2013.

11. F. Duchaine, A. Thevenin, A. Piacentini, E. Quémerais, and T. Morel. OpenPALM, an open source code coupler for massively parallel multi-physics/multi-components applications and dynamic algorithms. In BibliothŔques pour le calcul scientifique: outils, enjeux et écosystŔme, Paris, France, 2013.

12. F. Duchaine, T. Morel, S. Jauré, D. Poitou, G. Staffelbach, L. Gicquel and E. Quémerais. High Performance Conjugate Heat Transfer with the OpenPALM Coupler. Coupling Workshop, Boulder, CO, USA, February 20-22, 2013.

13. L.Y.M. Gicquel, B. Cuenot, G. Staffelbach, O. Vermorel, E. Riber, A. Dauptain, F. Duchaine, J. Dombard and T. Poinsot. Simulations of ignition and acoustic instabilities. In Workshop on Turbulent Combustion, University of Michigan, Ann Arbor, June 9th-10th, 2014.

14. F. Duchaine, G. Wang, D. Papadogiannis, S. Moreau and L. Gicquel. On code coupling - Focus on multi-fluid/components coupling. CRCT - Centre de Recherche sur la Combustion Turbulente, Centrale Paris, ChŁtenay-Malabry (France), March 27, 2014.

15. G. Staffelbach, A. Dauptain, E. Riber, O. Vermorel, L. Gicquel, B. Cuenot, F. Duchaine and J. Dombard. HPC and Combustion. EuroMPI 2015, September 21-23, Bordeaux, France.

16. F. Duchaine, D. Papadogiannis, J. De Laborderie, L.Y.M Gicquel, G. Wang and S. Moreau. Towards the simulation of compressor, combustion chamber and turbine interactions. 3rd ECCOMAS Young Investigators Conference. July 20-23, 2015, Aachen, Germany

17. F. Duchaine et al. Efficient Couplers for Extreme Computing. EESI Final Conference, May 28-29, 2015.

18. F. Duchaine et al. User presentation on Data Centric Approach in turbulent flows. EESI Final Conference, May 28-29, 2015.

19. F. Duchaine, S. Berger, G. Staffelbach and L. Gicquel. Partitioned High Performance Code Coupling Applied to CFD. JHPCS'16 - JARA-HPC Symposium. Oct. 4-5 2016. Aachen, Germany.

20. G. Staffelbach, B. Cuenot, A. Dauptain, J. Dombard, F. Duchaine, L. Gicquel, A. Misdariis, E. Riber, O. Vermorel T. Poinsot, J. Legaux, I. D'Ast, N. Monnier. JHPCS'16 - JARA-HPC Symposium. Oct. 4-5 2016. Aachen, Germany

8.4 Papers published in refereed conference proceedings

1. F. Duchaine, L.Y.M. Gicquel, T.J. Poinsot, D. Bissières, and C. Bérat. Optimization Loop Based on a CFD RANS Code. In ICAS 2006, Hamburg, Germany, 2006.

2. F. Wlassow, F. Duchaine, G. Leroy and N. Gourdain. 3D Simulation of Coupled Fluid Flow and Solid Heat Conduction for the Calculation of Blade Wall Temperature in a Turbine Stage. GT2010-22513. In ASME Turbo Expo 2010, Glasgow, Scotland UK.

3. N. Gourdain, F. Duchaine, E. Collado and L. Gicquel. Advanced Numerical Simulation Dedicated to the Prediction of Heat Transfer in a Highly Loaded Turbine Guide Vane. GT2010-22793. In ASME Turbo Expo 2010, Glasgow, Scotland UK.

4. T. Leonard, F. Duchaine, N. Gourdain and L. Gicquel. Steady / Unsteady Reynolds Averaged Navier-Stokes and Large Eddy Simulations of Turbine Blade at High Subsonic Outlet Mach Number. GT2010-22469. In ASME Turbo Expo 2010, Glasgow, Scotland UK.

5. S. Jauré, F. Duchaine and L. Gicquel. Comparisons of Coupling Strategies for Massively Parallel Conjugate Heat Transfer with Large Eddy Simulation. In IV International Conference on Computational Methods for Coupled Problems in Science and Engineering - Coupled Problems 2011, Kos Island, Greece, 2011

6. A. Piacentini, T. Morel, A. Thévenin and F. Duchaine. O-PALM : An Open Source Dynamic Parallel Coupler. In IV International Conference on Computational Methods for Coupled Problems in Science and Engineering - Coupled Problems 2011, Kos Island, Greece, 2011

7. J. Habert, S. Ricci, A. Piacentini, G. Jonville, T. Morel, F. Duchaine, A. Thevenin, E. Le Pape, O. Thual, N. Goutal, F. Zaoui and R. Ata. Estimation of lateral inflows using data assimilation in the context of real-time flood forecasting for the Marne catchment in France. In XIXth TELEMAC-MASCARET User Conference. Oxford, UK, October 18-19, 2012.

8. M. Rochoux, J.-M. Bart, S. Ricci, B. Cuenot, A. Trouvé, F. Duchaine and T. Morel. Towards Data-Driven Simulations of Wildfire Spread using Ensemble-based Data Assimilation. H23C-1367. In 2012 AGU Fall Meeting, 3-7 December 2012, San Francisco, USA.

9. A. Piacentini, S. Ricci, E. Le Pape, J. Habert, G. Jonville, N. Goutal, S. Barthélémy, T. Morel, F. Duchaine and O. Thual. Towards operational flood forecasting using Data Assimilation. H23C-1367. In 2012 AGU Fall Meeting, 3-7 December 2012, San Francisco, USA.

10. S. Ricci, A. Piacentini, R. Ata, N. Goutal, E. Razafindrakoto, F. Zaoui, M. Gant, T. Morel, F. Duchaine, O. Thual. A variational Data Assimilation algorithm to better estimate the salinity for the Berre lagoon with Telemac3D. H21J-03. In 2012 AGU Fall Meeting, 3-7 December 2012, San Francisco, USA.

11. B. Cuenot, A. Dauptain, F. Duchaine, L. Gicquel, T. Poinsot, E. Riber, G. Staffelbach, O. Vermorel. Simulations aux Grandes Echelles : instabilites thermo-acoustiques, combustion diphasique et couplages multi-physiques. In 21ieme Congres Francais de Mecanique, Bordeaux, 26 au 30 aout 2013.

12. G. Wang, S. Moreau, F. Duchaine, N. Gourdain, and L.Y.M. Gicquel. Large Eddy Simulations of the MT1 high-pressure turbine using TurboAVBP. In CFD Canada, May 6-9, 2013, Sherbrooke, Quebec.

13. T. Leonard, F. Duchaine, L.Y.M. Gicquel, G. Wang and N. Gourdain. Application of Large-Eddy Simulation to rotor/stator configurations. In CongrŔs FranÐais de Mécanique, August 26-30, 2013, Bordeaux, France.

14. F. Duchaine, S. Jauré, D. Poitou, E. Quémerais, G. Staffelbach, T. Morel and L. Gicquel. High performance conjugate heat transfer with the OpenPALM coupler. In V International Conference on Coupled Problems in Science and Engineering - Coupled Problems 2013, Ibiza, Spain, 2013.

15. G. Wang, D. Papadogiannis, F. Duchaine, G. Staffelbach, N. Gourdain, L.Y.M. Gicquel. Towards Massively Parallel Large Eddy Simulation of Turbine Stages. GT2013-94852. In ASME Turbo Expo 2013, San Antonio, Texas USA.

16. F. Duchaine, N. Maheu, V. Moureau, G. Balarac and S. Moreau. Large Eddy Simulation and Conjugate Heat Transfer Around a Low-Mach Turbine Blade. GT2013-94257. In ASME Turbo Expo 2013, San Antonio, Texas USA.

17. G. Wang, S. Moreau, F. Duchaine, J. de Laborderie and L.Y.M. Gicquel. LES Investigation of Aerodynamics Performance in an Axial Compressor Stage. In CFD Canada, June 1-4, 2014, Toronto, Canada.

18. D. Papadogiannis, F. Duchaine, F. Sicot, L.Y.M. Gicquel, G. Wang and S. Moreau. Large Eddy Simulation of a high pressure turbine stage: effects of sub-grid scale modelling and mesh resolution. GT2014-25876. In ASME Turbo Expo 2014, Dusseldorf, Germany.

19. C. Koupper, G. Bonneau, G. Caciolli, B. Facchini, L. Tarchi, L.Y.M. Gicquel and F. Duchaine. Development of an Engine Representative Combustor Simulator Dedicated to Hot Streak Generation. GT2014-25120. In ASME Turbo Expo 2014, Dusseldorf, Germany.

20. F. Shum Kivan, F. Duchaine and L.Y.M. Gicquel. Large-Eddy Simulation and Conjugate Heat Transfer in a round impinging jet. GT2014-25152. In ASME Turbo Expo 2014, Dusseldorf, Germany.

21. M.P. Errera and F. Duchaine. Stable and fast numerical schemes for conjugate heat transfer. In ICHMT International Symposium on Advances in Computational Heat Transfer, May 25-29, 2015, Rutgers University, Piscataway, USA.

22. S. Scholl, T. Verstraete, J. Torres-Garcia, F. Duchaine, L. Y. M. Gicquel Influence of the Thermal Boundary Conditions on the Heat Transfer of a Rib-Roughened Cooling Channel using LES. In 11th European Turbomachinery Conference, 2015, March 23-27, Madrid, Spain.

23. C. Koupper, T. Bacci, B. Facchini, A. Picchi, L. Tarchi, L. Gicquel, F. Duchaine and G. Bonneau. Experimental and numerical calculation of turbulent timescales at the exit of an engine representative combustor simulator. GT2015-42278. In ASME Turbo Expo 2015, Montreal, Canada.

24. D. Papadogiannis, F. Duchaine, L. Gicquel, G. Wang, S. Moreau and F. Nicoud. Assessement of the indirect combustion noise generated in a transonic high-pressure turbine stage. GT2015-42399. In ASME Turbo Expo 2015, Montreal, Canada.

25. S. Berger, S. Richard, G. Staffelbach, F. Duchaine and L. Gicquel. Aerothermal prediction of an aeronautical combustion chamber based on the coupling of Large Eddy Simulation, solid conduction and radiation solvers. GT2015-42457. In ASME Turbo Expo 2015, Montreal, Canada.

26. S. Berger, S. Richard, F. Duchaine and L. Gicquel. Variations of anchoring pattern of a bluff-body stabilized laminar premixed flame as a function of the wall temperature. GT2016-56473. In ASME Turbo Expo 2016, Seoul, South Korea.

27. P. Aillaud, F. Duchaine and L. Gicquel. LES of a round impinging jet: investigation of the link between Nusselt secondary peak and near-wall vorical structures. GT2016-56111. In ASME Turbo Expo 2016, Seoul, South Korea.

28. D. Lahbib, A. Dauptain, F. Duchaine and F. Nicoud. Large-Eddy Simulation of conjugate heat transfer around a multi-perforated plate with deviation. GT2016-56442. In ASME Turbo Expo 2016, Seoul, South Korea.

29. J. de Laborderie, F. Duchaine, O. Vermoreli, L. Gicquel and S. Moreau. Application of an overset grid method to the Large-Eddy Simulation of a high speed multistage axial compressor. GT2016-56344. In ASME Turbo Expo 2016, Seoul, South Korea.

30. C. Koupper, G. Bonneau, L. Gicquel and F. Duchaine. Large-Eddy Simulation of the combustor turbine interface: study of the potential and clocking effects. GT2016-56443. In ASME Turbo Expo 2016, Seoul, South Korea.

31. P. Aillaud, F. Duchaine, L. Gicquel. Analyse aerothermique d'un jet circulaire impactant sur plaque plane a l'aide de la SGE. In Congres Francais de Thermique 2016. 31 may - 3 june 2016. Toulouse, France.

32. S. Berger, F. Duchaine and L. Gicquel. Influence des conditions aux limites thermiques sur la stabilisation d'une flamme laminaire premelangee. In Congres Francais de Thermique 2016. 31 may - 3 june 2016. Toulouse, France.

33. T. Leonard, M. Sanjose, S. Moreau and F. Duchaine. Large Eddy Simulation of a scale-model turbofan for fan noise source diagnostic. In 22nd AIAA/CEAS Aeroacoustics Conference. 30 May - 1 June 2016. Lyon, France.

34. L.M. Segui, L.Y.M. Gicquel, F. Duchaine and J. de Laborderie. LES of the LS89 cascade: influence of inflow turbulence on the flow predictions. In Proceedings of 12th European Conference on Turbomachinery Fluid dynamics & Thermodynamics ETC12, April 3-7, 2017; Stockholm, Sweden.

35. J. de Laborderie, F. Duchaine and L. Gicquel. Analysis of a high-pressure multistage axial compressor at off-design conditions with coarse Large-Eddy Simulation. In Proceedings of 12th European Conference on Turbomachinery Fluid dynamics & Thermodynamics ETC12, April 3-7, 2017; Stockholm, Sweden.

36. N. Odier, F. Duchaine, L. Gicquel, G. Dufour, N. Garcia Rosa LES validation in an actual fan configuration through experimental and RANS comparison. In Proceedings of 12th European Conference on Turbomachinery Fluid dynamics & Thermodynamics ETC12, April 3-7, 2017; Stockholm, Sweden.

37. T. Grosnickel, F. Duchaine, L.Y.M Gicquel and C. Koupper. Large-Eddy Simulations of static and rotating ribbed channels in adiabatic and isothermal conditions. GT2017-64241. In ASME Turbo Expo 2017, Charlotte, NC, USA.

38. M. Harnieh, L.Y.M. Gicquel and F. Duchaine. Sensitivity of Large-Eddy Simulations to inflow condition and modeling if applied to a transonic high-pressure cascade vane. GT2017-64686. In ASME Turbo Expo 2017, Charlotte, NC, USA.

39. F. Duchaine. Sensitivity analysis of heat transfer in a honeycomb acoustic liner to inlet conditions with Large-Eddy Simulation. GT2017-63243. In ASME Turbo Expo 2017, Charlotte, NC, USA.

40. F. Duchaine, J. Dombard, L.Y.M. Gicquel and C. Koupper. Integrated Large-Eddy Simulation of combustor and turbine interactions: effect of turbine stage inlet conditions. GT2017-63473. In ASME Turbo Expo 2017, Charlotte, NC, USA.

41. P. Aillaud, F. Duchaine, L.Y.M. Gicquel and S. Didorally. Characterization of the surface curvature effect using LES for a single impinging jet. GT2017-64159. In ASME Turbo Expo 2017, Charlotte, NC, USA.

42. M. Thomas, A. Dauptain, F. Duchaine, L.Y.M. Gicquel and C. Koupper. Heterogeneous coolant injection model for Large-Eddy Simulation of multiperforated liners present in a combustor simulator. GT2017-64622. In ASME Turbo Expo 2017, Charlotte, NC, USA.

43. M. Thomas, F. Duchaine, L.Y.M. Gicquel and C. Koupper. Advanced statistical analysis estimating the heat load issued bu hot streaks and turbulence on a high-pressure vane in the context of adiabatic Large-Eddy Simulations. GT2017-64648. In ASME Turbo Expo 2017, Charlotte, NC, USA.

44. P. Aillaud, F. Duchaine, G. Staffelbach and L.Y.M Gicquel. Large Eddy Simulation of trailing edge cutback film cooling: Impact of internal stiffening ribs on the adiabatic effectiveness. In 7th European Conference for Aeronautics and Space Sciences, 3 - 6 July, 2017 - Milan, Italy.

8.5 Papers presented at meeting without reviews

1. F. Duchaine, L.Y.M. Gicquel, D. Bissières, C. Bérat, and T.J. Poinsot. Automatic Design Optimization Applied to Lean Premixed Combustor Cooling. In 1st Workshop INCA, pages 295-304, SNECMA Villaroche, France, 2005.

2. F. Duchaine, S. Mendez, F. Nicoud, A. Corpron, V. Moureau, and T. Poinsot. Conjugate heat transfer with large eddy simulation. Application to gas turbine components. In 2ème Colloque INCA, CORIA, Rouen, France, 2008.

3. R. Fransen, E. Collado Morata, F. Duchaine, N. Gourdain, L.Y.M. Gicquel, L. Vial and G. Bonneau. Comparison of RANS and LES in high pressure turbines. In 3Ŕme Colloque INCA, ONERA, Toulouse, France, 2011.

4. A. Dauptain, G Frichet, F. Duchaine, E. Riber, G. Dejean, T. Poinsot. Transferring Large Eddy Simulation tools from laboratories experts to industry users: a challenge for the INCA community. In 3Ŕme Colloque INCA, ONERA, Toulouse, France, 2011.

5. J. Amaya, D. Poitou, E. Collado, F. Duchaine, B. Cuenot and T. Poinsot. Couplage combustion - thermique structure - rayonnement. In Journée SFT Rayonnement thermique en milieu semi-transparent, Lyon, France, 2011.

6. S. Ricci, A. Piacentini, R. Ata, N. Goutal, E. Razafindrakoto, F. Zaoui, M. Gant, T. Morel, F. Duchaine, O. Thual. A variational Data Assimilation algorithm to better estimate the salinity for the Berre lagoon with Telemac3D. Workshop Telemac-Mascaret. 2012.

7. F. Cadieux, J.A. Domaradzki, T. Sayadi, S. Bose, F. Duchaine. DNS and LES of Separated Flows at Moderate Reynolds Numbers. Bulletin of the American Physical Society. 65th Annual Meeting of the APS Division of Fluid Dynamics Volume 57, Number 17. 2012.

8. S. Berger, F. Duchaine, L. Gicquel and S. Richard. Aerothermal prediction of an aeronautical combustion chamber based on the coupling of Large Eddy Simulation, solid conduction and radiation numerical solvers. 15th International Conference on Numerical Combustion. Avignon, France. April 19-22, 2015.

9. M. Rochoux, B. Cuenot, F. Duchaine, E. Riber, D. Veynante and N. Darabiha. Analysis of Large Eddy Simulations of a laboratory-scale fire. 15th International Conference on Numerical Combustion. Avignon, France. April 19-22, 2015.

10. T. Poinsot, B. Cuenot, L. Gicquel, G. Staffelbach, A. Dauptain and F. Duchaine. Using LES of ignition, quenching and instabilities to design future gas turbines. 15th International Conference on Numerical Combustion. Avignon, France. April 19-22, 2015.